A Multiwavelength Study of the Intracluster Medium and the Characterization of the Multiwavelength Sub/millimeter Inductance Camera

Thesis by

Seth Robert Siegel

In Partial Fulfillment of the Requirements

for the Degree of

Doctor of Philosophy

California Institute of Technology

Pasadena, California

2016

(Defended July 14, 2015)

To Mom, Dad, Caitlin, and Brittany.

Acknowledgments

I am truly fortunate to have studied physics at Caltech and observed at the Caltech Submillimeter Observatory. The highlight of the past six years has been working alongside many outstanding scientists, from whom I have learned an enormous amount and to whom I will now attempt to convey my sincere appreciation.

I would like to express my deepest gratitude to my advisor, Sunil Golwala, who offered me the opportunity to work on an exciting project, provided unwavering guidance and support, and allowed me the freedom to investigate my ideas and develop my interests. Sunil was always eager to meet and discuss my work. He ensured that I had countless opportunities to present my research to others and to grow professionally. I honestly could not imagine a better advisor. I am amazed at the breadth of his knowledge, his experimental creativity, his perseverance, and his enthusiasm. I aspire to one day be a physicist and leader of the same caliber.

I am indebted to Jack Sayers, who acted as mentor and role model throughout my graduate school career. During my first year, he taught me all about our camera as we outfitted its cryostat at JPL. During my last year, he coached me on presenting my results at conferences. Jack took a central advisory role on the multiwavelength analysis of galaxy clusters that constitutes the first part of this thesis. I admire his focus, dedication, and grasp of our field. I will follow his example as I transition into the next phase of my career.

I would like to thank Nicole Czakon, Matt Hollister, and Ran Duan for training me in the lab and teaching me everything I know about cryogenics and microwave/RF engineering. Nicole took me under her wing the first two years of graduate school. She was quick to challenge my ideas and have me explain my motivations and reasoning, which forced me to work hard to genuinely understand my research. She was always happy to extend an invitation to a social event; I greatly valued her friendship. Matt was the go-to-person for any question or problem I encountered in the lab and also a great person to grab a beer with. I enjoyed his sense of humor and cynicism. Ran Duan was the source of many fun conversations during which I learned all about our readout electronics.

I would like to thank my officemates Zeeshan Ahmed, David Moore, Randol Aikin, Becky Tucker, Brett Cornell, Bade Uzgil, Alicia Lanz, and Chenguang Ji for making Cahill 361 an enjoyable place to work. I would like to thank the ObsCos group as a whole for providing a unique and exciting atmosphere to study observational cosmology. I benefitted immensely from discussions with Michael Zemcov, Tom Downes, Omid Noroozian, David Miller, and James Schlaerth.

It has been a true pleasure to work with our collaborators at the University of Colorado. Amandeep Gill, Clint Bockstiegel, Spencer Brugger, Jordan Wheeler, and Phil Maloney were superb team members and observing partners. Time spent on Mauna Kea was often stressful and exhausting. Still, I look back on it fondly, in part because of their company. I am extremely fortunate to have had Jason Glenn as a mentor. He offered a unique perspective on my research and professional development that I greatly appreciated.

None of the work presented here would have been possible without the staff of the Caltech Submillimeter Observatory. Much of the data used to characterize the MUSIC detectors was collected at the CSO with the help of Ed Bufil and Steve Baca. Simon Radford kept the entire operation running and was sympathetic to our desire to understand our camera. The result is the second part of this thesis.

I would like to thank Jonas Zmuidzinas for illuminating discussions on superconducting detectors. Andisheh Mahdavi is due special thanks for not only allowing me to use the joint analysis of cluster observations software, but also providing in-person tutorials. He was an excellent host during my visits to San Francisco.

I am grateful to Jonas Zmuidzinas, Phil Hopkins, Richard Ellis, and James Bartlett for serving on my candidacy exam and thesis defense committees. They remained engaged throughout my lengthy talks, asking important questions and providing many helpful ideas and criticisms.

Kathy Deniston provided administrative assistance throughout my graduate school career. She dealt with countless fellowship applications, travel plans, and expense reports on my behalf. Thank you Kathy. I have enjoyed our chats about family, travel, and Caltech.

This thesis is dedicated to my family, who provided constant love and support over the past six year. They helped me through many difficult times and believed in me when I did not believe in myself. I travelled across the country to study at Caltech, but thanks to their frequent visits and calls I never felt alone.

This research has been supported by a NASA Earth and Space Science Fellowship and a generous donation from the Gordon and Betty Moore Foundation.

Abstract

The first part of this thesis combines Bolocam observations of the thermal Sunyaev-Zeldovich (SZ) effect at 140 GHz with X-ray observations from *Chandra*, strong lensing data from the Hubble Space Telescope (HST), and weak lensing data from HST and Subaru to constrain parametric models for the distribution of dark and baryonic matter in a sample of six massive, dynamically relaxed galaxy clusters. For five of the six clusters, the full multiwavelength dataset is well described by a relatively simple model that assumes spherical symmetry, hydrostatic equilibrium, and entirely thermal pressure support. The multiwavelength analysis yields considerably better constraints on the total mass and concentration compared to analysis of any one dataset individually. The subsample of five galaxy clusters is used to place an upper limit on the fraction of pressure support in the intracluster medium (ICM) due to nonthermal processes, such as turbulent and bulk flow of the gas. We constrain the nonthermal pressure fraction at r_{500c} to be < 0.11 at 95% confidence, where r_{500c} refers to radius at which the average enclosed density is 500 times the critical density of the Universe. This is in tension with state-of-the-art hydrodynamical simulations, which predict a nonthermal pressure fraction of ≈ 0.25 at r_{500c} for the clusters in this sample.

The second part of this thesis focuses on the characterization of the Multiwavelength Sub/millimeter Inductance Camera (MUSIC), a photometric imaging camera that was commissioned at the Caltech Submillimeter Observatory (CSO) in 2012. MUSIC is designed to have a 14 arcminute, diffraction-limited field of view populated with 576 spatial pixels that are simultaneously sensitive to four bands at 150, 220, 290, and 350 GHz. It is well-suited for studies of dusty star forming galaxies, galaxy clusters via the SZ Effect, and galactic star formation. MUSIC employs a number of novel detector technologies: broadband phased-arrays of slot dipole antennas for beam formation, on-chip lumped element filters for band definition, and Microwave Kinetic Inductance Detectors (MKIDs) for transduction of incoming light to electric signal. MKIDs are superconducting micro-resonators coupled to a feedline. Incoming light breaks apart Cooper pairs in the superconductor, causing a change in the quality factor and frequency of the resonator. This is read out as amplitude and phase modulation of a microwave probe signal centered on the resonant frequency. By tuning each resonator to a slightly different frequency and sending out a superposition of probe signals, hundreds of detectors can be read out on a single feedline. This natural capability for large scale, frequency domain multiplexing combined with relatively simple fabrication makes MKIDs a promising low temperature detector for future kilopixel sub/millimeter instruments. There is also considerable interest in using MKIDs

for optical through near-infrared spectrophotometry due to their fast microsecond response time and modest energy resolution. In order to optimize the MKID design to obtain suitable performance for any particular application, it is critical to have a well-understood physical model for the detectors and the sources of noise to which they are susceptible. MUSIC has collected many hours of on-sky data with over 1000 MKIDs. This work studies the performance of the detectors in the context of one such physical model. Chapter 2 describes the theoretical model for the responsivity and noise of MKIDs. Chapter 3 outlines the set of measurements used to calibrate this model for the MUSIC detectors. Chapter 4 presents the resulting estimates of the spectral response, optical efficiency, and on-sky loading. The measured detector response to Uranus is compared to the calibrated model prediction in order to determine how well the model describes the propagation of signal through the full instrument. Chapter 5 examines the noise present in the detector timestreams during recent science observations. Noise due to fluctuations in atmospheric emission dominate at long timescales ($\lesssim 0.5$ Hz). Fluctuations in the amplitude and phase of the microwave probe signal due to the readout electronics contribute significant $1/f$ and drift-type noise at shorter timescales. The atmospheric noise is removed by creating a template for the fluctuations in atmospheric emission from weighted averages of the detector timestreams. The electronics noise is removed by using probe signals centered off-resonance to construct templates for the amplitude and phase fluctuations. The algorithms that perform the atmospheric and electronic noise removal are described. After removal, we find good agreement between the observed residual noise and our expectation for intrinsic detector noise over a significant fraction of the signal bandwidth.

Contents

Part I

A Multiwavelength Study of the Intracluster Medium

Chapter 1

Spherical Analysis of the CLASH Sample

1.1 Introduction

Galaxy clusters occupy a unique position in the Universe as the largest objects to have undergone gravitational collapse. This makes them a powerful tool for understanding the hierarchical process of structure formation and the cosmological backdrop in which it occurred. The number of clusters above a given mass as a function of redshift is sensitive to the dynamical properties of the dark energy that comprises 73% of the energy density of the Universe and drives its acceleration. This is because dark energy counteracts gravitational attraction, thereby slowing structure formation and exhibiting a strong influence over the resulting number of massive clusters. Consequently, cluster number counts $N(M,z)$ can constrain the dark energy density Ω_Λ and its equation of state w, as well as the average matter density Ω_M and the amplitude of the initial density perturbations σ_8 [1, 2, 3].

As large nonlinear excursions in the matter density field, clusters are individually identifiable objects with a wealth of observables through which they can be detected and studied. They are populated with luminous galaxies that emit light in the optical and infrared regions of the spectrum. They also gravitationally lens the light emitted from background galaxies. The vast majority ($\sim 90\%$) of a cluster's baryonic mass lies not in galaxies and stars but rather in a diffuse and hot, ionized gas known as the intracluster medium (ICM). This gas emits X-rays through thermal bremsstrahlung radiation [4] and inverse-Compton scatters Cosmic Microwave Background (CMB) photons through the thermal Sunyaev-Zel'dovich (SZ) effect [5].

The net result of the SZ effect is a small distortion of the CMB spectrum in the direction of a cluster. The distortion manifests itself as a temperature decrement at low frequencies and an increment at high frequencies, with a null at $\nu \simeq 220$ GHz or $\lambda \simeq 1.36$ mm. The magnitude of the temperature change at any given frequency is proportional to the thermal electron pressure $P_e = k_B n_e T_e$ integrated along the line of sight. This simple linear relationship makes the SZ effect an ideal probe of the ICM gas pressure. X-ray surface brightness, on the other hand, is proportional to a slightly different combination of the number density and temperature

— specifically $n_e^2 T_e^{1/2}$ — and thus provides a slightly different probe of the ICM thermal state, one that is extremely sensitive to the electron density.

The hydrodynamical state of the ICM can be predicted from analytical considerations and, more often, from numerical simulations. However, it is not yet known how well these simulations account for many of the complicated but relevant baryonic processes that take place during cluster formation. These include star formation, energy loss via radiative cooling, energy injection and metal enrichment via active galactic nuclei and supernovae winds, and nonthermal processes at the cluster outskirts such as turbulence, bulk flow, and incomplete virialization. These processes are most certainly occurring in clusters, but their relative importance and impact on the basic thermal characteristics of the ICM are poorly characterized. Our lack of knowledge is especially evident in the cluster outskirts, where there is sparse observational data to ground the predictions made by hydrodynamical simulations.

In our current understanding of cluster formation, an initial fast collapse and series of major mergers is followed by slow growth of the cluster outskirts through accretion of the surrounding intergalactic medium (IGM). The cold IGM infalls at supersonic speeds and is shock heated near the virial radius. These accretion shocks are strong, thermalizing the majority of the kinetic energy acquired by the gas during infall. Recent work suggests, however, that this mechanism does not result in complete virialization, and that some fraction of the kinetic energy remains in bulk, turbulent flow of the gas [6]. This turbulent component contributes to the total pressure required to maintain the ICM in a state of hydrostatic equilibrium, but is nonthermal in nature. Recent numerical simulations predict the nonthermal component to contribute $10-30\%$ of the total pressure at the virial radius, and an even larger fraction in unrelaxed clusters [7, 8, 9].

Quantifying the level of nonthermal support is of critical importance if one is to use clusters to perform precision cosmology. Recently, the South Pole Telescope used maps of 800 deg^2 of sky at 95, 150, and 220 GHz to remove astrophysical foregrounds and measure the CMB power spectrum at angular scales $2,000 < \ell < 9,400$. They found excess power over the primary CMB anisotropy in the 150 GHz band due to the SZ effect, and measured the amplitude of the thermal SZ power spectrum at $\ell = 3000$ to be $3.65 \pm 0.69\ \mu\mathrm{K}^2$ [10]. The amplitude of the thermal SZ power spectrum is sensitive to several parameters in the standard ΛCDM cosmology, primarily the amplitude of the initial density perturbations σ_8. However, in order to predict how much power one should expect to see in the thermal SZ signal for a given cosmology, one must know the level of nonthermal support in clusters over a wide range of masses and redshifts, and at large radii. Current simulations differ in their treatment of the cluster thermal state and thus vary by over 50% in their predictions of the thermal SZ amplitude [11]. As a result, theoretical modeling uncertainties limited the constraint on σ_8 that could be derived from this measurement, offering only marginal improvements over the existing constraint from measurements of the CMB, H_0, and BAO.

As another example, the most stringent cosmological constraints derived from cluster abundances to date have been made using X-ray constructed catalogs [12, 13]. In these analyses the X-ray observables that are measured — such as T_X, Y_X, and $M_{\rm gas}$ — must be related to the underlying cluster mass that our theories and

numerical simulations predict. In order to do this, one must invert the equation of hydrostatic equilibrium assuming that the entirety of the ICM pressure is thermal in nature. A nonthermal component will bias low the resulting estimates of the total mass by tens of percent [14, 7]. Moreover, since the actual amount of nonthermal pressure support and its variation between clusters is so poorly constrained observationally, and since hydrodynamical simulations offer different predictions based on the input physics, a simple correction for this nonthermal component is difficult to make. Instead this possible bias is usually included as a systematic uncertainty in the analyses, which degrades the precision of the observable-mass relation and the resulting cosmological parameters. The same is true for recent and ongoing SZ cluster surveys that use the integrated SZ flux as a proxy for total cluster mass. Benson et al found that the cosmological constraints that could be derived from the SPT survey consisting of only 18 clusters was not limited by sample size, but rather by the assumed systematic uncertainty on the normalization of the observable-mass relation [15].

The Cluster Lensing and Supernova survey with Hubble (CLASH) was awarded 524 orbits on the *Hubble Space Telescope* over a three year period to study the distribution of dark matter at cluster scales via gravitational strong lensing [16]. The CLASH sample consists of 25 clusters, of which 20 were selected from X-ray data alone. These 20 clusters have large X-ray temperatures $T_X > 5$ keV and surface brightness maps characterized by a single well-defined peak and nearly concentric isophotes. This suggests that the clusters are massive, dynamically relaxed, and not undergoing major mergers. The other 5 clusters were chosen based on the presence of large Einstein radii and also serve the separate science goal of discovering magnified high-z galaxies at $z > 7$. The sample as a whole covers a significant portion of cluster formation history $(0.2 < z < 0.9)$ and spans almost an order of magnitude in mass $(5 - 30 \times 10^{14}\ \mathrm{M}_{\odot})$.

The CLASH sample is the most comprehensive and detailed dataset to date on the distribution of dark and baryonic matter in massive galaxy clusters. All 25 clusters have been observed with the *Chandra X-ray Observatory* and 15 of the clusters also have XMM-Newton data available. The thermal SZ effect has been measured at 140 GHz for all 25 of the clusters with Bolocam, a millimeter-wave imaging camera at the Caltech Submillimeter Observatory. HST provides 16-band, high-precision strong lensing data in the cluster core and weak lensing data at intermediate radii, while the multi-band Suprime camera on Subaru provides wide-field weak lensing data of the outskirts, thereby characterizing the dark matter distribution over a wide range of scales. In this chapter, we fit parametric models to the combined multiwavelength dataset for a subset of the CLASH clusters. Doing so we are able to constrain the distribution of dark and baryonic matter and the level of nonthermal pressure support.

The layout of this chapter is as follows. Section 1.2 presents the theoretical model used to describe the multiwavelength dataset. Section 1.3 provides an overview of the Bolocam observations of the SZ effect, *Chandra* observations of the X-ray emission, HST gravitational strong lensing measurements, and HST and Subaru weak lensing measurements. Section 1.4 describes the specifics of our analysis: the fitting method employed, the definition of our sample, and the determination of the optimal sub-model. Section 1.5 presents the results and Section 1.6 concludes with a discussion of the results. Throughout this work we assume a ΛCDM

cosmology with $\Omega_m = 0.30$, $\Omega_\Lambda = 0.70$, and $h \equiv 0.70 \times h_{70} = 0.70$, where $H_0 = h \times 100$ km s^{-1} Mpc^{-1}.

1.2 Model

Our model assumes that the galaxy cluster is spherically symmetric. We model the total matter density with the Navarro-Frenk-White profile (NFW hereafter) [17]

$$\rho_{\rm tot}(r) = \rho_{\rm tot,0} \left(\frac{r}{r_s}\right)^{-1} \left(1+\frac{r}{r_s}\right)^{-2} , \tag{1.1}$$

which is defined by two parameters, a normalization $\rho_{\rm tot,0}$ and scale radius r_s. It is standard to reparameterize in terms of the total mass and concentration at a particular overdensity radius

$$M_{\rm tot,\,\Delta ref} \equiv 4\pi r_s^3 \rho_{\rm tot,0} \left[\ln\left(\frac{r_s + r_{\Delta\rm ref}}{r_s}\right) - \frac{r_{\Delta\rm ref}}{r_s + r_{\Delta\rm ref}}\right] , \qquad c_{\Delta\rm ref} \equiv \frac{r_{\Delta\rm ref}}{r_s} , \tag{1.2}$$

where $r_{\Delta\rm ref}$ denotes the radius at which the average enclosed density is Δ times some reference density. Two common references, both of which we will employ in this work, are the critical density of the universe and the mean matter density of the universe

$$\rho_c(z) = \frac{3H_0^2}{8\pi G}(\Omega_m(1+z)^3 + \Omega_\Lambda), \tag{1.3}$$

$$\rho_m(z) = \frac{3H_0^2}{8\pi G}\Omega_m(1+z)^3 . \tag{1.4}$$

The overdensity radius is determined by solving the implicit equation

$$M_{\rm tot,\,\Delta ref} = \frac{4}{3}\pi r_{\Delta\rm ref}^3 \Delta\rho_{\rm ref} . \tag{1.5}$$

We model the gas density as

$$\rho_{\rm gas}(r) = \rho_{\rm gas,0} \left(\frac{r}{r_x}\right)^{-\alpha} \left(1+\left(\frac{r}{r_x}\right)^2\right)^{(\alpha-3\beta)/2} \left(1+\left(\frac{r}{r_o}\right)^\delta\right)^{-\varepsilon/\delta} + \rho_{\rm gas,c} \left(1+\left(\frac{r}{r_c}\right)^2\right)^{-3\beta_c/2} , \tag{1.6}$$

which is inspired by the expression used in Vikhlinin et al. [18] to describe the X-ray surface brightness of nearby relaxed galaxy clusters. Equation (1.6) is the sum of two β-models [19], with the first β-model modified by two additional factors. The $r^{-\alpha}$ power-law factor allows for a central cusp instead of the flat core inherent to the β-model. This is necessary to describe cool-core clusters, which tend to exhibit a nonzero logarithmic slope $\alpha \approx 0.5$ in the cluster core [20]. The $r^{-\varepsilon}$ factor allows for the logarithmic slope of the gas density to steepen by some amount ε at radius r_o (with $r_o > r_x$). The parameter δ controls how quickly the gas density transitions from the $r^{-3\beta}$ power-law to the $r^{-3\beta-\varepsilon}$ power-law. Steepening of the gas density profile in

the cluster outskirts is observed in hydrodynamical simulations [21], X-ray observations of individual clusters [22, 23, 18, 24, 20], and the stacked analysis of X-ray data from many clusters [25]. Our primary motivation for including this factor, however, is that it results in more realistic uncertainty estimates on the gas density profile at large radii where we do not have X-ray data. The second β-model aids in the description of the core region of the cluster. To ensure this role we force $r_c < 50$ kpc and fix $\beta_c = 1$. We note that our model differs from that presented in Vikhlinin et al. [18] in two regards. First, we assume a value $\delta = 4$ which results in a slightly more rapid transition than their model which assumes a value $\delta = 3$. Second, we model the gas density $\rho_{\rm gas}$ whereas they model the surface brightness, which is proportional to $\rho^2_{\rm gas}$. Hence, our prediction for the surface brightness will have a cross-term between the first and second β-model that is not present in their model. This will result in slightly different gas density profiles for the same set of parameter values in the region where the core β-model transitions to the primary β-model.

We assume that the total pressure is the sum of the thermal pressure and the nonthermal pressure due to internal gas motions

$$P_{\rm tot} = P_{\rm th} + P_{\rm nth} \tag{1.7}$$

$$= \frac{k_B T \rho_{\rm gas}}{\mu m_p} + P_{\rm nth} \ . \tag{1.8}$$

Here m_p is the proton mass, μ is the mean molecular weight of the ICM, and T is the temperature of the ICM. We model the nonthermal pressure fraction as

$$\frac{P_{\rm nth}}{P_{\rm tot}}(r) \equiv \mathcal{F}(r) = \mathcal{F}_{\rm out}(r) + \mathcal{F}_{\rm in}(r) \tag{1.9}$$

with

$$\mathcal{F}_{\rm out}(r) = C\left\{1 - A\left(1 + \exp\left[\left(\frac{r/r_{200m}}{B}\right)^{\gamma}\right]\right)\right\} \tag{1.10}$$

and

$$\mathcal{F}_{\rm in}(r) = D\left(1 + \left(\frac{r/r_{200m}}{E}\right)^4\right)^{-\zeta/4} \ . \tag{1.11}$$

The $\mathcal{F}_{\rm out}$ term is a scaled version of the Nelson et al. [9] empirical fitting formula used to describe the mean nonthermal pressure fraction observed in a mass-limited sample of clusters from a high-resolution hydrodynamical simulation. We fix the radial dependence to that observed in the simulation by fixing the parameters $[A,\ B,\ \gamma]$ at their best fit values $[0.452,\ 0.841,\ 1.628]$, and allow only the normalization C to float. The $\mathcal{F}_{\rm in}$ term allows the nonthermal pressure fraction to increase by some amount D in the cluster core. We require that $E < 0.1$, which corresponds to the minimum radius examined in the simulation. There are a number of

physical processes that can strongly influence the thermodynamic state of the ICM in the cluster core. Our goal in introducing the second term is to decouple the nonthermal pressure in the outer regions of the cluster, which is the quantity we would like to constrain, from that in the core.

We assume that the ICM is in a state of equilibrium where the inward gravitational pull is balanced by a pressure gradient. This assumption of hydrostatic equilibrium is expressed as the following differential equation:

$$\nabla P_{\rm tot} = -\rho_{\rm gas} \nabla \Phi \ , \tag{1.12}$$

where Φ is the gravitational potential. We note that Equation (1.12) differs from the standard definition of hydrostatic equilibrium that is commonly used in the literature and implies entirely thermal pressure support. We are allowing a nonthermal pressure component sourced by bulk and turbulent motions of the gas to provide some fraction of the support necessary to prevent gravitational collapse. We integrate Equation (1.12) to determine the temperature,

$$\begin{aligned} \frac{d}{dr}\left[\frac{1}{1-\mathcal{F}(r)}\frac{\rho_{\rm gas}(r) k_B T(r)}{\mu m_p}\right] &= -\frac{G M_{\rm tot}(r)\rho_{\rm gas}(r)}{r^2} \\ k_B T(r) = k_B T_{\rm trunc} &+ (1-\mathcal{F}(r))\frac{\mu m_p}{\rho_{\rm gas}(r)}\int_r^{r_{\rm trunc}} \frac{G M_{\rm tot}(x)\rho_{\rm gas}(x)}{x^2} dx \ , \end{aligned} \tag{1.13}$$

where G is the gravitational constant, k_B is the Boltzmann constant, and $T_{\rm trunc}$ is the temperature at some radius $r_{\rm trunc}$ that designates the outer boundary of the ICM. Our model does not assume an explicit parameterization for the temperature, rather it is an internal variable that is derived from the total density, gas density, and nonthermal pressure fraction assuming hydrostatic equilibrium.

We describe the metallicity with the function

$$\frac{Z}{Z_\odot}(r) = Z_0 \left(1 + \left(\frac{r}{r_Z}\right)^2\right)^{-3\beta_Z/2} \ , \tag{1.14}$$

which allows for a central metallicity Z_0 that transitions to a power-law $r^{-3\beta_Z}$ at radius r_Z [26]. The electron and hydrogen number density are given by

$$n_H = \frac{X\rho_{\rm gas}}{m_p} \ , \qquad\qquad n_e = \left\langle \frac{n_e}{n_H} \right\rangle \frac{X\rho_{\rm gas}}{m_p} \ , \tag{1.15}$$

where X denotes the hydrogen mass fraction and $< n_e/n_H >$ the ion to hydrogen ratio. The quantities μ, X, and $< n_e/n_H >$ are all mild functions of the metallicity, and are calculated using an absolute metallicity given by Equation (1.14) with the relative abundances fixed on the Grevesse and Sauval [27] scale.

All observable quantities of interest can be predicted from the above model. Let $D_A(z)$ denote the angular diameter distance, θ the angular separation from the cluster center, and $R = D_A\theta$ the radius from the cluster

center projected on the plane of the sky. The X-ray flux from the cluster measured at a frequency ν within an annulus of inner radius R_1 and outer radius R_2 is given by

$$F = \frac{1}{4\pi D_L^2} \int_{R_1}^{R_2} 2\pi R dR \int_R^{r_{\rm trunc}} n_e(r) n_H(r) \Lambda\left[\nu', T(r), Z(r)\right] \frac{2rdr}{\sqrt{r^2 - R^2}} \,, \tag{1.16}$$

where $D_L(z)$ is the luminosity distance, $\nu' = \nu/(1+z)$ is the frequency in the cluster rest frame, and $\Lambda[\nu', T(r), Z(r)]$ is the X-ray cooling function. In addition to the X-ray flux from the cluster our model includes X-ray flux from a uniform thermal background:

$$F_{\rm sbkg} = A_{\rm sbkg}\, \Lambda\left[\nu, T_{\rm sbkg}, Z_\odot\right] \,. \tag{1.17}$$

This accounts for galactic soft X-ray emission which varies across the sky and therefore is not adequately subtracted using a background observation. Here $A_{\rm sbkg}$ acts as an overall normalization and $T_{\rm sbkg} \sim 0.5$ keV is the temperature of the galactic gas.

The thermal SZ effect results in a distortion of the CMB blackbody spectrum. The change in the temperature of the CMB measured at a frequency ν and projected radius R is given by

$$T_{\rm SZ} = T_{\rm CMB} f(x) y \,. \tag{1.18}$$

The function $f(x)$ encodes the frequency dependence of the classical distortion

$$f(x) = x \frac{e^x + 1}{e^x - 1} - 4 \,, \tag{1.19}$$

where $x \equiv h\nu/k_B T_{\rm CMB}$. The Compton y parameter sets the magnitude of the distortion and is proportional to the integral of the thermal electron pressure along the line of sight

$$y = \frac{\sigma_T}{m_e c^2} \int_R^{r_{\rm trunc}} n_e(r) k_B T(r) \left[1 + \delta_R(x, T(r))\right] \frac{2rdr}{\sqrt{r^2 - R^2}} \,, \tag{1.20}$$

where σ_T is the Thomson cross section, c is the speed of light, and m_e is the mass of the electron. The quantity $\delta_R(x, T(r))$ is a correction for the relativistic motion of the electrons, which we approximate using the expansion given in Itoh et al. [28].

Gravitational lensing of the light from background galaxies is described by a lens equation $\boldsymbol{\beta} = \boldsymbol{\theta} - \boldsymbol{\alpha}(\boldsymbol{\theta})$ which maps the coordinates of the galaxy in the source plane $\boldsymbol{\beta} = [\beta_1, \beta_2]$ to the coordinates in the lens plane $\boldsymbol{\theta} = [\theta_1, \theta_2]$ through a deflection angle $\boldsymbol{\alpha} = [\alpha_1, \alpha_2]$. We can define a lensing potential

$$\Psi(\boldsymbol{\theta}) = \frac{D_{ls}}{D_l D_s} \frac{2}{c^2} \int_{-\infty}^{\infty} \Phi(R, \ell) d\ell \,, \tag{1.21}$$

which is just the three-dimensional gravitational potential projected along the line of sight and rescaled. In the

above equation D_s, D_l, and D_{ls} denote the angular diameter distance between observer-source, observer-lens, and lens-source, respectively. The deflection angle is then equal to the gradient of the lensing potential

$$\boldsymbol{\alpha}(\boldsymbol{\theta}) = \nabla\Psi(\boldsymbol{\theta}) \; . \tag{1.22}$$

The convergence κ and complex shear $\gamma = [\gamma_1, \gamma_2]$ of the lens are also related to the lensing potential through the equations

$$\kappa(\boldsymbol{\theta}) = \frac{1}{2}\left(\frac{\partial^2}{\partial\theta_1^2} + \frac{\partial^2}{\partial\theta_2^2}\right)\Psi(\boldsymbol{\theta}) = \frac{\Sigma(\boldsymbol{\theta})}{\Sigma_{\rm crit}} \tag{1.23}$$

$$\gamma_1(\boldsymbol{\theta}) = \frac{1}{2}\left(\frac{\partial^2}{\partial\theta_1^2} - \frac{\partial^2}{\partial\theta_2^2}\right)\Psi(\boldsymbol{\theta}) \tag{1.24}$$

$$\gamma_2(\boldsymbol{\theta}) = \frac{\partial}{\partial\theta_1}\frac{\partial}{\partial\theta_2}\Psi(\boldsymbol{\theta}) \; . \tag{1.25}$$

Here $\Sigma(\boldsymbol{\theta})$ is the surface mass density and $\Sigma_{\rm crit}$ is the critical surface mass density for lensing, given by

$$\Sigma_{\rm crit} = \frac{c^2}{4\pi G}\frac{D_s}{D_{ls}D_l} \; , \tag{1.26}$$

where G is the gravitational constant.

In the weak lensing regime ($\kappa \ll 1$) the gravitational shear introduces a complex ellipticity $\boldsymbol{e}$ to the images of background galaxies

$$< \boldsymbol{e} >= \frac{\gamma}{1-\kappa} \; , \tag{1.27}$$

where $< \boldsymbol{e} >$ denotes a local average necessary to mitigate the intrinsic ellipticity of the galaxies. In the strong lensing regime ($\kappa > 1$) the lens equation becomes multi-valued, which can result in multiple images of a single source. These multiple images straddle critical curves whose location are set by the relation

$$(1-\kappa)^2 - \gamma^2 = 0 \; . \tag{1.28}$$

The combined strong and weak lensing analysis outlined in the following section employs the location of the critical curves and the ellipticity of background galaxies to measure the convergence of the galaxy cluster. According to our model the convergence measured at a projected radius R is given by

$$\kappa = \frac{1}{\Sigma_{\rm crit}}\int_R^\infty \rho_{\rm tot}(r)\frac{2rdr}{\sqrt{r^2-R^2}} \; . \tag{1.29}$$

1.3 Description of the Multiwavelength Dataset

1.3.1 *Chandra* X-ray

The 25 CLASH clusters have been observed by the *Chandra* satellite with a median exposure time of 63 ksec. The reduction of the CLASH X-ray data is described in detail in Donahue et al. [29], which we now briefly summarize. The data is processed using CIAO 4.6.1 (released February 2014) and CALDB 4.5.9 (released November 2013). Flares are identified as time intervals with outlier event rates in $0.5-7.0$ keV light curves extracted from source-free areas of the detector. Events coincident with a flare are removed from the event lists. Bright point sources are identified using the CIAO *wavdetect* algorithm and a map of the PSF size as a function of location on the detector. Regions near the bright point sources are filtered from the event lists. Each dataset is matched to a deep background file from a similar observation epoch, which is used to subtract contamination from faint point sources, galactic soft X-ray emission, and non-flaring particle events [30, 31]. The background files are filtered, reprojected, and rescaled to match the target observation. The rescaling is done by adjusting the exposure time on the deep background file so that the event rate between $10-12$ keV is equal to that in the cluster field. This particular energy range is chosen because the effective area for X-ray photons is low and the event rate is dominated by high-energy particle events.

X-ray spectra are generated in concentric annular bins centered on the coordinates given in Table 1.1. The boundaries of the bins are selected so that at least 1500 photon counts from the cluster are contained in each annulus and the width of each annulus is at least a few times the width of the PSF. The spectra are binned in energy from $0.5-11.0$ keV with a bin width of 38 eV. The same binning scheme is applied to both the observation file and the deep background file. The individual weighted redistribution matrix file (RMFs) and ancillary response file (ARFs) are then computed. The cluster field spectra $\boldsymbol{S}^{\rm obs}$, deep background spectra $\boldsymbol{S}^{\rm bkg}$, RMFs, and ARFs are all input to the multiwavelength analysis.

The spectra generated from the deep background file are eventually subtracted from the spectra generated from the target observation file. Consider the energy bin $h\nu_j$ and the annulus with inner radius R_i and outer radius R_{i+1}. The resulting X-ray measurement is

$$S_{ij} = S_{ij}^{\rm obs} - S_{ij}^{\rm bkg} \tag{1.30}$$

and the associated Poisson error is

$$\sigma_{S_{ij}} = \sqrt{S_{ij}^{\rm obs} + S_{ij}^{\rm bkg}} \tag{1.31}$$

with units of counts/sec/keV.

1.3.2 Bolocam Thermal SZ Effect

The thermal SZ effect has been measured at 140 GHz in the 25 CLASH clusters using Bolocam, a 144-element bolometric imaging camera at the Caltech Submillimeter Observatory [32, 33]. Bolocam has an 8 arcmin diameter circular field of view (FOV) and a 58 arcsec full width at half maximum point spread function (PSF). The measurements were made over the course of 14 observing runs between 2006 and 2012 as part of a larger campaign that resulted in the creation of the Bolocam X-ray SZ (BOXSZ) sample of 45 galaxy clusters [34, 35]. We summarize the general properties of the SZ data products here, and direct the interested reader to Sayers et al. [36] for a description of the data reduction, flux calibration, and noise estimation, and Czakon et al. [35] for a description of the BOXSZ sample. The SZ data products for all of the clusters in the BOXSZ sample are publicly available. [1]

Noise sourced by fluctuations in atmospheric emission dominate the raw detector timestreams at long timescales. The atmospheric noise is mitigated by subtracting the response-weighted mean detector signal and applying a 250 mHz high pass filter [37]. This data processing attenuates the cluster signal in a way that is mildly dependent on the cluster shape and also results in the loss of the image's mean signal. To account for the attenuation of the cluster signal, a complex valued two-dimensional map space transfer function is calibrated for each cluster. The mean signal of the image is included as a free parameter $\bar{T}_{\rm SZ}$ in our model fits.

Pointing corrections are obtained from frequent observations of bright compact objects. The resulting pointing accuracy is 5 arcsec RMS. Flux calibration is based on twice-nightly observations of either Uranus, Neptune, or a secondary source from Sandell [38]. The absolute flux of the planetary sources are determined using the model of Griffin and Orton [39], with the overall normalization of the model corrected based on WMAP measurements [40] as outlined in Sayers et al. [41]. The resulting flux accuracy is 5% RMS.

Non-astronomical noise is estimated from 1000 jackknife realizations of the cluster image. To account for astronomical noise sourced by CMB anisotropies and unresolved point sources, a Gaussian random realization of the 140 GHz sky is generated from SPT power spectrum measurements [42, 10], passed through the data processing pipeline, and added to each of the 1000 jackknife realizations. Note that the SPT power spectrum measurements cover the full range of angular scales probed by the Bolocam images. It has been confirmed that the resulting noise realizations are statistically indistinguishable from observations of blank sky [36].

A total of six bright radio point sources are detected in the BOXSZ cluster images. These are fit with a template for the PSF and subtracted. In addition, radio point sources in the 1.4 GHz NVSS database [43] that are below the Bolocam detection threshold but have an extrapolated 140 GHz flux density > 0.5 mJy are also subtracted. The extrapolation is based on 1.4 GHz and 30 GHz measurements and has an uncertainty of $\simeq 30\%$. Random realizations of the estimated residual from the radio point source subtractions are injected into the set of jackknife realization. A description of the population of radio point sources in the BOXSZ

[1] `http://irsa.ipac.caltech.edu/data/Planck/release_2/ancillary-data/bolocam/`

cluster images can be found in Sayers et al. [34].

The pixel-to-pixel covariance matrix is estimated as

$$(\boldsymbol{C}_{T_{\rm SZ}})_{ij} = \begin{cases} \dfrac{(\text{sensitivity})^2}{t_i} & i = j \\ 0 & i \neq j \,, \end{cases}$$

where t_i is the (known) integration time for pixel i. The sensitivity is determined by fitting a Gaussian to a histogram of the product of pixel value and square root integration time for all pixels in all 1000 noise realizations. The assumption that the off-diagonal elements are zero is a good but not perfect description of the data. Unfortunately, the set of observations do not contain enough information to estimate the off-diagonal elements of the covariance matrix, and simplifying assumptions about the structure of the covariance matrix (e.g. that it is only a function of pixel separation) have proven false. Instead, we determine the effects that the small inter-pixel correlations in the SZ image have on our analysis by carrying out simulations using the 1000 noise realizations. We outline this procedure in Section 1.5.

The SZ images are 14 arcmin $\times$ 14 arcmin with 20 arcsec square pixels. The CLASH clusters have a median peak S/N of 10.6 and SZ signal is detected out to the edge of the images in azimuthally averaged profiles. For our analysis we only fit pixels that have an integration time $t > 0.25 \times t_{\rm max}$, where $t_{\rm max}$ is the maximum integration time achieved in the center of the image. This is equivalent to only fitting pixels with an angular separation $\theta \leq 6.33$ arcmin from the center of the image. The input to the multiwavelength analysis is the image $\boldsymbol{T}_{\rm SZ}$ in units of $\mu K_{\rm CMB}$, the diagonal covariance matrix $\boldsymbol{C}_{T_{\rm SZ}}$, and the transfer function of the data processing pipeline.

1.3.3 HST and Subaru Gravitational Lensing

The X-ray selected sample of CLASH clusters has HST strong lensing, HST weak lensing, and Subaru Suprime-Cam weak lensing constraints. Merten et al. [44] outlines the procedure used to self-consistently combine these constraints into a nonparametric estimate of the lensing convergence profile. We summarize the main steps of this procedure.

The strong lensing reduction begins by identifying multiple-image systems in the 16-band HST images using the Zitrin et al. [45] method. The redshift associated to each multiple-image system is either a spectroscopic redshift from the CLASH VLT-Vimos program [46], a Bayesian photometric redshift determined from HST photometry [47], or a value taken from the literature. The multiple-image systems are used to infer the location of the critical lines where the lensing equation becomes nonlinear using the method outlined in Merten et al. [48]. The locations of the critical lines are inputs to the reconstruction algorithm.

The weak lensing input take the form of a shear catalogs that list the coordinates, redshift, and complex ellipticity of background galaxies in the cluster field. The creation of the HST shear catalogs is outlined in Section 3.2 of Merten et al. [44] and the creation of the Subaru shear catalogs is outlined in Section 4 of

Umetsu et al. [49]. The HST and Subaru catalogs are combined into a single catalog. Before doing so, the HST complex ellipticity measurements are multiplied by a scale factor to refer them to the effective redshift of the Subaru catalog. The catalogs are concatenated and the signal-to-noise-weighted mean is computed for sources that appear in both catalogs.

The `SaWLens` algorithm [48] is used to perform a nonparametric reconstruction of the lensing potential $\psi(\boldsymbol{\theta})$ on an adaptively refined two-dimensional grid from the weak lensing shear catalog and the strong lensing critical lines. Three different grid sizes are employed: a coarse resolution grid ($25-36$ arcsec pixel) applicable to the wide field Subaru weak lensing data, an intermediate resolution grid ($8-13$ arcsec pixel) applicable to the HST weak lensing data, and a fine resolution grid ($6-10$ arcsec pixel) applicable to the HST strong lensing data. The lensing potential at each pixel of the grid is estimated by minimizing a χ^2 function that accounts for measurements of the average ellipticity of nearby background galaxies and the location of nearby critical lines. The assumption of spherical symmetry is not used in this reconstruction, nor are any other prior assumptions about the mass distribution of the cluster. The convergence of the lens $\kappa(\boldsymbol{\theta})$ is then obtained by taking second order numerical derivatives of the reconstructed lensing potential as prescribed by Equation (1.23). The `SaWLens` algorithm has been shown to recover the convergence (or, equivalently, surface mass density) of simulated clusters over a wide range of scales (50 kpc – several Mpc) with an accuracy of 10% [50].

The convergence map is azimuthally binned about the coordinates given in Table 1.1. The inner boundary is set by the resolution of the highest refinement level of the adaptive grid. The outer boundary is fixed at the angular scale corresponding to 2 Mpc$/h \approx 2.85$ Mpc$/h_{70}$. The radial range defined by these two boundaries is split into 15 bins, with the bin width decreasing as the level of refinement is increased.

Errors are estimated from 1000 resampled realizations of the $\kappa(\boldsymbol{\theta})$ map. Each realization is created by taking a boot-strap resampling of the shear catalog in the case of weak lensing and a random sampling of the allowed redshift range of the multiple-image systems in the case of strong lensing. The full reconstruction process and azimuthal binning is carried out on the 1000 realizations. The set is use to estimate the covariance matrix $\mathcal{C}$ of the 15 radial bins. The convergence profile $\boldsymbol{\kappa}$ and associated covariance matrix $\boldsymbol{C}_\kappa$ then act as input to the multiwavelength analysis.

The only difference in the procedure outlined above and that presented in Merten et al. [44] is that we center the convergence profile on the peak of the X-ray emission, rather than the peak of the convergence map. As a result, we measure a lower convergence in the innermost bin than what is presented in that work. The choice of center does not have a significant effect on the convergence profile beyond the innermost bin.

1.4 Method

1.4.1 Joint Analysis of Cluster Observations (JACO)

We use the Joint Analysis of Cluster Observations (JACO) software package to fit the model outlined in Section 1.2 to the X-ray, SZ, and lensing data described in Section 1.3. JACO provides a self-consistent framework for modeling and fitting multiwavelength observations of galaxy clusters [51]. The general principle underlying JACO is "forward model fitting". The data is manipulated as little as possible; instead the candidate model is projected, convolved, and filtered so that it can be compared to the data directly. The software is well tested; JACO has been used to examine X-ray and weak lensing scaling relations for a sample of 50 massive galaxy clusters in the Canadian Cluster Comparison Project (CCCP) [52]. It has also been used to estimate the hydrostatic mass, gas mass fraction, and ICM temperature from *Chandra* and XMM observations of the CLASH sample [29].

JACO employs a Markov Chain Monte Carlo (MCMC) algorithm to perform Metropolis-Hastings sampling of the joint posterior distribution

$$p(\boldsymbol{\theta}_p|\boldsymbol{S},\boldsymbol{T}_{\rm SZ},\boldsymbol{\kappa}) \propto \mathcal{L}(\boldsymbol{S},\boldsymbol{T}_{\rm SZ},\boldsymbol{\kappa}|\boldsymbol{\theta}_p)\,\pi(\boldsymbol{\theta}_p)\ , \tag{1.32}$$

where

$$\boldsymbol{\theta}_p = [\rho_{\rm tot,0},\ r_s,\ \rho_{\rm gas,0},\ r_x,\ \beta,\ r_o,\ \varepsilon,\ \alpha,\ \rho_{\rm gas,c},\ r_c,\ \beta_c,\ T_{\rm trunc},\ C,\ D,\ E,\ \zeta,\ Z_0,\ r_Z,\ \beta_Z,\ \bar{T}_{\rm SZ},\ T_{\rm bkg},\ A_{\rm bkg}] \tag{1.33}$$

is the set of all model parameters, $\mathcal{L}(\boldsymbol{\theta}_p|\boldsymbol{S},\boldsymbol{T}_{\rm SZ},\boldsymbol{\kappa})$ is the likelihood function, and $\pi(\boldsymbol{\theta}_p)$ is the set of prior constraints for the model parameters.

The likelihood function is, up to an overall normalization, given by

$$\mathcal{L}(\boldsymbol{\theta}_p|\boldsymbol{S},\boldsymbol{T}_{\rm SZ},\boldsymbol{\kappa}) \propto \exp\left(-\chi^2\right); \qquad \chi^2 = \chi^2_{\rm XR} + \chi^2_{\rm SZ} + \chi^2_{\rm SW}\ . \tag{1.34}$$

That is, we assume that the X-ray, SZ, and lensing measurements are independent, and therefore the total χ^2 is the sum of the χ^2 of the individual datasets. We use a uniform prior for each parameter with physically reasonable lower and upper bounds.

For a given set of parameters, JACO generates a set of synthetic X-ray event spectra $\widehat{\boldsymbol{S}}(\boldsymbol{\theta}_p)$ using Equation (1.16) and the input ARF and RMF files. The cooling function is computed using the MEKAL plasma code. The model spectra are convolved with the energy-dependent instrument PSF. The details of how the PSF is calculated for a given set of annular bins can be found in Mahdavi et al. [51]. The X-ray contribution

to χ^2 is then given by

$$\chi^2_{\rm XR} = \sum_{i,j} \frac{(S_{ij} - \widehat{S}_{ij}(\boldsymbol{\theta}_p))^2}{\sigma^2_{S_{ij}}} \ , \tag{1.35}$$

where the summation runs over the desired annular bins and energy bins.

For a given set of parameters, JACO generates a model SZ image $\widehat{\boldsymbol{T}}_{\rm SZ}(\boldsymbol{\theta}_p)$ using Equations (1.18)−(1.20). Prior to calculating $\chi^2_{\rm SZ}$, it accounts for instrumental effects by simulating the act of observing the model SZ image with Bolocam. The model image has a larger size (25 arcmin × 25 arcmin) and a finer resolution (10 arcsec) than the data to avoid edge effects and sampling effects during convolution. It is is convolved with a Gaussian kernel with a 60.33 arcsec FWHM in order to account for the instrument PSF (59.17 arcsec FWHM) and pointing uncertainty (11.77 arcsec FWHM). Afterwards it is rebinned and resized to an identical grid as that of the data. It is then convolved with the transfer function of the data processing pipeline. Finally, the parameter $\bar{T}_{\rm SZ}$ is added to the image to represent the unknown mean signal offset. The SZ contribution to χ^2 is calculated as

$$\chi^2_{\rm SZ} = \sum_{i} \frac{(T_{{\rm SZ},\,i} - \widehat{T}_{{\rm SZ},\,i}(\boldsymbol{\theta}_p))^2}{(C_{T_{\rm SZ}})_{ii}} \ , \tag{1.36}$$

where the summation runs over all pixels with an angular separation $\theta \leq 6.33$ arcmin.

Finally, for a given set of parameters, JACO generates a convergence profile $\widehat{\boldsymbol{\kappa}}(\boldsymbol{\theta}_p)$ using Equation (1.29). This is compared directly to the convergence profile determined by the `SaWLens` algorithm. The lensing contribution to χ^2 is calculated as

$$\chi^2_{\rm SW} = (\boldsymbol{\kappa} - \widehat{\boldsymbol{\kappa}}(\boldsymbol{\theta}_p))^{\intercal} \ \boldsymbol{C}_{\boldsymbol{\kappa}}^{-1} \ (\boldsymbol{\kappa} - \widehat{\boldsymbol{\kappa}}(\boldsymbol{\theta}_p)) \ , \tag{1.37}$$

which accounts for the nonzero covariance between the radial bins.

We divide the parameters into two subsets

$$\boldsymbol{\theta}_{p,1} = [\rho_{\rm tot,0},\ r_s,\ \rho_{\rm gas,0},\ r_x,\ \beta,\ r_o,\ \varepsilon,\ \alpha,\ \rho_{\rm gas,c},\ r_c,\ \beta_c,\ C,\ D,\ E,\ \zeta], \tag{1.38}$$

$$\boldsymbol{\theta}_{p,2} = [T_{\rm trunc},\ Z_0,\ r_Z,\ \beta_Z,\ \bar{T}_{\rm SZ},\ A_{\rm sbkg},\ T_{\rm sbkg}] \ , \tag{1.39}$$

where $\boldsymbol{\theta}_{p,1}$ contains the parameters of interest and $\boldsymbol{\theta}_{p,2}$ contains the nuisance parameters. While the nuisance parameters do have some effect on the likelihood function, they are not tightly constrained by the data. We allow the nuisance parameters to vary over physically reasonable bounds and then marginalize to obtain constraints on the parameters of interest. Figure 1.1 shows an example of the marginalized two-dimensional joint posterior distributions for the parameters $\boldsymbol{\theta}_{p,1}$ resulting from a JACO fit to the multiwavelength dataset.

The version of JACO employed in this work differs from the version described in Mahdavi et al. [51, 52] in the following ways. We have added the ability to fit Bolocam SZ images. We use the convergence

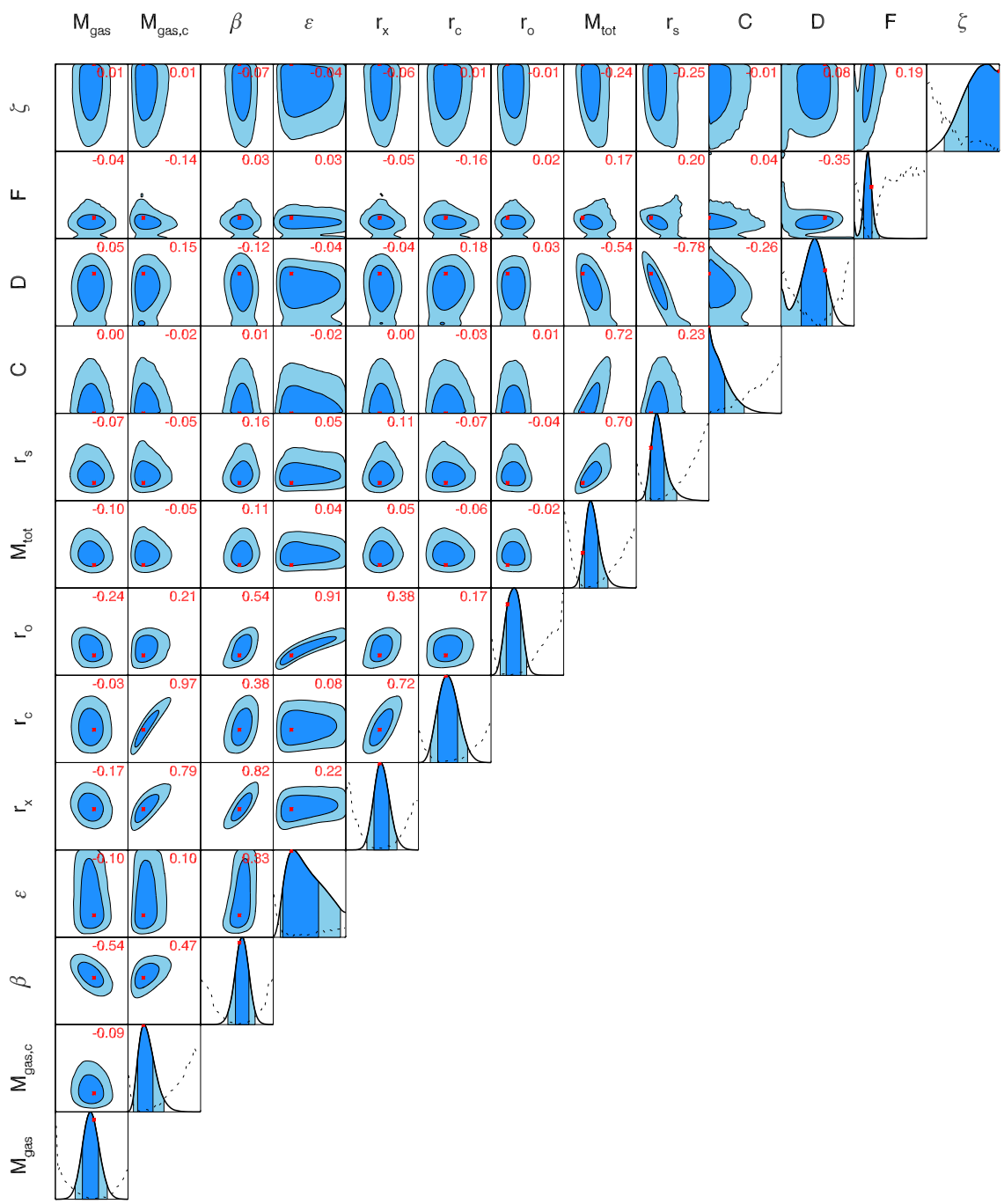

Figure 1.1: The marginalized two-dimensional joint posterior distributions for the parameters of interest from a fit to the complete multiwavelength dataset of MACS J1532.8+3021. Contours denote 68% and 95% credible regions. Red stars denote the maximum likelihood values. The red annotation in the upper right corner of each panel is the Pearson correlation coefficient between the two parameters. The diagonal panels show the marginalized one-dimensional posterior distributions and the dashed black line denotes the negative log-likelihood profile of that parameter. The purpose of this plot is to illustrate the various parameter degeneracies and the general shape of the posterior distribution. We have foregone units and tick-marks to simplify the presentation.

Table 1.1: Basic properties of the six CLASH clusters in our sample.

Name	z	RA (J2000)	DEC (J2000)	SZ S/N	*Chandra* Time [ksec]	$N_{\rm sys}$	HST $\rho_{\rm gal}$ [arcmin^{-2}]	Subaru $\rho_{\rm gal}$ [arcmin^{-2}]
Abell 383	0.187	02:48:03.40	-03:31:44.9	9.6	38.8	9	50.7	9.0
Abell 611	0.288	08:00:56.82	+36:03:23.6	10.8	36.1	4	42.3	8.8
MACS J1532.8+3021	0.363	15:32:53.78	+30:20:59.4	8.0	89.0	0	35.9	16.6
MACS J0429.6-0253	0.399	04:29:36.05	-02:53:06.1	8.9	23.2	3	42.4	12.0
MACS J1311.0-0310	0.494	13:11:01.80	-03:10:39.8	9.6	63.2	2	33.7	20.2
MACS J1423.8+2404	0.545	14:23:47.88	+24:04:42.5	9.4	115.6	5	75.3	9.8

rather than the tangential shear as the lensing observable. We include constraints from both weak and strong lensing. We use a slightly different parameterization for the gas density. Finally, we include nonthermal pressure support in our model.

1.4.2 Sample Definition

The spherically symmetric model presented in Section 1.2 does not provide a good fit to the full multiwavelength dataset for a significant number of the CLASH clusters. It is likely that a more complex model that accounts for the three-dimensional shape and orientation of the cluster is necessary. In this work, we restrict our attention to a subsample of the CLASH clusters whose X-ray and SZ images show a high degree of regularity. A cluster must satisfy two requirements in order to be placed in our sample. First, the SZ image must be circular. This requirement is implemented by fitting the SZ data alone using a circular and elliptical version of the generalized-NFW model (gNFW) for the thermal pressure [53, 54], and examining whether the elliptical model is preferred by performing a statistical F-test. Czakon et al. [35] outlines this procedure and presents the results for all BOXSZ clusters. Second, we require that the centroid shift parameter $w_{500c} < 0.006$. The centroid shift parameter is the standard deviation in units of r_{500c} of the separation between the peak and centroid of the X-ray emission calculated in increasing aperture sizes up to r_{500c}. The w_{500c} values for all BOXSZ clusters were calculated according to the procedure described in Maughan et al. [55, 56] and are presented in Sayers et al. [57]. Of the 25 CLASH clusters, 8 satisfy both of our requirements. However, for 2 of the 8 clusters — MACS J1931.8-2634 and MS 2137 — the lensing convergence profiles κ from two independent analyses of the same underlying data differed significantly. Since we are not confident in the lensing constraints for these two clusters we remove them from our sample. Some basic properties of the six cluster that make up our sample are presented in Table 1.1.

1.4.3 Model Determination

We must first choose a radius $r_{\rm trunc}$ that defines the outer boundary of the ICM. We use JACO to fit the NFW model for the total density to the lensing data only. From these fits, we obtain an estimate of r_{500c}. We then refit the full multiwavelength dataset with the value of $r_{\rm trunc}$ fixed at integer multiples of r_{500c} between 3 and 10. In all cases, it was found that the resulting constraints on the thermodynamic properties of the ICM

converged for values of $r_{\rm trunc} \geq 7xr_{500c}$. We fix the radius at which we truncate the ICM to the physical radius corresponding to $r_{\rm trunc} = 7 \times r_{500c}$ for all further analysis.

The data does not warrant the full complexity of the model presented in Section 1.2 for any of the clusters in the spherical sample. We perform a series of F-test decision trees in order to determine the minimally complex submodel that provides an adequate fit to the data. The F-test is a statistical test that can be used to quantify whether adding additional model parameters results in a significantly better fit to the data. The test statistic is the fractional increase in the minimum χ^2 that results from restricting the additional parameters divided by the fractional change in the number of degrees of freedom

$$F = \frac{\left(\chi^2_{\rm restricted} - \chi^2_{\rm complete}\right)/\chi^2_{\rm complete}}{\left(\nu_{\rm restricted} - \nu_{\rm complete}\right)/\nu_{\rm complete}} \, . \tag{1.40}$$

The test statistic will follow an $F(\nu_{\rm restricted} - \nu_{\rm complete}, \nu_{\rm complete})$ distribution under the null hypothesis that the complete model does not provide a significantly better fit than the restricted model. We reject the null hypothesis and add the additional model parameters if the probability of observing the measured value of F is less than 0.05.

The first F-test decision tree is used to determine if the $r^{-\alpha}$ power-law and the second β-model are necessary to describe the gas density in the cluster core. We construct the following hierarchy of models ordered by the number of free parameters:

G-0 We fix $\alpha = 0$ and $\rho_{\rm gas,c} = 0$.

G-1a We let α float, but fix $\rho_{\rm gas,c} = 0$.

G-1b We let $\rho_{\rm gas,c}$ and r_c float (recall that $\beta_c = 1$), but fix $\alpha = 0$.

G-2 We let α, $\rho_{\rm gas,c}$, and r_c float.

We fit all four models to the data. Since the constraints on $\rho_{\rm gas}$ originate from the X-ray and SZ data, we perform this test without the lensing data. It should be noted that, in the core region, the constraints are driven almost entirely by the X-ray data. We examine the two branches of the tree: 0→1a→2 and 0→1b→2. We move along each branch, applying the F-test at each step, and stop when we either accept the restricted model or reach the end of the branch. We then compare the stoping points on each branch and choose the model that yields an acceptable fit to the data with the fewest parameters. Of the six clusters, one prefers model G-0, two prefer model G-1a, and three prefer model G-1b.

After we have settled on a model for the gas density, we carry out a second F-test decision tree to determine if a nonthermal pressure component is necessary. In this case the hierarchy of models is

F-0 We assume completely thermal pressure support by fixing $C = 0$ and $D = 0$.

F-1a We allow for an outer nonthermal pressure component by floating C, but fix $D = 0$.

F-1b We allow for an inner nonthermal pressure component by floating D, E, and ζ, but fix $C = 0$.

F-2 We allow for both outer and inner nonthermal pressure components by floating C, D, E, and ζ.

We fit all four models to the full multiwavelength dataset and apply the F-test decision tree. We find that only two of the clusters prefer a nonthermal pressure component; Abell 0383 prefers model 1a and MACS J1532.8+3021 prefers model 1b. The other four clusters prefer model 0. We compare the constraints on C obtained when fitting model 1a and model 2 and find that they are nearly identical, suggesting that the constraints on C are not driven by the core region of the cluster.

1.5 Results

In order to investigate the interplay between the various datasets, we fit lensing only (SW), X-ray only (XR), joint X-ray and SZ (XR+SZ), and the complete dataset (XR+SZ+SW). When we fit the complete dataset, we use the minimally complex model determined in Section 1.4.3 for each cluster. When we fit subsets of the complete dataset we use restricted versions of this model. In the case of SW, the model reduces to an NFW density profile fully described by two parameters. In the case of XR and XR+SZ, we assume entirely thermal pressure support (by fixing $C = 0$ and $D = 0$) because our ability to constrain the nonthermal pressure component relies on comparison of the lensing and X-ray/SZ data.

For each fit, we first employ a Levenberg−Marquardt (LM) minimization algorithm to search for the global maximum of the likelihood function. We then run 8 MCMC chains in parallel all starting from the best-fit parameter values determined by the LM algorithm. Each chain is run for $22,500 \times N_{\rm param}$ total iterations. The first 10% of the iterations are discarded as burn-in and the chains are concatenated. This yields 2-3 million draws from the joint posterior distribution. The acceptance rate of the MCMC algorithm is close to optimal with approximately 25% of the proposed steps accepted [58]. However, the chains have significant serial correlation; we observe an exponential decay in the autocorrelation function with an e-folding time $\tau \sim 1000$ iterations. We thin the chains by τ when calculating statistics, which results in an effective sample size of $2,000 - 3,000$. We apply the Geweke diagnostic [59], Heidelberger-Welch diagnostic [60, 61], and Raftery-Lewis diagnostic [62] to the individual parameter chains to confirm that they have converged at an acceptable level.

The minimum χ^2 for each fit is presented in Table 1.2 along with the number of model parameters, number of degrees of freedom, and the probability to exceed (PTE). All of the clusters have an acceptable quality of fit for all of the data combinations, with the exception of Abell 383. There is modest tension between the X-ray and SZ data for MACS J04296-0253 and MACS J1532.8+3021, which is evident in the decrease in PTE when including the SZ data (XR $\rightarrow$ XR+SZ). We address this tension in the subsections below where we discuss each cluster individually. The best-fit models corresponding to the XR+SZ+SW rows are compared to the data in Figures 1.4−1.8.

Table 1.2: Quality of fit to different combinations of data sets.

Name	$\chi^2_{\rm XR}$	$\chi^2_{\rm SZ}$	$\chi^2_{\rm SW}$	χ^2	N	$N_{\rm param}$	ν	PTE
Abell 383								
SW	–	–	2.0	2.0	15	2	13	1.00
XR	1636.4	–	–	1636.4	1477	16	1461	0.00086
XR+SZ	1637.8	1203.3	–	2841.1	2601	16	2585	0.00027
XR+SZ+SW	1636.7	1201.9	6.9	2845.5	2616	17	2599	0.00044
XR+SZ+SW (Nonthermal)	1636.7	1201.9	6.9	2845.5	2616	17	2599	0.00044
Abell 611								
SW	–	–	4.2	4.2	15	2	13	0.99
XR	1015.0	–	–	1015.0	1037	14	1023	0.56
XR+SZ	1016.1	1134.9	–	2150.9	2161	14	2147	0.47
XR+SZ+SW	1016.3	1135.6	7.9	2159.8	2176	14	2162	0.51
XR+SZ+SW (Nonthermal)	1016.5	1135.3	8.0	2159.7	2176	15	2161	0.50
MACS J0429.6-0253								
SW	–	–	2.9	2.9	15	2	13	1.00
XR	246.7	–	–	246.7	258	14	244	0.44
XR+SZ	248.7	1200.2	–	1448.9	1382	14	1368	0.063
XR+SZ+SW	249.2	1200.0	5.4	1454.6	1397	14	1383	0.088
XR+SZ+SW (Nonthermal)	249.2	1200.0	5.4	1454.6	1397	14	1382	0.085
MACS J1311.0-0310								
SW	–	–	3.8	3.8	15	2	13	0.99
XR	295.8	–	–	295.8	337	13	324	0.87
XR+SZ	297.2	1143.3	–	1440.5	1461	13	1448	0.55
XR+SZ+SW	297.1	1143.4	3.9	1444.4	1476	13	1463	0.63
XR+SZ+SW (Nonthermal)	297.1	1143.4	3.9	1444.4	1476	13	1462	0.62
MACS J1423.8+2404								
SW	–	–	6.4	6.4	15	2	13	0.93
XR	820.9	–	–	820.9	909	15	894	0.96
XR+SZ	824.5	1076.0	–	1900.5	2033	15	2018	0.97
XR+SZ+SW	823.2	1076.5	7.2	1907.0	2048	15	2033	0.98
XR+SZ+SW (Nonthermal)	823.4	1075.9	7.4	1906.7	2048	16	2032	0.98
MACS J1532.8+3021								
SW	–	–	5.2	5.2	15	2	13	0.97
XR	2708.1	–	–	2708.1	2808	15	2793	0.87
XR+SZ	2719.9	1249.0	–	3968.9	3932	15	3917	0.28
XR+SZ+SW	2704.8	1245.1	17.6	3967.5	3947	18	3929	0.33
XR+SZ+SW (Nonthermal)	2704.8	1245.1	17.6	3967.5	3947	19	3928	0.33

We present the resulting constraints on the total mass $M_{\rm tot}$, concentration c, and gas mass fraction $f_{\rm gas}(r) = M_{\rm gas}(r)/M_{\rm tot}(r)$ at several overdensity radii in Table 1.3. The quoted value and error correspond to the center and half of the span of the smallest 68% credible region determined from the marginalized posterior distribution for that parameter. We also plot the two-dimensional constraints on $M_{\rm tot,500c} - c_{500c}$ in Figure 1.2.

As mentioned in Section 1.4.3, Abell 383 is the only cluster that requires an outer nonthermal pressure component based on our F-test decision tree. For this cluster, the total mass inferred from the SW analysis is 2-3 times larger than that inferred from the XR or XR+SZ analysis. This forces the nonthermal pressure fraction to very large values when performing the XR+SZ+SW analysis, and even that does not resolve the discrepancy, as evidenced by the poor quality of fit. We do not believe that a spherically symmetric model is a reasonable approximation for Abell 383 for reasons outlined in Section 1.5.1. Both nonthermal pressure support and an elongation of the cluster along the line-of-sight direction will elevate the lensing inferred mass compared to the X-ray/SZ inferred mass. Hence, if the cluster is elongated along the line of sight direction, the nonthermal pressure fraction inferred from a spherical fit will be overestimated. We do not include Abell 383 in our analysis of the nonthermal pressure support for this reason, and stress caution in interpreting the resulting mass estimates.

We use the other five clusters to place an upper bound on the nonthermal pressure support. We perform a second fit to the full multiwavelength data set allowing the normalization C of the nonthermal pressure fraction profile calibrated from simulation to vary. This fit is labeled "XR+SZ+SW (Nonthermal)" in Table 1.2 and Table 1.3. Note that a uniform prior $U(0,\ 1.825)$ is placed on C. The lower bound $C = 0$ corresponds to entirely thermal pressure support at all radii. The upper bound $C = 1.825$ corresponds to zero thermal pressure support at the cluster outskirts ($r \gtrsim r_{200m}$). The marginalized posterior distribution for C is shown in Figure 1.3 for each of the five clusters. We find that MACS J0429.6-0253, MACS J1311.0-0310, and MACSJ 1423.8+2404 have fairly flat posterior distributions, although there is a definite preference for $C < 1.0$ over $C > 1.0$. Abell 611 and MACSJ1532.8+3021 have higher quality X-ray data and as a result are able to place meaningful upper bounds on the nonthermal pressure fraction. Since the constraints from the individual clusters are consistent with a common value of C, we multiply the posterior distributions together to obtain a combined constraint. The resulting 95% credible interval on the normalization C is $(0,\ 0.43)$. Hence, the universal nonthermal pressure fraction profile observed in simulations ($C = 1.0$) is an extremely unlikely description of this sample of five clusters. We also derive the combined constraint on the nonthermal pressure fraction $\mathcal{F}(r)$ at several over-density radii $r = [r_{2500c},\ r_{500c},\ r_{200c},\ r_{200m}]$ using the same procedure. These are presented in Table 1.4.

Table 1.3: Constraints on the concentration, total mass, and gas mass fraction at several overdensity radii.

Name	r_{2500c} [kpc/h_{70}]	$M_{\rm tot,2500c}$ [10^{14} M$_\odot/h_{70}$]	$f_{\rm gas,2500c}$	r_{500c} [kpc/h_{70}]	$M_{\rm tot,500c}$ [10^{14} M$_\odot/h_{70}$]	$f_{\rm gas,500c}$	r_{200c} [kpc/h_{70}]	c_{200c}	$M_{\rm tot,200c}$ [10^{14} M$_\odot/h_{70}$]	$f_{\rm gas,200c}$
Abell 383										
SW	645 ± 45	4.5 ± 1.0	–	1460 ± 100	10.5 ± 2.2	–	2220 ± 170	4.6 ± 1.2	14.8 ± 3.4	–
XR	460 ± 10	1.7 ± 0.1	0.098 ± 0.004	1020 ± 35	3.6 ± 0.4	0.117 ± 0.011	1545 ± 60	5.1 ± 0.4	5.0 ± 0.6	0.129 ± 0.020
XR+SZ	475 ± 10	1.8 ± 0.1	0.093 ± 0.004	1075 ± 40	4.2 ± 0.5	0.104 ± 0.011	1630 ± 70	4.6 ± 0.3	5.9 ± 0.7	0.102 ± 0.018
XR+SZ+SW	535 ± 20	2.6 ± 0.3	0.075 ± 0.005	1210 ± 50	6.0 ± 0.8	0.080 ± 0.010	1840 ± 85	4.6 ± 0.3	8.5 ± 1.2	0.076 ± 0.016
XR+SZ+SW (Nonthermal)	535 ± 20	2.6 ± 0.3	0.075 ± 0.005	1210 ± 50	6.0 ± 0.8	0.080 ± 0.010	1840 ± 85	4.6 ± 0.3	8.5 ± 1.2	0.076 ± 0.016
Abell 611										
SW	495 ± 35	2.3 ± 0.5	–	1285 ± 105	7.9 ± 2.0	–	2035 ± 200	2.5 ± 0.7	12.6 ± 3.8	–
XR	570 ± 20	3.5 ± 0.4	0.083 ± 0.005	1380 ± 95	9.9 ± 2.0	0.094 ± 0.011	2140 ± 170	3.2 ± 0.6	14.8 ± 3.6	0.105 ± 0.016
XR+SZ	545 ± 15	3.1 ± 0.2	0.089 ± 0.004	1280 ± 60	8.0 ± 1.2	0.107 ± 0.009	1970 ± 115	3.7 ± 0.5	11.7 ± 2.0	0.123 ± 0.013
XR+SZ+SW	545 ± 15	3.1 ± 0.2	0.089 ± 0.003	1305 ± 55	8.4 ± 1.0	0.104 ± 0.008	2025 ± 95	3.4 ± 0.4	12.5 ± 1.8	0.118 ± 0.011
XR+SZ+SW (Nonthermal)	550 ± 15	3.1 ± 0.3	0.088 ± 0.004	1315 ± 60	8.7 ± 1.2	0.102 ± 0.008	2045 ± 105	3.4 ± 0.4	12.9 ± 2.0	0.115 ± 0.011
MACS J0429.6-0253										
SW	470 ± 70	2.0 ± 1.0	–	1160 ± 110	6.6 ± 1.9	–	1840 ± 165	2.6 ± 1.2	10.6 ± 2.9	–
XR	515 ± 35	2.9 ± 0.6	0.095 ± 0.010	1145 ± 115	6.4 ± 2.0	0.116 ± 0.027	1740 ± 195	4.8 ± 1.0	8.9 ± 3.0	0.117 ± 0.041
XR+SZ	485 ± 20	2.4 ± 0.3	0.103 ± 0.007	1060 ± 60	5.2 ± 0.9	0.143 ± 0.016	1595 ± 100	5.4 ± 0.8	7.0 ± 1.3	0.177 ± 0.025
XR+SZ+SW	495 ± 15	2.6 ± 0.3	0.099 ± 0.006	1110 ± 55	5.9 ± 0.9	0.132 ± 0.013	1680 ± 100	4.8 ± 0.6	8.2 ± 1.4	0.161 ± 0.022
XR+SZ+SW (Nonthermal)	510 ± 25	2.9 ± 0.4	0.093 ± 0.007	1150 ± 65	6.5 ± 1.1	0.125 ± 0.014	1735 ± 110	5.0 ± 0.7	8.9 ± 1.7	0.152 ± 0.022
MACS J1311.0-0310										
SW	425 ± 35	1.8 ± 0.5	–	960 ± 75	4.2 ± 1.0	–	1455 ± 120	4.7 ± 1.3	5.8 ± 1.5	–
XR	435 ± 25	2.0 ± 0.3	0.099 ± 0.009	1020 ± 95	5.0 ± 1.4	0.107 ± 0.021	1565 ± 165	3.7 ± 0.8	7.3 ± 2.3	0.117 ± 0.031
XR+SZ	430 ± 15	1.9 ± 0.2	0.102 ± 0.007	1005 ± 65	4.9 ± 1.0	0.112 ± 0.015	1545 ± 120	3.7 ± 0.7	7.0 ± 1.7	0.124 ± 0.022
XR+SZ+SW	425 ± 10	1.8 ± 0.1	0.104 ± 0.005	980 ± 40	4.5 ± 0.6	0.119 ± 0.011	1500 ± 75	4.1 ± 0.5	6.5 ± 1.0	0.134 ± 0.015
XR+SZ+SW (Nonthermal)	435 ± 20	2.0 ± 0.3	0.099 ± 0.007	1005 ± 50	4.9 ± 0.7	0.113 ± 0.011	1540 ± 80	4.2 ± 0.5	7.0 ± 1.1	0.128 ± 0.015
MACS J1423.8+2404										
SW	455 ± 45	2.4 ± 0.7	–	1025 ± 100	5.4 ± 1.6	–	1560 ± 165	4.8 ± 1.5	7.6 ± 2.4	–
XR	470 ± 20	2.6 ± 0.4	0.100 ± 0.008	1025 ± 60	5.5 ± 1.0	0.132 ± 0.026	1540 ± 100	5.6 ± 0.6	7.4 ± 1.5	0.155 ± 0.045
XR+SZ	440 ± 20	2.2 ± 0.3	0.110 ± 0.008	950 ± 50	4.4 ± 0.7	0.149 ± 0.027	1415 ± 80	6.3 ± 0.6	5.8 ± 1.0	0.175 ± 0.048
XR+SZ+SW	450 ± 20	2.3 ± 0.3	0.108 ± 0.008	965 ± 50	4.6 ± 0.7	0.138 ± 0.027	1445 ± 80	6.1 ± 0.5	6.2 ± 1.1	0.160 ± 0.046
XR+SZ+SW (Nonthermal)	470 ± 25	2.7 ± 0.4	0.098 ± 0.009	1020 ± 60	5.4 ± 1.0	0.123 ± 0.025	1525 ± 95	6.2 ± 0.5	7.2 ± 1.4	0.137 ± 0.042
MACS J1532.8+3021										
SW	435 ± 35	1.6 ± 0.4	–	1060 ± 85	4.7 ± 1.2	–	1655 ± 150	3.1 ± 1.0	7.2 ± 2.0	–
XR	540 ± 10	3.2 ± 0.2	0.109 ± 0.004	1245 ± 40	7.9 ± 0.8	0.109 ± 0.008	1905 ± 70	4.1 ± 0.2	11.3 ± 1.2	0.103 ± 0.010
XR+SZ	510 ± 10	2.7 ± 0.1	0.120 ± 0.004	1155 ± 30	6.2 ± 0.5	0.128 ± 0.007	1755 ± 45	4.6 ± 0.2	8.8 ± 0.7	0.129 ± 0.009
XR+SZ+SW	500 ± 10	2.5 ± 0.1	0.126 ± 0.004	1070 ± 35	5.0 ± 0.5	0.150 ± 0.011	1605 ± 65	6.2 ± 0.8	6.7 ± 0.8	0.162 ± 0.016
XR+SZ+SW (Nonthermal)	505 ± 15	2.6 ± 0.2	0.123 ± 0.006	1090 ± 45	5.3 ± 0.7	0.146 ± 0.013	1630 ± 80	6.2 ± 0.8	7.0 ± 1.0	0.155 ± 0.018

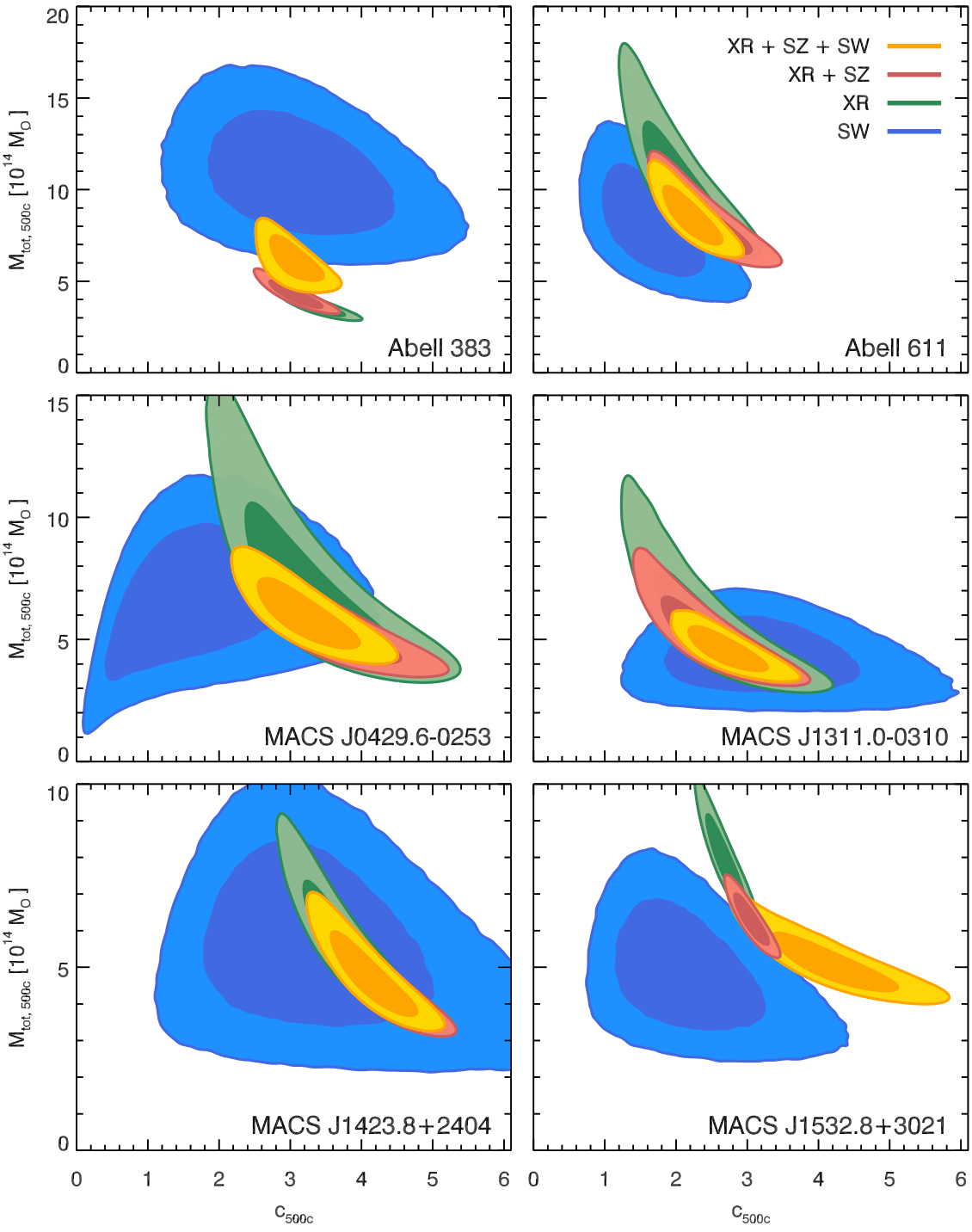

Figure 1.2: Constraints on the concentration and total mass of the galaxy clusters in the spherical sample measured at r_{500c}. Contours denote 68% and 95% credible regions. The colors denote fits to different combinations of data sets. The X-ray + SZ + Lensing fit, shown in orange and gold, assumes entirely thermal pressure support (model F-0).

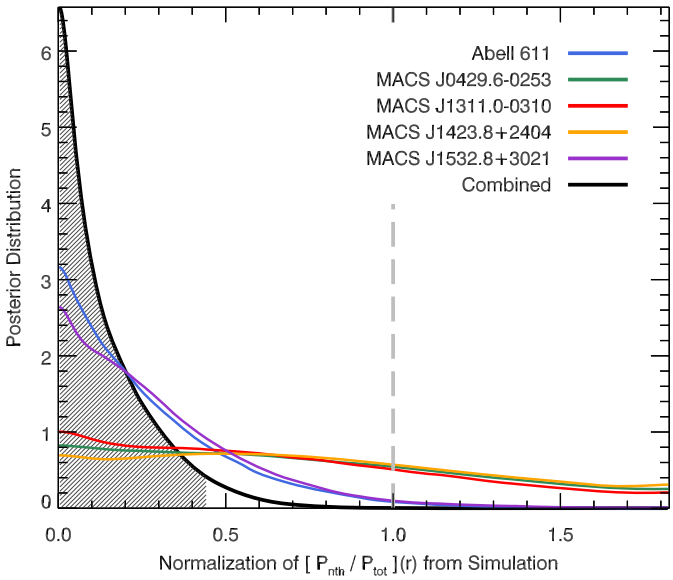

Figure 1.3: Posterior distribution of the normalization C of the best-fit nonthermal pressure fraction profile from the simulation of Nelson et al. [9]. The different colors denote the different galaxy clusters in the spherical samples (excluding Abell 383). Black denotes the combined posterior distribution obtained by multiplying the posterior distributions from the individual clusters. The shading denotes the 95% credible region determined from the combined posterior distribution. The dashed gray line at $C = 1.0$ corresponds to the median value observed in simulation.

In order to test the robustness of our result to the particular parameterization of the nonthermal pressure fraction profile, we have repeated the above analysis using a simple piecewise linear function

$$\mathcal{F}_{\rm out}(r) = \begin{cases} a + b\left(\frac{r}{r_{200m}}\right) & r < r_{200m} \\ a + b & r \geq r_{200m} \end{cases}$$

with both the intercept a and slope b allowed to vary. A uniform prior $U(0,1)$ is placed on both a and b, resulting in a nonthermal pressure fraction that linearly increases with radius until r_{200m} and is constant thereafter. This model has one more parameter than the simulation-based model and allows for greater freedom in the shape of the profile. We must, however, correct for the fact that the implicit prior on the nonthermal pressure fraction at a particular radius is nonuniform and radially dependent. After making this correction we find nearly identical constraints as those obtained with the simulation-based model.

We have also derived frequentist confidence intervals on the normalization C using the following method. We step over a grid of C values between 0 and 1.825. At each point in the grid, we fix C to the same value for all five clusters and use JACO to find the minimum χ^2 allowing the other parameters of the model to float. We then sum over the five clusters and examine $\left(\sum\chi^2\right)(C)$. We find that the minimum value of $\sum\chi^2$ occurs at $C = 0$. We obtain a 95% confidence interval by determining the value of C where $\left(\sum\chi^2\right)(C) - \left(\sum\chi^2\right)(0) = 4.0$. This results in $C = (0,\ 0.35)$, which is similar to the constraints obtained with the Bayesian approach.

Table 1.4: 95% upper bound on the nonthermal pressure fraction $\mathcal{F}$ at several radii.

	$N_{\rm cluster}$	95% Upper Bound	Nelson et al. (2014)
C	5	0.44	1.00
$\mathcal{F}(r_{2500c})$	5	0.06	0.15
$\mathcal{F}(r_{500c})$	4	0.11	0.26
$\mathcal{F}(r_{200c})$	1	0.29	0.35
$\mathcal{F}(r_{200m})$	1	0.35	0.43

1.5.1 Abell 383

We now discuss each cluster individually, starting with Abell 383. This is the closest cluster in our sample at a redshift of $z = 0.188$ and has relatively high quality X-ray data. The best fit to XR has a PTE of 0.00086. This cluster has two independent measurements of the X-ray spectrum in each annular bin from the ACIS-I and ACIS-S imaging spectrometers. This poor XR quality of fit is driven primarily by differences in these two measurements in three of the annular bins: the two innermost bins and the outermost bin.

As mentioned in the previous section, the mass inferred from SW is $1.6-2$ times larger than the mass inferred from XR or XR+SZ. In addition, the X-ray and SZ data disagree with one another. The SZ signal predicted from the XR determined pressure is systematically lower than what is actually observed in the region between $200-500$ kpc. The X-ray data dominates the XR+SZ+SW fit, and hence underestimation of both the SZ and lensing signal by the best fit model is apparent in Figure 1.4.

These results further support the idea that Abell 383 is elongated along the line of sight direction [63, 64]. Such a geometry would naturally produce the discrepancies observed in our spherical fits to X-ray, SZ, and lensing data. The equation of hydrostatic equilibrium implies that the ICM "follows" the gravitational potential. More specifically surfaces of constant gas density (and pressure) coincide with surfaces of constant gravitational potential. A consequence of the Poisson equation is that the gravitational potential is more spherical than the density field that produces it. In general then the gas density will be more spherical than the total density in dynamically relaxed galaxy clusters. The X-ray and SZ observables are proportional to the gas density projected along the line of sight, whereas the lensing observable is proportional to the total density projected along the line of sight. Elongation of the cluster along the line of sight will be more pronounced in the total density than the gas density, and will therefore result in a larger lensing signal than what is predicted based on either SZ or X-ray. In addition, elongation will result in a larger SZ signal than what is predicted from the X-ray, because the SZ observable scales as $\rho_{\rm gas}$ whereas the X-ray observable scales as $\rho_{\rm gas}^2$.

Newman et al. [63] combined X-ray mass estimates with HST strong lensing data, Subaru weak lensing data, and measurements of the brightest cluster galaxy (BCG) stellar velocity dispersion profile to constrain a triaxial gNFW model for the dark matter halo assuming a major axis oriented along the line of sight. The X-ray mass estimates were derived assuming spherical symmetry and hydrostatic equilibrium with a

constant 10% nonthermal pressure fraction, and were taken to represent the true, spherically averaged three-dimensional mass. The projected mass profile measured by the lensing data was then used to constrain the line of sight extent of the dark matter halo $\eta_{\rm DM,a}^{-1} = 1.97^{+0.28}_{-0.16}$. Morandi et al. [64] performed a joint analysis of *Chandra* X-ray and HST strong lensing data in which they fit a fully triaxial model for the dark matter and gas distribution. They found that the data was well described by a triaxial dark matter halo with axis ratios $\eta_{\rm DM,a} = 0.55 \pm 0.06$ (minor/major) and $\eta_{\rm DM,b} = 0.71 \pm 0.10$ (intermediate/major) with the major axis of the dark matter halo inclined $21.1^\circ \pm 10.1^\circ$ from the line of sight direction. They also included a constant nonthermal pressure fraction in their model and obtained the constraint $\mathcal{F} = 0.11 \pm 0.05$. Both of these works suggest that Abell 383 has a line of sight extent that is roughly a factor of 2 larger than its extent in the plane of sky.

1.5.2 Abell 611

The peak convergence map is offset from the peak of the X-ray emission for Abell 611. We have chosen to center on the peak of the X-ray emission. This results in a slightly lower concentration from the lensing only fit compared to that found in Merten et al. [44]. The effect on the multiwavelength analysis is minimal. The multiwavelength data is in good agreement under a spherical model with completely thermal pressure support. This places a significant upper bound on the nonthermal pressure fraction.

1.5.3 MACS J0429.6-0253

MACS J0429.6-0253 also has an offset between the X-ray and lensing determined center. The net result is the same as in Abell 611. There is slight tension between the X-ray and SZ data. This manifests as an excess in the measured SZ signal over what is expected based on the XR determined pressure in the region between $500 - 900$ kpc. This difference is not statistically significant, however, and our model is able to provide a good quality of fit.

1.5.4 MACS J1311.0-0310 and MACS J1423.8+2404

The multiwavelength data for these two clusters is well described by a spherical model with completely thermal pressure support. The lack of constraining power on the nonthermal pressure fraction is likely due to their relatively high redshifts, which results in X-ray data that only extends out to $1.40 \times r_{2500c}$ in the case of MACS J1311.0-0310 and $0.60 \times r_{2500c}$ in the case of MACS J1423.8+2404. The X-ray data is necessary to constrain the gas density which can be degenerate with the nonthermal pressure fraction.

1.5.5 MACS J1532.8+3021

No strong lensing features were found in the HST data for MACSJ1532.8+3021, making it the only cluster in our sample without gravitational strong lensing constraints. It does have high quality X-ray data that

extends out to $0.7 \times r_{200c}$. The X-ray data dominates the multiwavelength fits. The X-ray and SZ data agree remarkably well outside of ~ 400 kpc. Within this radius, however, there is a significant discrepancy between the X-ray and SZ data. This cluster contains a powerful AGN that is almost certainly responsible for the disagreement in the cluster core [65]. In our multiwavelength analysis, this results in a significant innner nonthermal pressure component $\mathcal{F}_{\rm in}$ that approaches $\simeq 28\%$ as $r \to 0$. This is the only cluster in our sample where the F-test prefers an inner nonthermal pressure component.

1.6 Discussion

The multiwavelength analysis results in significant improvement in the constraints on both the concentration and mass of the five galaxy clusters examined. First, comparing the XR analysis to the XR+SZ analysis, there is a median reduction of 8% in the uncertainty on the concentration and $35-40\%$ in the uncertainty on the total mass over the radial range $r_{2500c} - r_{200c}$. This type of joint X-ray and SZ analysis is well-suited for obtaining mass estimates for high-z clusters, where deep X-ray observations are expensive due to cosmological dimming. Next, comparing the XR+SZ analysis to the XR+SZ+SW analysis, we find that the median reduction in the uncertainty on the mass and concentration is minimal, at the $0-10\%$ level. However, the addition of lensing data allows us to examine whether nonthermal pressure support is necessary to describe the cluster, and if so, include it in our model, thereby mitigating this known systematic bias in the resulting mass estimate. Finally, comparing the SW analysis to the XR+SZ+SW analysis, we see a dramatic improvement in the constraints on both the concentration and mass. There is a median reduction of $50-55\%$ in the uncertainty on the concentration and $50-70\%$ in the uncertainty on the total mass over the radial range $r_{2500c} - r_{200c}$. This results in a $80-85\%$ reduction in the area of the 68% and 95% concentration-mass credible regions.

Compared to hydrodynamical simulations, we observe a distinct lack of nonthermal pressure support in the subset of five galaxy clusters. We now discuss assumptions implicit to our analysis that may effect these results.

- We do not include systematic errors for the possible miscalibration of X-ray temperatures. Donahue et al. [29] performed a comparison of the density and temperature profiles derived from *Chandra* and XMM data for the X-ray selected sample of CLASH clusters. They found that the gas density profiles measured by the two instruments were in excellent agreement. The temperature profiles were also in good agreement in the cluster core. However, the XMM temperatures systematically declined relative to the *Chandra* temperatures with increasing radius. If *Chandra* overestimates the gas temperature, then that would result in a underestimation of the level of nonthermal pressure support. We point out that our analysis includes SZ data, which provides the majority of the constraining power on the gas temperature at large radii, where the discrepancy between the two X-ray satellites is observed.

- Our model assumes spherically symmetry; however, there is significant evidence from both observation

[66, 67, 68, 69, 70, 71, 72, 36, 73] and numerical simulation [74, 75, 76, 77, 78, 50, 79, 80, 81, 82] that galaxy clusters are better approximated as triaxial ellipsoids. Departures from sphericity could potentially bias our estimate of the nonthermal pressure fraction due to the degenerate manner in which it affects the multiwavelength observables. Specifically, both nonthermal pressure and line of sight elongation (or compression) result in differences between the lensing and X-ray/SZ inferred mass. We have selected clusters that are circular in the plane of the sky as evidenced by both X-ray and SZ data. Therefore any departure from sphericity would have to occur primarily along the line of sight direction. If the clusters were elongated along the line of sight, our analysis would overestimate the level of nonthermal pressure support, similar to what is seen in Abell 383. Only a compression of the galaxy cluster along the line of sight would result in an underestimation of the nonthermal pressure support necessary to explain the discrepancy between our results and hydrodynamical simulations. That is to say the galaxy clusters would have to be oblate ellipsoids with minor axis oriented along the line of sight direction. However, this geometry would also result in discrepancies between the X-ray and SZ data under the spherical model, with the pressure inferred from the X-ray data predicting more SZ signal than what is actually observed. We do not see this type of behavior in any of the clusters. In general, other than the modest tension observed in MACS J0429.6-0253 and MACS J1532.8+3021, there is good agreement between the Bolocam SZ and *Chandra* X-ray data in the regions of radial overlap for these five clusters.

- Selection effects may also be responsible for the lack of nonthermal pressure support. The X-ray selected sample of 20 CLASH clusters were chosen to exhibit a high degree of regularity based on *Chandra* images of the X-ray surface brightness [16, 83]. In this work, we further restricted our attention to the five clusters in the sample with the most regular morphology by placing cuts on the X-ray centroid shift parameter w and the ellipticity of the SZ image. Therefore, our analysis is focused on very distinct type of cluster, namely ones with gas density and pressure distributions that are circularly symmetric when projected onto the plane of the sky.

The galaxy cluster Abell 383 illustrates the fact that even the most regular clusters can have significant elongation along the line of sight. Previous multiwavelength analyses of Abell 383 employed X-ray and lensing data [63, 64]. The new insight gained from our analysis is that the SZ signal scales in the expected way for line of sight elongation. The tension between the X-ray and SZ can therefore be used to constrain the line of sight extent, breaking the degeneracy that exists between line of sight extent and nonthermal pressure support. Triaxial modeling of the dark matter and ICM mass distributions is necessary to do this properly. Future work will be directed towards generalizing the JACO software to fit triaxial models and performing a triaxial analysis of the sample of 20 X-ray selected CLASH clusters.

1.7 Summary

We have performed a multiwavelength analysis of a subsample of 6 of the 20 X-ray selected CLASH clusters. The subsample was selected by placing a stringent cut on the X-ray centroid shift parameter w derived from *Chandra* measurements of the X-ray surface brightness and also placing a cut on the ellipticity of the SZ image measured by Bolocam. These criteria select clusters with gas density and pressure distributions that are circularly symmetric when projected onto the plane of the sky. For each cluster, the JACO software was used to fit a parametric model to a set of radially binned X-ray spectra measured by *Chandra*, a radially binned convergence profile derived from HST/Subaru strong and weak lensing data, and a two-dimensional SZ image measured by Bolocam. A statistical F-test was employed to determine the minimally complex model necessary to describe the data. Various subsets of the multiwavelength data were fit to understand the relative contribution to the resulting constraints on the concentration and total mass of the galaxy cluster.

We find that for 5 of the 6 clusters, a relatively simple model that assumes spherical symmetry, hydrostatic equilibrium, and entirely thermal pressure support provides a good fit to the multiwavelength dataset. There are significant improvements $(35-40\%)$ in the constraints on the total mass when jointly fitting the X-ray and SZ data compared to fitting the X-ray data only. There are also significant improvements in the constraints on both the concentration $(50-55\%)$ and total mass $(50-70\%)$ when jointly fitting X-ray, SZ, and lensing data compared to fitting lensing data only.

The five clusters that are well described by the model are used to place an upper bound on the level of nonthermal pressure support present in the ICM. We find that the nonthermal pressure at r_{500c} is less than 11% of the total pressure at 95% confidence. This is in tension with state-of-the-art hydrodynamical simulations, which suggest nonthermal pressure fractions of 26% at r_{500c} for clusters of this mass and redshift. Possible causes for this discrepancy include X-ray temperature miscalibration, compression of the cluster along the line of sight direction, and selection effects.

We find that for one of the clusters, Abell 383, the multiwavelength data disagrees in a way that suggests the cluster is elongated along the line of sight direction. Future work will generalize the model to allow the cluster to have a triaxial shape and arbitrary orientation. In addition, the software will be upgraded to fit X-ray surface brightness images in addition to radially binned spectra. Currently the outer radius that we can reliably constrain the model is limited by the extent of the X-ray spectra, and including the surface brightness in the fit will extend results to larger radii. After these modifications, the analysis will be expanded to the full sample of 20 X-ray selected CLASH clusters.

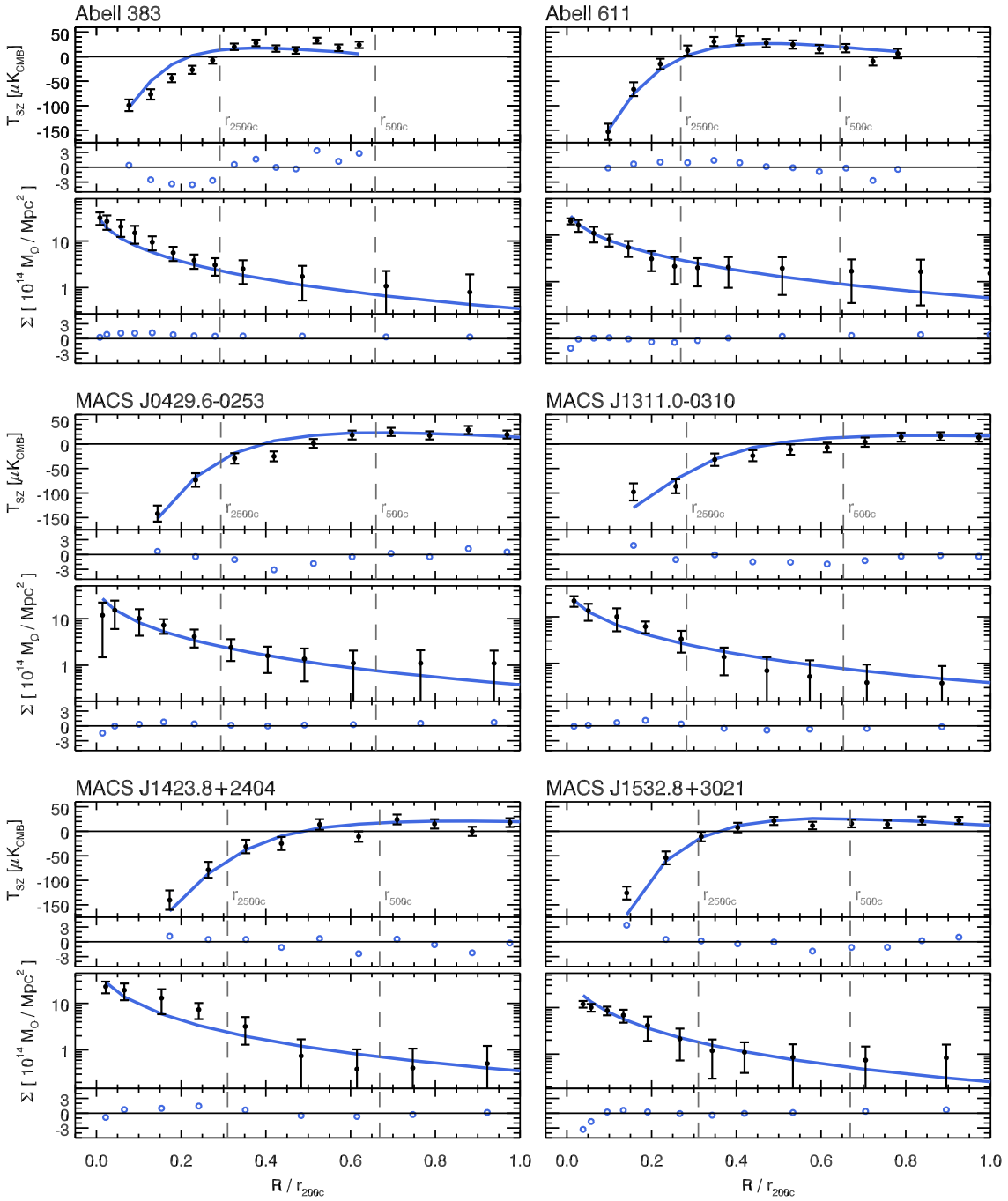

Figure 1.4: The SZ and lensing data compared to the best fit minimally complex model as a function of projected radius relative to r_{200c}. Note that the model is determined from a fit to the full multiwavelength dataset. The top portion of each panel displays the data and best fit model. The bottom portion of each panel displays the normalized residuals (i.e., [data − model]/error). The upper panel is the azimuthally averaged SZ image. Note that we fit the two-dimensional SZ image, but show the radial profile here for visualization purposes. Recall that the SZ effect results in a temperature decrement, and the positive excursion at intermediate radii is due to the filtering applied during data processing. The bottom panel is the convergence profile reconstructed by the `SaWLens` algorithm from both strong and weak lensing constraints, converted to a surface mass density profile $\Sigma = \kappa\Sigma_{\rm crit}$. The X-ray data are presented on the following pages.

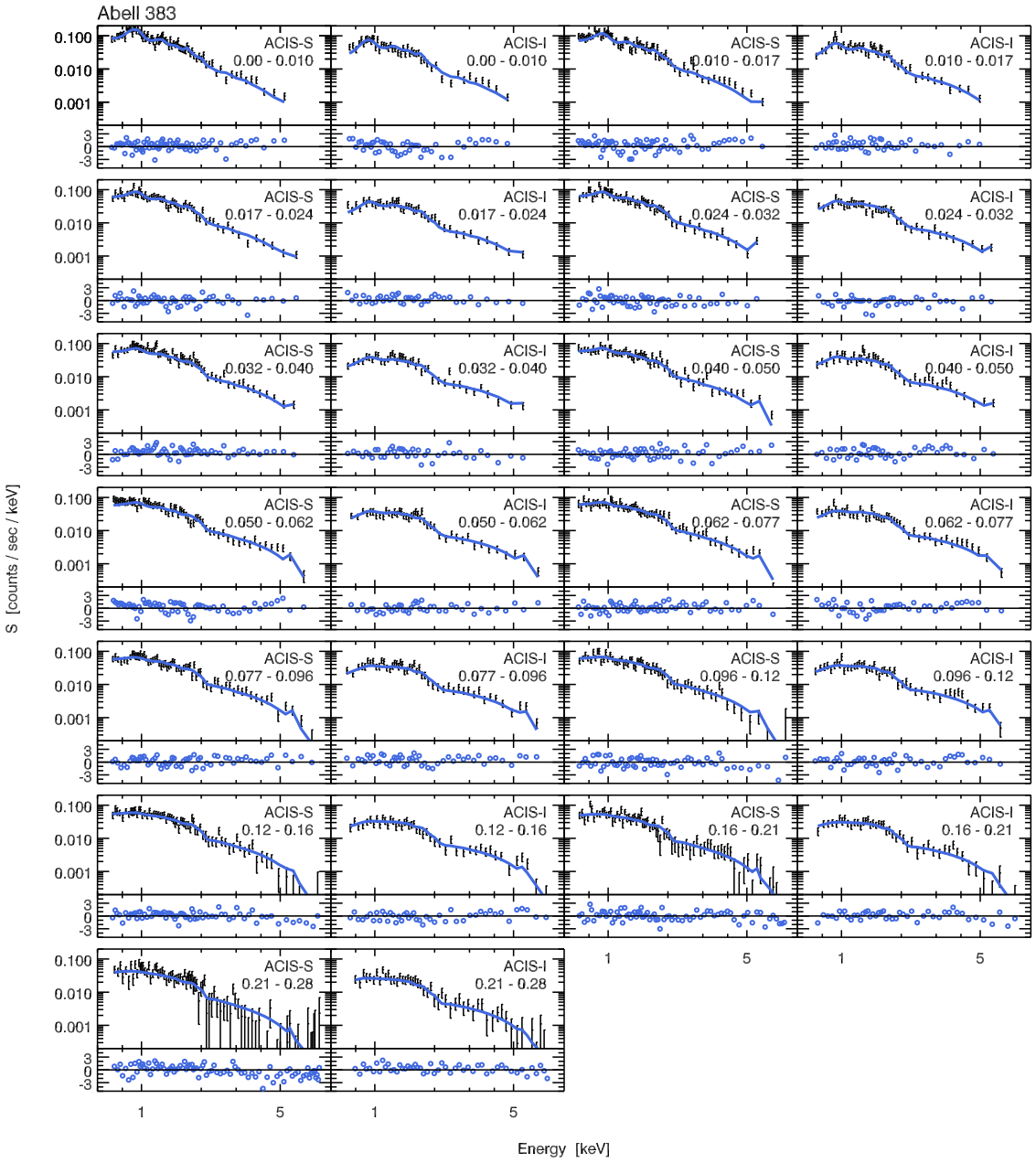

Figure 1.5: The measured cluster X-ray spectra compared to the best fit minimally complex model for Abell 383. Note that the model is determined from a fit to the full multiwavelength dataset. Each panel is a different detector/annular bin. The detector name and the inner and outer radii relative to r_{200c} are annotated in the upper right corner. The top portion of each panel displays the data and best fit model. The bottom portion of each panel displays the normalized residuals (i.e., [data − model]/error).

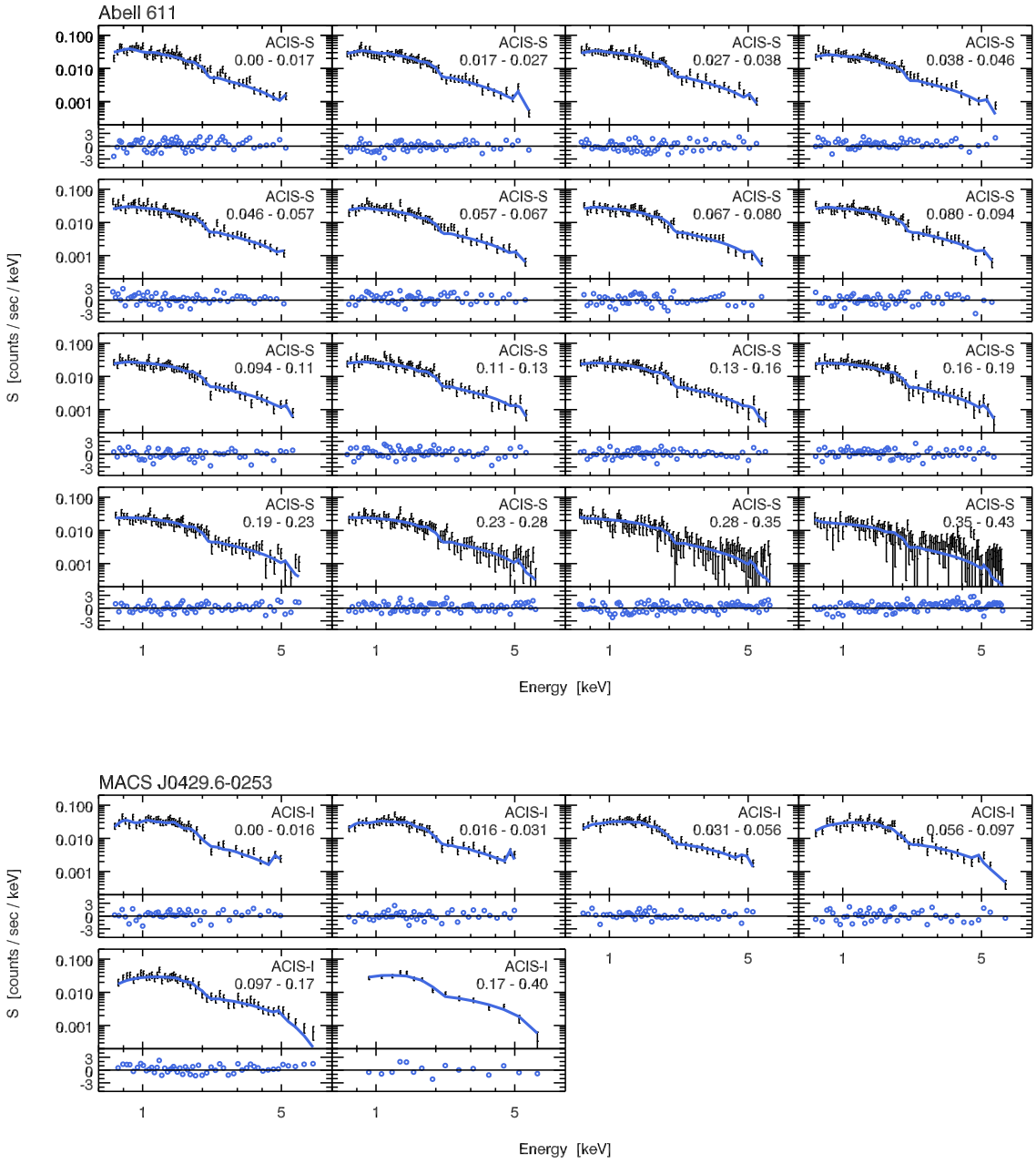

Figure 1.6: The measured cluster X-ray spectra compared to the best fit minimally complex model for Abell 611 and MACS J0429.6-0253.

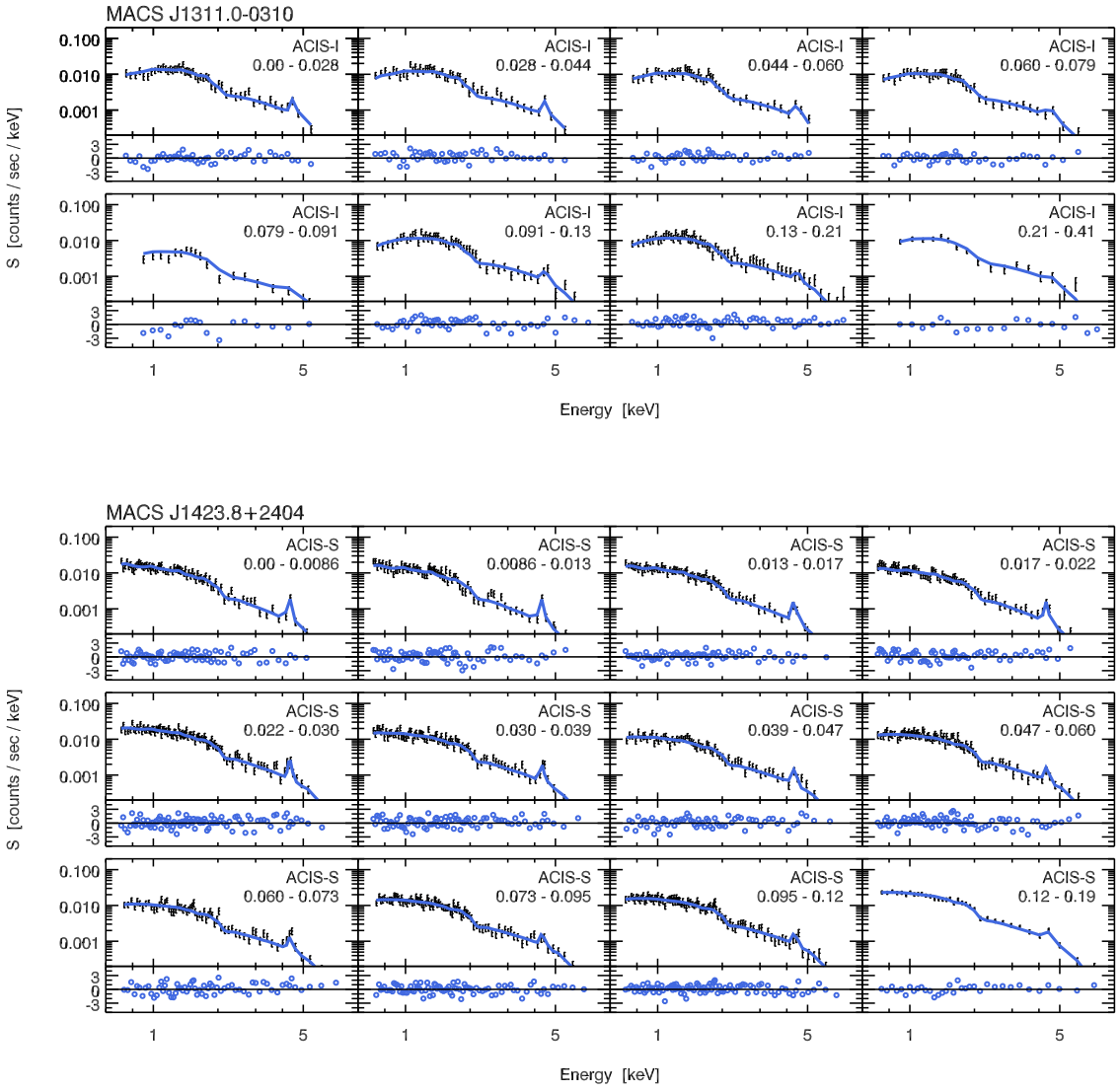

Figure 1.7: The measured cluster X-ray spectra compared to the best fit minimally complex model for MACS J1311.0-0310 and MACS J1423.8+2404.

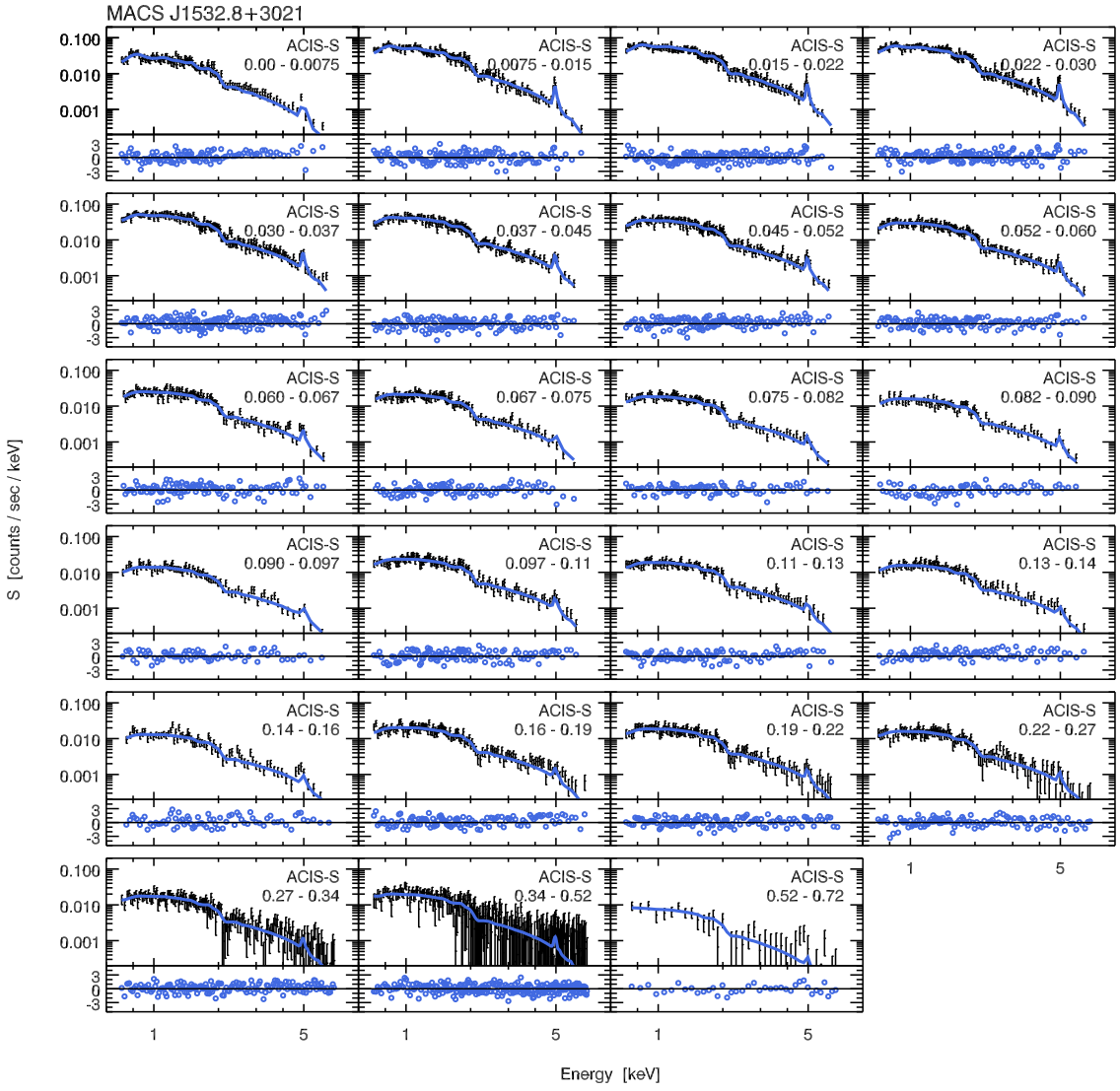

Figure 1.8: The measured cluster X-ray spectra compared to the best fit minimally complex model for MACS J1532.8+3021.

Part II

The Characterization of the Multiwavelength Sub/millimeter Inductance Camera

Chapter 2

Model for the Responsivity and Noise of Microwave Kinetic Inductance Detectors

2.1 Notation

The analysis that follows will be simplified by using complex arithmetic and phasor notation. We denote the voltage of a sinusoid of angular frequency $\omega = 2\pi f$ as

$$V(t) = \mathrm{Re}\left[\hat{V}(t)e^{j\omega t}\right] , \tag{2.1}$$

where $\hat{V}(t)$ is the time-dependent, complex amplitude. We will use sinusoids to describe the microwave signals that probe the MKIDs, and will refer to them as *carriers* or *carrier tones*.

We will often use the greek symbol δ to denote small, time-dependent fluctuations about the mean value, defined as

$$\delta x(t) = x(t) - < x(t) > , \tag{2.2}$$

where $x =< x(t) >$ is the time averaged value and $\delta x \ll x$. For simplicity, we will often suppress the explicit dependence on time in the notation, writing $\delta x(t)$ as δx and $< x(t) >$ as x.

We denote the one-sided power spectral density (PSD) of the real quantity $x(t)$ as $S_x(\nu)$. This is defined as

$$S_x(\nu) = \lim_{T\to\infty} \frac{1}{T}|\tilde{x}(\nu)|^2 , \tag{2.3}$$

where T is the sampling period, $\nu \geq 0$ is the temporal frequency, and $\tilde{x}(\nu)$ is the Fourier transform of $x(t)$. The Fourier transform is defined as

$$\tilde{x}(\nu) = \mathscr{F}\{x(t)\} = \int_{-\infty}^{\infty} x(t)e^{-2\pi jt\nu}dt \tag{2.4}$$

with the inverse relation given by

$$x(t) = \mathscr{F}^{-1}\{\tilde{x}(\nu)\} = \int_{-\infty}^{\infty} \tilde{x}(\nu) e^{2\pi j \nu t} d\nu \ . \tag{2.5}$$

We will occasionally label the PSD as $S_{\delta x}^{\text{source}}$. This should be read as the power spectral density of the fluctuations δx that were originally caused by "source".

Finally, we denote the one-sided cross power spectral density (CPSD) between the real quantities $x(t)$ and $y(t)$ as $S_{x,y}(\nu)$. This is defined as

$$S_{x,y}(\nu) = \lim_{T\to\infty} \frac{1}{T} \tilde{x}^*(\nu)\tilde{y}(\nu) \ , \tag{2.6}$$

where * denotes the complex conjugate.

2.2 Responsivity

In this section we present the theoretical model that is used to predict MKID responsivity. We start by considering the signal of interest: flux from an unresolved astronomical source. We follow this signal through the instrument and present the theoretical considerations necessary to describe its propagation. We end with the quantity that is directly measured by the readout electronics: the complex transmission through the system at microwave frequencies. This can be linked to the source flux in five steps:

1. Antenna theory relates source flux to optical power incident on the detector.
2. The generation-recombination equation converts incident optical power to changes in the quasi-particle density of the thin superconducting film.
3. Mattis-Bardeen theory relates quasi-particle density to the surface impedance of the resonator.
4. Circuit theory relates the surface impedance to the frequency and quality factor of the resonator.
5. Network transmission theory relates the frequency and quality factor to the complex transmission near resonance.

At the end we will address several complications that arise due to nonlinear kinetic inductance, nonuniform absorption of optical power, heating of the substrate, nonequilibrium dynamics, and direct pick-up of optical power by the resonator.

2.2.1 Antenna Theory

Consider the case where we have a beam-filling, black-body load at the cryostat window and a single-moded reception element feeding the MKID so that we can apply the throughput theorem $A\Omega = \lambda^2$, where A is

the area of the beam, Ω is the beam solid angle, and λ is the wavelength. The optical power in a single polarization from this load is given by

$$P_{\rm opt} = \eta_{\rm opt} k_B \left(T_{\rm load} + T_{\rm exc}\right) \Delta\nu_{\rm mm} \ , \tag{2.7}$$

where $\eta_{\rm opt}$ is the total optical efficiency of the system (accounting for all sources of loss between the cryostat window and the detector), $T_{\rm load}$ is the temperature of the beam-filling, black-body load, $T_{\rm exc}$ is the excess loading due to power reaching the detector from the inside of the cryostat referred to the cryostat window, and $\Delta\nu_{\rm mm}$ is the effective bandwidth of the detector. In the case where we are looking at the sky, the load temperature can be expressed as

$$\begin{aligned} T_{\rm load} &= f_{\rm spill} T_{\rm amb} + \left(1 - f_{\rm spill}\right) T_{\rm sky} \\ &= f_{\rm spill} T_{\rm amb} + \left(1 - f_{\rm spill}\right) \left(1 - e^{-\tau/\sin\mathfrak{e}}\right) T_{\rm atm} \ . \end{aligned} \tag{2.8}$$

That is, we assume that some fraction $f_{\rm spill}$ of the beam exiting the cryostat spills onto ambient temperature surfaces. This spill-over fraction includes the inefficiency $\left(1 - \eta_{\rm tel}\right)$ of the telescope. The remaining beam reaches the sky where the effective load due to atmospheric emission depends on the temperature of the atmosphere, the optical depth at zenith τ, and the airmass $1/\sin\mathfrak{e}$ (assuming a plane-parallel atmosphere) where $\mathfrak{e}$ is the elevation (altitude).

Of interest is the case where the telescope scans across an unresolved astronomical source with flux S. The change in load temperature due to this source is given by

$$T_{\rm src} = \frac{A_{\rm eff} \left(1 - f_{\rm spill}\right) e^{-\tau/\sin\mathfrak{e}} S}{2 k_B} \ , \tag{2.9}$$

where $A_{\rm eff}$ is the effective area of the telescope and the factor of $1/2$ accounts for the fact that our detectors are only sensitive to a single polarization. The throughput theorem for a single-moded system can be used to calculate the effective area as $A_{\rm eff} = \lambda^2/\Omega_{\rm beam}$ where λ is the bandpass weighted wavelength and $\Omega_{\rm beam}$ is the beam solid angle.

2.2.2 Generation-Recombination Equation

At zero temperature all of the conduction electrons in a superconductor are found in Cooper pairs, a state in which two electrons are bound together by the electron-phonon interaction [84]. The binding energy of a Cooper pair is equal to $2\Delta \approx 3.52 k_B T_c$ where Δ is the gap energy for a single excitation and T_c is the critical temperature of the superconductor. The binding energies of aluminum and niobium — the two superconductors that we employ in the MUSIC detectors — are approximately 0.36 meV and 2.80 meV, respectively. Although the binding is weak, it prevents inelastic scattering of the Cooper pairs with ions in

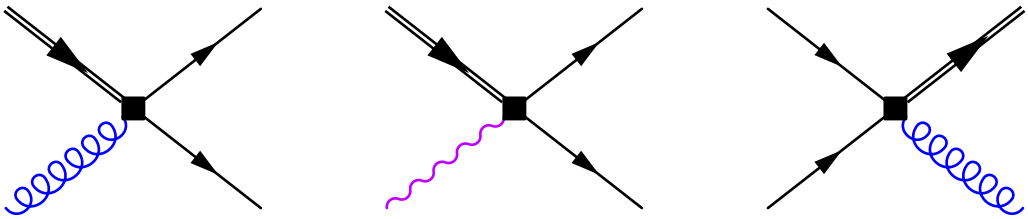

Figure 2.1: Diagram of the processes considered in the generation-recombination equation. (a). Thermal generation: a phonon with energy $\Omega \geq 2\Delta$ breaks apart a Cooper pair and produces two quasi-particles. (b). Optical generation: a photon with energy $h\nu \geq 2\Delta$ breaks apart a Cooper pair and produces two quasi-particles. (c). Recombination: two quasi-particles combine to form a Cooper pair and emit a phonon with energy $\Omega \geq 2\Delta$.

the lattice, resulting in the characteristic zero resistance.

Even at zero temperature superconductors have nonzero AC impedance. If an AC electromagnetic field is applied to the superconductor, then the Cooper pairs will oscillate with the field creating an AC current. Since the Cooper pairs have mass it will take the field some finite time to accelerate them. This results in a phase-lag between the current and the electric field that has a mathematical form equivalent to an inductance. We call it kinetic inductance because the inductive energy is stored in the kinetic energy of the Cooper pairs. Note that kinetic inductance only occurs with high mobility charge carriers. Unbound electrons do not have a significant kinetic inductance (at microwave frequencies) because they scatter so often that energy cannot be stored in their motion.

At finite temperatures some fraction of the conduction electrons are thermally excited from the Cooper pair state. These unbound electrons, known as quasi-particles, can inelastically scatter with ions in the lattice. We refer to the process by which Cooper pairs are thermally excited into quasi-particles *thermal generation*. In this process a lattice vibration (phonon) with energy greater than the binding energy breaks apart a Cooper pair creating two quasi-particles. The reverse process in which two quasi-particles combine to form a Cooper pair and emit a phonon can also occur. We refer to this as *recombination*. Finally, photons with energy $h\nu > 2\Delta$ can break apart Cooper pairs, resulting in the *optical generation* of quasi-particles. The three processes of thermal generation, optical generation, and recombination are illustrated in Figure 2.1

The first step in modeling the propagation of signal through the MKID is to relate incoming optical power to the quasi-particle density of the superconducting thin film. This can be done using the generation-recombination equation, which is simply the statement that over a given amount of time the change in the number of quasi-particles is equal to the number that were generated thermally plus the number that were generated optically minus the number that recombined. Writing this in differential form we have

$$\frac{\partial n_{\rm qp}}{\partial t} = \Gamma_{\rm G,th} + \Gamma_{\rm G,opt} - \Gamma_{\rm R} \ , \tag{2.10}$$

where Γ denotes the rate at which a particular process occurs in units of number of quasi-particles per unit

volume per unit time. In a steady state, $\partial n_{qp}/\partial t = 0$ and Equation (2.10) becomes

$$\Gamma_{G,th} + \Gamma_{G,opt} = \Gamma_R \ . \tag{2.11}$$

We will now calculate the rate at which these three processes occur. The optical generation rate is just

$$\Gamma_{G,opt} = \frac{2}{V}\frac{\eta_{ph} P_{opt}}{2\Delta} = \frac{\eta_{ph} P_{opt}}{V\Delta} \ , \tag{2.12}$$

where η_{ph} is the efficiency with which photons are converted to quasi-particles, P_{opt} is the optical power incident on the MKID from the antenna, and V is the volume of the absorbing section. The factor of 2 in the numerator accounts for the fact that two quasi-particles are created for every broken Cooper pair. The efficiency factor η_{ph} is intrinsic to pair-breaking detectors and will depend primarily on the frequency of the incident power. Consider the absorption of a single photon of frequency ν_{mm}. If the energy of the photon is exactly equal to the binding energy $h\nu_{mm} = 2\Delta$, then the entirety of the photon's energy goes into the creation of quasi-particles and $\eta_{ph} = 1$. For $h\nu_{mm} > 2\Delta$, only 2Δ will go into the creation of quasi-particles and the remainder will go into the kinetic energy of those quasi-particles. Hence, we expect a monotonic decrease in η_{ph} between $h\nu_{mm} = 2\Delta$ and $h\nu_{mm} = 4\Delta$, at which point it should reach $\eta_{ph} \approx 50\%$. For $h\nu_{mm} > 4\Delta$ the efficiency is expected to level off or slightly increase. This is because the quasi-particles created by the photon will relax to energies $E \sim \Delta$ through inelastic scattering with the lattice, which results in phonon emission. The timescale for relaxation $\tau_{cascade} \simeq 1 - 10$ ns is much shorter than the timescale for recombination τ_{qp} [85, 86]. When $h\nu_{mm} > 4\Delta$ the phonons produced via relaxation can have energy $\Omega \geq 2\Delta$, and therefore can break Cooper pairs creating secondary quasi-particles. In the limit that $h\nu_{mm} \gg 4\Delta$ the energy will cascade down through multiple pair breakings. Guruswamy et al. [87] performed a proper simulation of $\eta_{ph}(\nu_{mm})$ for Al superconductors over a wide range of film thicknesses. They measure overall trends with ν_{mm} that are consistent with the somewhat simplistic explanation that was just given. They confirmed previous results that showed $\eta_{ph} \approx 0.58$ in the limit of thick films and highly energetic photons $h\nu_{mm} \gg 4\Delta$ [88, 85]. However, they found that the loss of nonequilibrium phonons to the substrate becomes significant for thin films, and that this degrades the pair breaking efficiency relative to the thick film value. For the MUSIC detectors with film thickness $d \approx 50$ nm and observing bands $h\nu_{mm} = [3.3,\ 4.9,\ 6.2,\ 7.5] \times \Delta$, their simulations predict that $\eta_{ph} = [0.60,\ 0.50,\ 0.46,\ 0.43]$.

The recombination rate is defined as

$$\Gamma_R = -\frac{1}{V}\left(\frac{dN_{qp}}{dt}\right)_R \ . \tag{2.13}$$

If each individual quasi-particle recombines at a rate τ_{qp}^{-1} then the change in the the total number of quasi-particles N_{qp} per unit time will be

$$\left(\frac{dN_{qp}}{dt}\right)_R = -\frac{N_{qp}}{\tau_{qp}} \ . \tag{2.14}$$

Solving this equation results in a exponential decay in the total number of quasi-particles with time

$$N_{\mathrm{qp}}(t) \propto \exp\left(-t/\tau_{\mathrm{qp}}\right) . \tag{2.15}$$

We refer to τ_{qp} as the quasi-particle lifetime. It is given by the equation

$$\frac{1}{\tau_{\mathrm{qp}}} = R n_{\mathrm{qp}} + \frac{1}{\tau_{\mathrm{max}}} , \tag{2.16}$$

where the recombination coefficient R is the recombination rate per unit density of quasi-particles and τ_{max}^{-1} is the maximum quasi-particle lifetime. Note that the physical mechanism responsible for saturation of the lifetime at τ_{max} is not fully understood, but this behavior is observed experimentally [89, 90, 91]. The expression for Γ_{R} is then

$$\Gamma_{\mathrm{R}} = R n_{\mathrm{qp}}^2 + \frac{n_{\mathrm{qp}}}{\tau_{\mathrm{max}}} . \tag{2.17}$$

We see that the rate due to pair recombination scales as n_{qp}^2. This is exactly what one would expect since two quasi-particles have to "find each other" in order to recombine.

Plugging Equations (2.12) and (2.17) into the generation-recombination equation yields

$$\Gamma_{\mathrm{G,th}} + \frac{\eta_{\mathrm{ph}} P_{\mathrm{opt}}}{V\Delta} = R n_{\mathrm{qp}}^2 + \frac{n_{\mathrm{qp}}}{\tau_{\mathrm{max}}} . \tag{2.18}$$

We still need to determine the thermal generation rate $\Gamma_{\mathrm{G,th}}$. Now the total number of quasi-particles is just the sum of the number generated thermally and the number generated optically, i.e., $n_{\mathrm{qp}} = n_{\mathrm{qp,\,th}} + n_{\mathrm{qp,\,opt}}$. Consider the limit of no optical loading. Then $P_{\mathrm{opt}} \to 0$ and $n_{\mathrm{qp,\,opt}} \to 0$, giving us

$$\Gamma_{\mathrm{G,th}} = R n_{\mathrm{qp,\,th}}^2 + \frac{n_{\mathrm{qp,\,th}}}{\tau_{\mathrm{max}}} . \tag{2.19}$$

The above expression is useful because the thermal quasi-particle density $n_{\mathrm{qp,\,th}}$ is completely determined by the temperature and gap energy. We will derive an analytical expression for it in the following section. Inserting Equation (2.19) back into Equation (2.18) yields

$$\frac{\eta_{\mathrm{ph}} P_{\mathrm{opt}}}{V\Delta} = R\left(n_{\mathrm{qp}}^2 - n_{\mathrm{qp,\,th}}^2\right) + \frac{1}{\tau_{\mathrm{max}}}\left(n_{\mathrm{qp}} - n_{\mathrm{qp,\,th}}\right) . \tag{2.20}$$

We can then use the quadratic formula to obtain an explicit expression for the quasi-particle density

$$n_{\mathrm{qp}} = \left[\frac{\eta_{\mathrm{ph}} P_{\mathrm{opt}}}{RV\Delta} + n_{\mathrm{qp,\,th}}^2 + \frac{1}{R\tau_{\mathrm{max}}}\left(n_{\mathrm{qp,\,th}} + \frac{1}{4R\tau_{\mathrm{max}}}\right)\right]^{1/2} - \frac{1}{2R\tau_{\mathrm{max}}} . \tag{2.21}$$

Here we have discarded the second root since it implies negative values. In the limit that the optical generation of quasi-particles dominates over thermal generation and that the recombination of quasi-particles dominates

over the decay due to $\tau_{\rm max}$ this becomes

$$n_{\rm qp} \approx \left(\frac{\eta_{\rm ph} P_{\rm opt}}{RV\Delta} \right)^{1/2} \qquad \text{for } n_{\rm qp} \gg n_{\rm qp,th} \text{ and } \tau_{\rm qp} \ll \tau_{\rm max} \tag{2.22}$$

and we find that the quasi-particle density scales as the square root of the incident optical power. Note that in all analysis that follows we use the full expression given in Equation (2.21).

Going forward we will be interested in how small changes in incident optical power — due to scanning across an astronomical source, for example — translate to changes in the quasi-particle density. This is given by

$$\begin{aligned} \delta n_{\rm qp} &= \frac{\partial n_{\rm qp}}{\partial P_{\rm opt}} \delta P_{\rm opt} \\ &= \frac{\eta_{\rm ph} \delta P_{\rm opt}}{V\Delta(2Rn_{\rm qp} + \tau_{\rm max}^{-1})} \ , \end{aligned} \tag{2.23}$$

where we have evaluated the partial derivative using Equation (2.20). It is traditional to then define

$$\frac{1}{\tau_{\rm qp}^{\rm eff}} = 2Rn_{\rm qp} + \frac{1}{\tau_{\rm max}} \ . \tag{2.24}$$

We call $\tau_{\rm qp}^{\rm eff}$ the effective quasi-particle lifetime. It is the timescale for the decay of a small perturbation to the quasi-particle population. Note that it differs from $\tau_{\rm qp}$ only in the factor of two in front of the recombination term. Equation (2.23) can then be written as

$$\delta n_{\rm qp} = \frac{\tau_{\rm qp}^{\rm eff} \eta_{\rm ph} \delta P_{\rm opt}}{V\Delta} \ . \tag{2.25}$$

We will discuss the effective quasi-particle lifetime further in Section 2.3.2.1.

2.2.3 Mattis-Bardeen Theory

In 1958 Mattis and Bardeen used the BCS theory of superconductivity to describe the response of a superconductor to an AC electromagnetic field [92]. We use Mattis-Bardeen theory to determine the relationship between the quasi-particle density of a thin superconducting film and its surface impedance, which is a crucial step in understanding how the detectors operate. To do this we follow the analysis of Gao [93]. Let $\omega = 2\pi f$ denote the angular frequency of the field and T the temperature of the superconductor. We can introduce a complex conductivity $\sigma = \sigma_1 - j\sigma_2$ to describe the superconducting state [94]. Then for $\hbar\omega < \Delta$

the following integrals hold:

$$\sigma_1 = \frac{2\sigma_n}{\hbar\omega}\int_{\Delta}^{\infty}\frac{[f(E)-f(E+\hbar\omega)]\left(E^2+\Delta^2+\hbar\omega E\right)}{\sqrt{(E^2-\Delta^2)\left[(E+\hbar\omega)^2-\Delta^2\right]}}dE \tag{2.26}$$

$$\sigma_2 = \frac{\sigma_n}{\hbar\omega}\int_{\Delta-\hbar\omega}^{\Delta}\frac{[1-2f(E+\hbar\omega)]\left(E^2+\Delta^2+\hbar\omega E\right)}{\sqrt{(\Delta^2-E^2)\left[(E+\hbar\omega)^2-\Delta^2\right]}}dE\ . \tag{2.27}$$

Here Δ is the gap energy, σ_n is the normal state conductivity, and $f(E)$ is the distribution function for quasi-particles. Assuming that the quasi-particles are in thermal equilibrium, $f(E)$ is given by the Fermi-Dirac distribution

$$f(E) = \frac{1}{1+\exp\left(\frac{E-\mu^*}{k_BT}\right)}\ . \tag{2.28}$$

The chemical potential μ^* in Equation (2.28) is used to account for optically generated quasi-particles [95]. Essentially we are assuming that the quasi-particles are in thermal equilibrium with the lattice, but are not in chemical equilibrium. The assumption of thermal equilibrium should be valid even for optically generated quasi-particles because the timescale for an excited quasi-particle to relax through scattering processes is much shorter than timescale for recombination. We will return to this assumption in Section 2.2.9. The density of excited states in a superconductor is given by

$$N_s(E) = \frac{N_0E}{\sqrt{E^2-\Delta^2}}\ , \tag{2.29}$$

where N_0 is the single-spin density of electron states at the Fermi energy level. Equation (2.29) implies that energies below the gap $|E|<\Delta$ are forbidden and that there is an increase in the density of states just above the gap. This occurs because the total number of available energy states is constant, and the states that are below the gap in a normal metal are shifted out. The quasi-particle density is obtained by integrating the product of $f(E)$ and $N_s(E)$ over all energies

$$n_{\text{qp}} = 4N_0\int_{\Delta}^{\infty}\frac{Ef(E)}{\sqrt{E^2-\Delta^2}}dE\ . \tag{2.30}$$

The final equation required is the self-consistent integral for the band gap

$$\frac{1}{N_0V_{\text{BCS}}} = \int_{\Delta}^{\hbar\omega_D}\frac{1-2f(E)}{\sqrt{E^2-\Delta^2}}dE\ , \tag{2.31}$$

where ω_D is the Debye frequency and V_{BCS} is the interaction strength in the BCS model [84]. The limit of weak electron-phonon coupling holds for aluminum so that $k_BT_c \ll \hbar\omega_D$. By examining Equation (2.31) in

the limit that $T \to 0$ one can derive the expression

$$\frac{\Delta_0 - \Delta}{\Delta_0} = 2\int_{\Delta}^{\infty} \frac{f(E)}{\sqrt{E^2 - \Delta^2}} dE \ , \tag{2.32}$$

which relates the gap at temperature $T < T_c$ to the gap at zero temperature $\Delta_0 = \Delta(T = 0)$. At finite temperatures the quasi-particle population suppresses the gap relative to the zero temperature value.

In the limit that $k_B T \ll \Delta$, $\hbar\omega \ll \Delta$, and $\exp(-(E-\mu^*)/(k_B T)) \ll 1$ the integrals expressed in Equations (2.30), (2.32), (2.26), and (2.27) can be simplified to the following analytical formulae:

$$n_{\rm qp} = 2N_0\sqrt{2\pi k_B T\Delta}\exp\left(-\frac{\Delta-\mu^*}{k_B T}\right) \tag{2.33}$$

$$\frac{\Delta}{\Delta_0} = 1 - \sqrt{\frac{2\pi k_B T}{\Delta}}\exp\left(-\frac{\Delta-\mu^*}{k_B T}\right) = 1 - \frac{n_{\rm qp}}{2N_0\Delta} \tag{2.34}$$

$$\frac{\sigma_1}{\sigma_n} = \frac{4\Delta}{\hbar\omega}\exp\left(-\frac{\Delta-\mu^*}{k_B T}\right)\sinh(\xi)K_0(\xi) \tag{2.35}$$

$$\frac{\sigma_2}{\sigma_n} = \frac{\pi\Delta}{\hbar\omega}\left[1 - 2\exp\left(-\frac{\Delta-\mu^*}{k_B T}\right)\exp(-\xi)I_0(\xi)\right] \ , \tag{2.36}$$

where $\xi = \hbar\omega/2k_B T$ is a dimensionless frequency and I_0 and K_0 are the zero'th order modified Bessel functions of the first and second kind, respectively. We now evaluate the three conditions to determine if the analytical formula are appropriate for the MKIDs in MUSIC. We are interested in examining the behavior of our detectors over a range of temperatures from $T_{\rm lb} = 200$ mK to $T_{\rm ub} = 500$ mK and under optical loads that have temperatures up to $T_{\rm load,ub} = 300$ K when referred to the cryostat window.

$\underline{k_B T \ll \Delta}$

The critical temperature of aluminum is $T_c = 1.2$ K. Therefore $T_{\rm lb} = 0.17\ T_c$ and $T_{\rm ub} = 0.42\ T_c$. Over this range of temperatures Δ does not differ from Δ_0 by more than 5% so we may write $\Delta = \Delta_0 = 1.76 k_B T_c$. We then have that $k_B T_{\rm lb}/\Delta_0 = 0.10$ and $k_B T_{\rm ub}/\Delta_0 = 0.25$.

$\underline{\hbar\omega \ll \Delta}$

The gap energy of aluminum is $\Delta_0 = 0.18$ meV, which corresponds to a frequency of 45 GHz. The MKIDs have resonant frequencies between $3-4$ GHz. Therefore, $\hbar\omega/\Delta_0 = 0.08$.

$\underline{\exp(-(E-\mu^*)/(k_B T)) \ll 1}$

Since we are always considering $E \geq \Delta$ in the integrals above, we can use $\exp(-(\Delta-\mu^*)/(k_B T))$ as an upper bound. This quantity can be approximated by Equation (2.33) with the quasi-particle density $n_{\rm qp}$ inferred from Equation (2.22) for our expected optical loading. We are interested in obtaining an upper bound so we assume that the detectors are 100% efficient and have a bandwidth of 45 GHz. Then $T_{\rm load,ub}$ results in 185 pW of absorbed power. Assuming $N_0 = 1.07 \times 10^{29}$ J^{-1} μm^{-3} and $R = 9.4$ μm^3 s^{-1}, we obtain $\exp(-(\Delta-\mu^*)/(k_B T)) \leq 0.02$.

The second and third conditions are certainly satisfied. The first condition will begin to break down as the

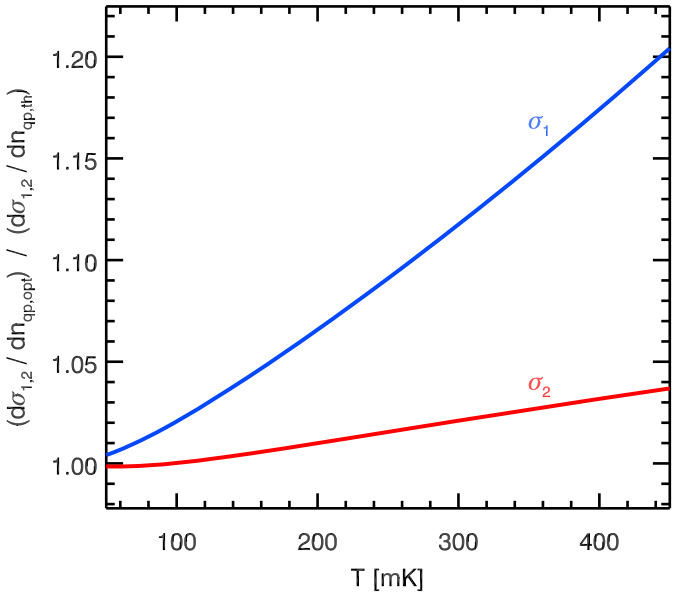

Figure 2.2: The ratio of $\frac{\partial\sigma(T,n_{qp})}{\partial n_{qp}}$ calculated using Equations (2.40)−(2.41) to $\frac{\partial\sigma(T)/\partial T}{\partial n_{qp}(T)/\partial T}$ calculated using Equations (2.37)−(2.39) as a function of temperature. Blue (red) denote the real (imaginary) part of the complex conductivity.

temperature approaches T_{ub}. This exercise suggests that the analytical formula provide a good approximation for the behavior of our detectors over all operating conditions of interest, but to obtain accurate conclusions the full integrals should be used, especially at large temperatures.

We are interested in two scenarios. The first is a *dark* scenario in which the number of optically generated quasi-particles is negligible. This can be accessed experimentally by placing an aluminum cover over the detector array and cooling it down to sub-Kelvin temperatures. In this case we can set $\mu^* = 0$ and obtain explicit expressions for all quantities of interest in terms of the temperature

$$n_{qp,th}(T) = 2N_0\sqrt{2\pi k_B T\Delta_0}\exp\left(-\frac{\Delta_0}{k_B T}\right) \tag{2.37}$$

$$\frac{\sigma_1^{dark}(T)}{\sigma_n} = \frac{4\Delta_0}{\hbar\omega}\exp\left(-\frac{\Delta_0}{k_B T}\right)\sinh(\xi)K_0(\xi) \tag{2.38}$$

$$\frac{\sigma_2^{dark}(T)}{\sigma_n} = \frac{\pi\Delta_0}{\hbar\omega}\left[1-\sqrt{\frac{2\pi k_B T}{\Delta_0}}\exp\left(-\frac{\Delta_0}{k_B T}\right)-2\exp\left(-\frac{\Delta_0}{k_B T}\right)\exp(-\xi)I_0(\xi)\right]. \tag{2.39}$$

The second scenario is where the detectors are illuminated and the number of optically generated quasi-particles is significant compared to the number of thermally generated quasi-particles. In this scenario we write Equations (2.26) and (2.27) in terms of n_{qp} in order to suppress the dependence on the chemical potential.

This yields

$$\frac{\sigma_1(T,n_{qp})}{\sigma_n} = \frac{1}{N_0\hbar\omega}\sqrt{\frac{2\Delta_0}{\pi k_B T}}\sinh(\xi)K_0(\xi)n_{qp} \tag{2.40}$$

$$\frac{\sigma_2(T,n_{qp})}{\sigma_n} = \frac{\pi\Delta_0}{\hbar\omega} - \frac{\pi}{2N_0\hbar\omega}\left(1+\sqrt{\frac{2\Delta_0}{\pi k_B T}}\exp(-\xi)I_0(\xi)\right)n_{qp}\,. \tag{2.41}$$

The important result here is that the complex conductivity is a linear function of the quasi-particle density. We can take the partial derivative of Equations (2.40) and (2.41) with respect to n_{qp} to determine the conversion factor $\partial\sigma/\partial n_{qp}$ between changes in quasi-particle density and changes in the complex conductivity. We can do the same for the dark scenario by evaluating $\partial\sigma/\partial n_{qp} = (\partial\sigma/\partial T)/(\partial n_{qp}/\partial T)$ using Equations (2.37)−(2.39). The ratio of these two conversion factors as a function of temperature is shown in Figure 2.2 for a typical MUSIC detector. The two are equal to within 20% over the temperature range of interest. This implies that theoretically the change in the complex conductivity that results from the thermal generation of a quasi-particle (through a change in the bath temperature) is approximately equivalent to the change that results from the optical generation of a quasi-particle. This equivalence enables calibration of the optical response by measuring the thermal response in a dark scenario. If this were not the case, the optical response would have to be measured directly using a calibrated black-body source, which is much more challenging. The equivalence between thermally and optically generated quasi-particles was confirmed experimentally in an early version of the MUSIC detectors that consisted of Al CPWs on a sapphire substrate [96]. More recently Janssen et al. [97] performed a rigorous comparison of thermal and optical response in two hybrid NbTiN-Al MKIDs and found them to be equal to within a factor of two. The factor of two discrepancies were larger than their measurement uncertainties, and they suspected that the discrepancies were due to the inability to accurately determine Δ_0 and η_{ph}, parameters necessary to compare the thermal and optical response within their model. We will have to address similar difficulties with our calibration procedure.

Examining Equations (2.40) and (2.41) we see that the complex conductivity of the superconductor will depend on the normal state conductivity $\sigma_n = 1/\rho_n$. This can be obtained by measuring the sheet resistance of the superconductor above T_c. It can also be predicted theoretically. However, as we will see in the following sections it is the fractional change in the complex conductivity — not the absolute value — that is important in predicting detector response. We define this change with respect to the dark value at zero temperature. In the dark scenario, as $T \to 0$ the quasi-particle density vanishes exponentially, and as a result so too does the real component of the complex conductivity $\sigma_1^{dark}(0) = 0$. The imaginary component exponentially approaches a finite value of $\sigma_2^{dark}(0) = (\pi\Delta_0/\hbar\omega)\sigma_n$ due to the kinetic inductance of the Cooper pairs. Therefore

$$\sigma_0 = \sigma_1^{dark}(0) - j\sigma_2^{dark}(0) = -j\frac{\pi\Delta_0}{\hbar\omega}\sigma_n\,. \tag{2.42}$$

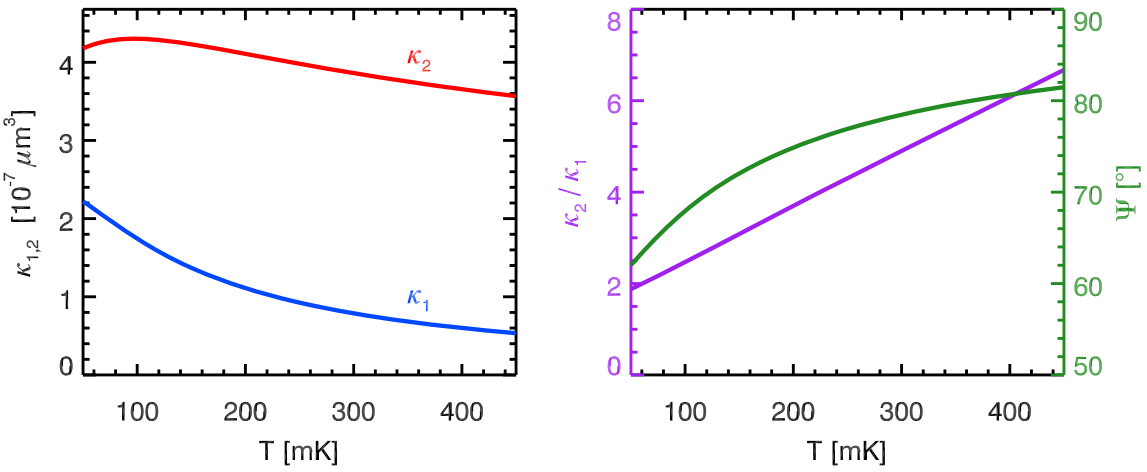

Figure 2.3: *Left:* Mattis-Bardeen prediction for a typical MUSIC resonator with frequency $f_{\rm res} = 3.2$ GHz and gap energy $\Delta_0 = 0.21$ meV. *Right:* the ratio of frequency to dissipation response is shown in purple and the angle between the quasi-particle direction and the direction normal to the resonance curve is shown in green.

We can then write

$$\frac{\delta\sigma}{|\sigma|} \equiv \frac{\sigma - \sigma_0}{|\sigma_0|} = (\kappa_1 + j\kappa_2)\, n_{\rm qp}\ ,$$

where

$$\kappa_1(T,\omega,\Delta_0) = \frac{1}{\pi N_0 \Delta_0}\sqrt{\frac{2\Delta_0}{\pi k_B T}}\sinh(\xi) K_0(\xi) \tag{2.43}$$

$$\kappa_2(T,\omega,\Delta_0) = \frac{1}{2N_0\Delta_0}\left[1 + \sqrt{\frac{2\Delta_0}{\pi k_B T}}\exp(-\xi) I_0(\xi)\right]\ . \tag{2.44}$$

The functions κ_1 and κ_2 are plotted as a function of temperature in the left panel of Figure 2.3 for values of ω and Δ_0 typical of a MUSIC detector. These functions act as the conversion between changes in quasi-particle density and changes in the complex conductivity. We examine the ratio of κ_2 to κ_1 in the right panel of Figure 2.3. This corresponds to the ratio of the imaginary and real response to the generation of quasi-particles. The imaginary response is intrinsically larger than the real response, and their ratio increases approximately linearly with temperature. The MUSIC detectors operate at a temperature $T = 240$ mK where $\kappa_2/\kappa_1 \approx 4$. We can further simplify the presentation of Equation (2.43) by writing it as

$$\frac{\delta\sigma}{|\sigma|} = |\kappa| e^{j\Psi} n_{\rm qp}\ , \tag{2.45}$$

with $\kappa = \sqrt{\kappa_1^2 + \kappa_2^2}$ and $\Psi = \arctan(\kappa_2/\kappa_1)$. This makes it clear that changes in quasi-particle density will appear in a well defined direction in the complex plane. The angle Ψ is also shown in the right panel of Figure 2.3. At our operating temperature $\Psi(240\ {\rm mK}) \simeq 78^\circ$ so that the response is only slightly rotated from the imaginary direction.

We note that the quantity $\delta\sigma/|\sigma|$ is small, even for quasi-particle densities corresponding to temperatures as large as 0.5 T_c. This is due to the suppression of the quasi-particle density by the factor $\exp(-\Delta_0/k_BT) \approx \exp(-1.76\,T_c/T)$. At temperatures $T \leq 0.5\ T_c$ we have that $\kappa_1 n_{\text{qp}} < 0.01$ and $\kappa_2 n_{\text{qp}} < 0.10$ for the typical MUSIC detector [98]. Therefore, going forward we will only consider up to first order in $\delta\sigma/|\sigma|$ in the development of the model.

2.2.4 Complex Conductivity and Surface Impedance

In general, the relationship between the surface impedance Z_s and the complex conductivity σ of a superconductor is determined by an integral over the Mattis-Bardeen kernel that must be performed numerically. However, simple relationships emerge in several limiting cases. The thin film limit should hold for the MUSIC detectors. In the thin film limit, the film thickness d is on the order of the electron mean free path l and is much less than the effective penetration depth λ_{eff}. In this limit we have that

$$Z_s = R_s + j\omega L_s = \frac{1}{(\sigma_1 - j\sigma_2)\,d}\ , \qquad \text{Thin film limit} \tag{2.46}$$

where R_s is the surface resistance in units of $\Omega/\square$ and L_s is the kinetic inductance of the superconducting thin film in units of $H/\square$. Using this equation we can equate first order perturbations to Z_s and σ to obtain the relationship

$$\frac{\delta Z_s}{Z_s} = -\frac{\delta\sigma}{\sigma}\ . \tag{2.47}$$

Since we are defining changes in the complex conductivity relative to σ_0 this becomes

$$\begin{aligned}
\frac{\delta Z_s}{Z_{s,0}} &= -\frac{\delta\sigma}{\sigma_0} \\
\frac{\delta R_s + i\omega\delta L_s}{i\omega L_s^{\text{dark}}(0)} &= -\frac{\delta\sigma_1 - i\delta\sigma_2}{-i\sigma_2^{\text{dark}}(0)} \\
\frac{\delta L_s}{L_s^{\text{dark}}(0)} - i\frac{\delta R_s}{\omega L_s^{\text{dark}}(0)} &= -\frac{\delta\sigma_2}{\sigma_2^{\text{dark}}(0)} - i\frac{\delta\sigma_1}{\sigma_2^{\text{dark}}(0)}\ ,
\end{aligned} \tag{2.48}$$

where we have used the fact that $R_s^{\text{dark}}(0) = \sigma_1^{\text{dark}}(0) = 0$. Equating the imaginary parts on either side of Equation (2.48) yields

$$\frac{\delta R_s}{\omega L_s^{\text{dark}}(0)} = \frac{\delta\sigma_1}{\sigma_2^{\text{dark}}(0)} = \kappa_1(T,\omega,\Delta_0)n_{\text{qp}}\ . \tag{2.49}$$

Similarly equating the real parts yields

$$\frac{\delta L_s}{L_s^{\text{dark}}(0)} = -\frac{\delta\sigma_2}{\sigma_2^{\text{dark}}(0)} = \kappa_2(T,\omega,\Delta_0)n_{\text{qp}}\ , \tag{2.50}$$

which says that the change in inductance is in the opposite direction as the change in σ_2. Note that Equations (2.49) and (2.50) can be combined into the following concise formula

$$\frac{\delta Z_s}{|Z_s|} = \frac{\delta \sigma}{|\sigma|} = |\kappa(T,\omega,\Delta_0)| e^{j\Psi(T,\omega,\Delta_0)} n_{\text{qp}} \ . \tag{2.51}$$

The properties of the resonator that we can easily measure are the frequency f_{res} and quality factor Q_i. We would like to relate these measurable properties to the quasi-particle density of the thin superconducting film. For an AC current at angular frequency ω the impedance of the resonant circuit is given by

$$Z = R + j\omega L + \frac{1}{j\omega C} \ , \tag{2.52}$$

where R is the resistance, L is the inductance, and C is the capacitance. The capacitance is set by the geometry of the resonator. The resistance is set by the surface resistance R_s that originates from quasi-particles in the thin superconducting film. The inductance has contributions from both the magnetic inductance L_m due to the geometry of the resonator and the surface inductance of the thin superconducting film due to the kinetic inductance L_s of the Cooper pairs

$$L = L_m + L_s \ . \tag{2.53}$$

Hence Equation (2.52) can be written as

$$Z = R_s + j\omega(L_m + L_s) + \frac{1}{j\omega C} \ . \tag{2.54}$$

It is useful to define a kinetic inductance fraction

$$\alpha = \frac{L_s}{L} = \frac{L_s}{L_s + L_m} \ . \tag{2.55}$$

The frequency and quality factor of the resonant circuit are given by the well known equations

$$f_{\text{res}} = \frac{1}{2\pi\sqrt{LC}} \qquad\qquad \frac{1}{Q_i} = \frac{R}{\omega L} \ . \tag{2.56}$$

Consider small perturbations in the resistance δR_s and kinetic inductance δL_s due to changes in the quasi-

particle density. This will result in a fractional shift in the frequency of the resonator

$$\begin{aligned}\frac{\delta f_{\rm res}}{f_{\rm res}} &= \frac{\sqrt{L}}{\sqrt{L+\delta L_s}} - 1 \\ &= \left(1+\frac{\delta L_s}{L}\right)^{-1/2} - 1 \\ &= -\frac{1}{2}\frac{\delta L_s}{L} \\ &= -\frac{\alpha}{2}\frac{\delta L_s}{L_s} \ . \end{aligned} \tag{2.57}$$

Similarly the shift in the resonator loss is given by

$$\begin{aligned}\delta\frac{1}{Q_i} &= \frac{R+\delta R_s}{\omega\left(L+\delta L_s\right)} - \frac{R}{\omega L} \\ &= \frac{R+\delta R_s}{\omega L}\left(1-\frac{\delta L_s}{L}\right) - \frac{R}{\omega L} \\ &= \frac{\delta R_s}{\omega L} - \frac{R\delta L_s}{\omega L^2} - \frac{\delta R_s \delta L_s}{\omega L^2} \\ &= \alpha\frac{\delta R_s}{\omega L_k} \ , \end{aligned} \tag{2.58}$$

where in the last line we have dropped the $\delta R_s \delta L_s$ term since it is the product of two small numbers and also dropped the $R\delta L_s/\omega L^2$ term since at temperatures well below T_c the resistance of the superconductor will be much less than the inductance and thus $R/\omega L$ will be small.

Again, referencing these changes relative to the value at zero temperature and zero optical loading, we can combine Equations (2.50) and (2.57) to write

$$\frac{\delta f_{\rm res}}{f_{\rm res}} \equiv \frac{f_{\rm res}(T) - f_{\rm res}^{\rm dark}(0)}{f_{\rm res}^{\rm dark}(0)} = -\frac{\alpha}{2}\kappa_2(T,\omega,\Delta_0)n_{\rm qp} \ . \tag{2.59}$$

Similarly we can combine Equations (2.49) and (2.58) to write

$$\delta\frac{1}{Q_i} \equiv \frac{1}{Q_i(T)} - \frac{1}{Q_i^{\rm dark}(0)} = \alpha\kappa_1(T,\omega,\Delta_0)n_{\rm qp} \ . \tag{2.60}$$

According to Mattis-Bardeen theory the loss at zero temperature and zero optical loading should be zero. However, we find that at low temperatures the quality factors of our resonators saturate at a value on the order of 10^5, suggesting the presence of an additional loss mechanism. To account for this we include $1/Q_{i,0} \equiv 1/Q_i^{\rm dark}(0)$ as a parameter in our model and define the quasi-particle induced shift relative to this value. Saturation of the quality factor at low temperatures is observed by other groups as well [99, 100, 101]. Possible causes include dielectric loss, loss at the surface of the superconductor, or a population of

nonthermal quasi-particles.

Equations (2.59) and (2.60) give the desired relationship between the measurable quantities — the frequency and loss of the resonator — and the quasi-particle density of the superconducting thin film. The final step is to examine how the frequency and loss of the resonator are probed by the readout electronics.

2.2.5 Resonant Circuit

The MUSIC readout electronics perform fast measurements of the complex transmission through the system at microwave (RF) frequencies using a homodyne mixing technique. The basic principle is illustrated in Figure 2.4, and the actual implementation is pictured in Figure 2.5. A detailed discussion of the implementation can be found in Duan [102].

Consider a single carrier tone at microwave frequency $f = f_{\mathrm{BB}} + f_{\mathrm{LO}}$. The readout electronics measure the complex amplitude $\hat{V}(f, f_{\mathrm{BB}})$ of the carrier tone at the output of the system. This can be expressed as

$$\begin{aligned}\hat{V}(f, f_{\mathrm{BB}}) &= \mathrm{I}(f, f_{\mathrm{BB}}) + j\mathrm{Q}(f, f_{\mathrm{BB}}) \\ &= S_{21}^{\mathrm{res}}(f) S_{21}^{\mathrm{RF}}(f) S_{21}^{\mathrm{BB}}(f_{\mathrm{BB}}) A_0 e^{i\phi_0} \ , \end{aligned} \tag{2.61}$$

where I and Q are the in-phase (real) and quadrature-phase (imaginary) components of the complex amplitude, A_0 and ϕ_0 are the amplitude and phase of the carrier tone at the input of the system, and S_{21}^{res}, S_{21}^{RF}, and S_{21}^{BB} are the complex forward transmission through the resonance, the RF electronics, and the baseband electronics, respectively. See the caption of Figure 2.4 for further explanation.

The equivalent circuit for the MKID consists of an RLC tank circuit capacitively coupled to a feedline. The derivation of the scattering matrix for this circuit has been worked out by a number of authors [103, 93, 104]. The end result is the following expression for the complex forward transmission through the resonance

$$S_{21}^{\mathrm{res}}(f) = 1 - \frac{Q/Q_c}{1 + 2jQ\frac{f - f_{\mathrm{res}}}{f_{\mathrm{res}}}} \ , \tag{2.62}$$

where f_{res} is the resonant frequency, Q is the quality factor, and Q_c is the coupling quality factor. The total loss is the sum of the loss internal to the resonator and the loss due to coupling to the feedline, or

$$\frac{1}{Q} = \frac{1}{Q_i} + \frac{1}{Q_c} \ , \tag{2.63}$$

where Q_i is the internal quality factor. We will use the terms resonator loss and resonator dissipation interchangeably to refer to the quantity $1/Q_i$.

Equation (2.62) maps the carrier frequency f into a circle in the complex plane as shown in the right panel of Figure 2.6. The diameter of the circle is Q/Q_c. If the carrier tone is placed far from resonance, $S_{21}^{\mathrm{res}}(\pm\infty) = 1$ and the resonance has no effect on its transmission. If the carrier tone is tuned directly to the

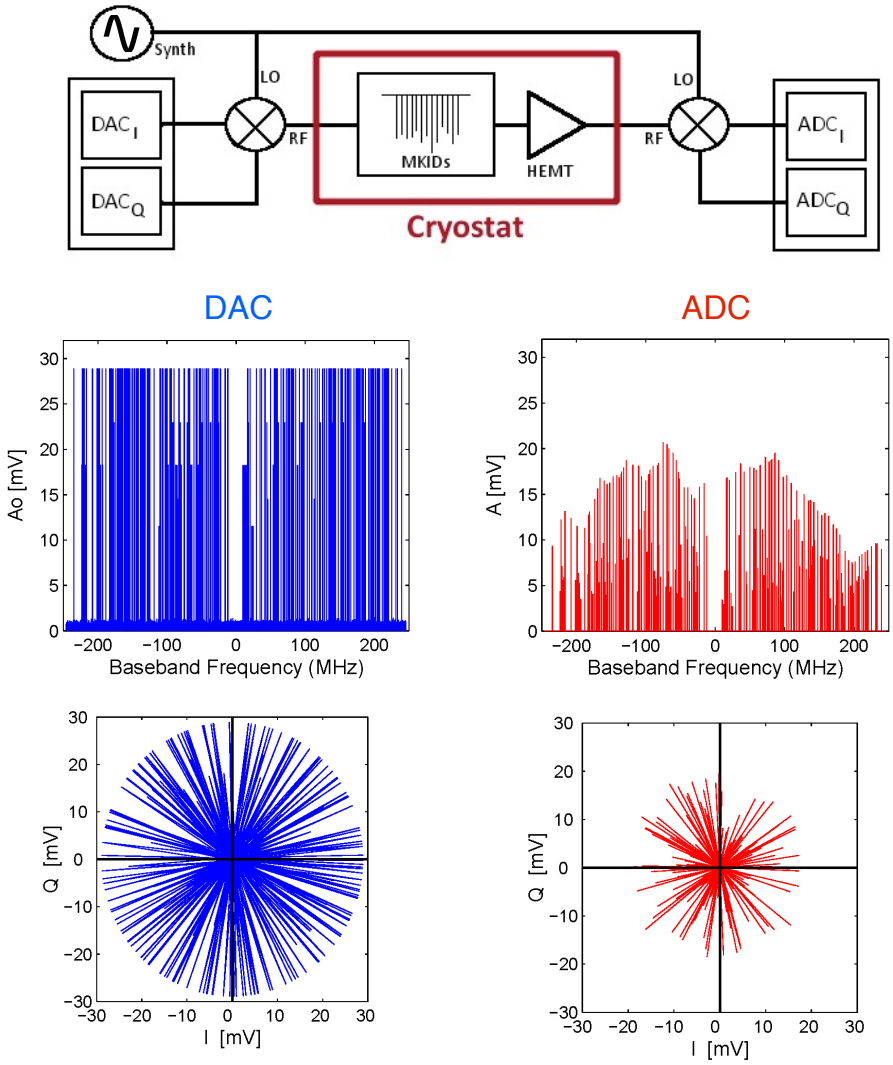

Figure 2.4: Diagram illustrating the basic principle behind the MUSIC readout electronics. Two digital-to-analog converters (DACs) output the real (in-phase or I) and imaginary (quadrature-phase or Q) components of a pre-programmed waveform that consists of a superposition of sinusoids (carriers or carrier tones) at baseband frequencies (-225 to 225 MHz). The absolute magnitude of the FFT of an example waveform is shown in the upper left panel; it has the appearance of a "frequency comb". The FFT of this waveform is also shown in the complex plane in the lower left panel. Note that the phases of the carriers are randomized in order to prevent clipping and utilize as much of the dynamic range of the DACs as possible. The I and Q components are up-mixed with a local oscillator (LO) to microwave (RF) frequencies and sent through the cryostat on coaxial cable. The baseband frequencies are chosen so that each carrier is centered on the resonant frequency of an MKID after mixing. The MKIDs modulate both the amplitude and phase of the carriers. The carriers are then amplified by a cryogenic high-electron-mobility transistor (HEMT) and down-mixed with the same LO back to baseband frequencies. The I and Q components are digitized by two analog-to-digital converters (ADCs). A field-programmable gate array (FPGA) is used to FFT the raw ADC timestreams, select the bins corresponding to the carrier tones, and low-pass filter and decimate them to the desired sampling rate of 100 Hz. The final output is the I and Q components of all of the frequency bins that contain carrier tones, sampled at 100 Hz. An example of the output at a single time sample is shown in the right column. The difference between the left and right columns provides a measurement of the overall gain and phase delay through the system.

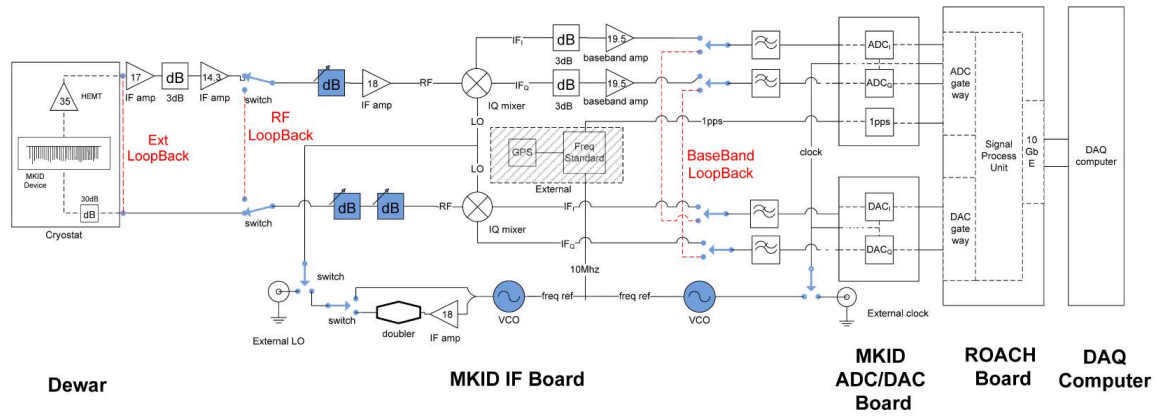

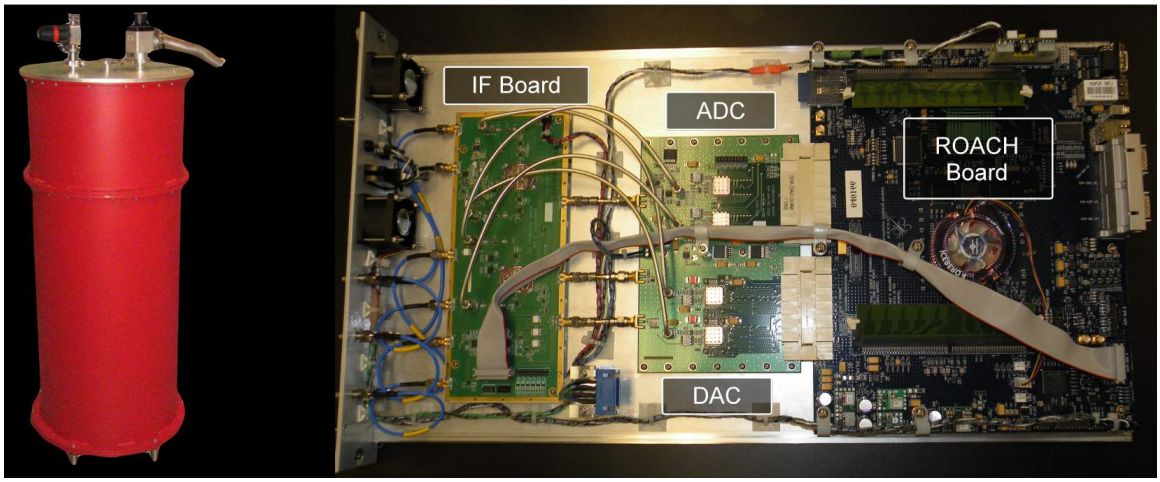

Figure 2.5: *Top:* Schematic of the MUSIC readout electronics board. *Bottom:* Picture of one of the MUSIC readout electronics board. Each board output 144 carrier tones and measures the complex amplitude of these tones at the output of the system at a rate of 100 Hz. Two boards are used to probe each detector array.

resonant frequency, $S_{21}^{\text{res}}(f_{\text{res}}) = 1 - Q/Q_c = Q/Q_i$ and it is maximally attenuated.

The squared magnitude of the transmission near resonance is given by

$$|S_{21}^{\text{res}}(f)|^2 = 1 - \frac{1-(Q/Q_i)^2}{1+4Q^2\left(\frac{f-f_{\text{res}}}{f_{\text{res}}}\right)^2}\,. \tag{2.64}$$

It is a Lorentzian dip from unity with depth $1 - Q^2/Q_i^2$ and full width at half maximum $\text{FWHM} = 2\Delta f_{\text{res}} = f_{\text{res}}/Q$. We denote the half width at half maximum as Δf_{res} and also refer to it as the resonator bandwidth. The magnitude $|S_{21}^{\text{res}}(f)|$ and argument $\theta = \arg(S_{21}^{\text{res}}(f))$ are shown in the left panel of Figure 2.6.

It is useful to introduce the variables

$$x = \frac{f-f_{\text{res}}}{f_{\text{res}}}\,, \qquad\qquad y = Qx = \frac{f-f_{\text{res}}}{2\Delta f_{\text{res}}}\,, \tag{2.65}$$

where x is the fractional detuning of the carrier tone from the resonant frequency and y is the normalized

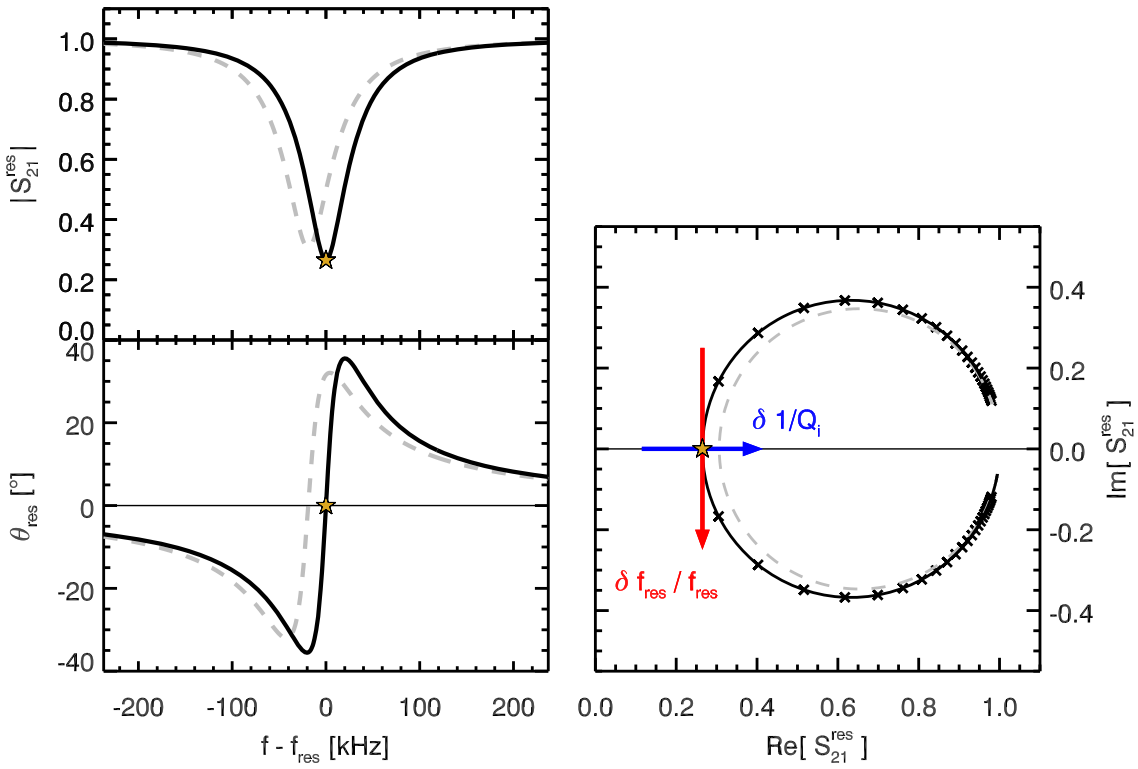

Figure 2.6: The magnitude (upper left), phase (lower left), and complex transmission (right) near resonance. Stars denote the location of the resonant frequency. The cross symbols in the right panel are separated by $\Delta f = 10$ kHz with increasing f corresponding to clockwise motion along the circle. The resonance curve changes from the solid black line to the dashed gray line when the optical loading is increased. Note that we measure the phase with respect to the complex origin, whereas many others measure the phase with respect to the center of the resonance circle. All curves were calculated using Equation (2.62) with parameters typical of a MUSIC resonator under sky loading: $f_{\rm res} = 3.2$ GHz, $Q = 40,000$, and $Q/Q_c = 0.75$.

detuning in terms of the full width at half maximum of the resonance. Equation (2.62) then becomes

$$S_{21}^{\rm res}(f) = 1 - \frac{Q/Q_c}{1+2jy}\,. \tag{2.66}$$

In the previous section we showed that a change in the quasi-particle density results in a change in both the frequency and dissipation of the resonator. We now calculate how these perturbations $\frac{\delta f_{\rm res}}{f_{\rm res}}$ and $\delta\frac{1}{Q_i}$ affect the transmission of the carrier tone. This is given by

$$\begin{aligned}\delta S_{21}^{\rm res} &= \left(\frac{\partial S_{21}^{\rm res}}{\partial \frac{1}{Q_i}}\right)\delta\frac{1}{Q_i} + \left(\frac{\partial S_{21}^{\rm res}}{\partial x}\right)\delta x \\ &= \left(\frac{\partial S_{21}^{\rm res}}{\partial \frac{1}{Q_i}}\right)\delta\frac{1}{Q_i} - \left(\frac{\partial S_{21}^{\rm res}}{\partial x}\right)\frac{\delta f_{\rm res}}{f_{\rm res}}\,,\end{aligned} \tag{2.67}$$

where in the last line we have used the fact that $\delta x \approx -\frac{\delta f_{\rm res}}{f_{\rm res}}$. The partial derivatives are evaluated using

Equation (2.62) to be

$$\frac{\partial S_{21}^{\text{res}}}{\partial \frac{1}{Q_i}} = \frac{Q^2/Q_c}{(1+2jy)^2} , \qquad \frac{\partial S_{21}^{\text{res}}}{\partial x} = \frac{2jQ^2/Q_c}{(1+2jy)^2} \tag{2.68}$$

and therefore

$$\delta S_{21}^{\text{res}} = \frac{Q^2/Q_c}{(1+2jy)^2}\left(\delta\frac{1}{Q_i} - 2j\frac{\delta f_{\text{res}}}{f_{\text{res}}}\right) . \tag{2.69}$$

If the carrier is centered directly on the resonant frequency, then $y = 0$ and the response is at a maximum. In this case perturbations to the resonator frequency (dissipation) will result in purely imaginary (real) changes in the transmission. The factor $(1+2jy)^{-2}$ encodes the effect of detuning on the small signal response. It is helpful to write it in the form $(1+2jy)^{-2} = \chi_y\, e^{j\phi_y}$ with

$$\chi_y = \frac{1}{1+4y^2} , \qquad \phi_y = -2\arctan(2y) . \tag{2.70}$$

If the carrier is mis-centered, then the response will be degraded by a factor χ_y. The frequency and dissipation response will still be orthogonal, and will still be oriented tangential and normal to the resonance curve. However, this "frequency and dissipation basis" will be rotated with respect to the real and imaginary basis by an angle ϕ_y. It is traditional to define a coupling efficiency

$$\chi_c = \frac{4\frac{Q_i}{Q_c}}{\left(1+\frac{Q_i}{Q_c}\right)^2} , \tag{2.71}$$

which takes a maximum value of 1 when the coupling quality factor is matched to the internal quality factor, or $Q_c = Q_i$. Equation (2.69) can then be written as

$$\delta S_{21}^{\text{res}} = \frac{1}{4}Q_i\chi_c\chi_y\left(\delta\frac{1}{Q_i} - 2j\frac{\delta f_{\text{res}}}{f_{\text{res}}}\right)e^{j\phi_y} . \tag{2.72}$$

This equation suggest three steps should be taken in order to maximize response to a fixed change in frequency and dissipation. The sources of loss intrinsic to the resonator — including the loss sourced by optically generated quasi-particles due to the background loading — should be minimized so that Q_i is large. The coupling to the feedline should then be designed so that under typical loading conditions $Q_c \approx Q_i$ ensuring that $\chi_c \approx 1$. Finally the carrier tone should be centered on the resonant frequency so that $\chi_y \approx 1$. The coupling efficiency χ_c and tuning efficiency χ_y are plotted as a function of their respective arguments in Figure 2.7.

Equation (2.72) holds for slow perturbations to the resonator frequency and dissipation. For fast perturbations we must account for the resonator ring-down response. This effect can be described in the Fourier

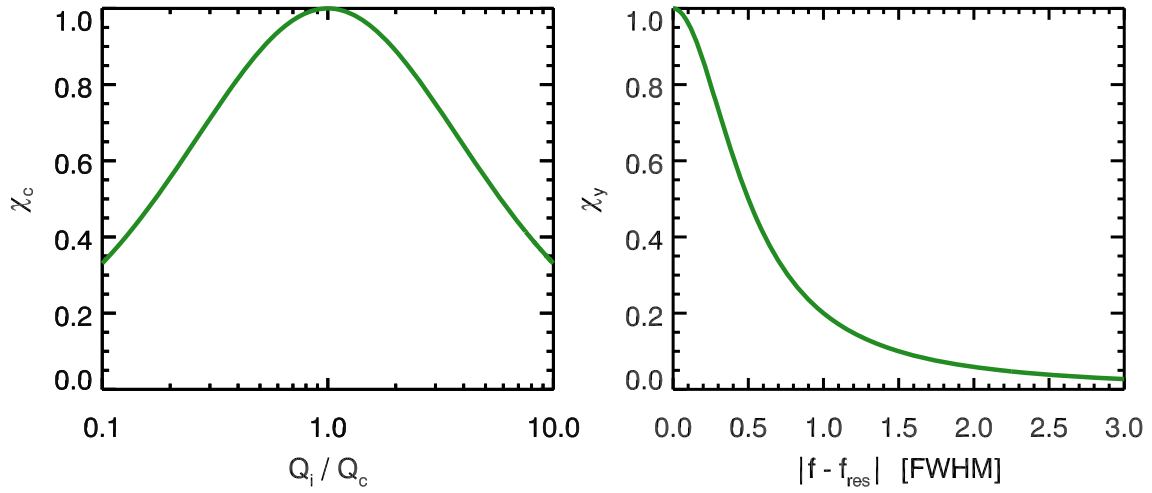

Figure 2.7: The coupling efficiency (left) and tuning efficiency (right). The FWHM of the resonator is defined as $f_{\rm res}/Q$.

domain as [105]

$$\delta\widetilde{S}_{21}^{\rm res}(\nu) = \frac{1}{4}Q_i\chi_c\chi_y H_{\rm res}(\nu,f)\left(\delta\widetilde{Q_i}^{-1}(\nu) - 2j\frac{\delta\widetilde{f}_{\rm res}}{f_{\rm res}}(\nu)\right)e^{j\phi_y}\ . \tag{2.73}$$

where $H_{\rm res}(\nu,f)$ is the resonator transfer function given by

$$H_{\rm res}(\nu,f) = \frac{1-S_{21}^{\rm res}(f+\nu)}{1-S_{21}^{\rm res}(f)}\ . \tag{2.74}$$

If the carrier tone is centered on resonance this reduces to

$$H_{\rm res}(\nu,f_{\rm res}) = \frac{1}{1+j\frac{\nu}{\Delta f_{\rm res}}} \tag{2.75}$$

and the resonator acts as a low-pass filter with bandwidth $\Delta f_{\rm res} = \frac{f_{\rm res}}{2Q}$. We are interested in signals at temporal frequencies $\nu \leq 50$ Hz (the readout electronics sample at a rate $\nu_s = 100$ Hz). Since $\Delta f_{\rm res} \gtrsim 20$ kHz for the MUSIC resonators, the transfer function can safely be ignored for our purposes.

We now consider perturbations to the frequency and dissipation that are sourced by perturbations in the quasi-particle density $\delta n_{\rm qp}$. In this case Equation (2.72) becomes

$$\begin{aligned}\delta S_{21}^{\rm res} &= \frac{1}{4}Q_i\chi_c\chi_y\alpha\left[\kappa_1(T,\omega,\Delta_0) + j\kappa_2(T,\omega,\Delta_0)\right]e^{j\phi_y}\delta n_{\rm qp} \\ &= \frac{1}{4}Q_i\chi_c\chi_y\alpha|\kappa(T,\omega,\Delta_0)|e^{j\left(\Psi(T,\omega,\Delta_0)+\phi_y\right)}\delta n_{\rm qp}\ .\end{aligned} \tag{2.76}$$

This can easily be converted into changes in the amplitude of the carrier tone using Equation (2.61). This is the quantity that is digitized by the readout electronics, which means that we have followed the propagation

of signal through the entire instrument. We are now in a position to derive an expression for the response to an astronomical source. Before doing that, we should address several complications to the model just presented.

2.2.6 Nonlinear Kinetic Inductance

As we will discuss in Section 2.3, increasing the power of the microwave probe signal decreases the amplitude of both additive electronics noise and TLS noise relative to astronomical signal. Hence, one can improve sensitivity by pushing to higher readout powers. However, as the power increases the MKID enters a nonlinear regime where the frequency and/or quality factor of the resonator are dependent on the power of the microwave probe signal. There are several mechanisms by which the power of the probe signal can effect the resonance; however, one mechanism that has been known to exist [106, 107] and that is also relatively easy to model is a nonlinear kinetic inductance.

The derivation and notation below are based on the analysis of Swenson et al. [108]. We start by expanding the kinetic inductance in terms of the current

$$L_s(I) = L_s(0)\left(1 + \frac{I^2}{I_\star^2} + \dots\right) . \tag{2.77}$$

Odd terms are dropped in the expansion, because we do not expect the kinetic inductance to depend on the direction of the current. The quantity $I_\star$ sets the scale for the onset of nonlinearity. We would like to determine the effect that the quadratic term has on the transmission near resonance. Let $f_{\text{res}}(I=0) \equiv f_{\text{res},0}$ denote the resonant frequency in the low-power limit and let $\Delta f_{\text{res}} \equiv f_{\text{res}} - f_{\text{res},0}$ denote the shift relative to this value due to the quadratic term. Examining Equation (2.57) it clear that the fractional shift Δx is given by

$$\Delta x = \frac{\Delta f_{\text{res}}}{f_{\text{res},0}} = -\frac{\alpha}{2}\frac{I^2}{I_\star^2} , = -\frac{E}{E_\star} \tag{2.78}$$

where we have used the equation $E = LI^2/2$ for the energy stored in a resonator and defined a characteristic energy $E_\star = LI_\star^2/\alpha$. The fractional detuning is given by

$$\begin{aligned} x &= \frac{f - f_{\text{res}}}{f_{\text{res}}} \\ &= \frac{f - f_{\text{res},0} - \Delta f_{\text{res}}}{f_{\text{res},0} + \Delta f_{\text{res}}} \\ &= \left(\frac{f - f_{\text{res},0}}{f_{\text{res},0}} - \frac{\Delta f_{\text{res}}}{f_{\text{res},0}}\right)\left(1 + \frac{\Delta f_{\text{res}}}{f_{\text{res},0}}\right)^{-1} \\ &= (x_0 - \Delta x)(1 - \Delta x) \\ &= x_0 - \Delta x , \end{aligned} \tag{2.79}$$

where in the last line we keep only terms up to first order in x_0 and Δx, since we are always operating in a regime where $x_0 \ll 1$ and $\Delta x \ll 1$.

We would like to determine x for a given value of low-power detuning x_0 and the microwave carrier power P. We start with the standard definition for the quality factor of a resonator as the maximum energy stored divided by the energy dissipated in one cycle, or

$$Q_i = \frac{E}{P_{\text{diss}}/2\pi f_{\text{res}}} \qquad \Longrightarrow \qquad E = \frac{P_{\text{diss}} Q_i}{2\pi f_{\text{res}}} \,, \tag{2.80}$$

where P_{diss} is the power dissipated by the resonator. We can derive an expression for P_{diss} through conservation of energy considerations. The microwave probe signal can either be reflected, transmitted, or absorbed by the resonator. Therefore

$$\begin{aligned} P &= |S_{11}^{\text{res}}|^2 P + |S_{21}^{\text{res}}|^2 P + P_{\text{diss}} \\ P_{\text{diss}} &= P\left(1 - |S_{11}^{\text{res}}|^2 - |S_{21}^{\text{res}}|^2\right) \,. \end{aligned} \tag{2.81}$$

The reflection is related to the transmission via

$$S_{11}^{\text{res}} = S_{21}^{\text{res}} - 1 = -\frac{Q/Q_c}{1 + 2jQx} \,, \tag{2.82}$$

where we have used Equation (2.62) for the forward transmission. Taking the squared magnitude of Equation (2.62) and Equation (2.82) and inserting into Equation (2.81) yields

$$P_{\text{diss}} = \frac{2Q^2}{Q_i Q_c} \frac{1}{1 + 4Q^2 x^2} P \,. \tag{2.83}$$

Therefore the energy stored in the resonator is

$$E = \frac{2Q^2}{Q_c} \frac{1}{1 + 4Q^2 x^2} \frac{P}{2\pi f_{\text{res}}} \tag{2.84}$$

and the fractional shift due to the quadratic term is

$$\Delta x = -\frac{2Q^2}{Q_c} \frac{1}{1 + 4Q^2 x^2} \frac{P}{2\pi f_{\text{res}} E_\star} \,. \tag{2.85}$$

Inserting this into Equation (2.79) yields

$$x_0 = x - \frac{2Q^2}{Q_c} \frac{1}{1 + 4Q^2 x^2} \frac{P}{2\pi f_{\text{res}} E_\star} \,, \tag{2.86}$$

which is an implicit equation for the power-shifted detuning x. In order to clean up the presentation of this equation we define the nonlinearity parameter

$$a = \frac{2Q^3}{Q_c} \frac{P}{2\pi f_{\text{res}} E_\star} \tag{2.87}$$

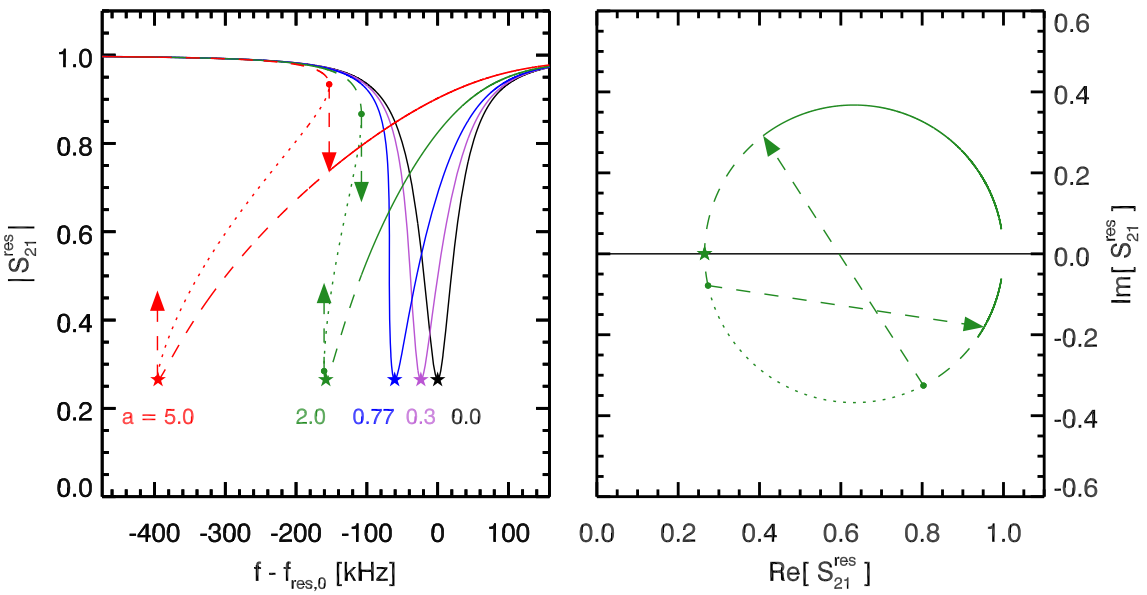

Figure 2.8: *Left:* magnitude of the forward transmission for several values of the nonlinearity parameter a. *Right:* forward transmission in the complex plane for $a = 2.0$. Stars denote the power-shifted resonant frequency. Regions of bifurcation are designated with dashed lines. In these cases the measured curve will depend on whether one is sweeping upward or downward in frequency and there will be a discontinuity at the location of the arrow. The dotted line is the third (unstable) root corresponding to intermediate stored energies. All curves were calculated using Equations (2.66) and (2.89) with parameters typical of a MUSIC resonator under sky loading: $f_{\text{res},0} = 3.2$ GHz, $Q = 40{,}000$, and $Q/Q_c = 0.75$.

as well as $y = Qx$ and $y_0 = Qx_0$. Equation (2.86) can then be written as

$$y_0 = y - \frac{a}{1+4y^2} \,, \tag{2.88}$$

which is a cubic equation for the normalized detuning y. Rearranging gives

$$4y^3 - 4y_0y^2 + y - (y_0 + a) = 0 \,. \tag{2.89}$$

Solving for the roots it is clear that there is a critical value of the nonlinearity parameter, $a_{\text{crit}} = 4\sqrt{3}/9 \approx 0.77$. For $a \leq a_{\text{crit}}$ there is only one purely real solution for all values of y_0. For $a > a_{\text{crit}}$ there is range of y_0 values for which there are three purely real solutions, corresponding to three possible values for the resonant frequency and stored energy. This means that multiple internal states exist for a single value of the carrier frequency and power. Only two of these states, corresponding to the smallest and largest stored energies, are stable. Therefore we say that the resonator has undergone *bifurcation*.

Figure 2.8 shows resonance curves for several values of a. As the carrier power is increased, the Lorentzian shape becomes distorted and compressed towards lower frequencies. When the carrier power exceeds the value corresponding to a_{crit} the resonator undergoes bifurcation. Two different curves will be measured depending on whether one is sweeping upward or downward in frequency, and a discontinuity appears at the

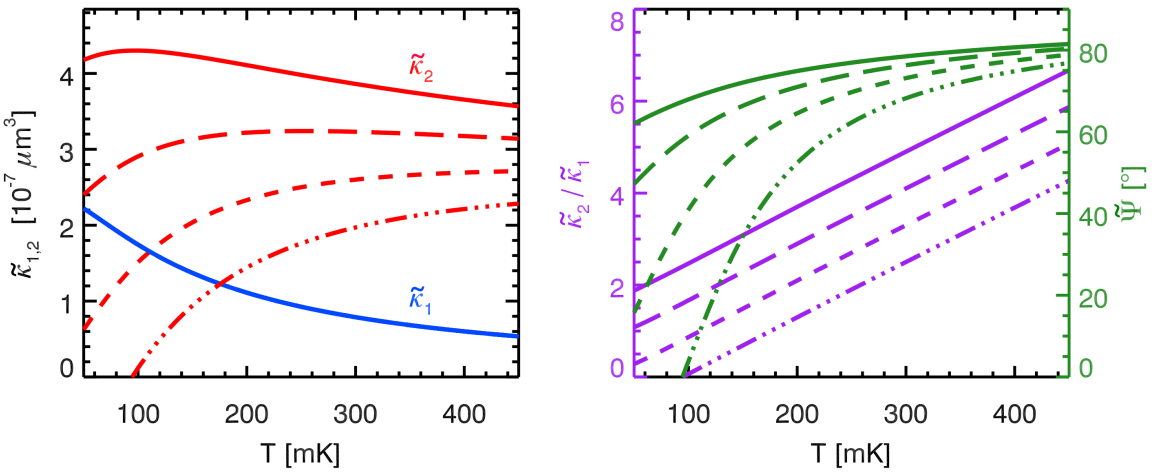

Figure 2.9: *Left:* Prediction for $\tilde{\kappa}_1$ and $\tilde{\kappa}_2$. The solid, long-dash, short-dash, and dash-dot lines correspond to a =0.0, 0.2, 0.4, and 0.6 respectively. *Right:* the ratio of frequency to dissipation response is shown in purple and the angle between the quasi-particle direction and the direction normal to the resonance circle is shown in green.

frequency where the resonator transitions from the bifurcated to nonbifurcated state.

In this model, the transmission near resonance is still given by Equation (2.66), but now y is determined by Equation (2.88). This means that the resonance will still trace out a circle in the complex plane; although, if one is operating in a regime where $a > a_{\text{crit}}$ then the full circle will be inaccessible due to bifurcation. The model also predicts that the depth of the resonance is constant with carrier power. Therefore, if one measures a non-circular resonance curve or a power-dependent resonance depth, then it is likely that some other mechanism is causing a nonlinear dissipation (recall that in this model only the resonator frequency is nonlinear). One example of such a mechanism is heating of the quasi-particle population by the microwave readout power [100, 109].

We now examine how fractional perturbations to the frequency $\delta f_{\text{res},0}/f_{\text{res},0}$ and dissipation $\delta\frac{1}{Q_i}$ translate into perturbations to the complex transmission under the nonlinear model. We can write

$$\begin{aligned}\delta S_{21}^{\text{res}} &= \left(\frac{\partial S_{21}^{\text{res}}}{\partial \frac{1}{Q_i}}\right)\delta\frac{1}{Q_i} + \left(\frac{\partial S_{21}^{\text{res}}}{\partial x}\right)\delta x \\ &= \left(\frac{\partial S_{21}^{\text{res}}}{\partial \frac{1}{Q_i}}\right)\delta\frac{1}{Q_i} + \left(\frac{\partial S_{21}^{\text{res}}}{\partial x}\right)\left[\left(\frac{\partial x}{\partial \frac{1}{Q_i}}\right)\delta\frac{1}{Q_i} + \left(\frac{\partial x}{\partial x_0}\right)\delta x_0\right], \end{aligned} \tag{2.90}$$

where we now assume that x depends on $1/Q_i$ (first term in the square brackets), since a change in the quality factor will change the energy stored in the resonator, thereby changing the resonant frequency through the nonlinear kinetic inductance. Inserting the derivatives presented in Equation (2.68) and using the fact that

$\delta x_0 = -\delta f_{\text{res},0}/f_{\text{res},0}$, we have

$$\delta S_{21}^{\text{res}} = \frac{1}{4} Q_i \chi_c \chi_y \left(\delta \frac{1}{Q_i} + 2j \left[\left(\frac{\partial x}{\partial \frac{1}{Q_i}} \right) \delta \frac{1}{Q_i} - \left(\frac{\partial x}{\partial x_0} \right) \frac{\delta f_{\text{res},0}}{f_{\text{res},0}} \right] \right) e^{j\phi_y} \, . \tag{2.91}$$

The derivatives $\partial x/\partial \frac{1}{Q_i}$ and $\partial x/\partial x_0$ are evaluated using Equation (2.88) to be

$$\frac{\partial x}{\partial \frac{1}{Q_i}} = -\frac{2a}{\left(1+4y^2\right)^2 + 8ay} = -\frac{2a\chi_y^2}{1+8ay\chi_y^2} \tag{2.92}$$

$$\frac{\partial x}{\partial x_0} = \frac{\left(1+4y^2\right)^2}{\left(1+4y^2\right)^2 + 8ay} = \frac{1}{1+8\chi_y^2 ay} \, . \tag{2.93}$$

Inserting these into Equation (2.91) yields

$$\delta S_{21}^{\text{res}} = \frac{1}{4} Q_i \chi_c \chi_y \left[\left(1 - j \frac{4a\chi_y^2}{1+8ay\chi_y^2} \right) \delta \frac{1}{Q_i} - j \frac{2}{1+8ay\chi_y^2} \frac{\delta f_{\text{res},0}}{f_{\text{res},0}} \right] e^{j\phi_y} \, . \tag{2.94}$$

We see that it is no longer the case that the frequency and dissipation response are orthogonal. While the frequency response is still confined to the direction tangent to the resonance curve, the dissipation response now leaks into the direction tangent to the resonance curve as well. We also see that detuning the carrier tone from the power shifted resonant frequency has interesting, asymmetric effects on the response. The factor of $(1+8ay\chi_y^2)^{-1}$ implies that for $f > f_{\text{res}}$ the frequency response will be attenuated, while for $f < f_{\text{res}}$ the frequency response will be amplified. The further the resonance is driven into the nonlinear regime, the greater this attenuation and amplification.

We now consider changes in frequency and dissipation sourced by changes in the quasi-particle density. This is given by

$$\begin{aligned} \delta S_{21}^{\text{res}} &= \frac{1}{4} Q_i \chi_c \chi_y \alpha \left[\left(1 - j \frac{4a\chi_y^2}{1+8ay\chi_y^2} \right) \kappa_1(T,\omega,\Delta_0) + j \frac{1}{1+8ay\chi_y^2} \kappa_2(T,\omega,\Delta_0) \right] e^{j\phi_y} \delta n_{\text{qp}} \\ &= \frac{1}{4} Q_i \chi_c \chi_y \alpha \, |\tilde{\kappa}(T,\omega,\Delta_0,a,y)| \, e^{j\left(\tilde{\Psi}(T,\omega,\Delta_0,a,y)+\phi_y\right)} \delta n_{\text{qp}} \, , \end{aligned} \tag{2.95}$$

where we have defined $\tilde{\kappa} = \tilde{\kappa_1} + j\tilde{\kappa_2}$ and $\tilde{\Psi} = \arctan\left(\tilde{\kappa_2}/\tilde{\kappa_1}\right)$ with

$$\begin{bmatrix} \tilde{\kappa_1}(T,\omega,\Delta_0,a,y) \\ \tilde{\kappa_2}(T,\omega,\Delta_0,a,y) \end{bmatrix} = \begin{bmatrix} 1 & 0 \\ \frac{-4a\chi_y^2}{1+8ay\chi_y^2} & \frac{1}{1+8ay\chi_y^2} \end{bmatrix} \times \begin{bmatrix} \kappa_1(T,\omega,\Delta_0) \\ \kappa_2(T,\omega,\Delta_0) \end{bmatrix} \, . \tag{2.96}$$

If we are centered on the power-shifted resonant frequency so that $y = 0$, this simplifies to

$$\delta S_{21}^{\text{res}} = \frac{1}{4} Q_i \chi_c \alpha \, |\tilde{\kappa}(T,\omega,\Delta_0,a,0)| \, e^{j\tilde{\Psi}(T,\omega,\Delta_0,a,0)} \delta n_{\text{qp}} \tag{2.97}$$

with

$$\begin{bmatrix} \tilde{\kappa}_1(T,\omega,\Delta_0,a,0) \\ \tilde{\kappa}_2(T,\omega,\Delta_0,a,0) \end{bmatrix} = \begin{bmatrix} 1 & 0 \\ -4a & 1 \end{bmatrix} \times \begin{bmatrix} \kappa_1(T,\omega,\Delta_0) \\ \kappa_2(T,\omega,\Delta_0) \end{bmatrix} . \tag{2.98}$$

In Figure 2.9 we show the predicted values of $\tilde{\kappa_1}$, $\tilde{\kappa_2}$, their ratio, and the corresponding angle $\tilde{\Psi}$ for a typical MUSIC detector operated at $y = 0$ and $a = [0.0,\ 0.2,\ 0.4,\ 0.6]$. We see that as the carrier power is increased the quasi-particle response normal to the resonance curve remains fixed, while the quasi-particle response tangential to the resonance curve declines. This results in a decrease in the overall magnitude of the response and a clockwise rotation of the quasi-particle direction. The reduction in response should be taken into account in readout power optimization. Assuming that the carrier is tuned to the resonant frequency so that $y = 0$ and Equation (2.98) applies, then when $a > \kappa_2/4\kappa_1$ the dissipative frequency response will be larger than the reactive frequency response. Since $\kappa_2/\kappa_1 \simeq 4$ for our resonators at base temperature, this corresponds to a value of the nonlinearity parameter $a \simeq 1$, which is just past the point of bifurcation. As the carrier power is increased beyond this point, the quasi-particle direction rotates past the direction normal to the resonance curve. This means that the frequency response will occur in the opposite direction as it does in the low power regime, so that a small increase in optical loading results in an increase in the resonator frequency.

2.2.7 Impedance Mismatch

Equation (2.66) does not provide an adequate description of the transmission near the MUSIC resonators. We observe a small rotation of the resonance circle relative to the transmission far from resonance that results in an asymmetric line shape, even in the low-power regime. This asymmetry has been observed by a number of authors [93, 110, 111, 112]. Khalil et al. [113] demonstrated that asymmetry can arise from a mismatch between the input and output transmission line impedance. This introduces an imaginary component to the coupling quality factor

$$\frac{1}{\widehat{Q}_c} = \frac{1}{|\widehat{Q}_c|} e^{j\phi_c} = \mathrm{Re}\left\{\frac{1}{\widehat{Q}_c}\right\} + \mathrm{Im}\left\{\frac{1}{\widehat{Q}_c}\right\} \tag{2.99}$$

and results in the following expression for the complex transmission near resonance

$$\begin{aligned} S_{21}^{\mathrm{res}}(f) &= 1 - \frac{Q/\widehat{Q}_c}{1+2jy} \\ &= 1 - \frac{1}{1+2jy}\frac{Q}{|\widehat{Q}_c|}e^{j\phi_c} \\ &= 1 - \frac{1}{1+2jy}\frac{Q}{Q_c\cos\phi_c}e^{j\phi_c} . \end{aligned} \tag{2.100}$$

Here we have defined

$$\frac{1}{Q_c} \equiv \mathrm{Re}\left\{\frac{1}{\widehat{Q}_c}\right\} = \frac{\cos\phi_c}{|\widehat{Q}_c|} \tag{2.101}$$

so that the internal quality factor is still given by Equation (2.63).

Equation (2.100) allows for a rotation ϕ_c of the resonance circle relative to the transmission off resonance, as observed. The small signal response is then given by

$$\delta S_{21}^{\mathrm{res}} = \frac{1}{4\cos\phi_c} Q_i \chi_c \chi_y \left[\left(1 - j\frac{4a\chi_y^2}{1+8ay\chi_y^2}\right)\delta\frac{1}{Q_i} - j\frac{2}{1+8ay\chi_y^2}\frac{\delta f_{\mathrm{res},0}}{f_{\mathrm{res},0}}\right] e^{j(\phi_y+\phi_c)} \ , \tag{2.102}$$

which reduces to Equation (2.94) in the case that $\phi_c = 0$. If we are considering fluctuations in quasi-particle density this becomes

$$\delta S_{21}^{\mathrm{res}} = \frac{1}{4\cos\phi_c} Q_i \chi_c \chi_y \alpha \left|\tilde{\kappa}(T,\omega,\Delta_0,a,y)\right| e^{j\left(\tilde{\Psi}(T,\omega,\Delta_0,a,y)+\phi_y+\phi_c\right)} \delta n_{\mathrm{qp}} \ . \tag{2.103}$$

Going forward we will absorb the $(\cos\phi_c)^{-1}$ term into the coupling efficiency

$$\chi_c \equiv \frac{\chi_c}{\cos\phi_c} \tag{2.104}$$

in order to simplify notation.

2.2.8 Nonantenna Response

In the above analysis we have assumed that the entirety of the response is due to optical power coupled through the antenna. However, there are a number of other (unwanted) mechanisms through which the detectors might respond to optical power. A not necessarily exhaustive list includes

- Radiation heats the substrate, resulting in a thermal response.
- The IDC acts as an antenna and couples radiation to the MKID.
- Radiation is directly absorbed by the aluminum section of the MKID.

Evidence for all three of these mechanisms has been observed in engineering grade detector arrays. The nonantenna response will have a beam that, in a time-reverse sense, terminates on either the interior of the cryostat, room temperature surfaces, or the sky. This will result in an increase in loading which will increase photon noise and degrade responsivity. Significant effort has been made to understand and mitigate the nonantenna response. There is strong evidence that in the final production arrays substrate heating and capacitive coupling are minimal, and the nonantenna response is dominated by direct absorption in the aluminum section.

Including the effects of direct absorption in our full instrument model is relatively straightforward. The optical power from a beam-filling, black-body load at the cryostat window (i.e. Equation (2.7)) will now be the sum of the power coupled through the antenna and the power directly absorbed, or

$$\begin{aligned} P_{\rm opt} &= P_{\rm opt,ant} + P_{\rm opt,dir} \\ &= \eta_{\rm opt,ant} k_B \left(T_{\rm load,ant} + T_{\rm exc,ant}\right) \Delta\nu_{\rm mm,ant} + \eta_{\rm opt,dir} k_B \left(T_{\rm load,dir} + T_{\rm exc,dir}\right) \Delta\nu_{\rm mm,dir} \ , \end{aligned} \tag{2.105}$$

where we have expressed the powers in terms of effective Rayleigh-Jeans temperatures. In the case where we are looking at the sky, the load temperatures are parameterized as

$$T_{\rm load,ant} = f_{\rm spill,ant} T_{\rm amb} + \left(1 - f_{\rm spill,ant}\right) \left(1 - e^{-\tau_{\rm ant}/\sin\mathfrak{e}}\right) T_{\rm atm} \tag{2.106}$$

and similarly

$$T_{\rm load,dir} = f_{\rm spill,dir} T_{\rm amb} + \left(1 - f_{\rm spill,dir}\right) \left(1 - e^{-\tau_{\rm dir}/\sin\mathfrak{e}}\right) T_{\rm atm} \ . \tag{2.107}$$

That is we assume independent spillover fractions and optical depths for antenna response and direct absorption.

We can make some reasonable assumptions about the direct absorption. It is most likely unpolarized. It is expected that the efficiency will scale with the area of the aluminum section $\eta_{\rm opt,dir} \propto A$. Finally, it is extremely broadband, with a lower cutoff at ~ 90 GHz set by the gap energy of aluminum and an upper cutoff at ~ 420 GHz set by the metal mesh filter. This means that $\Delta\nu_{\rm mm,dir}$ is 10-15 times greater than $\Delta\nu_{\rm mm,ant}$ and that even if the efficiency $\eta_{\rm opt,dir}$ is small the fractional load from direct absorption can be substantial.

We use "dark resonators" — resonators not coupled to an antenna — to calibrate the nonantenna response. These resonators are interspersed evenly throughout the focal plane. In the final detector arrays, they constitute 8% of the total number of resonators. Since $\eta_{\rm opt,ant} = 0$ for dark resonators, the optical power is given by

$$P_{\rm opt}^{\rm dark} = \eta_{\rm opt,dir} k_B \left(T_{\rm load,dir} + T_{\rm exc,dir}\right) \Delta\nu_{\rm mm,dir} \ . \tag{2.108}$$

The calibration procedure enables us to measure the quantities $\eta\Delta\nu_{\rm mm}$, $T_{\rm exc}$, and $f_{\rm spill}$ for each resonator. This corresponds to $\eta_{\rm opt,dir}\Delta\nu_{\rm mm,dir}$, $T_{\rm exc,dir}$, and $f_{\rm spill,dir}$ for the dark resonators. We take the average of these quantities over all dark resonators and then correct the values measured for the antenna-coupled resonators to isolate the antenna response. This procedure is discussed in greater detail in Section 3.2.

2.2.9 Substrate Heating and Nonequilibrium Dynamics

As mentioned in Section 2.2.8, radiation can heat the silicon substrate, elevating its temperature above that of the copper focal plane unit. Let $T_{\rm sub}$ denote the temperature of the substrate and $T_{\rm bath}$ the temperature of the

focal plane unit as measured by the Array GRT. The power that must be absorbed by the substrate in order to maintain the elevated temperature is given by a thermal conductance function of the form

$$P_{\text{sub}} = g\left(T_{\text{sub}}^{n} - T_{\text{bath}}^{n}\right) \ , \tag{2.109}$$

where g is the thermal coupling constant and n is the thermal coupling power-law exponent, the exact value of which will depend on the coupling model. We can solve this equation to obtain an expression for the temperature of the substrate

$$\begin{aligned} T_{\text{sub}} &= \left(T_{\text{bath}}^{n} + \frac{P_{\text{sub}}}{g}\right)^{1/n} \\ &= \left(T_{\text{bath}}^{n} + \tilde{P}_{\text{sub}}\right)^{1/n} \ , \end{aligned} \tag{2.110}$$

where we have defined $\tilde{P}_{\text{sub}} = P_{\text{sub}}/g$ since the expression depends only on the ratio of P_{sub} and g.

Substrate heating was substantial in several generations of engineering grade arrays, dominating the nonantenna response measured by the dark resonators. In order to model the substrate heating we used Equation (2.110) and assumed that the temperature T appearing in the Mattis-Bardeen equations was equal to T_{sub}. This added $1 + N_{\text{load}}$ parameters to the overall model since a different value of P_{sub} was required for each loading condition under consideration.

Eventually the problem of substrate heating was remedied by connecting (via gold wirebonds) a border of gold metal film on the detector tiles to the copper on the focal plane unit, thereby improving the thermal conductance. After adding the gold wirebonds, measurements of the resonant frequency as a function of temperature of a set of all Nb test resonators located on an engineering grade array placed strong upper limits on the temperature difference $T_{\text{sub}} - T_{\text{bath}} \lesssim 3$ mK for all operating conditions of interest. To briefly summarize this measurement: since the critical temperature of Nb is 9.2 K, the number of thermally and optically generated quasi-particles is negligible for the test resonators at the bath temperatures and optical wavelengths at which we operate. Their resonant frequency is entirely set by the temperature-dependent resonant response of a thin layer of two-level systems (TLS) on the substrate. TLS are discussed in greater detail in Section 2.3.2.2, suffice it to say that the temperature dependence of the TLS induced resonant frequency shift is theoretically understood, is approximately linear with a positive slope (see Equation (2.179)), and is observed in the test resonators. Therefore, we can effectively use the test resonators as "TLS thermometers". We found that their resonant frequencies did not change when we switched from a LN_2 blackbody load to a room-temperature blackbody load at the cryostat window. If there was substrate heating, the resonant frequency would increase between the LN_2 and room temperature load. We use this fact to place an upper limit of 1.5 mK on the difference in substrate temperature between the LN_2 and room-temperature load. If we then make the reasonable assumption that the change in substrate temperature between a 0 K and LN_2 load is not larger than the change between a LN_2 and room temperature load, we obtain the quoted $T_{\text{sub}} - T_{\text{bath}} \lesssim 3$ mK.

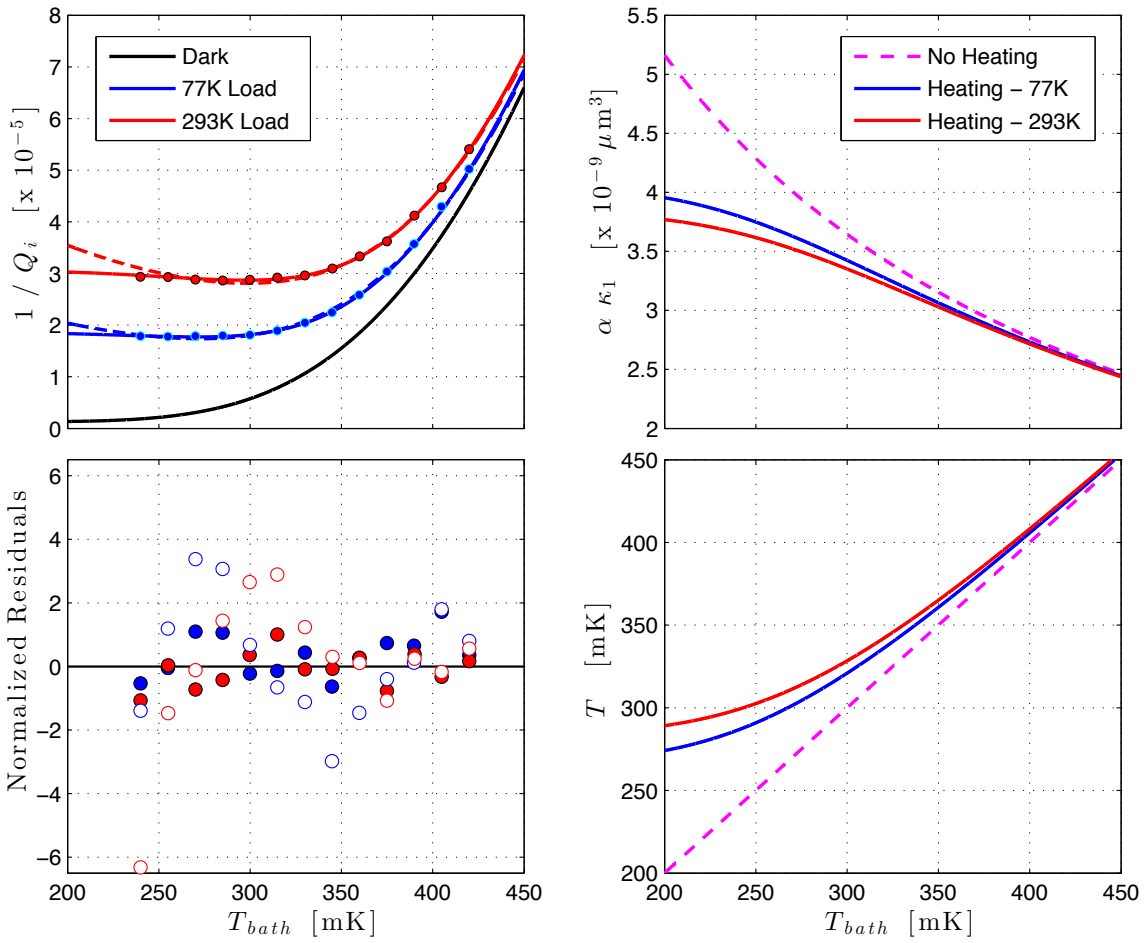

Figure 2.10: Experimental evidence for quasi-particle heating. *Top Left:* The dissipation $1/Q_i$ as a function of bath temperature and loading for a typical MUSIC detector. Black denotes negligible optical loading. Blue (red) denote a 77K (293K) beam-filling, black-body load in front of the cryostat window. The circles are measured data points and the lines are best-fit models. Error bars are less than the radius of the circle. The dashed line is a model without heating and the solid line is a model with heating. *Bottom Left:* Normalized residuals (i.e., $(\mathrm{data} - \mathrm{model})/\mathrm{error}$) for the best-fit models shown in the plot above. Unfilled circles correspond to the model without heating and filled circles correspond to the model with heating. *Top Right:* The factor that converts quasi-particle density to dissipation as a function of temperature. The dashed pink line corresponds to the model without heating and the solid blue and red lines correspond to the model with heating. *Bottom Right:* The temperature as a function of bath temperature. The legend is the same as in the plot above.

But even after adding the gold wirebonds, the frequency and dissipation of the resonators as a function of temperature and loading exhibited behavior that could not be explained by the full instrument model without including an effect akin to substrate heating. This is illustrated in Figure 2.10. At low temperatures ($250\ \text{mK} < T_{\text{bath}} < 300\ \text{mK}$) and under both 77 K and 293 K loads the measured dissipation is constant as a function of temperature. The model without substrate heating is unable to replicate this behavior, it actually predicts a decrease in the dissipation with increasing temperature. This is because under the model the number of optically generated quasi-particles is much greater than the number of thermally generated quasi-particles at low temperatures. So as the temperature increases, the total number of quasi-particles remains roughly constant, but the factor that converts quasi-particles to complex conductivity κ_1 decreases. Not until one reaches a temperature at which the thermally generated quasi-particles become significant does the dissipation begin to increase. We do not observe this curvature, the measured dissipation and the frequency are flat at low temperatures for nearly all of the resonators. In order to replicate this behavior the model without substrate heating moves toward unphysical parameter values — particularly very low values of τ_{max} — and even then it yields poor fits.

We include heating in our model to explain this behavior. However, our interpretation is not that the substrate is sitting at an elevated temperature, but rather the quasi-particles. That is, we assume that under heavy optical loading, the quasi-particles are out of equilibrium with the lattice phonons. We further assume that the quasi-particles can be described by a Fermi-Dirac distribution at an effective temperature T, which is set by the thermal conductance formula

$$\begin{aligned} T &= \left(T_{\text{bath}}^{n} + \frac{P_{\text{e}}}{g} \right)^{1/n} \\ &= \left(T_{\text{bath}}^{n} + \frac{\eta_{\text{e}} P_{\text{opt}}}{g} \right)^{1/n}, \end{aligned} \tag{2.111}$$

where we have made the reasonable assumption that the power maintaining the elevated quasi-particle temperature is proportional to the absorbed optical power, $P_{\text{e}} = \eta_{\text{e}} P_{\text{opt}}$. This adds two additional parameters n and $\tilde{\eta}_{\text{e}} = \eta_{\text{e}}/g$ to the model.

2.2.10 Nonuniform Absorption

Incident optical power from the antenna will not be absorbed uniformly along the overlap between the Nb/Si_3N_4 microstrip and the Al section of the MKID. There will be some position-dependent power absorption profile that will result in a position-dependent distribution of quasi-particles. Since the incident photons are above the pair-breaking energy, the Al can be treated as a normal metal in the calculation of the power absorption profile. The result will depend only on the resistivity and dimensions of the Al and therefore can be constrained by a single measurement of the surface resistance. The position-dependent quasi-particle density can then be determined by solving a position-dependent generation-recombination equation that includes the

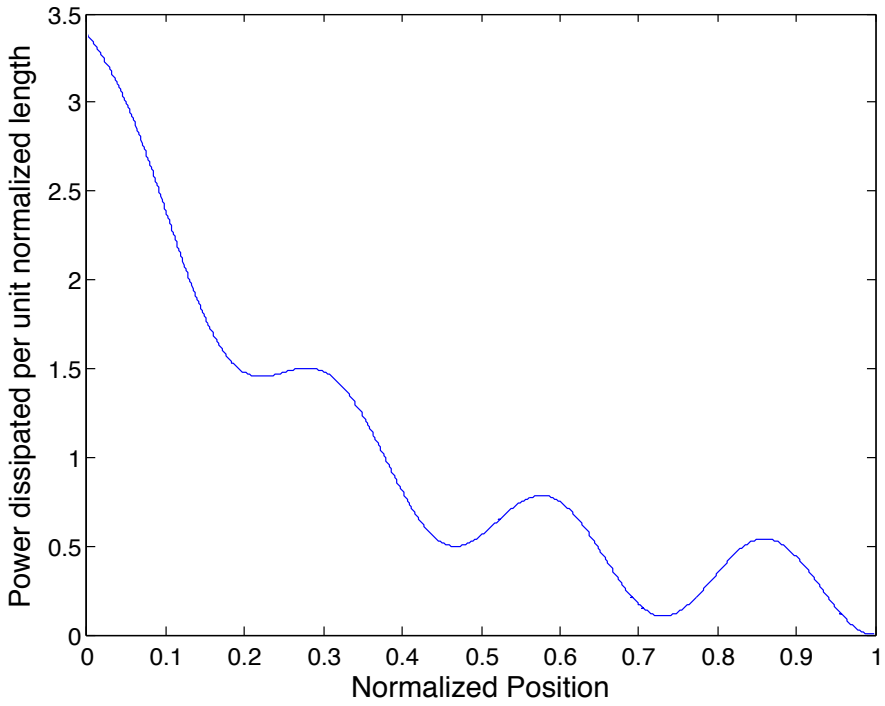

Figure 2.11: Power absorption profile $\psi(z)$ for a 1 mm long Nb/SiO_2/Al microstrip line at 250 GHz. Taken from Zmuidzinas [114].

effects of diffusion. We briefly outline this procedure below following the analysis of Golwala [98].

Let z denote position along the length of the Al section, so that $0 \leq z \leq l$. Power from the antenna is incident on the microstrip from $z = 0$ and the microstrip terminates in an open circuit at $z = l$. Define the power absorption profile $\psi(z)$ as the fractional power absorbed per unit length

$$\frac{dP}{dz} = \psi(z) P_{\text{opt,ant}} \ , \qquad \int_0^l \psi(z) dz = 1 \ . \tag{2.112}$$

Note that not all power incident from the microstrip will be absorbed by the Al section. In the definitions above we have lumped the absorption efficiency η_{abs} into the overall optical efficiency $\eta_{\text{opt,ant}}$ presented in Equation (2.105) for $P_{\text{opt,ant}}$. Zmuidzinas [114] derives an analytical expression for $\psi(z)$, assuming perfect reflection at $z = l$ and neglecting impedance mismatch at the microstrip and aluminum interface. We use this analytical expression and a measurement of the Al sheet resistance at 4 K to determine $\psi(z)$. An example power absorption profile is shown in Figure 2.11.

If the distribution of quasi-particles is nonuniform then the quasi-particles will tend to diffuse out of high density regions and into low density regions. This process is described by a diffusion current

$$J(\boldsymbol{r},t) = -D \boldsymbol{\nabla} n_{\text{qp}}(\boldsymbol{r},t) \ , \tag{2.113}$$

where we assume that the diffusion constant D is independent of position. We can write a general continuity equation to describe the local conservation of quasi-particles

$$\frac{\partial n_{\rm qp}}{\partial t} + \boldsymbol{\nabla} \cdot \boldsymbol{J} = \Gamma_{\rm G,th}(\boldsymbol{r},t) + \Gamma_{\rm G,opt}(\boldsymbol{r},t) - \Gamma_{\rm R}(\boldsymbol{r},t) \ , \tag{2.114}$$

where the now position-dependent optical and thermal generation rates act as *source* terms that adds quasi-particles into the system, and the recombination rate acts as a *sink* term that removes quasi-particles from the system. The diffusion length is expected to be much greater than either the width w or thickness d of the Al section, so it is safe to assume that the quasi-particle density is constant over the cross-sectional area. This reduces Equation (2.114) to the one-dimensional partial differential equation

$$\frac{\partial n_{\rm qp}(z,t)}{\partial t} - D\frac{\partial^2 n_{\rm qp}(z,t)}{\partial z^2} = \Gamma_{\rm G,th}(z,t) + \Gamma_{\rm G,opt}(z,t) - \Gamma_{\rm R}(z,t) \ . \tag{2.115}$$

If we consider the steady state behavior where $\frac{\partial n_{\rm qp}}{\partial t} = 0$, then Equation (2.115) yields a position-dependent version of the generation-recombination equation

$$\frac{\eta_{\rm ph} P_{\rm opt,ant}\,\psi(z) + \eta_{\rm ph} p_{\rm opt,dir}}{\Delta} = -DA\frac{\partial^2 n_{\rm qp}(z)}{\partial z^2} + RA\left[n_{\rm qp}^2(z) - n_{\rm qp,th}^2\right] + \frac{A}{\tau_{\rm max}}\left[n_{\rm qp}(z) - n_{\rm qp,th}\right] \ , \tag{2.116}$$

where $p_{\rm opt,dir} = P_{\rm opt,dir}/l$ is the power directly absorbed per unit length and $A = wd$ is the *cross-sectional area*. Here we are making the reasonable assumptions that the direct absorption and thermal generation occur uniformly throughout the aluminum section. Given $\psi(z)$ the differential equation above can be solved numerically to obtain $n_{\rm qp}(z)$. The boundary conditions for the equation are

$$\left.\frac{\partial n_{\rm qp}(z)}{\partial z}\right|_{z=0,l} = 0 \ , \tag{2.117}$$

which physically correspond to the fact that the quasi-particles cannot diffuse out of the Al section.

It can be shown [103] that a position-dependent quasi-particle distribution is weighted by the square of the resonator current distribution in the determination of the resonator response. For a $\lambda/4$ transmission line resonator the current has a standing wave distribution at resonant frequency that is given by $I(z) = I(0)\cos(\pi z/2L)$ where L is the total length of the transmission line. The current is a maximum at the shorted, inductive end (z=0) and a minimum at the open, capacitive end (z=L). As a result the "effective" quasi-particle density is calculated as

$$n_{\rm qp} = \frac{\int_0^l \cos^2\left(\frac{\pi z}{2L}\right) n_{\rm qp}(z)dz}{\int_0^l \cos^2\left(\frac{\pi z}{2L}\right) dz} \ . \tag{2.118}$$

The MUSIC resonators are of a hybrid design in which the inductive portion is a distributed CPW transmission line and the capacitive portion is a nearly lumped element IDC. The current should be approximately

uniform over the length of Al section, since it occupies a small fraction of the total length of the inductive portion at the high current, shorted end. We assume that $\cos^2\left(\frac{\pi z}{2L}\right) \approx 1$ for $0 \leq z \leq l$. The mean quasi-particle density over the length of the Al section is then the quantity that determines resonator response. We separate the expression for the position-dependent quasi-particle density $n_{\rm qp}(z)$ into the mean value $n_{\rm qp}$ and a position-dependent factor $\phi(z)$:

$$n_{\rm qp}(z) = n_{\rm qp}\phi(z) \ , \qquad\qquad \frac{1}{l}\int_0^l \phi(z)dz = 1 \ . \tag{2.119}$$

We can then integrate Equation (2.116) over the length of the Al section to obtain an implicit expression for the mean density

$$\frac{\eta_{\rm ph}\left(P_{\rm opt,ant}+P_{\rm opt,dir}\right)}{\Delta} = -DAn_{\rm qp}\int_0^l \frac{\partial^2\phi(z)}{\partial z^2}dz + RV\left[\frac{n_{\rm qp}^2}{l}\int_0^l \phi^2(z)dz - n_{\rm qp,th}^2\right] + \frac{V}{\tau_{\rm max}}\left[n_{\rm qp}-n_{\rm qp,th}\right] \ . \tag{2.120}$$

The diffusion term disappears due to the boundary condition

$$\int_0^l \frac{\partial^2\phi(z)}{\partial z^2}dz = \left.\frac{\partial\phi(z)}{\partial z}\right|_0^l = 0 \ . \tag{2.121}$$

If we then introduce the correction factor

$$\zeta = \frac{1}{l}\int_0^l \phi^2(z)dz \tag{2.122}$$

we obtain the relatively simple equation

$$\frac{\eta_{\rm ph}P_{\rm opt,ant}+\eta_{\rm ph}P_{\rm opt,dir}}{\Delta} = RV\left(\zeta n_{\rm qp}^2 - n_{\rm qp,th}^2\right) + \frac{V}{\tau_{\rm max}}\left(n_{\rm qp}-n_{\rm qp,th}\right) \ . \tag{2.123}$$

An explicit expression for $n_{\rm qp}$ can then be obtained by applying the quadratic formula

$$n_{\rm qp} = \left[\frac{\eta_{\rm ph}P_{\rm opt,ant}+\eta_{\rm ph}P_{\rm opt,dir}}{\zeta RV\Delta} + \frac{1}{\zeta}n_{\rm qp,th}^2 + \frac{1}{\zeta R\tau_{\rm max}}\left(n_{\rm qp,th}+\frac{1}{4\zeta R\tau_{\rm max}}\right)\right]^{1/2} - \frac{1}{2\zeta R\tau_{\rm max}} \ , \tag{2.124}$$

where again we have discarded the second root since it corresponds to negative values. Comparing to Equation (2.21) we see that, in regards to the steady-state quasi-particle density, the nonuniform absorption essentially just increases the recombination constant R by a factor ζ. The factor of ζ^{-1} in front of the $n_{\rm qp,th}^2$ term also means that the influence of the thermal quasi-particle population is suppressed due to the nonuniform absorption.

We now consider the effect of nonuniform absorption on the quasi-static, small-signal response. Let $\delta P_{\rm opt,ant}$ and $\delta P_{\rm opt,dir}$ denote small changes in power absorbed through the antenna and the power directly absorbed, respectively. This will result in a small position-dependent change in the quasi-particle density

$\delta n_{\rm qp}(z) = n_{\rm qp}\delta\phi(z)$. Performing a perturbation analysis of Equation (2.116) yields

$$\frac{\eta_{\rm ph}\delta P_{\rm opt,ant}\psi(z) + \eta_{\rm ph}\delta P_{\rm opt,dir}/l}{\Delta} = -DAn_{\rm qp}\frac{\partial^2(\delta\phi(z))}{\partial z^2} + An_{\rm qp}\left[2Rn_{\rm qp}\phi(z) + \frac{1}{\tau_{\rm max}}\right]\ \delta\phi(z)\ , \tag{2.125}$$

which is a differential equation similar to Equation (2.116) but now for the small signal response profile $\delta\phi(z)$. We would like to derive an expression for the mean response over the length of the Al section, since this is the quantity that we actually measure. Integrating both sides of Equation (2.125) from 0 to l and dropping the diffusion term, again due to boundary conditions, yields

$$\begin{aligned}\frac{\eta_{\rm ph}\left(\delta P_{\rm opt,ant} + \delta P_{\rm opt,dir}\right)}{\Delta} &= Vn_{\rm qp}\frac{1}{l}\int_0^l\left(2Rn_{\rm qp}\phi(z) + \frac{1}{\tau_{\rm max}}\right)\ \delta\phi(z)dz \\ &= V\left(2Rn_{\rm qp}\zeta_\delta + \frac{1}{\tau_{\rm max}}\right)n_{\rm qp}\frac{1}{l}\int_0^l\delta\phi(z)dz \\ &= V\left(2Rn_{\rm qp}\zeta_\delta + \frac{1}{\tau_{\rm max}}\right)\delta n_{\rm qp}\ .\end{aligned} \tag{2.126}$$

Here we have defined the mean change in quasi-particle density

$$\begin{aligned}\delta n_{\rm qp} &= \frac{1}{l}\int_0^l\delta n_{\rm qp}(z)dz \\ &= \frac{1}{l}n_{\rm qp}\int_0^l\delta\phi(z)dz\end{aligned} \tag{2.127}$$

and also the correction factor

$$\zeta_\delta = \frac{\int_0^l\phi(z)\delta\phi(z)dz}{\int_0^l\delta\phi(z)dz}\ , \tag{2.128}$$

which is the average value of $\phi(z)$ when weighted by the small signal response profile $\delta\phi(z)$. Equation (2.126) is nonlinear because the factor that scales $\delta P_{\rm opt}$ to $\delta n_{\rm qp}$ depends on ζ_δ, which depends on $\delta\phi(z)$, which depends on $\delta P_{\rm opt}$ through the differential Equation (2.125). We would like to find the linear expression that must hold in the limit of very small changes. If we make the reasonable ansatz that the fluctuation in the quasi-particle density at a given position is proportional to the mean quasi-particle density at that position or $\delta\phi(z) \propto \phi(z)$ then $\zeta_\delta = \zeta$ and Equation (2.126) becomes

$$\frac{\eta_{\rm ph}\left(\delta P_{\rm opt,ant} + \delta P_{\rm opt,dir}\right)}{\Delta} = V\left(2\zeta Rn_{\rm qp} + \frac{1}{\tau_{\rm max}}\right)\delta n_{\rm qp}\ . \tag{2.129}$$

We recover linearity so that the small signal responsivity only depends on the steady-state properties as desired. In addition, a single parameter ζ completely characterizes the effects of nonuniform absorption and diffusion. We point out that in order to calculate ζ one must numerically solve the differential Equation (2.116)

for the quasi-particle profile $\phi(z)$. If we simply redefine the effective quasi-particle lifetime as

$$\frac{1}{\tau_{\rm qp}^{\rm eff}} = 2\zeta R n_{\rm qp} + \frac{1}{\tau_{\rm max}} \tag{2.130}$$

then we obtain

$$\delta n_{\rm qp} = \frac{\tau_{\rm qp}^{\rm eff}\eta_{\rm ph}\left(\delta P_{\rm opt,ant} + \delta P_{\rm opt,dir}\right)}{V\Delta} \ , \tag{2.131}$$

which is the counterpart to Equation (2.25) that accounts for direct absorption, nonuniform absorption, and diffusion.

2.2.11 Response to Unresolved Astronomical Source

We are now ready to derive an expression for the response to an unresolved astronomical source. We assume that the flux density of the source is small enough that the detectors behave linearly. The response is then given by

$$r_{\rm src} = \frac{\partial \hat{V}}{\partial S} = \left(\frac{\partial \hat{V}}{\partial S_{21}^{\rm res}}\right)\left(\frac{\partial S_{21}^{\rm res}}{\partial n_{\rm qp}}\right)\left(\frac{\partial n_{\rm qp}}{\partial P_{\rm opt,ant}}\right)\left(\frac{\partial P_{\rm opt,ant}}{\partial T_{\rm load,ant}}\right)\left(\frac{\partial T_{\rm src}}{\partial S}\right) \ . \tag{2.132}$$

The chain of partial derivatives describes the propagation of signal through the instrument. The quantity $r_{\rm src}$ will have units of volts per Jansky. We specify $P_{\rm opt,ant}$ here because we are interested in the narrow-band power at frequency $\nu_{\rm mm}$ that is coupled through the antenna, not the wide band power due to direct absorption by the aluminum section. The partial derivatives on the right hand side are evaluated using Equations (2.61), (2.103), (2.131), (2.105), and (2.9) from left to right. We express the first partial derivative as

$$\begin{aligned}\frac{\partial \hat{V}}{\partial S_{21}^{\rm res}} &= S_{21}^{\rm RF} S_{21}^{\rm BB} A_0 e^{j\phi_0} \\ &= (S_{21}^{\rm res})^{-1} A e^{j\phi} \\ &= |S_{21}^{\rm res}|^{-1} A e^{j(\phi-\theta_{\rm res})} \ ,\end{aligned} \tag{2.133}$$

where A and ϕ are the mean carrier amplitude and phase at the output of the system. The end result is

$$r_{\rm src} = \frac{A Q_i \chi_c \chi_y \alpha \left|\tilde{\kappa}\right| \eta_{\rm ph}\eta_{\rm opt,ant}\left(1-f_{\rm spill,ant}\right) e^{-\tau_{\rm ant}/\sin\mathfrak{e}} A_{\rm eff}\ \Delta\nu_{\rm mm,ant}}{8\left|S_{21}^{\rm res}\right| V\Delta\left(2\zeta R n_{\rm qp} + \tau_{\rm max}^{-1}\right)}\ e^{j\left(\tilde{\Psi}+\phi_y+\phi_c+\phi-\theta_{\rm res}\right)} \ . \tag{2.134}$$

We see that the response occurs in a well defined direction in the complex plane that is rotated by an angle $\theta_{\rm qp} = \tilde{\Psi} + \phi_y + \phi_c + \phi - \theta_{\rm res}$ from the I-Q basis in which the data is collected. We call this the quasi-particle direction and will discuss it further in Section 2.4. The response has several dependencies that are not explicitly stated in Equation (2.134). In particular, $\tilde{\kappa} \equiv \tilde{\kappa}(T,\omega,\Delta_0,a,y)$ and $\tilde{\Psi} \equiv \tilde{\Psi}(T,\omega,\Delta_0,a,y)$. In addition, the quantities Q_i, χ_c, and $\tau_{\rm qp}^{\rm eff} = \left(2\zeta R n_{\rm qp} + \tau_{\rm max}^{-1}\right)^{-1}$ will depend on the background loading conditions under

which the source is observed.

The response is easily measured by scanning the telescope across a bright unresolved source of known flux density and examining the peak height in the quadrature sum of the I and Q timestreams. If the response due to direct absorption is small compared to the antenna response, then the ratio of the peak height to the flux density is a good measure of r_{src}. The response can also be predicted by calibrating the full instrument model that was put forward in this section and then calculating r_{src} directly using Equation (2.134). One of the main goals of this thesis is to compare the measured response to the predicted response based on our calibrated model for each MUSIC detector. If the two are equal for all detectors and observing conditions, then it suggests we have a good understanding of the propagation of signal through the instrument.

Equation (2.134) provides insight into how to design a responsive instrument using MKIDs. However, it is not the responsivity that characterizes instrument performance, but rather the sensitivity. In order to predict sensitivity we must develop a model for the sources of noise inherent to MKIDs and their readout electronics. We set upon this task in the next section, and discuss instrument optimization in the chapter summary.

Table 2.1: Expected sources of noise in the on-resonance and off-resonance carriers. Correlated sources of noise can (partially) be removed. The second column gives the direction in the complex plane that the noise occurs, with Freq denoting the frequency direction (tangent to the IQ sweep) and QP denoting the quasi-particle direction (explained in text). The third column specifies how the power spectral density is expected to scale with temporal frequency.

Noise	Direction	PSD	On-Res	Off-Res	Correlated
Additive Electronics	Isotropic	white	✓	✓	
Multiplicative Electronics	Amplitude / Phase	$1/f$ and drift	✓	✓	✓
TLS	Freq	$\nu^{-1/2}$	✓		
Atmospheric	QP	$\nu^{-8/3}$	✓		✓
Photon	QP	white	✓		
Generation - Recombination	QP	white	✓		

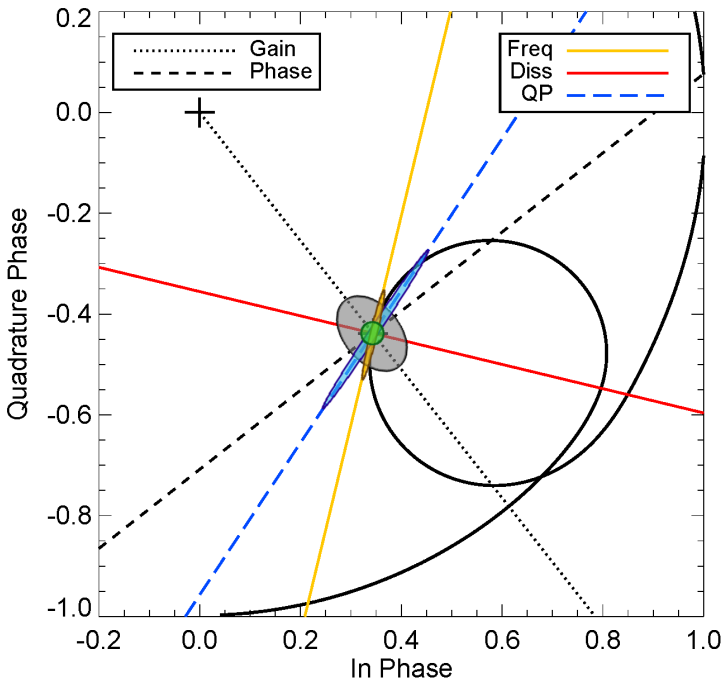

Figure 2.12: Illustration of the various noise sources in the complex plane. The solid black line denotes the complex transmission near resonance as a function of frequency. The ellipses are centered on the resonant frequency and provide a rough approximation of the relative covariance of the various noise sources. The green ellipse is amplifier noise. The gray ellipse is multiplicative electronics noise. The yellow ellipse is TLS noise. The light blue ellipse is atmospheric noise. Note that photon, generation, and recombination noise, as well as astronomical signal, will also lie in the QP direction.

2.3 Noise

The MUSIC detectors are susceptible to several sources of noise, listed in Table 2.1 and illustrated in Figure 2.12. The purpose of this section is to derive an expression for the power spectral density of each noise source and to determine how each noise source translates into fluctuations in the complex carrier amplitude $\hat{V}(f,t)$. We divide the noise into two categories, that which is sourced by the readout electronics and that which is inherent to the detector element.

2.3.1 Electronics Noise

Approximately 40% of the carrier tones read out during observations are not probing resonances but instead are interspersed throughout the bandpass in the regions between resonances. These off-resonance carriers are far enough from the resonant frequencies that they are not modulated by detector noise fluctuations. They enable the noise sourced by the readout electronics to be isolated and studied separate from the detector noise. The placement of on-resonance and off-resonance carriers is illustrated in Figure 2.13.

2.3.1.1 Additive

Figure 2.5 shows a schematic of the MUSIC readout electronics. Each device pictured will introduce some additive noise $\delta V(t)$ into the system whose variance can be characterized by a power spectral density $S_{\delta V}$ in units of volts squared per hertz. We describe the white component of $S_{\delta V}$ with an effective input noise temperature T_n defined as the physical temperature a perfect resistor at the input to the device would need in order to produce that level of Johnson-Nyquist noise

$$T_n = \frac{S_{\delta V}}{k_B Z_0} \,, \tag{2.135}$$

where $Z_0 = 50\ \Omega$ is the characteristic impedance of the system. The electronics were designed so that the white noise floor of the full system would be set principally by the $T_{\text{HEMT}} \approx 4$ K noise temperature of the cryogenic HEMT amplifier that immediately follows the detector array, with the ADC being the second largest contributor. In order to achieve this we used cold attenuators to substantially reduce the noise from the room temperature electronics on the input side of the cryostat, and we designed the receiver chain on the output side so that it would not add significant noise when referred back to the input of the HEMT while

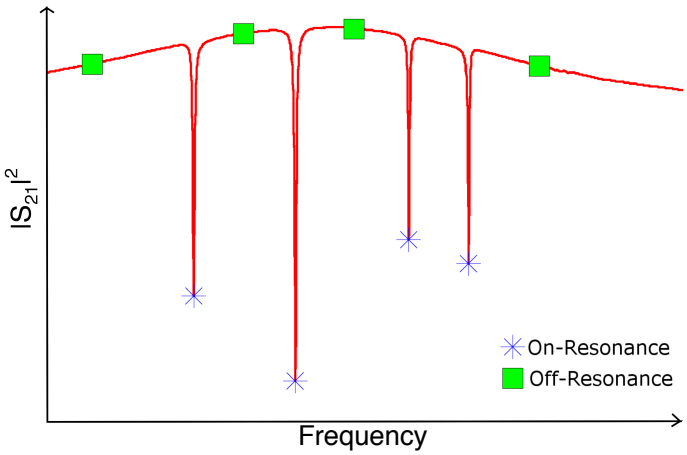

Figure 2.13: Squared magnitude of the forward transmission through the system as a function of microwave frequency. Shown are four resonators on one of the final MUSIC production arrays. Blue asterisks (green squares) denote the typical placement of on-resonance (off-resonance) carriers.

simultaneously avoiding amplifier compression.

We first consider the input side of the readout electronics, which we define as everything between the DAC and the HEMT. The noise temperature of a passive two-port device with attenuation α (measured in decibels) is given by

$$T_n = (A-1)\,T\ , \tag{2.136}$$

where T is its physical temperature and $A = 1/G = 10^{\alpha/10}$. Let T_{in} denote the noise temperature at the input to the device. The noise temperature at the output of the device T_{out} is then given by

$$\begin{aligned} T_{\text{out}} &= G\,(T_{\text{in}} + T_{\text{n}}) \\ &= \frac{T_{\text{in}}}{A} + \left(1 - \frac{1}{A}\right) T\ . \end{aligned} \tag{2.137}$$

In the limit that the device is lossless, $A = 1$ and $T_{\text{out}} = T_{\text{in}}$. In this case noise passes through the device unattenuated. In the limit that A is very large then $T_{\text{out}} \approx T$. In this case the input noise is absorbed by the device and the entirety of the output noise is generated internal to the device according to its physical temperature.

The room temperature electronics on the input side are primarily passive and will inject room temperature noise into the cryostat. We place fixed attenuators (with large α) at the 4 K and IC stages so that the majority of the $T_{\text{room}} = 290$ K noise is dissipated at these stages and replaced with $T_{\text{4K}} = 4$ K and $T_{\text{IC}} = 400$ mK noise. Cascading Equation (2.137) for the room temperature, 4 K, and IC attenuators one obtains the following expression for the noise temperature of the input side of the readout electronics

$$T_{\text{sys,in}} = \frac{T_{\text{room}}}{A_{\text{4K}} A_{\text{IC}}} + \left(1 - \frac{1}{A_{\text{4K}}}\right) \frac{T_{\text{4K}}}{A_{\text{IC}}} + \left(1 - \frac{1}{A_{\text{IC}}}\right) T_{\text{IC}}\ . \tag{2.138}$$

When we first commissioned MUSIC in 2012 we used $\alpha_{\text{4K}} = 1$ dB and $\alpha_{\text{IC}} = 31$ dB for the cold attenuators, which corresponds to $T_{\text{sys,in}} = 0.58$ K. This results in a 15% increase in the noise floor set by the HEMT. In January 2014 we switched to $\alpha_{\text{4K}} = 21$ dB and $\alpha_{\text{IC}} = 6$ dB, which corresponds to $T_{\text{sys,in}} = 1.87$ K or a 50% increase in the noise floor set by the HEMT. We made this switch because with the old setup the majority of the resonators were well below their bifurcation point under the maximum carrier power that the system could provide. The new setup allowed us to increase the carrier power used to probe the resonators by up to 5 dB. This was in an attempt to reduce TLS noise, which is the dominant source of noise in our detectors and has a power spectral density that scales as $P^{-1/2}$. We will give an introduction to TLS noise in Section 2.3.2.2. The point here is that the white noise from the input side of the readouts electronics is determined by the cold attenuators and is fairly modest compared to the white noise from the HEMT.

We now consider the output side of the readout electronics, which we define as everything between the HEMT and the ADC. Let G_i and $T_{n,i}$ denote the gain and noise temperature of the i-th electronic component following the HEMT. These are listed in the first two rows of Table 2.2. We can cascade the $T_{n,i}$ using Friis

Table 2.2: Characterization of the additive white noise for several readout boards during the 2013/09 and 2014/09 observing runs. The columns list the components from left to right in the order in which they appear in the receiver chain, starting with the cryogenic HEMT amplifier. The first two rows denote the gain and effective input noise temperature. The noise temperature of all passive devices are calculated using Equation (2.136) assuming a physical temperature $T = 290$ K. The third column denotes median carrier power at the input to that stage. The fourth column is the accumulated gain, or the cumulative sum of the first column. The fifth column is the accumulated noise temperature, referred to the input of the HEMT. The sixth (seventh) column is the corresponding noise floor at the output of that stage in units of dBm/Hz (dBc/Hz).

2013/09 - Device A2L - HEMT 289D														
	HEMT	**Coax**	**Preamp**	**Att-1**	**IF-Amp-1**	**SW-1**	**Att-2**	**IF-Amp-2**	**Att-Var**	**Demod-Mixer**	**BB-Amp-1**	**SW-2**	**LP-Filt**	**ADC**
G [dB]	39	-7	17	-9	14	-2	-6	14	-14	-6	17	0	-3	0
T_n [K]	4	1103	120	2014	527	120	865	527	6994	739	527	35	289	429683
$P_{carrier}$ [dBm]	-81	-42	-49	-32	-41	-27	-28	-34	-20	-34	-39	-23	-23	-26
Acc G [dB]	39	32	49	40	54	53	47	61	47	42	58	58	55	55
Acc T_n at HEMT Input [K]	4.6	4.7	4.8	4.8	4.9	4.9	4.9	4.9	4.9	4.9	4.9	4.9	4.9	6.3
Acc Noise Floor [dBm/Hz]	-153	-160	-143	-152	-137	-139	-145	-130	-144	-150	-133	-134	-137	-136
Acc Noise Floor [dBc/Hz]	-111	-111	-111	-111	-111	-111	-111	-111	-111	-111	-111	-111	-111	-109
2013/09 - Device A2U - HEMT 289D														
	HEMT	**Coax**	**Preamp**	**Att-1**	**IF-Amp-1**	**SW-1**	**Att-2**	**IF-Amp-2**	**Att-Var**	**Demod-Mixer**	**BB-Amp-1**	**SW-2**	**LP-Filt**	**ADC**
G [dB]	39	-9	17	-9	14	-2	-6	14	-9	-6	17	0	-3	0
T_n [K]	4	2269	120	2014	527	120	865	527	2014	739	527	35	289	429683
$P_{carrier}$ [dBm]	-83	-44	-53	-36	-45	-31	-33	-39	-24	-33	-39	-22	-23	-26
Acc G [dB]	39	30	47	38	52	50	44	59	50	44	61	60	57	57
Acc T_n at HEMT Input [K]	4.6	4.9	5.0	5.0	5.1	5.1	5.1	5.2	5.2	5.2	5.2	5.2	5.2	6.0
Acc Noise Floor [dBm/Hz]	-153	-162	-145	-154	-140	-141	-147	-133	-142	-147	-131	-131	-134	-133
Acc Noise Floor [dBc/Hz]	-109	-109	-109	-109	-108	-108	-108	-108	-108	-108	-108	-108	-108	-108
2013/09 - Device B2L - HEMT 258D														
	HEMT	**Coax**	**Preamp**	**Att-1**	**IF-Amp-1**	**SW-1**	**Att-2**	**IF-Amp-2**	**Att-Var**	**Demod-Mixer**	**BB-Amp-1**	**SW-2**	**LP-Filt**	**ADC**
G [dB]	37	-10	17	-9	14	-2	-6	14	-15	-6	17	0	-3	0
T_n [K]	4	2518	120	2014	527	120	865	527	8881	739	527	35	289	429683
$P_{carrier}$ [dBm]	-76	-39	-49	-32	-41	-27	-28	-34	-20	-35	-41	-24	-24	-27
Acc G [dB]	37	27	44	35	49	48	42	56	41	36	52	52	49	49
Acc T_n at HEMT Input [K]	4.6	5.1	5.3	5.4	5.6	5.6	5.6	5.6	5.6	5.7	5.8	5.8	5.8	11.3
Acc Noise Floor [dBm/Hz]	-155	-164	-147	-156	-142	-143	-149	-135	-150	-155	-139	-139	-142	-139
Acc Noise Floor [dBc/Hz]	-116	-115	-115	-115	-115	-115	-115	-115	-115	-115	-115	-115	-115	-112
2013/09 - Device B2U - HEMT 258D														
	HEMT	**Coax**	**Preamp**	**Att-1**	**IF-Amp-1**	**SW-1**	**Att-2**	**IF-Amp-2**	**Att-Var**	**Demod-Mixer**	**BB-Amp-1**	**SW-2**	**LP-Filt**	**ADC**
G [dB]	37	-14	17	-9	14	-2	-6	14	-7	-6	17	0	-3	0
T_n [K]	4	6390	120	2014	527	120	865	527	1163	739	527	35	289	429683
$P_{carrier}$ [dBm]	-80	-43	-56	-39	-48	-34	-36	-42	-27	-34	-40	-23	-24	-27
Acc G [dB]	37	23	40	31	46	44	38	52	45	40	57	56	53	53
Acc T_n at HEMT Input [K]	4.6	5.9	6.4	6.6	7.0	7.0	7.0	7.1	7.1	7.1	7.2	7.2	7.2	9.2
Acc Noise Floor [dBm/Hz]	-155	-168	-150	-159	-144	-146	-152	-138	-145	-150	-133	-134	-137	-136
Acc Noise Floor [dBc/Hz]	-112	-111	-111	-111	-110	-110	-110	-110	-110	-110	-110	-110	-110	-109
2014/07 - Device B2L - HEMT 321D														
	HEMT	**Coax**	**Preamp**	**Att-1**	**IF-Amp-1**	**SW-1**	**Att-2**	**IF-Amp-2**	**Att-Var**	**Demod-Mixer**	**BB-Amp-1**	**SW-2**	**LP-Filt**	**ADC**
G [dB]	37	-13	17	-9	14	-2	-6	14	-10	-6	17	0	-3	0
T_n [K]	4	6055	120	2014	527	120	865	527	2610	739	527	35	289	429683
$P_{carrier}$ [dBm]	-77	-40	-53	-36	-45	-31	-33	-39	-24	-34	-40	-23	-24	-27
Acc G [dB]	37	24	41	32	46	44	38	53	43	37	54	53	50	50
Acc T_n at HEMT Input [K]	5.9	7.1	7.6	7.8	8.1	8.1	8.2	8.3	8.3	8.3	8.4	8.4	8.4	12.3
Acc Noise Floor [dBm/Hz]	-154	-167	-149	-158	-144	-145	-151	-137	-147	-152	-135	-136	-139	-137
Acc Noise Floor [dBc/Hz]	-114	-113	-113	-113	-112	-112	-112	-112	-112	-112	-112	-112	-112	-111
2014/07 - Device B2U - HEMT 321D														
	HEMT	**Coax**	**Preamp**	**Att-1**	**IF-Amp-1**	**SW-1**	**Att-2**	**IF-Amp-2**	**Att-Var**	**Demod-Mixer**	**BB-Amp-1**	**SW-2**	**LP-Filt**	**ADC**
G [dB]	37	-18	17	-9	14	-2	-6	14	-4	-6	17	0	-3	0
T_n [K]	4	17188	120	2014	527	120	865	527	438	739	527	35	289	429683
$P_{carrier}$ [dBm]	-78	-41	-59	-42	-51	-37	-38	-44	-30	-34	-40	-23	-23	-26
Acc G [dB]	37	19	36	27	41	40	34	48	44	39	56	55	52	52
Acc T_n at HEMT Input [K]	5.9	9.3	10.7	11.2	12.2	12.2	12.3	12.5	12.5	12.6	12.6	12.6	12.6	15.4
Acc Noise Floor [dBm/Hz]	-154	-170	-152	-161	-146	-148	-154	-139	-143	-149	-132	-133	-136	-135
Acc Noise Floor [dBc/Hz]	-112	-110	-110	-110	-109	-109	-109	-109	-109	-109	-109	-109	-109	-108

formula to obtain the effective noise temperature of the system referred to the input of the HEMT

$$\begin{aligned} T_{\text{sys}} &= \frac{T_{\text{sys}}^{\text{ADC}}}{G_{\text{post-HEMT}}} \\ &= T_{\text{sys,in}} + T_{\text{HEMT}} + \frac{T_{n,1}}{G_{\text{HEMT}}} + \frac{T_{n,2}}{G_{\text{HEMT}}G_1} + \frac{T_{n,3}}{G_{\text{HEMT}}G_1G_2} + \cdots \\ &= T_{\text{sys,in}} + T_{\text{HEMT}} + T_{\text{sys,out}} \ , \end{aligned} \tag{2.139}$$

where $T_{\text{sys}}^{\text{ADC}}$ is the noise temperature of the system measured at the ADC and $G_{\text{post-HEMT}} = G_{\text{HEMT}}G_1G_2\cdots G_N$ is the total gain of the HEMT and all components that follow it.

The increase in T_{sys} due to each component can be inferred from the fifth row of Table 2.2. It is clear examining the values for 2013/09 that on the output side the majority of the components do not contribute significantly to the system noise temperature. This is due to the large gain of the HEMT, as each term in $T_{\text{sys,out}}$ is divided by $G_{\text{HEMT}} \approx 10,000$. The exceptions is the digitization noise from the ADC (the column labeled *ADC*), which causes a non-negligible increases in system noise temperature as expected. The coaxial cables that follow the HEMT (the column labeled *Coax*) can also have significant adverse effects by reducing the gain post-HEMT, thereby increasing the noise of all components where referred to the input of the HEMT. It should be noted that *Coax* refers to the niobium, copper, and stainless steel coaxes inside the cryostat, the SMA cables that connect the output of the cryostat to the input of the readout boards, and the power-splitter that sends the power coming from a single channel into two separate readouts boards for the upper and lower half-bands. The power-splitter itself has an insertion loss of 4-5 dB. The coaxial cables will have an effective physical temperature somewhere in between the temperature of the IC stage and room temperature, but in the tables above we have assumed that they sit at T_{room} in order to obtain an upper limit on their noise temperature.

The carrier power at which the resonators undergo bifurcation is much higher than we anticipated when the electronics were designed. As a result, we would like to drive the resonators with the maximum carrier power that the readout electronics can provide. Unfortunately doing so causes the first IF amplifier following the HEMT (the column labeled *Preamp*) to enter compression. This is especially true for the 2014/07 setup because we decreased the cold attenuation on the input side of the cryostat. This forces us attenuate the power on the output side of the cryostat before it reaches the first IF amplifier, and this is why the attenuation listed in the *Coax* column increases between 2013/09 and 2014/07. Examining Table 2.2 it is clear that the increase in post-HEMT attenuation causes a fairly large increase in the accumulated noise temperature. However, this increase in white noise from the electronics should be offset by the decrease in TLS noise due to the higher read out powers. We find that the value of $T_{\text{sys,out}}$ varies between 6 K and 15.4 K depending on the half-band and attenuator set-up. This corresponds to a 2-6 dB increase in the $T_{\text{HEMT}} = 4$ K noise floor from the HEMT alone.

2.3.1.2 Multiplicative

The various electronic components also suffer from multiplicative amplitude and phase noise. Examples include fluctuations in reference voltages, fluctuations in amplifier gains, jitter in sampling clocks, and drift in cable delays. These noise sources are modeled with the following expression for the complex amplitude of an off-resonance carrier tone at microwave frequency $f = f_{\mathrm{BB}} + f_{\mathrm{LO}}$:

$$\begin{aligned}\hat{V}(t) &= g_{\mathrm{RF}}(f)\, g_{\mathrm{BB}}(f_{\mathrm{BB}})\, A_0 e^{j(\phi_0 - 2\pi f \tau_{\mathrm{RF}} - 2\pi f_{\mathrm{BB}} \tau_{\mathrm{BB}})} \left(1 + \delta A + j\delta\phi\right) + \delta \boldsymbol{w} \\ &= A(f, f_{\mathrm{BB}}) e^{j\phi(f, f_{\mathrm{BB}})} \left(1 + \delta A + j\delta\phi\right) + \delta \boldsymbol{w} \; . \end{aligned} \tag{2.140}$$

In this equation, $A = g_{\mathrm{RF}} g_{\mathrm{BB}} A_0$ and $\phi = \phi_0 - 2\pi f \tau_{\mathrm{RF}} - 2\pi f_{\mathrm{BB}} \tau_{\mathrm{BB}}$ are the DC carrier amplitude and phase measured at the output of the system. The amplitude at the output A is related to the amplitude at the input A_0 by some overall voltage gain $g_{\mathrm{RF}} g_{\mathrm{BB}} = \sqrt{G_{\mathrm{RF}} G_{\mathrm{BB}}}$. Similarly the phase ϕ at the output is related to the phase at the input ϕ_0 by some overall baseband cable delay τ_{BB} and RF cable delay τ_{RF}. The $\delta \boldsymbol{w} = \delta w_{\mathrm{I}} + j\delta w_{\mathrm{Q}}$ term is the additive white noise from the entire system, which was discussed in the previous section. Finally δA and $\delta\phi$ denote the amplitude and phase fluctuations, respectively. The quantity δA is a linear combination of the amplitude fluctuations from the individual electronic components. Likewise the quantity $\delta\phi$ is a linear combination of the phase fluctuations from the individual electronic components. The primary assumption underlying Equation (2.140) is that the amplitude and phase fluctuations are multiplicative. In other words the fluctuations in the complex carrier amplitude $\delta\hat{V}$ due to these noise sources scale with the mean carrier amplitude A.

We suspect that the amplitude and phase fluctuations are coherent with microwave frequency, so that carriers placed at different microwave frequencies (but measured with the same readout board) measure the same δA and $\delta\phi$. This enables us to write the following model for the in-phase and quadrature-phase data for off-resonance carrier i at time sample j:

$$\begin{aligned}\mathrm{I}_{ij} &= A_i \left[(1 + \delta A_j)\cos\phi_i - \delta\phi_j \sin\phi_i\right] + \delta w_{\mathrm{I}} \\ \mathrm{Q}_{ij} &= A_i \left[(1 + \delta A_j)\sin\phi_i + \delta\phi_j \cos\phi_i\right] + \delta w_{\mathrm{Q}} \; . \end{aligned} \tag{2.141}$$

The fluctuations δA and $\delta\phi$ can then be treated as a common signal that is measured by all carriers on a given readout board. The off-resonance data can be used to determine the weighted least-squares estimate of δA and $\delta\phi$ in the presence of the additive white noise. This enables us to subtract the amplitude and phase noise from the on-resonance data.

From Equation (2.141) the one-sided power spectral density of the I and Q components of an off-

resonance carrier are given by

$$\begin{aligned} S_{\delta \mathrm{I}}(\nu) &= A_i^2 \left[\cos^2(\phi_i) S_{\delta A}(\nu) + \sin^2(\phi_i) S_{\delta\phi}(\nu) - \sin(2\phi_i) S_{\delta A,\delta\phi}(\nu)\right] + S_{\delta w} \\ S_{\delta \mathrm{Q}}(\nu) &= A_i^2 \left[\sin^2(\phi_i) S_{\delta A}(\nu) + \cos^2(\phi_i) S_{\delta\phi}(\nu) + \sin(2\phi_i) S_{\delta A,\delta\phi}(\nu)\right] + S_{\delta w} \,, \end{aligned} \tag{2.142}$$

where $S_{\delta A}$ and $S_{\delta\phi}$ are the one-sided power spectral densities of the amplitude and phase fluctuations, and $S_{\delta A,\delta\phi}$ is their cross power spectral density. The inclusion of a cross term accounts for the fact that the amplitude and phase fluctuations may be correlated. This can occur if the amplitude and phase fluctuations are generated by the same underlying physical mechanism [115]. The power spectral densities $S_{\delta A}$ and $S_{\delta\phi}$ have a spectral shape that is combination of ν^{-1} (1/f) and ν^{-2} (drift). The white noise is assumed to be isotropic so that $S_{\delta w_{\mathrm{I}}} = S_{\delta w_{\mathrm{Q}}} \equiv S_{\delta w}$. The value of $S_{\delta w}$ is given by the last column of the *Acc Noise Floor* row in Table 2.2.

2.3.2 Detector Noise

In addition to the electronics noise, on-resonance carriers are sensitive to statistical fluctuations in the rate at which quasi-particles are generated and recombine, fluctuations in the resonator frequency due to a surface layer of two-level systems on the device, and fluctuations in the atmospheric emission about Mauna Kea. These additional sources of noise all appear as fluctuations in the complex forward transmission through resonance

$$\begin{aligned} \hat{V} + \delta\hat{V} &= (S_{21}^{\mathrm{res}} + \delta S_{21}^{\mathrm{res}})\, S_{21}^{\mathrm{RF}} S_{21}^{\mathrm{BB}} A_0 e^{i\phi_0} \\ &= S_{21}^{\mathrm{res}} S_{21}^{\mathrm{RF}} S_{21}^{\mathrm{BB}} A_0 e^{j\phi_0} \left(1 + |S_{21}^{\mathrm{res}}|^{-1} e^{-j\theta_{\mathrm{res}}} \delta S_{21}^{\mathrm{res}}\right) \\ &= A e^{j\phi} \left(1 + |S_{21}^{\mathrm{res}}|^{-1} e^{-j\theta_{\mathrm{res}}} \delta S_{21}^{\mathrm{res}}\right) \,, \end{aligned} \tag{2.143}$$

and therefore result in a modulation of the complex amplitude of the carrier tone

$$\delta\hat{V} = A e^{j(\phi - \theta_{\mathrm{res}})} \frac{\delta S_{21}^{\mathrm{res}}}{\left|S_{21}^{\mathrm{res}}\right|} \,. \tag{2.144}$$

The rest of this section will be devoted to obtaining expressions for the power spectral density of the $\delta S_{21}^{\mathrm{res}}$ fluctuations due to each of these noise sources.

2.3.2.1 Fundamental

The fundamental sources of noise in MKIDs are photon, generation, and recombination noise. These are due to statistical fluctuations in the rate at which quasi-particles are generated optically, the rate at which they are generated thermally, and the total rate at which they recombine. In order to model these noise sources we

must use the time dependent version of the generation-recombination equation

$$\frac{\partial n_{\rm qp}(t)}{\partial t} = \Gamma_{\rm G,th}(t) + \Gamma_{\rm G,opt}(t) - \Gamma_{\rm R}(n_{\rm qp}(t),t) \ . \tag{2.145}$$

We assume that there is a small fluctuation in the quasi-particle density about its steady state value $n_{\rm qp}(t) = n_{\rm qp} + \delta n_{\rm qp}(t)$ due to fluctuations in the three rates about their steady state values

$$\begin{aligned} \Gamma_{\rm G,th}(t) &= \Gamma_{\rm G,th} + \gamma_{\rm G,th}(t) \\ \Gamma_{\rm G,opt}(t) &= \Gamma_{\rm G,opt} + \gamma_{\rm G,opt}(t) \\ \Gamma_{\rm R}(n_{\rm qp}(t),t) &= \Gamma_{\rm R} + \frac{\partial \Gamma_{\rm R}}{\partial n_{\rm qp}} \delta n_{\rm qp}(t) + \gamma_{\rm R}(t) \ , \end{aligned} \tag{2.146}$$

where $\gamma_{\rm X} \ll \Gamma_{\rm X}$. The derivative in the recombination rate can be evaluated using Equation (2.17)

$$\frac{\partial \Gamma_{\rm R}}{\partial n_{\rm qp}} = 2Rn_{\rm qp} + \frac{1}{\tau_{\rm max}} = \frac{1}{\tau_{\rm qp}^{\rm eff}} \ . \tag{2.147}$$

Inserting the above expressions into Equation (2.145) and applying the steady-state solution $\Gamma_{\rm G,opt} + \Gamma_{\rm G,th} - \Gamma_{\rm R} = 0$ yields

$$\frac{\partial \delta n_{\rm qp}(t)}{\partial t} + \frac{\delta n_{\rm qp}(t)}{\tau_{\rm qp}^{\rm eff}} = \gamma_{\rm G,th}(t) + \gamma_{\rm G,opt}(t) - \gamma_{\rm R}(t) \ . \tag{2.148}$$

Taking the Fourier transform of both sides and solving for $\delta \tilde{n}_{\rm qp}(\nu)$ then gives

$$\delta \tilde{n}_{\rm qp}(\nu) = \frac{\tau_{\rm qp}^{\rm eff}}{1 + j2\pi\tau_{\rm qp}^{\rm eff}\nu} \left[\tilde{\gamma}_{\rm G,th}(\nu) + \tilde{\gamma}_{\rm G,opt}(\nu) - \tilde{\gamma}_{\rm R}(\nu)\right] \ . \tag{2.149}$$

We see that the noise spectrum will be low-pass filtered by the effective quasi-particle lifetime with bandwidth $\Delta\nu_{\rm qp} = (2\pi\tau_{\rm qp}^{\rm eff})^{-1}$. Since the lifetime $\tau_{\rm qp}^{\rm eff} \lesssim 10$ μs for on-sky loading conditions, $\Delta\nu_{\rm qp} \gtrsim 15$ kHz and the low-pass filter will have no effect at the temporal frequencies probed with our readout electronics. We can obtain an expression for the power spectral density of the fundamental noise by taking the square magnitude of both sides of Equation (2.149) and using the fact that the three processes are independent. This yields

$$S_{\delta n_{\rm qp}}^{\rm fund}(\nu) = \frac{\tau_{\rm qp}^{\rm eff\,2}}{1 + \left(2\pi\tau_{\rm qp}^{\rm eff}\nu\right)^2} \left[S_{\gamma_{\rm G,th}}(\nu) + S_{\gamma_{\rm G,opt}}(\nu) + S_{\gamma_{\rm R}}(\nu)\right] \ . \tag{2.150}$$

We now set out to derive the one-sided power spectral density for the three processes, starting with optical generation.

2.3.2.1.1 Photon Fluctuations in the rate at which quasi-particles are generated optically are sourced by fluctuations in the incident photon rate. It can be shown [116] that for a narrow-band, single-moded detector

sensitive to a single polarization this photon noise will have a white power spectral density given by the following equation,

$$S_{\delta P_{\rm opt}}(\nu) = \frac{2}{\eta_{\rm qe}} (h\nu_{\rm mm})^2 \left(n_{\rm opt} + \eta_{\rm qe} n_{\rm opt}^2\right) \Delta\nu_{\rm mm} \ , \tag{2.151}$$

where $\nu_{\rm mm}$ is the center frequency of the observation, $\Delta\nu_{\rm mm}$ is the bandwidth of the detector, $\eta_{\rm qe}$ is the quantum efficiency of the detector, and $n_{\rm opt}$ is the mean occupation number or the number of photons in the $h\nu_{\rm mm}$ mode. Assuming the background loading is due to thermal radiation with a black-body spectrum at temperature $T_{\rm opt}$, the occupation number is given by the Bose-Einstein distribution

$$n_{\rm opt}(\nu_{\rm mm}, T_{\rm opt}) = \frac{1}{\exp\left(h\nu_{\rm mm}/k_B T_{\rm opt}\right) - 1} \ . \tag{2.152}$$

The first term in Equation (2.151) scales as $n_{\rm opt}$ and corresponds to the Poisson fluctuations in the photon arrival time. It is commonly referred to as *shot noise*. The second term scales as $n_{\rm opt}^2$ and arises because photons bunch together, resulting in arrival times that are not entirely independent. It is commonly referred to as *Bose noise*. In the limit that $h\nu_{\rm mm} \gg k_B T_{\rm opt}$, then $n \ll 1$ and shot noise will dominate. This is usually the case for wavelengths shorter than the near-infrared, where light is often conceptualized as a particle. In the opposite limit that $h\nu_{\rm mm} \ll k_B T_{\rm opt}$, then $n \gg 1$ and Bose noise will dominate. This is usually the case for radio wavelengths, where light is often conceptualized as a wave. Indeed, Equation (2.151) is a manifestation of wave-particle duality. For the submillimeter and millimeter wavelengths $n \sim 1$ and the contributions from shot and boise noise are similar; both must be taken into account.

We can write Equation (2.151) in terms of the steady state optical power

$$P_{\rm opt} = n_{\rm opt} h\nu_{\rm mm} \Delta\nu_{\rm mm} \ . \tag{2.153}$$

Doing so yields

$$S_{\delta P_{\rm opt}}(\nu) = 2\left[\frac{P_{\rm opt} h\nu_{\rm mm}}{\eta_{\rm qe}} + \frac{P_{\rm opt}^2}{\Delta\nu_{\rm mm}}\right] \ . \tag{2.154}$$

The above expression gives the spectrum of fluctuations in optical power. We can convert this to fluctuations in the quasi-particle generation rate using the equation

$$\gamma_{\rm G,opt} = \frac{\eta_{\rm ph}}{V\Delta} \delta P_{\rm opt} \ . \tag{2.155}$$

This results in the desired expression

$$S_{\gamma_{\rm G,opt}} = 2\left(\frac{\eta_{\rm ph}}{V\Delta}\right)^2 \left[\frac{P_{\rm opt} h\nu_{\rm mm}}{\eta_{\rm qe}} + \frac{P_{\rm opt}^2}{\Delta\nu_{\rm mm}}\right] \ . \tag{2.156}$$

2.3.2.1.2 Recombination The quantity $\Gamma_{\rm R}(t)$ denotes the number of quasi-particles that recombine per unit volume per unit time. This is related to the number of recombination events $N_{\rm R}(t)$ by the formula

$$\Gamma_{\rm R}(t) = \frac{2}{V}\frac{dN_{\rm R}(t)}{dt} \ , \tag{2.157}$$

where the factor of 2 accounts for the fact that each recombination event annihilates two quasi-particles. We model the recombination events $N_{\rm R}(t)$ as a homogeneous Poisson process, where the probability of observing k recombination events in some time interval $(t, t+\tau]$ is given by

$$P[N_{\rm R}(t+\tau) - N_{\rm R}(t) = k] = \frac{(\lambda\tau)^k}{k!}e^{-\lambda\tau} \qquad\qquad k = 0, 1, 2, \ldots \ . \tag{2.158}$$

We would like to determine the power spectral density of this type of process. Referencing $N(t \geq 0)$ with respect to $N(0) = 0$, it is easy to show that the expected number of recombination events is given by

$$< N_{\rm R}(t) >= \lambda t \tag{2.159}$$

with variance

$$\begin{aligned} < N_{\rm R}^2(t) > - < N_{\rm R}(t) >^2 &= \lambda t \\ < N_{\rm R}^2(t) > &= \lambda t + (\lambda t)^2 \ . \end{aligned} \tag{2.160}$$

The autocorrelation function can be calculated by considering positive and negative lags separately. Let t and s denote two points in time separated by lag $\tau = t - s$. For $\tau > 0$ we have that

$$\begin{aligned} R\left(N_{\rm R}(s), N_{\rm R}(t);\ t > s\right) &= < N_{\rm R}(t) N_{\rm R}(s) > \\ &= \left\langle \left[N_{\rm R}(t) - N_{\rm R}(s) + N_{\rm R}(s)\right] N_{\rm R}(s) \right\rangle \\ &= \left\langle \left[N_{\rm R}(t) - N_{\rm R}(s)\right] N_{\rm R}(s) + N_{\rm R}^2(s) \right\rangle \\ &= < N_{\rm R}(t) - N_{\rm R}(s) >< N_{\rm R}(s) > + < N_{\rm R}^2(s) > \\ &= \lambda\left(t - s\right)\lambda s + \lambda s + (\lambda s)^2 \\ &= \lambda^2 ts + \lambda s \ . \end{aligned} \tag{2.161}$$

The derivation above breaks up the expectation value into disjoint intervals and then uses the fact that for a Poisson process the number of events observed in disjoint intervals of time are independent. We can perform an identical calculation for the case where $\tau < 0$ to obtain

$$R\left(N_{\rm R}(s), N_{\rm R}(t);\ t < s\right) = \lambda^2 ts + \lambda t \ . \tag{2.162}$$

Equations (2.160), (2.161), and (2.162) can be combined into a single function

$$R\left(N_{\mathrm{R}}(s),N_{\mathrm{R}}(t)\right)=\lambda^2 ts+\lambda\left[\Theta(t-s)s+\Theta(s-t)t\right]\ , \tag{2.163}$$

which is valid for all t and s. Here $\Theta(x)$ is the Heaviside step function

$$\Theta(x)=\begin{cases}0 & x<0\\ \frac{1}{2} & x=0\\ 1 & x>0\ .\end{cases} \tag{2.164}$$

We are not necessarily interested in the number of recombination events that have occurred but rather the rate of recombination events. The average rate is given by

$$\left\langle\frac{dN_{\mathrm{R}}(t)}{dt}\right\rangle=\frac{d<N_{\mathrm{R}}(t)>}{dt}=\frac{d\left(\lambda t\right)}{dt}=\lambda\ . \tag{2.165}$$

Similarly, the autocorrelation function is given by

$$\begin{aligned}R\left(\frac{dN_{\mathrm{R}}(s)}{ds},\frac{dN_{\mathrm{R}}(t)}{dt}\right)&=\frac{\partial}{\partial t}\left[\frac{\partial R\left(N_{\mathrm{R}}(s),N_{\mathrm{R}}(t)\right)}{\partial s}\right]\\ &=\frac{\partial}{\partial t}\left[\lambda^2 t+\lambda\Theta(t-s)\right]\\ &=\lambda^2+\lambda\delta(t-s)\ ,\end{aligned} \tag{2.166}$$

where $\delta(t-s)$ is the Dirac delta function. We see that the autocorrelation function of the rate at two different times depends only on the lag between those times. This enables us to write

$$R\left(\frac{dN_{\mathrm{R}}(s)}{ds},\frac{dN_{\mathrm{R}}(t)}{dt}\right)=R_{dN_{\mathrm{R}}/dt}(\tau)=\lambda^2+\lambda\delta(\tau)\ . \tag{2.167}$$

The two-sided power spectral density can then be calculated as the Fourier transform of the autocorrelation function

$$\begin{aligned}S_{dN_{\mathrm{R}}/dt}(\nu)&=\int_{-\infty}^{\infty}R_{dN_{\mathrm{R}}/dt}(\tau)e^{-2\pi j\nu\tau}d\tau\\ &=\int_{-\infty}^{\infty}\left[\lambda^2+\lambda\delta(\tau)\right]e^{-2\pi j\nu\tau}d\tau\\ &=\left[\lambda^2\delta(\nu)+\lambda\right]\ .\end{aligned} \tag{2.168}$$

This result holds for any homogenous Poisson process and is actually just a simple description of shot noise, which was mentioned in the previous section in the context of photon noise. In order to convert this into an expression for the shot noise due to recombination, recall from Equation (2.165) that λ is just the average

rate

$$\lambda = \left\langle \frac{dN_{\mathrm{R}}}{dt} \right\rangle = \frac{V}{2} \left\langle \Gamma_{\mathrm{R}}(t) \right\rangle = \frac{V}{2} \Gamma_{\mathrm{R}} \, . \tag{2.169}$$

and therefore

$$\begin{aligned} S_{\Gamma_{\mathrm{R}}}(\nu) &= \left(\frac{\partial \Gamma_{\mathrm{R}}(t)}{\partial \left(dN_{\mathrm{R}}(t)/dt \right)} \right)^2 S_{dN_{\mathrm{R}}/dt} \\ &= \left(\frac{2}{V} \right)^2 \left[\left(\frac{V}{2} \Gamma_{\mathrm{R}} \right)^2 \delta(\nu) + \frac{V}{2} \Gamma_{\mathrm{R}} \right] \qquad (2.170) \\ &= \Gamma_{\mathrm{R}}^2 \delta(\nu) + \frac{2}{V} \Gamma_{\mathrm{R}} \, . \qquad (2.171) \end{aligned}$$

This is the two-sided power spectral density of $\Gamma_{\mathrm{R}}(t)$. The first term is zero for all frequencies except $\nu = 0$; it is just the DC or steady state value. We are interested in the second term which characterizes the $\gamma_{\mathrm{R}}(t)$ fluctuations about the steady state value

$$S_{\gamma_{\mathrm{R}}}(\nu) = \frac{4}{V} \Gamma_{\mathrm{R}} \, . \tag{2.172}$$

Here $\nu \geq 0$ and we have multiplied by 2 to convert to a one-sided power spectral density. We find that fluctuations in the quasi-particle recombination rate have a white spectrum. Inserting Equation (2.17) for the steady state recombination rate Γ_{R} yields

$$S_{\gamma_{\mathrm{R}}}(\nu) = \frac{4}{V} \left(R n_{\mathrm{qp}}^2 + \frac{n_{\mathrm{qp}}}{\tau_{\max}} \right) \, , \tag{2.173}$$

which is the desired expression for recombination noise.

2.3.2.1.3 Generation The noise associated with the optical generation of quasi-particles has been accounted for in the photon noise term. However we still have to derive an expression for the power spectral density of fluctuations in the thermal generation rate. This can be treated in an identical manner as the recombination noise. The rate at which quasi-particles are generated thermally $\Gamma_{\mathrm{G,th}}(t)$ is related to the number of thermal generation events $N_{\mathrm{G,th}}(t)$ by the equation

$$\Gamma_{\mathrm{G,th}}(t) = \frac{2}{V} \frac{dN_{\mathrm{G,th}}(t)}{dt} \, . \tag{2.174}$$

We model $N_{\mathrm{G,th}}$ as a homogeneous Poisson process. The one sided power spectral density of $\gamma_{\mathrm{G,th}}$ is then given by

$$S_{\gamma_{\mathrm{G,th}}}(\nu) = \frac{4}{V} \Gamma_{\mathrm{G,th}} = \frac{4}{V} \left(R n_{\mathrm{qp,th}}^2 + \frac{n_{\mathrm{qp,th}}}{\tau_{\max}} \right) \, , \tag{2.175}$$

where we have used Equation (2.19) for the steady-state value $\Gamma_{\mathrm{G,th}}$. In a steady state under zero optical loading, thermal generation must balance recombination. This sets the value of $\Gamma_{\mathrm{G,th}}$, and hence the value of $S_{\gamma_{\mathrm{G,th}}}$.

There is some uncertainty in the τ_{max}^{-1} term in Equation (2.173) and Equation (2.175). We do not know what physical process is responsible for the saturation of the quasi-particle lifetime. If it is caused, for example, by trapping of quasi-particles in localized, sub-gap states by magnetic impurities [91], then one could still model it with a Poisson process; however, only a single quasi-particle would annihilate per trapping event. As a result, Equation (2.157) which relates the quasi-particle rate to the event rate would not contain the factor of 2 and the contribution to $S_{\gamma_{\mathrm{R}}}$ due to τ_{max}^{-1} would be $2n_{\mathrm{qp}}/V\tau_{\mathrm{max}}$ instead of $4n_{\mathrm{qp}}/V\tau_{\mathrm{max}}$. Barends et al. [90] observed a clear decrease in τ_{max} by increasing the concentration of ion implanted impurities in Al and Ta superconducting films, lending experimental support to this theory. However, the decrease occurred for both magnetic and nonmagnetic impurities. The interpretation they put forward is that the impurities increase disorder in the superconductor and this causes an enhancement of the recombination rate. In our model for the noise, we assume that it is indeed an enhancement of the recombination rate that is occurring and retain the factor of 4 in our equations. Note that the exact form used for this term does not have a significant impact on our results since $\tau_{\mathrm{qp}} \gg \tau_{\mathrm{max}}$.

Thermal generation-recombination noise has been measured by de Visser et al. [117] in Al CPW resonators between 100 and 300 mK under negligible optical loading. They used the bandwidth and intensity of the resonator dissipation fluctuations to constrain the quasi-particle lifetime and quasi-particle density, respectively. The model for generation-recombination noise just outlined provided a good description of the measured values of $[\tau_{\mathrm{qp}}^{\mathrm{eff}}, n_{\mathrm{qp}}](T_{\mathrm{bath}})$. Interestingly, both the lifetime *and* the density saturated in a consistent manner below 160 mK, suggesting that τ_{max} is sourced by the recombination of an excess, nonthermal population of quasi-particles in these particular Al superconductors. In order to maintain this nonthermal quasi-particle population there must some source of power dissipation. One likely candidate is the absorption of microwave photons [109, 118].

Up until this point we have assumed that there is a uniform distribution of quasi-particles in our derivation of the fundamental noise. It is straightforward to determine the effects of a nonuniform distribution using techniques similar to those employed in Section 2.2.10. The end result is that the recombination noise will increase by a factor ζ and the effective quasi-particle lifetime will be given by Equation (2.130) instead of Equation (2.24).

We now insert Equations (2.156), (2.173), and (2.175) into Equation (2.150) to obtain an expression for the power spectral density of the fundamental noise sources

$$S_{\delta n_{\mathrm{qp}}}^{\mathrm{fund}}(\nu) = \frac{2\tau_{\mathrm{qp}}^{\mathrm{eff}\,2}}{1+\left(2\pi\tau_{\mathrm{qp}}^{\mathrm{eff}}\nu\right)^2}\left[\left(\frac{\eta_{\mathrm{ph}}}{V\Delta}\right)^2\left(\frac{P_{\mathrm{opt}}h\nu_{\mathrm{mm}}}{\eta_{\mathrm{qe}}}+\frac{P_{\mathrm{opt}}^2}{\Delta\nu_{\mathrm{mm}}}\right)+\frac{2R}{V}\left(\zeta n_{\mathrm{qp}}^2+n_{\mathrm{qp,th}}^2\right)+\frac{2}{V\tau_{\mathrm{max}}}\left(n_{\mathrm{qp}}+n_{\mathrm{qp,th}}\right)\right]. \tag{2.176}$$

We find that the fundamental noise has a white spectrum up to $\Delta\nu_{qp}$. Consider the case where $\nu \ll \Delta\nu_{qp}$, $n_{qp} \gg n_{qp,th}$ and $\tau_{qp} \ll \tau_{max}$ which is a good approximation for the MUSIC detectors during on-sky loading conditions. Then Equation (2.176) can be written as

$$S^{\text{fund}}_{\delta P_{\text{opt}}}(\nu) \approx 2P_{\text{opt}}\left(\frac{h\nu_{\text{mm}}}{\eta_{\text{qe}}} + \frac{P_{\text{opt}}}{\Delta\nu_{\text{mm}}} + \frac{2\Delta}{\eta_{\text{ph}}}\right) \qquad \text{for } n_{\text{qp}} \gg n_{\text{qp,th}} \text{ and } \tau_{\text{qp}} \ll \tau_{\text{max}}\ , \tag{2.177}$$

where we have used Equation (2.124) to express the quasi-particle density in terms of the optical power and Equation (2.131) to convert fluctuations in quasi-particle density to fluctuations in optical power. The three terms correspond to photon shot noise, photon Bose noise, and recombination noise from left to right. In this limit, for a given observing band and superconductor the fundamental noise is entirely set by the background optical loading P_{opt}. Ideally all other sources of noise would be subdominant to the above expression when referred to fluctuations in incident optical power. In that case we say that the detector has achieved background-limited performance or BLIP.

2.3.2.2 Two-Level Systems

MKIDs suffer from an excess noise in the frequency direction that originates from a surface layer of two-level systems (TLS) [119, 120]. The material hosting the TLS is likely a thin oxide layer that forms on exposed metal or substrate during fabrication. TLS are defects common to amorphous solids in which an atom or group of atoms can tunnel between two potential energy minima [121, 122]. Each TLS can be treated quantum mechanically as a particle in double-well potential. The variations in local environment that are present in amorphous material result in TLS with an extremely broad distribution of energy splittings [123]. The tunneling process has an electric dipole moment that couples to the electric field of the resonator and affects the dielectric function $\varepsilon = \varepsilon_1 - i\varepsilon_2$.

At microwave frequencies and low temperatures ($T < 1$ K) the resonant response of the ensemble of TLS results in a temperature-dependent contribution to the real and imaginary parts of the dielectric function. This causes a temperature-dependent shift in the frequency and loss of the resonator, respectively. The TLS-induced dielectric loss is given by

$$\frac{1}{Q_i(T)} = F\delta^0_{\text{TLS}} \tanh\left(\frac{\hbar\omega}{2k_BT}\right)\left[1 + \frac{|\boldsymbol{E}|^2}{E_c^2}\right]^{-1/2}\ , \tag{2.178}$$

where $\omega = 2\pi f$ is the microwave angular frequency, $\boldsymbol{E}$ is the electric field, δ^0_{TLS} is the loss tangent due to TLS at zero temperature and weak electric field, F is the filling factor defined as the fraction of the electric field energy contained in material hosting TLS, and E_c is the critical electric field for saturation of the TLS-induced loss. Similarly, the expression for the TLS-induced fractional frequency shift is given by

$$\frac{f_{\text{res}}(T) - f_{\text{res}}(0)}{f_{\text{res}}(0)} = \frac{F\delta^0_{\text{TLS}}}{\pi}\left[\text{Re}\left\{\Psi\left(\frac{1}{2} + \frac{\hbar\omega}{2\pi jk_BT}\right)\right\} - \log\left(\frac{\hbar\omega}{2\pi k_BT}\right)\right]\ , \tag{2.179}$$

where Ψ is the complex digamma function. Note that the frequency shift does not saturate with electric field strength in the same way as the loss. This is because only TLS with excitation frequencies in a narrow region around the microwave frequency contribute to the imaginary part of the dielectric function, whereas TLS with a broad range of excitation frequencies contribute to the real part of the dielectric function. Said another way, only the on-resonance TLS contribute to the loss, whereas both on-resonance and off-resonance TLS contribute to the frequency shift [124]. The on-resonance TLS saturate with microwave power; they undergo rapid oscillations between the two potential minima and are therefore unable to absorb additional energy. The off-resonance TLS do not. As a result the TLS-induced frequency shift should be nearly independent of power.

A microscopic theory for the TLS-induced frequency noise does not exist. However, a semi-empirical model which describes how the noise scales with temporal frequency, microwave carrier power, temperature, and resonator geometry does exist [125] and is sufficient for our purposes. The semi-empirical model assumes a uniform spatial distribution of independently fluctuating TLS within some volume V_{TLS} of host material. It is assumed that there is some mechanism by which the TLS can cause fluctuations in the real component of the dielectric function $\delta\varepsilon_1$ and that the magnitude of these fluctuations saturates with electric field strength in a similar manner as the TLS-induced loss, i.e.,

$$S_{\delta\varepsilon_1}(\boldsymbol{E}) \propto \left[|\boldsymbol{E}|^2 + E_{c,\delta\varepsilon_1}^2\right]^{-1/2} . \tag{2.180}$$

In the limit that one is operating in a high power regime where the TLS are fully saturated or $|\boldsymbol{E}| \gg E_{c,\delta\varepsilon_1}$, the power spectral density of fractional fluctuations in the resonator frequency $\delta f_{\text{res}}/f_{\text{res}}$ is given by

$$S_{\delta f_{\text{res}}/f_{\text{res}}}^{\text{TLS}}(\nu) = \mathcal{K}(\nu, f, T_{\text{bath}}) \frac{\int_{V_{\text{TLS}}} |\boldsymbol{E}(\boldsymbol{r})|^3 d^3\boldsymbol{r}}{4\left(\int_V \varepsilon(\boldsymbol{r})|\boldsymbol{E}(\boldsymbol{r})|^2 d^3\boldsymbol{r}\right)^2} , \tag{2.181}$$

where the term $\mathcal{K}(\nu, f, T_{\text{bath}})$ encodes the scaling with temporal frequency ν, microwave frequency f, and bath temperature T_{bath} and is to be constrained empirically. This model has been experimentally validated by examining the excess frequency noise in CPW resonators as a function of the center strip width s, and confirming the $s^{-1.55}$ geometrical scaling that is predicted by the integral in the equation above assuming a surface distribution of TLS [125]. Since $|\boldsymbol{E}(\boldsymbol{r})| \propto P_{\text{int}}^{1/2}$, where P_{int} is the internal resonator power, Equation (2.181) implies that the power spectral density scales as $P_{\text{int}}^{-1/2}$. This unique scaling with power also been confirmed experimentally.

Equation (2.181) implies that individual TLS are weighted by the cube of the electric field, so that TLS located in the high voltage, capacitive section of the resonator have the most significant contributions to the noise. This offers a strategy for reducing the TLS noise by designing the capacitor in such a way that the field strength is reduced at the surface where the TLS reside. This is indeed the approach that we have taken with the interdigitated capacitor (IDC) design used in MUSIC, which increases the area and electrode spacing of

the capacitor in order to "spread out" the E field. This resulted in a factor of 30 reduction in the TLS noise compared to previous CPW designs [126, 104].

The internal resonator power is given by

$$P_{\rm int} = Q_i P_{\rm diss} = 2\frac{Q^2}{Q_c}\chi_y P = \frac{1}{2} Q_i \chi_c \chi_y P \,, \tag{2.182}$$

where we have used Equation (2.83) to express $P_{\rm diss}$ in terms of P, the carrier power on the feedline at the device. There have been several measurements that have shown

$$\mathcal{K}(\nu, f, T_{\rm bath}) = \mathcal{K}(f)\nu^{-1/2}\, T_{\rm bath}^{-\beta} \tag{2.183}$$

with $\beta = 1.2 - 2.0$ [127, 93, 128]. Equation (2.181) can then be written as

$$S^{\rm TLS}_{\delta f_{\rm res}/f_{\rm res}}(\nu) = B^2_{\rm TLS}(f)\, \left(\frac{1}{2} Q_i \chi_y \chi_c P\right)^{-1/2}\, \nu^{-1/2}\, T_{\rm bath}^{-\beta} \,, \tag{2.184}$$

where the normalization $B_{\rm TLS}$ will have some dependence on the microwave frequency and resonator geometry. Compared to other sources of noise intrinsic to MKIDs, TLS noise has a unique scaling with temporal frequency, bath temperature, and carrier power. We will make use of this fact to isolate the TLS noise and measure $B_{\rm TLS}$ for each resonator. This is subject of Section 3.3.4.

2.3.2.3 Atmospheric

Ground-based observations at submillimeter and millimeter wavelengths are strongly affected by water vapor (and to a lesser extent oxygen and ozone) in the atmosphere. Atmospheric absorption results in significant attenuation of astronomical signal as shown in Figure 2.14. Atmospheric emission increases background loading, which increases photon noise and degrades detector responsivity. Finally, fluctuations in atmospheric emission results in long-timescale noise that prevents the recovery of signal at large spatial scales. This sensitivity to the amount and variability of atmospheric water vapor has driven the location of large (sub)millimeter telescopes to dry and stable (and often inhospitable) sites such as Antartica, the Atacama Desert in Chile, and the summit of Mauna Kea in Hawaii.

The majority of atmospheric water vapor is located in the troposphere at an effective height $h_{\rm avg} \sim 1$ km. The water vapor is poorly mixed with the other dry components of the atmosphere because the temperature of the atmosphere is near its condensation point [130]. This nonuniform distribution of water vapor is the dominant cause of fluctuations in atmospheric emission, which we will henceforth refer to as atmospheric noise.

Atmospheric noise above Mauna Kea has been studied at 143 and 268 GHz by Sayers et al. [37] using data collected with Bolocam. They find that the atmospheric noise is consistent with a Kolmogorov-Taylor (K-T) thin screen model [131]. This model assumes that there is a thin turbulent layer of thickness Δh

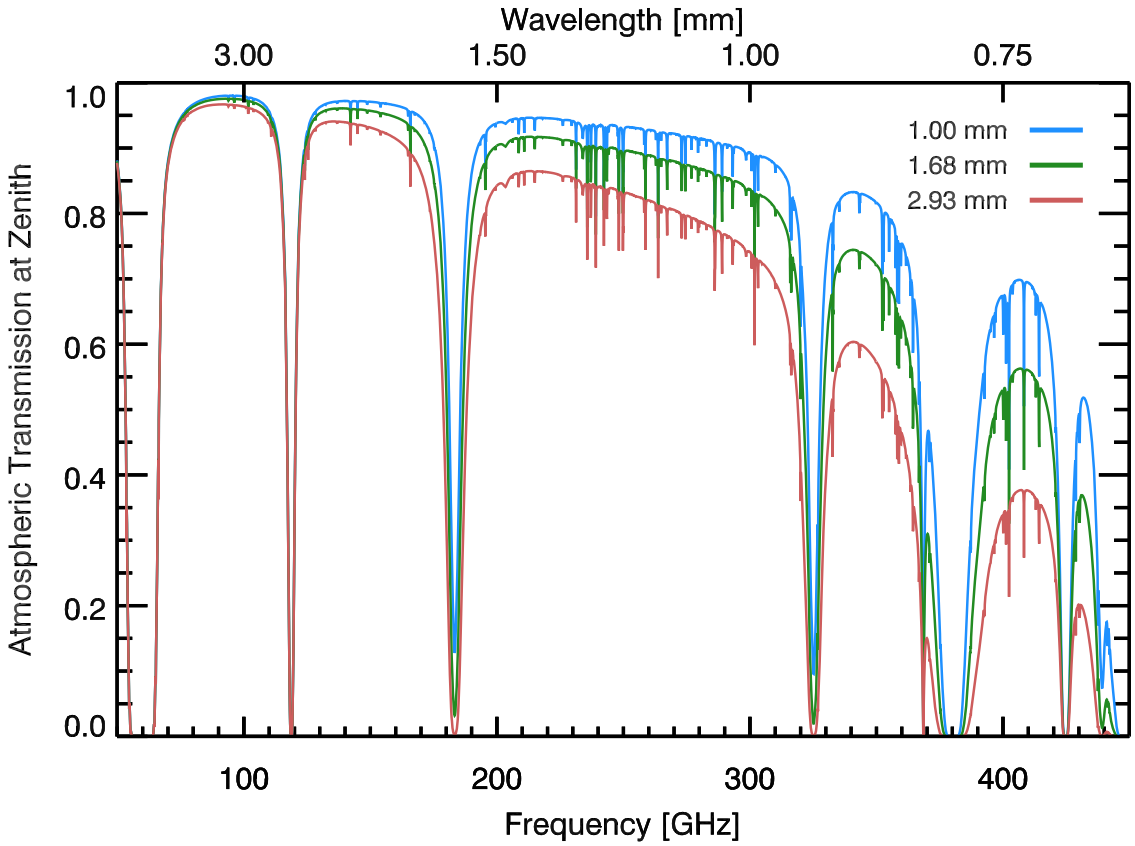

Figure 2.14: The atmospheric transmission on Mauna Kea when looking at zenith. The blue, green, and red curves correspond to the historical 25th, 50th, and 75th percentiles for the column depth of precipitable water vapor $\mathcal{C}_{\rm PW}$ on Mauna Kea. The curves were calculated using the ATM software [129].

at some height $h_{\rm avg}$ that moves horizontally across the sky with an angular velocity $\boldsymbol{w}$, and that within the layer the atmosphere behaves according to the K-T model of turbulence [132, 133, 134]. In the K-T model turbulent energy is constantly injected into the atmosphere at large scales by processes such as wind shear and convection. The energy cascades down to smaller scales through an inertial mechanism, producing a hierarchy of eddies. Eventually it reaches a small enough scale that it can be dissipated by viscous effects. For a three-dimensional volume the model predicts that between the injection scale L and the dissipative scale η there will be a power spectrum of fluctuations due to turbulence that scales as $|\boldsymbol{q}|^{-11/3}$, where $\boldsymbol{q}$ is the three-dimensional spatial frequency. It can be shown (e.g., [131, 135, 136]) that this gives rise to a power spectral density of fluctuations in the brightness temperature of the sky that is given by

$$S_{\delta T_{\rm sky}}(\boldsymbol{\alpha}) = \begin{cases} B_{\rm 3D}^2 |\boldsymbol{\alpha}|^{-11/3} & \frac{h_{\rm avg}}{2\Delta h \sin \mathfrak{e}} \ll |\boldsymbol{\alpha}| \ll \eta \\ B_{\rm 2D}^2 |\boldsymbol{\alpha}|^{-8/3} & L \ll |\boldsymbol{\alpha}| \ll \frac{h_{\rm avg}}{2\Delta h \sin \mathfrak{e}} \end{cases}, \tag{2.185}$$

where $\boldsymbol{\alpha} = [\alpha_x, \alpha_y] = [q_x, q_y] \times \frac{h_{\rm avg}}{\sin \mathfrak{e}}$ is the angular wave number on the sky in units of 1/radians, $B_{\rm 2D,3D}$ are normalizations in units of mK rad$^{-5/6}$, and $\mathfrak{e}$ is the elevation. The transition from the three-dimensional

to two-dimensional regime occurs at a physical scale of approximately $2\Delta h$, at which point the projected power spectral density is expected to transition from a $-11/3$ to $-8/3$ power law. The normalizations will depend on several parameters — the average height $h_{\rm avg}$ and thickness Δh of the turbulent layer, the elevation angle $\mathfrak{e}$, the observing wavelength $\nu_{\rm mm}$, and the column depth of precipitable water vapor $\mathcal{C}_{\rm PW}$ — so that $B_{\rm 2D,3D} \equiv B_{\rm 2D,3D}(h_{\rm avg}, \Delta h, \mathfrak{e}, \nu_{\rm mm}, \mathcal{C}_{\rm PW})$. In the three-dimensional regime the exact dependence on the elevation, height, and thickness can be derived

$$B^2_{\rm 3D}(h_{\rm avg}, \Delta h, \mathfrak{e}, \nu_{\rm mm}, \mathcal{C}_{\rm PW}) = B^2_{\rm 3D}(\nu_{\rm mm}, \mathcal{C}_{\rm PW})\, h_{\rm avg}^{5/3}\, (\sin\mathfrak{e})^{-8/3} \ . \tag{2.186}$$

In the two-dimensional regime the dependence on these parameters is much more complicated and should be calculated numerically.

Sayers et al. [37] examined the cross-PSD between pairs of bolometers to constrain the angular wind speed and found a median value of $|\boldsymbol{w}| \simeq 30$ arcmin/sec. Assuming $h_{\rm avg} = 1$ km this corresponds to a physical value of $\simeq 10$ m/sec, which is reasonable. We note that this is much faster than the maximum scan speed that can be achieved at the CSO of 4 arcmin/sec. Sayers et al. [37] then employed random simulations of the sky in order to fit the timestream correlation between bolometers pairs as a function of pair separation to Equation (2.185). They attempted to constrain $h_{\rm avg}$ and the normalization and exponent of the power-law. The data was insensitive to $h_{\rm avg}$ but was able to constrain the exponent to -3.3 ± 1.1, consistent with the $-11/3$ scaling predicted for K-T fluctuations in the three-dimensional regime. They then set $h_{\rm avg} = 1$ km and fixed the exponent at $-11/3$ to constrain the median amplitude of the fluctuations

$$\begin{aligned} B^2_{\rm 3D}(143\ {\rm GHz}, 1.68\ {\rm mm}) &= 280\ {\rm mK}^2\ {\rm rad}^{-5/3}\ , \\ B^2_{\rm 3D}(268\ {\rm GHz}, 1.68\ {\rm mm}) &= 4000\ {\rm mK}^2\ {\rm rad}^{-5/3}\ . \end{aligned} \tag{2.187}$$

Note that the choice of $h_{\rm avg} = 1$ km is based on radiosonde measurements of the water vapor profile above Mauna Kea [137].

The fluctuations in the brightness temperature of the sky characterized by Equation (2.185) are caused by changes in the emissivity of the sky due to fluctuations in the column depth of precipitable water vapor. That is to say

$$S_{\delta T_{\rm sky}}(\boldsymbol{\alpha}) = \left(\frac{\partial T_{\rm sky}}{\partial \tau}\right)^2 \left(\frac{\partial \tau}{\partial \mathcal{C}_{\rm PW}}\right)^2 S_{\delta \mathcal{C}_{\rm PW}}(\boldsymbol{\alpha})\ , \tag{2.188}$$

where $\tau(\nu_{\rm mm}, \mathcal{C}_{\rm PW})$ is the atmospheric opacity. It is reasonable to assume that the size of the fluctuations in the precipitable water vapor will scale with the amount of precipitable water vapor, or $\delta\mathcal{C}_{\rm PW} \propto \mathcal{C}_{\rm PW}$ so that

$S_{\delta \mathcal{C}_{\rm PW}}(\boldsymbol{\alpha}) \propto \mathcal{C}_{\rm PW}^2$. In this case

$$B_{\rm 3D}^2(\nu_{\rm mm}, \mathcal{C}_{\rm PW}) \propto \left[T_{\rm atm} e^{-\tau} \left(\frac{\partial \tau}{\partial \mathcal{C}_{\rm PW}} \right) \mathcal{C}_{\rm PW} \right]^2 , \tag{2.189}$$

where we have used the equation $T_{\rm sky} = (1 - e^{-\tau}) T_{\rm atm}$ for the sky temperature at zenith since the dependence on elevation angle has already been addressed. Sayers et al. [37] found that Equation (2.189) explained the dominant trend in the value of $B_{\rm 3D}^2$ with $\mathcal{C}_{\rm PW}$ and observing band. However, there was significant scatter on the order of $100 - 300\%$ about this trend, suggesting that the assumption $\delta \mathcal{C}_{\rm PW} \propto \mathcal{C}_{\rm PW}$ only holds in a statistical sense, and that the value of $\mathcal{C}_{\rm PW}$ at the time of an observation should only be used as a rough proxy for the amplitude of the atmospheric noise.

We are primarily interested in how the atmospheric noise will manifest in the timestreams of the MUSIC detectors. Since $S(\boldsymbol{\alpha})$ is azimuthally symmetric and since the wind speed is much greater than the scan speed of the telescope, we should have that

$$\nu \approx |\boldsymbol{\alpha}||\boldsymbol{w}| , \tag{2.190}$$

where ν is the temporal frequency. This assumes that the wind velocity is constant over the course of a scan. If we neglect beam smoothing and windowing effects we can directly insert Equation (2.190) into Equation (2.185) to obtain an expression for $S_{\delta T_{\rm sky}}(\nu)$. The atmospheric noise will be transduced via changes in quasi-particle density, just like astronomical signal, so we can express the power spectral density as

$$\begin{aligned} S_{\delta n_{\rm qp}^{\rm atm}}(\nu) &= \left(\frac{\partial n_{\rm qp}}{\partial P_{\rm opt}} \right)^2 \left(\frac{\partial P_{\rm opt}}{\partial T_{\rm sky}} \right)^2 B_{\rm atm}^2 \left(\frac{\nu}{|\boldsymbol{w}|} \right)^{-b_{\rm atm}} \\ &= \left(\frac{\tau_{\rm qp}^{\rm eff} \eta_{\rm ph} \eta_{\rm opt} (1 - f_{\rm spill}) \Delta \nu_{\rm mm}}{V \Delta} \right)^2 k_B^2 B_{\rm atm}^2 \left(\frac{\nu}{|\boldsymbol{w}|} \right)^{-b_{\rm atm}} , \end{aligned} \tag{2.191}$$

where $8/3 \leq b_{\rm atm} \leq 11/3$ and $B_{\rm 2D} \leq B_{\rm atm} \leq B_{\rm 3D}$ depending on the value of ν relative to $\frac{h_{\rm avg}|\boldsymbol{w}|}{2\Delta h \sin \mathfrak{e}}$. The partial derivatives were evaluated using Equations (2.7), (2.8), and (2.25). To summarize, the atmospheric noise will appear in the quasi-particle direction and will have a power spectral density that is a power-law in frequency with a steep spectral index between $8/3$ and $11/3$. The amplitude of the noise will on average scale with the column depth of precipitable water vapor $\mathcal{C}_{\rm PW}$.

We expect the atmospheric noise recorded by each detector to be highly correlated with the atmospheric noise recorded by every other detector for the following reasons. The separation between the near and far field of our instrument is given by the Fraunhofer distance

$$d_f = \frac{2D^2}{\lambda} , \tag{2.192}$$

where D is the diameter of the telescope and λ is the wavelength of the radiation. MUSIC uses a $D = 9$ m diameter illumination of the CSO primary mirror [138], resulting in $d_f = [80,\ 120,\ 155,\ 285]$ km for the

four bands. The vast majority of atmospheric water vapor resides in the troposphere between 0 and 10 km, and therefore is well within the near field of our instrument. In the near field, the beam patterns of individual detectors are well approximated by the primary illumination pattern, which is approximately a 9 m diameter top-hat. Assuming $h_{\rm avg} = 1$ km, the 14 arcmin field of view translates to a physical size of approximately 4 m at the height of the turbulent layer. This means that even detectors on opposite sides of the focal plane will have significant beam overlap at this height and at any given time the detectors will see many of the same atmospheric fluctuations. Therefore, the atmospheric noise present in the timestreams of different detectors will be highly correlated. One can perform a correlation analysis to remove this common signal [139, 140, 141]. Note that the atmospheric noise will be coherent across observing bands and spectral information can be used to improve its removal [142, 143, 144].

The atmospheric noise drops off quickly with frequency. Sayers et al. [37] found that for Bolocam the atmospheric noise is negligible compared to photon noise at frequencies $\nu \gtrsim 0.5$ Hz. Likewise for MUSIC the atmospheric noise is subdominant at $\nu \gtrsim 0.5 - 1.0$ Hz, as we will show in Section 3.3.5. The long-timescales at which the atmospheric noise is of consequence correspond to fluctuations in atmospheric emission at large spatial scales. Again, assuming a height $h_{\rm avg} = 1$ km and using the median wind speed of 10 m/sec found by Sayers et al. [37], $\nu \lesssim 0.5$ Hz corresponds to physical scales $\gtrsim 20$ m or angular scales $\gtrsim 70$ arcmin. Hence, the atmospheric fluctuations that we are actually sensitive to occur on scales that are much larger than the size of the focal plane, and therefore should be slowly varying over the focal plane. This further supports our assertion that the atmospheric noise will be highly correlated between detectors.

2.4 Summary

The sources of noise discussed in this section can be combined into a single equation for the complex amplitude of an on-resonance carrier tone as a function of time

$$\begin{aligned}\hat{V}(t) = {} & Ae^{j\phi} + \delta\boldsymbol{w} + A\left(\delta A + j\delta\phi\right)e^{j\phi} \\ & + \frac{1}{2}A|S_{21}^{\rm res}|^{-1}Q_i\chi_c\chi_y\left(1+8ay\chi_y^2\right)^{-1}\left(\frac{\delta f_{\rm res}}{f_{\rm res}}\right)^{\rm TLS}e^{j\left(3\pi/2+\phi+\phi_y+\phi_c-\theta_{\rm res}\right)} \\ & + \frac{1}{4}A|S_{21}^{\rm res}|^{-1}Q_i\chi_c\chi_y\alpha|\tilde{\kappa}|\left(\delta n_{\rm qp}^{\rm atm}+\delta n_{\rm qp}^{\rm fund}\right)e^{j\left(\tilde{\Psi}+\phi+\phi_y+\phi_c-\theta_{\rm res}\right)} \\ & + \frac{1}{4}A|S_{21}^{\rm res}|^{-1}Q_i\chi_c\chi_y\alpha|\tilde{\kappa}|\frac{\tau_{\rm qp}^{\rm eff}\eta_{\rm ph}}{V\Delta}\delta P_{\rm opt}^{\rm signal}e^{j\left(\tilde{\Psi}+\phi+\phi_y+\phi_c-\theta_{\rm res}\right)}\ . \end{aligned} \tag{2.193}$$

The equation describes how small fluctuations due to the various noise sources translate into fluctuations in the measured quantity. Here $\delta\boldsymbol{w} = \delta w_{\rm I} + j\delta w_{\rm Q}$ represents the additive white noise from the electronics, δA and $\delta\phi$ represent the multiplicative amplitude and phase noise from the electronics, $\left(\delta f_{\rm res}/f_{\rm res}\right)^{\rm TLS}$ represents fractional fluctuations in the resonator frequency due to TLS, and $\delta n_{\rm qp}^{\rm fund}$ and $\delta n_{\rm qp}^{\rm atm}$ represent fluctuations in

the quasi-particle density due to fundamental and atmospheric noise. The astronomical signal is included as a fluctuation in the incident optical power $\delta P_{\text{opt}}^{\text{signal}}$. The average value of Equation (2.193) is defined to be $<\hat{V}(t)>=\hat{V}=Ae^{j\phi}$.

It is evident from Equation (2.193) that different sources of noise appear in different directions in the complex plane. This is illustrated in Figure 2.12. The readout electronics sample the in-phase $\mathrm{I}(t)=\mathrm{Re}\left[\hat{V}(t)\right]$ and quadrature-phase $\mathrm{Q}(t)=\mathrm{Im}\left[\hat{V}(t)\right]$ components. But the I-Q basis is not useful in terms of studying noise nor isolating signal. Suppose that a particular noise/signal lies in a direction that is rotated by an angle θ_X with respect to the I-Q basis. If θ_X can be determined, then the digitized I-Q data can be rotated into the X-Y basis so that the noise/signal occurs in $X(t)$ and is absent in $Y(t)$. This rotation is given by the following linear transformation

$$\begin{bmatrix} X(t) \\ Y(t) \end{bmatrix} = \frac{1}{A_{\mathrm{X}}} \begin{bmatrix} \cos\theta_{\mathrm{X}} & \sin\theta_{\mathrm{X}} \\ -\sin\theta_{\mathrm{X}} & \cos\theta_{\mathrm{X}} \end{bmatrix} \times \begin{bmatrix} \mathrm{I}(t) \\ \mathrm{Q}(t) \end{bmatrix} , \tag{2.194}$$

or equivalently

$$X(t)+jY(t)=\frac{e^{-j\theta_x}}{A_X}\hat{V}(t)\ . \tag{2.195}$$

Here A_X is a normalization that it might be sensible to apply alongside a particular rotation in order to extract the desired noise/signal. There are three notable bases:

Amplitude and Phase This basis is rotated by an angle $\theta_{\text{amp}}=\phi$ with respect to the I-Q basis. The angle ϕ can be estimated using the mean value of the carrier amplitude, $\overline{\phi}=\arctan(\overline{Q}/\overline{I})$. The basis is useful for studying the multiplicative electronics noise δA and $\delta\phi$. Rotation to this basis is usually accompanied with normalization by the carrier amplitude, i.e. $A_{\text{amp}}=A$. Again, this can be estimated using the mean value of the carrier amplitude $\overline{A}=[\overline{I}^2+\overline{Q}^2]^{-1/2}$. This transformation will isolate δA and $\delta\phi$ for the off-resonance carriers.

Frequency and Dissipation This basis is rotated by an angle $\theta_{\text{freq}}=\frac{3\pi}{2}+\phi+\phi_y+\phi_c-\theta_{\text{res}}$ with respect to the I-Q basis. Note that we have defined the rotation angle so that an increase in the resonant frequency moves in the positive frequency direction and an increase in carrier frequency moves in the negative frequency direction. This is necessary to ensure that an increase in resonator dissipation moves in the positive dissipation direction. The angle θ_{freq} can be accurately determined by measuring the direction tangent to the resonance curve. Indeed, this basis is more accurately described as the "tangent and normal to resonance curve basis", because when a resonator is operated in the nonlinear regime the frequency and dissipation response are no longer orthogonal, as we saw in Section 2.2.6. Still, we will use the name frequency and dissipation basis since it is standard. This basis is useful because TLS noise appears in the frequency direction but not the dissipation direction. This is true even when the detector is operated in the nonlinear regime, so long as the dissipation is independent of power. Rotation to this basis is usually accompanied with normalization by the quantity $A_{\text{freq}}=\frac{1}{2}A|S_{21}^{\text{res}}|^{-1}Q_i\chi_c\chi_y(1+8ay\chi_y^2)^{-1}$

in order to convert the timestreams into the equivalent fractional fluctuations in the resonator frequency. The angle and normalization can be determined by measuring the resonance curve as a function of frequency and then examining its derivative at the location of the carrier tone.

Quasi-particle and Orthogonal This basis is rotated by an angle $\theta_{\rm qp} = \tilde{\Psi} + \phi + \phi_y + \phi_c - \theta_{\rm res}$ with respect to the I-Q basis. The angle $\theta_{\rm qp}$ can be determined as $\theta_{\rm qp} = \theta_{\rm freq} + \frac{\pi}{2} + \tilde{\Psi}$ using the theoretical value of $\tilde{\Psi}$. However, the true value of $\tilde{\Psi}$ can deviate from the theoretical prediction for a number of reasons and the quantity $\theta_{\rm qp}$ is nontrivial to measure directly. This basis is useful because the astronomical signal as well as several sources of noise appear in the quasi-particle direction but not in the orthogonal direction.

We will examine the time-ordered data in each of these bases depending on the sources of noise we are interested in studying.

We now set out to derive an expression for the noise equivalent power (NEP), a common metric for detector performance. The NEP is defined as the optical power incident on the detector that yields a signal-to-noise ratio of 1 in a 1 Hz output bandwidth [145]. It is usually specified in units of W $\mathrm{Hz}^{-1/2}$. We will reference the NEP to optical power incident on the MKID from the antenna. We start by writing Equation (2.193) as

$$\hat{V}(t) = \hat{V} + \delta\hat{V}^{\,\rm signal} + \delta\hat{V}^{\,\rm noise}\,, \tag{2.196}$$

where

$$\delta\hat{V}^{\,\rm signal} = \frac{1}{4}A|S_{21}^{\rm res}|^{-1}Q_i\chi_c\chi_y\alpha|\tilde{\kappa}|\frac{\tau_{\rm qp}^{\rm eff}\eta_{\rm ph}}{V\Delta}\delta P_{\rm opt}^{\rm signal}e^{j\theta_{\rm qp}} \tag{2.197}$$

and

$$\begin{aligned}\delta\hat{V}^{\,\rm noise} = {} & \delta w + A\left(\delta A + j\delta\phi\right)e^{j\phi} \\ & + \frac{1}{2}A|S_{21}^{\rm res}|^{-1}Q_i\chi_c\chi_y\left(1+8ay\chi_y^2\right)^{-1}\left(\frac{\delta f_{\rm res}}{f_{\rm res}}\right)^{\rm TLS}e^{j\theta_{\rm freq}} \\ & + \frac{1}{4}A|S_{21}^{\rm res}|^{-1}Q_i\chi_c\chi_y\alpha|\tilde{\kappa}|\left(\delta n_{\rm qp}^{\rm atm} + \delta n_{\rm qp}^{\rm fund}\right)e^{j\theta_{\rm qp}}\,.\end{aligned} \tag{2.198}$$

Here we have used the definitions of $\theta_{\rm freq}$ and $\theta_{\rm qp}$ given above. At this point we have to pick a basis. We choose to present the NEP in the frequency and dissipation basis for two reasons. First, the data is easily rotated into this basis because the angle of rotation $\theta_{\rm freq}$ is accurately determined from a measurement of the resonance curve. Second, the TLS noise only appears in the frequency direction, so we expect the NEP in the

frequency and dissipation direction to differ significantly. The signal in this basis is given by

$$\begin{aligned}\delta\hat{V}_{\text{freq}}^{\text{signal}} &= \text{Re}\left[\delta\hat{V}^{\text{signal}} e^{-j\theta_{\text{freq}}}\right] \\ &= -\frac{1}{4}A|S_{21}^{\text{res}}|^{-1} Q_i \chi_c \chi_y \alpha \tilde{\kappa}_2 \frac{\tau_{\text{qp}}^{\text{eff}} \eta_{\text{ph}}}{V\Delta} \delta P_{\text{opt}}^{\text{signal}}\end{aligned} \tag{2.199}$$

$$\begin{aligned}\delta\hat{V}_{\text{diss}}^{\text{signal}} &= \text{Im}\left[\delta\hat{V}^{\text{signal}} e^{-j\theta_{\text{freq}}}\right] \\ &= \frac{1}{4}A|S_{21}^{\text{res}}|^{-1} Q_i \chi_c \chi_y \alpha \tilde{\kappa}_1 \frac{\tau_{\text{qp}}^{\text{eff}} \eta_{\text{ph}}}{V\Delta} \delta P_{\text{opt}}^{\text{signal}}\end{aligned} \tag{2.200}$$

and the noise is given by

$$\begin{aligned}\delta\hat{V}_{\text{freq}}^{\text{noise}} &= \text{Re}\left[\delta\hat{V}^{\text{noise}} e^{-j\theta_{\text{freq}}}\right] \\ &= \delta w + A\left[\delta A \cos\left(\phi - \theta_{\text{freq}}\right) - \delta\phi \sin\left(\phi - \theta_{\text{freq}}\right)\right] \\ &\quad + \frac{1}{2}A|S_{21}^{\text{res}}|^{-1} Q_i \chi_c \chi_y \left(1 + 8ay\chi_y^2\right)^{-1} \left(\frac{\delta f_{\text{res}}}{f_{\text{res}}}\right)^{\text{TLS}} \\ &\quad - \frac{1}{4}A|S_{21}^{\text{res}}|^{-1} Q_i \chi_c \chi_y \alpha \tilde{\kappa}_2 \left(\delta n_{\text{qp}}^{\text{atm}} + \delta n_{\text{qp}}^{\text{fund}}\right)\end{aligned} \tag{2.201}$$

$$\begin{aligned}\delta\hat{V}_{\text{diss}}^{\text{noise}} &= \text{Im}\left[\delta\hat{V}^{\text{noise}} e^{-j\theta_{\text{freq}}}\right] \\ &= \delta w + A\left[\delta A \sin\left(\phi - \theta_{\text{freq}}\right) + \delta\phi \cos\left(\phi - \theta_{\text{freq}}\right)\right] \\ &\quad + \frac{1}{4}A|S_{21}^{\text{res}}|^{-1} Q_i \chi_c \chi_y \alpha \tilde{\kappa}_1 \left(\delta n_{\text{qp}}^{\text{atm}} + \delta n_{\text{qp}}^{\text{fund}}\right) \ ,\end{aligned} \tag{2.202}$$

where we have used the fact that $e^{j(\theta_{\text{qp}} - \theta_{\text{freq}})} = -\sin(\tilde{\Psi}) + j\cos(\tilde{\Psi}) = -\tilde{\kappa}_2 + j\tilde{\kappa}_1$.

The one-sided power spectral density of the signal and noise are obtained by taking two times the squared magnitude of the Fourier transform of each of the equations above and dividing by the sampling period T. In doing so we assume that the frequencies of interest are much less than the quasi-particle and resonator bandwidths so that the roll-off due to the quasi-particle lifetime and the resonator ring-down can be ignored. This is certainly true for all analysis presented in this work. We assume that the multiplicative amplitude and phase noise are correlated, but that all other sources of noise are uncorrelated. This yields the following equations for the signal:

$$S_{\delta\hat{V}_{\text{freq}}}^{\text{signal}} = \left(\frac{AQ_i \chi_c \chi_y \alpha \tilde{\kappa}_2 \tau_{\text{qp}}^{\text{eff}} \eta_{\text{ph}}}{4|S_{21}^{\text{res}}|V\Delta}\right)^2 S_{\delta P_{\text{opt}}}^{\text{signal}} \tag{2.203}$$

$$S_{\delta\hat{V}_{\text{diss}}}^{\text{signal}} = \left(\frac{AQ_i \chi_c \chi_y \alpha \tilde{\kappa}_1 \tau_{\text{qp}}^{\text{eff}} \eta_{\text{ph}}}{4V|S_{21}^{\text{res}}|\Delta}\right)^2 S_{\delta P_{\text{opt}}}^{\text{signal}} \tag{2.204}$$

and similarly for the noise

$$S^{\text{noise}}_{\delta\hat{V}_{\text{freq}}} = S_{\delta w} + A^2\left[S_{\delta A}\cos^2(\phi-\theta_{\text{freq}}) + S_{\delta\phi}\sin^2(\phi-\theta_{\text{freq}}) - S_{\delta A,\delta\phi}\sin\left(2(\phi-\theta_{\text{freq}})\right)\right] + \left(\frac{AQ_i\chi_c\chi_y}{2|S^{\text{res}}_{21}|(1+8a y\chi_y^2)}\right)^2 S^{\text{TLS}}_{\delta f_{\text{res}}/f_{\text{res}}} + \left(\frac{AQ_i\chi_c\chi_y\alpha\tilde{\kappa}_2}{4|S^{\text{res}}_{21}|}\right)^2\left(S^{\text{atm}}_{\delta n_{\text{qp}}}(\nu) + S^{\text{fund}}_{\delta n_{\text{qp}}}\right) \tag{2.205}$$

$$S^{\text{noise}}_{\delta\hat{V}_{\text{diss}}} = S_{\delta w} + A^2\left[S_{\delta A}\sin^2(\phi-\theta_{\text{freq}}) + S_{\delta\phi}\cos^2(\phi-\theta_{\text{freq}}) + S_{\delta A,\delta\phi}\sin\left(2(\phi-\theta_{\text{freq}})\right)\right] + \left(\frac{AQ_i\chi_c\chi_y\alpha\tilde{\kappa}_1}{4|S^{\text{res}}_{21}|}\right)^2\left(S^{\text{atm}}_{\delta n_{\text{qp}}}(\nu) + S^{\text{fund}}_{\delta n_{\text{qp}}}\right) . \tag{2.206}$$

According to the definition given above, NEP is the value of $\sqrt{S^{\text{signal}}_{\delta P_{\text{opt}}}}$ that yields a signal-to-noise ratio of 1. This is obtained by setting $S_{\delta\hat{V}^{\text{signal}}_{\text{freq (diss)}}} = S_{\delta\hat{V}^{\text{noise}}_{\text{freq (diss)}}}$ and solving for $\text{NEP}^2_{\text{freq (diss)}} \equiv S^{\text{signal}}_{\delta P_{\text{opt}}}$. Doing so yields

$$\begin{aligned}\text{NEP}^2_{\text{freq}}(\nu) = {} & \left(\frac{4|S^{\text{res}}_{21}|V\Delta}{AQ_i\chi_c\chi_y\alpha\tilde{\kappa}_2\tau_{\text{qp}}^{\text{eff}}\eta_{\text{ph}}}\right)^2 S_{\delta w} \\ & + \left(\frac{4|S^{\text{res}}_{21}|V\Delta}{Q_i\chi_c\chi_y\alpha\tilde{\kappa}_2\tau_{\text{qp}}^{\text{eff}}\eta_{\text{ph}}}\right)^2\left[\cos^2(\phi-\theta_{\text{freq}})S_{\delta A}(\nu) + \sin^2(\phi-\theta_{\text{freq}})S_{\delta\phi}(\nu) - \sin\left(2(\phi-\theta_{\text{freq}})\right)S_{\delta A,\delta\phi}(\nu)\right] \\ & + \left(\frac{2V\Delta}{\left(1+8a y\chi_y^2\right)\alpha\tilde{\kappa}_2\tau_{\text{qp}}^{\text{eff}}\eta_{\text{ph}}}\right)^2 S^{\text{TLS}}_{\delta f_{\text{res}}/f_{\text{res}}}(\nu) \\ & + \left(\frac{V\Delta}{\tau_{\text{qp}}^{\text{eff}}\eta_{\text{ph}}}\right)^2\left(S^{\text{atm}}_{\delta n_{\text{qp}}}(\nu) + S^{\text{fund}}_{\delta n_{\text{qp}}}\right)\end{aligned} \tag{2.207}$$

$$\begin{aligned}\text{NEP}^2_{\text{diss}}(\nu) = {} & \left(\frac{4|S^{\text{res}}_{21}|V\Delta}{AQ_i\chi_c\chi_y\alpha\tilde{\kappa}_1\tau_{\text{qp}}^{\text{eff}}\eta_{\text{ph}}}\right)^2 S_{\delta w} \\ & + \left(\frac{4|S^{\text{res}}_{21}|V\Delta}{Q_i\chi_c\chi_y\alpha\tilde{\kappa}_1\tau_{\text{qp}}^{\text{eff}}\eta_{\text{ph}}}\right)^2\left[\cos^2(\phi-\theta_{\text{freq}})S_{\delta A}(\nu) + \sin^2(\phi-\theta_{\text{freq}})S_{\delta\phi}(\nu) - \sin\left(2(\phi-\theta_{\text{freq}})\right)S_{\delta A,\delta\phi}(\nu)\right] \\ & + \left(\frac{V\Delta}{\tau_{\text{qp}}^{\text{eff}}\eta_{\text{ph}}}\right)^2\left(S^{\text{atm}}_{\delta n_{\text{qp}}}(\nu) + S^{\text{fund}}_{\delta n_{\text{qp}}}\right) .\end{aligned} \tag{2.208}$$

We then insert Equation (2.184) for $S^{\text{TLS}}_{\delta f_{\text{res}}/f_{\text{res}}}$, Equation (2.176) for $S^{\text{fund}}_{\delta n_{\text{qp}}}$, and Equation (2.191) for $S^{\text{atm}}_{\delta n_{\text{qp}}}$. We also write the additive white noise term as

$$\left(\frac{|S^{\text{res}}_{21}|}{A}\right)^2 S_{\delta w} = \frac{k_B T_{\text{sys}}}{2P} , \tag{2.209}$$

where P is the carrier power at the resonator, $T_{\rm sys}$ is the system noise temperature referred to the input of the HEMT (Equation (2.139)), and the factor of $1/2$ arises in the conversion from peak amplitude to power. Our final expression is then

$$\begin{aligned}
\mathrm{NEP}^2_{\rm freq}(\nu) = \quad & \left(\frac{4V\Delta}{Q_i\chi_c\chi_y\alpha\tilde{\kappa}_2\tau_{\rm qp}^{\rm eff}\eta_{\rm ph}}\right)^2\frac{k_BT_{\rm sys}}{2P} \\
& + \left(\frac{4|S_{21}^{\rm res}|V\Delta}{Q_i\chi_c\chi_y\alpha\tilde{\kappa}_2\tau_{\rm qp}^{\rm eff}\eta_{\rm ph}}\right)^2\left[\cos^2(\phi-\theta_{\rm freq})S_{\delta A}(\nu)+\sin^2(\phi-\theta_{\rm freq})S_{\delta\phi}(\nu)-\sin\left(2(\phi-\theta_{\rm freq})\right)S_{\delta A,\delta\phi}(\nu)\right] \\
& + \left(\frac{2V\Delta\, B_{\rm TLS}}{\left(1+8ay\chi_y^2\right)\alpha\tilde{\kappa}_2\tau_{\rm qp}^{\rm eff}\eta_{\rm ph}}\right)^2\left(\frac{1}{2}Q_i\chi_y\chi_cP\right)^{-1/2}\ T_{\rm bath}^{-\beta}\ \nu^{-1/2} \\
& + \left[\eta_{\rm opt}(1-f_{\rm spill})\Delta\nu_{\rm mm}k_BB_{\rm atm}\right]^2\ |w|^{b_{\rm atm}}\ \nu^{-b_{\rm atm}} \\
& + \frac{2P_{\rm opt}h\nu_{\rm mm}}{\eta_{\rm qe}}+\frac{2P_{\rm opt}^2}{\Delta\nu_{\rm mm}}+\frac{4V\Delta^2}{\eta_{\rm ph}^2}\left[R\left(\zeta n_{\rm qp}^2+n_{\rm qp,th}^2\right)+\frac{1}{\tau_{\rm max}}\left(n_{\rm qp}+n_{\rm qp,th}\right)\right]
\end{aligned} \tag{2.210}$$

$$\begin{aligned}
\mathrm{NEP}^2_{\rm diss}(\nu) = \quad & \left(\frac{4V\Delta}{Q_i\chi_c\chi_y\alpha\tilde{\kappa}_1\tau_{\rm qp}^{\rm eff}\eta_{\rm ph}}\right)^2\frac{k_BT_{\rm sys}}{2P} \\
& + \left(\frac{4|S_{21}^{\rm res}|V\Delta}{Q_i\chi_c\chi_y\alpha\tilde{\kappa}_1\tau_{\rm qp}^{\rm eff}\eta_{\rm ph}}\right)^2\left[\cos^2(\phi-\theta_{\rm freq})S_{\delta A}(\nu)+\sin^2(\phi-\theta_{\rm freq})S_{\delta\phi}(\nu)-\sin\left(2(\phi-\theta_{\rm freq})\right)S_{\delta A,\delta\phi}(\nu)\right] \\
& + \left[\eta_{\rm opt}(1-f_{\rm spill})\Delta\nu_{\rm mm}k_BB_{\rm atm}\right]^2\ |w|^{b_{\rm atm}}\ \nu^{-b_{\rm atm}} \\
& + \frac{2P_{\rm opt}h\nu_{\rm mm}}{\eta_{\rm qe}}+\frac{2P_{\rm opt}^2}{\Delta\nu_{\rm mm}}+\frac{4V\Delta^2}{\eta_{\rm ph}^2}\left[R\left(\zeta n_{\rm qp}^2+n_{\rm qp,th}^2\right)+\frac{1}{\tau_{\rm max}}\left(n_{\rm qp}+n_{\rm qp,th}\right)\right]\ .
\end{aligned} \tag{2.211}$$

One thing to keep in mind is that these equations describe the raw NEP before any attempt at correlated noise removal. The noise removal results in a significant reduction in the contributions to the NEP from multiplicative electronics and atmospheric noise.

We will now discuss how to optimize MKID performance, which essentially corresponds to minimizing the NEP. It is helpful to simplify Equation (2.210) and Equation (2.211) by using several approximations that hold for MUSIC and are likely to hold reasonably well for other ground-based, photometric camera employing MKIDs. If one assumes that quasi-particle loss dominates, so that $Q_i^{-1} \gg Q_{i,0}^{-1}$, then the quality factor can be expressed in terms of the quasi-particle density using Equation (2.60). If we further assume that optically generated quasi-particles dominate, so that $n_{\rm qp} \gg n_{\rm qp,th}$, and that the quasi-particle lifetime is recombination limited, so that $\tau_{\rm qp} \ll \tau_{\rm max}$, then the quasi-particle density and quasi-particle lifetime have a simple relationship with optical power $P_{\rm opt}$. Under these assumptions Equation (2.210) and Equation (2.211)

become

$$\begin{aligned}
\mathrm{NEP}^2_{\mathrm{freq}}(\nu) = \quad & \left(\frac{8P_{\mathrm{opt}}}{\chi_c\chi_y}\frac{\tilde{\kappa}_1}{\tilde{\kappa}_2}\right)^2 \frac{k_B T_{\mathrm{sys}}}{2P} \\
& + \left(\frac{8|S_{21}^{\mathrm{res}}|P_{\mathrm{opt}}}{\chi_c\chi_y}\frac{\tilde{\kappa}_1}{\tilde{\kappa}_2}\right)^2 \left[\cos^2(\phi-\theta_{\mathrm{freq}})S_{\delta A}(\nu) + \sin^2(\phi-\theta_{\mathrm{freq}})S_{\delta\phi}(\nu) - \sin\left(2(\phi-\theta_{\mathrm{freq}})\right)S_{\delta A,\delta\phi}(\nu)\right] \\
& + \frac{P_{\mathrm{opt}}RV\Delta}{\eta_{\mathrm{ph}}}\left(\frac{4B_{\mathrm{TLS}}}{\left(1+8ay\chi_y^2\right)\alpha\tilde{\kappa}_2}\right)^2 \left(\frac{1}{2}Q_i\chi_y\chi_c P\right)^{-1/2} T_{\mathrm{bath}}^{-\beta}\ \nu^{-1/2} \\
& + \left[\eta_{\mathrm{opt}}(1-f_{\mathrm{spill}})\Delta\nu_{\mathrm{mm}}k_B B_{\mathrm{atm}}\right]^2\ |w|^{b_{\mathrm{atm}}}\ \nu^{-b_{\mathrm{atm}}} \\
& + 2P_{\mathrm{opt}}\left(\frac{h\nu_{\mathrm{mm}}}{\eta_{\mathrm{qe}}} + \frac{P_{\mathrm{opt}}}{\Delta\nu_{\mathrm{mm}}} + \frac{2\Delta}{\eta_{\mathrm{ph}}}\right), \qquad (2.212)
\end{aligned}$$

$$\begin{aligned}
\mathrm{NEP}^2_{\mathrm{diss}}(\nu) = \quad & \left(\frac{8P_{\mathrm{opt}}}{\chi_c\chi_y}\right)^2 \frac{k_B T_{\mathrm{sys}}}{2P} \\
& + \left(\frac{8|S_{21}^{\mathrm{res}}|P_{\mathrm{opt}}}{\chi_c\chi_y}\right)^2 \left[\cos^2(\phi-\theta_{\mathrm{freq}})S_{\delta A}(\nu) + \sin^2(\phi-\theta_{\mathrm{freq}})S_{\delta\phi}(\nu) - \sin\left(2(\phi-\theta_{\mathrm{freq}})\right)S_{\delta A,\delta\phi}(\nu)\right] \\
& + \left[\eta_{\mathrm{opt}}(1-f_{\mathrm{spill}})\Delta\nu_{\mathrm{mm}}k_B B_{\mathrm{atm}}\right]^2\ |w|^{b_{\mathrm{atm}}}\ \nu^{-b_{\mathrm{atm}}} \\
& + 2P_{\mathrm{opt}}\left(\frac{h\nu_{\mathrm{mm}}}{\eta_{\mathrm{qe}}} + \frac{P_{\mathrm{opt}}}{\Delta\nu_{\mathrm{mm}}} + \frac{2\Delta}{\eta_{\mathrm{ph}}}\right). \qquad (2.213)
\end{aligned}$$

It is evident from these equations that the NEP is highly dependent on the background loading. As we discussed in Section 2.3.2.1, the NEP for recombination noise and shot photon noise scale as $P_{\mathrm{opt}}^{1/2}$, and the NEP for Bose photon noise scales as P_{opt}. In addition, the contributions from the electronics noise and TLS noise scale as P_{opt} and $P_{\mathrm{opt}}^{1/2}$, respectively. These dependencies arise because increasing the optical power degrades detector responsivity by decreasing both the quality factor and the quasi-particle lifetime. It is therefore crucial to minimize background loading. This is accomplished by eliminating the nonantenna response, reducing the spill-over to the interior of the cryostat (lowering $T_{\mathrm{exc,ant}}$), reducing the spillover to ambient temperature surfaces (lowering $f_{\mathrm{spill,ant}}$), and observing in good weather conditions (lowering $\left[1-e^{-\tau_{\mathrm{ant}}/\sin\mathfrak{e}}\right]$).

Increasing the carrier power on the feedline at the device is a straightforward way to reduce the NEP from the additive electronics noise, which scales as $P^{-1/2}$, and from TLS noise, which scales as $P^{-1/4}$. Designing the coupling to the feedline so that Q_c is well matched to Q_i under the expected loading conditions ensures the $\chi_c \approx 1$ and reduces the contributions from the electronics NEP via the χ_c^{-1} scaling. Centering the carrier tone directly on the resonant frequency reduces the contribution from the electronics NEP via the χ_y^{-1} scaling. That said, both χ_c and χ_y are fairly mild functions of their respective arguments, as depicted in Figure 2.7.

There are two major differences between the NEP in the frequency and dissipation direction. First, the frequency direction suffers from TLS noise, while the dissipation direction does not. Second, the additive

and multiplicative electronics NEPs in the frequency direction are reduced by a factor of $\tilde{\kappa}_2/\tilde{\kappa}_1$. This ratio is plotted in Figure 2.9 as a function of temperature and the nonlinearity parameter a. At our operating temperature of 240 mK and at low power, this results in a factor of $\simeq 4$ reduction. The improvement is less significant as one pushes to higher readout powers and thus higher values of the nonlinearity parameter. The choice of readout power is then an optimization problem. We must balance the reduction of additive and multiplicative electronics noise (in the frequency direction) through the $\tilde{\kappa}_2/\tilde{\kappa}_1$ responsivity factor with the reduction of additive electronics and TLS noise through their respective $P^{-1/2}$ and $P^{-1/4}$ dependencies. We have found that, so long as one is able to remove the multiplicative electronics noise reasonably well using off-resonance carriers, it is best to operate at as high a readout power as possible. We operate the MUSIC resonators just below the onset of bifurcation. One interesting idea is to operate the resonators well past bifurcation so that the response in the frequency directions switches signs and $\tilde{\kappa}_2/\tilde{\kappa}_1$ begins to increase. Swenson et al. [108] demonstrated this successfully with a single Titanium Nitride (TiN) resonator and saw a factor of ~ 10 improvement in NEP. This is not possible with the current version of the MUSIC readout electronics, and would require significant redesign to increase the maximum power that they are able to deliver and modified firmware to enable careful placement of the carrier tones. Note that past a certain carrier power the nonlinear kinetic inductance model outlined in Section 2.2.6 will no longer provide a complete description of the effects of readout power on the device, as heating of the quasi-particle population by the microwave power will eventually introduce a dissipative response.

The ratio $\tilde{\kappa}_2/\tilde{\kappa}_1$ increases linearly with T/T_c. In addition, the TLS noise shows a fairly dramatic reduction with temperature, with the NEP scaling as $T_{\rm bath}^{-\beta/2}$ with $\beta = 1.2-2.0$. Thus, operating at higher temperatures offers possible improvements in frequency direction sensitivity. This, however, has other ramifications that must be carefully considered, and is beyond the scope of our discussion.

Increasing either α or $\tilde{\kappa}_2$ improves the frequency response of the resonator to changes in quasi-particles density, which directly translates to a reduction in the TLS NEP. There has been a recent push to use high-resistivity superconductors such as TiN for their high kinetic inductance fractions [146, 147, 148, 149, 150]. An increase in $\tilde{\kappa}_2$ can be achieved by decreasing the resonator frequency. This has the additional benefit of increasing the ratio $\tilde{\kappa}_2/\tilde{\kappa}_1$, which scales as approximately ω^{-1} at low frequencies. There are several instruments currently being developed that use kinetic inductance detectors at ~ 100 MHz as opposed to ~ 1 GHz for primarily this reason [151, 152, 153]. The lower limit on the resonator frequency is effectively set by the resonator bandwidth $\Delta f_{\rm res} = \frac{f_{\rm res}}{2Q}$, because at a certain point the resonator will begin to filter out signal. The exact frequency at which this occurs depends on the the quality factor of the resonator, the spatial extent of the signal, and the scan speed of the telescope.

The atmospheric noise enters into the expression for NEP in an almost identical way as astronomical signal. The best way to reduce atmospheric noise is to place the telescope in a location with a dry and stable atmosphere. It can also be avoided by modulating the signal of interest (e.g., scanning the telescope faster, chopping on and off source). The approach that we take, as discussed in Section 2.3.2.3, is to (partially)

remove it in software using the fact that it is correlated between detectors.

Finally, it is useful to examine the noise equivalent flux density

$$\begin{aligned} \mathrm{NEFD}_{\mathrm{freq\ (diss)}} &= \left(\frac{\partial S}{\partial P_{\mathrm{opt,ant}}} \right) \mathrm{NEP}_{\mathrm{freq\ (diss)}} \\ &= \frac{2\ \mathrm{NEP}_{\mathrm{freq\ (diss)}}}{A_{\mathrm{eff}}\ \Delta\nu_{\mathrm{mm,ant}}\ \eta_{\mathrm{opt,ant}}(1-f_{\mathrm{spill,ant}})\ e^{-\tau_{\mathrm{ant}}/\sin\mathfrak{e}}} \end{aligned} \tag{2.214}$$

and the noise equivalent temperature

$$\begin{aligned} \mathrm{NET}_{\mathrm{freq\ (diss)}} &= \frac{A_{\mathrm{eff}}}{2k_B}\ \mathrm{NEFD}_{\mathrm{freq\ (diss)}} \\ &= \frac{\mathrm{NEP}_{\mathrm{freq\ (diss)}}}{k_B\ \Delta\nu_{\mathrm{mm,ant}}\ \eta_{\mathrm{opt,ant}}(1-f_{\mathrm{spill,ant}})\ e^{-\tau_{\mathrm{ant}}/\sin\mathfrak{e}}} \end{aligned} \tag{2.215}$$

Note that these definitions assume single-polarization NEP/NET and dual-polarization NEFD. Whereas the NEP is a measure of detector performance, the NET and NEFD are measures of instrument and instrument plus telescope performance, respectively. For a given NEP, detector bandwidth, and telescope area, minimizing the NET/NEFD corresponds to maximizing the optical efficiency, reducing the amount of spill-over, and observing in good weather conditions.

Chapter 3

Calibration of the Full Instrument Model

3.1 Overview

In the previous chapter we presented a theoretical framework that describes the behavior of the MUSIC detectors. We introduced a number of parameters, many of which need to be measured in order to make meaningful predictions. In this chapter we discuss the series of measurements used to calibrate the full instrument model.

The primary measurement at our disposal is an "IQ sweep", or a measurement of the complex transmission through the system as a function of microwave frequency near a resonance. The IQ sweep is fit to extract the resonant frequency $f_{\rm res}$ and internal quality factor Q_i. By simply measuring $f_{\rm res}$ and Q_i at different bath temperatures and under different loading conditions, we can constrain many of the model parameters. We first measure these two quantities as a function of temperature in a dark scenario in order to calibrate the frequency and dissipation response to changes in quasi-particle density. We then measure them as as a function of temperature in an optical scenario, with first a room temperature and then a liquid nitrogen beam filling, black-body load in front of the cryostat window. This constrains the loading from inside the cryostat and the optical efficiency between the detectors and the cryostat window. Finally, we mount the cryostat on the telescope and examine $f_{\rm res}$ and Q_i as a function of the angle of elevation of the telescope pointing in order to determine how well the detectors are coupled to the sky. We also use Fourier Transform Spectroscopy (FTS) to measure the spectral response of the detectors.

We employ a variety of techniques to isolate each source of noise presented in Section 2.3. Additive and multiplicative electronics noise are measured directly with off-resonance carriers. TLS noise is calibrated in a dark scenario by examining the on-resonance noise power spectral density as a function of carrier power. Atmospheric noise is inferred from its unique spectral scaling and the fact that it is correlated between detectors. Finally, fundamental noise is estimated from the full instrument model predictions for optical loading and steady-state quasi-particle density, as well as the FTS measurements of the band center and band width.

3.2 Responsivity

3.2.1 IQ Sweeps

We collect IQ sweeps with the MUSIC readout electronics rather than a traditional vector network analyzer (VNA). This enables all resonances to be measured simultaneously [154, 102]. A pre-programmed buffer is output from the DACs that consists of a superposition of baseband frequency carrier tones that when up-mixed with the local oscillator (LO) will be centered on each of the resonances. The LO frequency is then stepped over some range around the nominal value. At each step a short, 0.5 sec long timestream is collected at the ADCs. The mean values of the timestreams are used as an estimate of the complex carrier amplitude at that frequency. Equations (2.61) and (2.100) suggest that an appropriate model for this quantity is

$$\hat{V}(f) = (u + jv)\, e^{-2j\pi f \tau_{\mathrm{RF}}} \left(1 - \frac{1}{1 + 2jQ\frac{f - f_{\mathrm{res}}}{f_{\mathrm{res}}}} \frac{Q}{Q_c \cos\phi_c} e^{j\phi_c} \right) , \tag{3.1}$$

where $u + jv$ acts as an overall complex normalization, τ_{RF} is the cable delay of the RF electronics, and $f_{\mathrm{res}} \equiv f_{\mathrm{res}}(f,\, f_{\mathrm{res},0},\, a)$ is the power-shifted resonant frequency, which is obtained by taking the appropriate root of Equation (2.89) depending on whether one is sweeping upward or downward in frequency. Note that the normalization $u + jv$ is dependent on the baseband frequency of the carrier tone.

Petersan and Anlage [155] performed a quantitative comparison of several popular methods for constraining the resonant frequency and internal quality factor from measurements of $S_{21}^{\mathrm{res}}(f)$. They found that a nonlinear least-squares fit to the squared magnitude of the forward transmission as a function of frequency yielded the most accurate and precise values for low signal-to-noise measurements. This agrees with our qualitative experience that fitting the squared magnitude $|\hat{V}(f)|^2$ yields more robust results than fitting either the complex data $\hat{V}(f)$ or the phase $\theta(f) = \arg\left(\hat{V}(f)\right)$. Therefore, all calibration data is fit to the model

$$|\hat{V}(f)|^2 = (A + Bf) \left| 1 - \frac{d e^{j\phi_c}}{1 + 2jQ\frac{f - f_{\mathrm{res}}}{f_{\mathrm{res}}}} \right|^2 , \tag{3.2}$$

where $d = Q/(Q_c \cos\phi_c)$ is the diameter of the resonance circle and the $(A + Bf)$ factor allows for a linear trend in the background transmission. This model has a total of seven parameters:

$$\boldsymbol{\theta}_{\mathrm{IQ}} = [f_{\mathrm{res},0},\, Q,\, d,\, \phi_c,\, a,\, A,\, B] \ . \tag{3.3}$$

The fit is performed in IDL with the MPFIT routine, which performs Levenberg-Marquardt minimization of the χ^2 function. In order to estimate the uncertainty on the best-fit model parameters, we require estimates of the error on our measurement of $|\hat{V}(f)|^2$. We assume the same error for all data points in the sweep and estimate it using the two-sample variance of the residuals from the fit. The two-sample variance is calculated

using the first and last 20% of the sweep, where the effect of the resonance on the transmission is small. The best-fit values of d, Q, and ϕ_c are then used to determine the real component of the coupling quality factor Q_c and the internal quality factor Q_i, with uncertainties propagated appropriately.

For calibration data (i.e., all measurements discussed in Section 3.2), we perform the IQ sweeps using very low carrier power, operating in a regime where the carrier power has no effect on the shape of the resonance curve. This typically corresponds to between -105 and -110 dBm at the device. We fix the nonlinearity parameter $a = 0$ for the fit, which reduces the number of free parameters to six. All calibration data is collected with an LO step size of 7.5 kHz.

When possible (usually once per dataset) a sweep is collected at approximately 1.2 K — just above the critical temperature of aluminum — to characterize the background transmission. The squared magnitude of the IQ sweeps are divided by the squared magnitude of the background sweep to isolate $|S_{21}^{res}|^2$ prior to performing the fit.

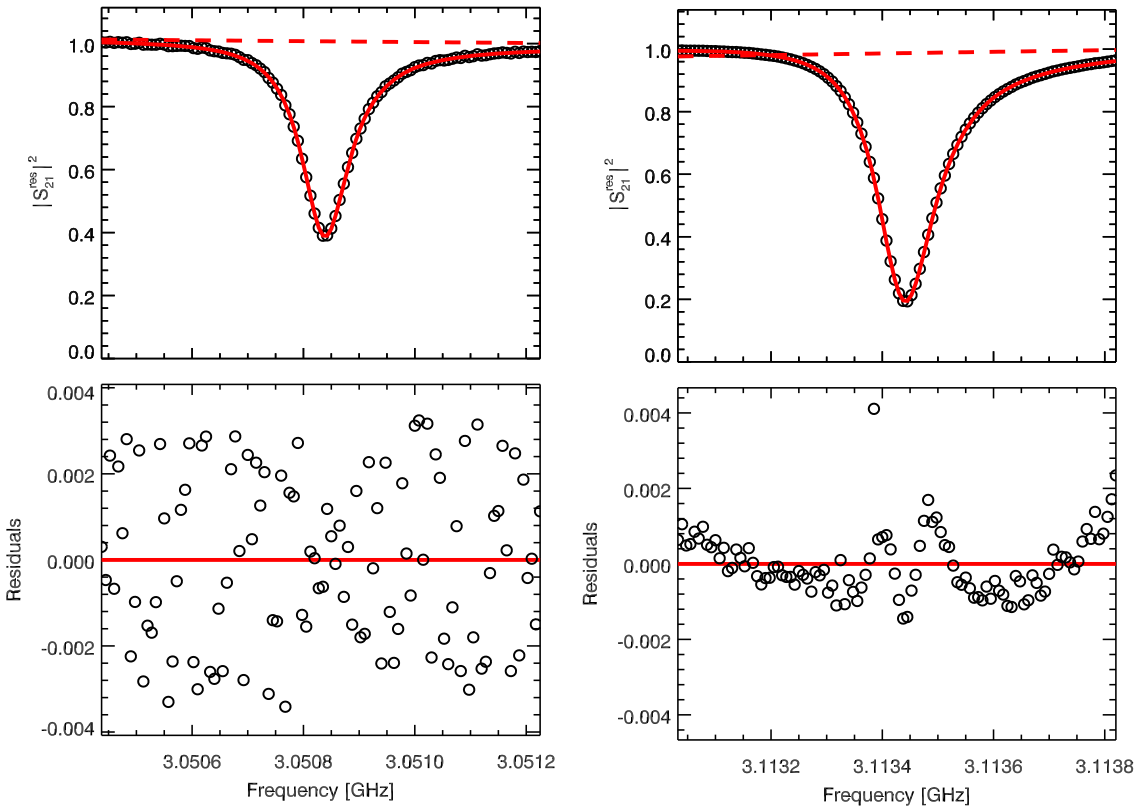

Figure 3.1: Example IQ sweep data. The left and right columns correspond to two different resonators. In the top panel, the black circles denote the measured data points, the solid red line denotes the best-fit model to Equation (3.2), and the dashed red line denotes the background component $(A + Bf)$ of the best-fit model. The data points have a frequency spacing of 7.5 kHz. In the bottom panel, the black circles denote the residuals calculated as (data - model).

We show two examples of a typical fit to an IQ sweep in Figure 3.1. In most cases the quality of fit is excellent, with a reduced χ^2 approximately equal to 1 and the residuals randomly distributed about zero, as illustrated in the left column. We occasionally see fits similar to that shown in the right column, where the quality of fit looks good based on a plot of the model overlaid on the data; however, systematic trends with frequency emerge at the sub-percent level and can be seen in the residuals. The general behavior of these "bad" fits is usually the same, with the residuals displaying a divot near the resonant frequency. We flag egregious cases by determining outliers based on the distribution of χ^2 values for all resonators on a given device half-band. Flagged data points are removed from the analysis. The less egregious cases are dealt with by multiplying all of the parameter uncertainty estimates by $\sqrt{\chi^2}$, effectively assuming that the model provides a good fit and using that to determine errors. It is possible that these small deviations from the model are artifacts of nonidealities in the IQ mixer. Typically a calibrated vector network analyzer is used to perform this type of measurements; unfortunately, this is not tractable for the large number of resonators employed in MUSIC. It is possible to measure and correct for nonidealities in the IQ mixer [93], which would be one way to improve the quality of these measurements in the future.

3.2.2 Dark Temperature Sweeps

The first calibration measurement consists of collecting IQ sweeps at 12-15 temperatures between 230 mK (base) and 455 mK with the detectors dark. In order to ensure negligible optical loading during this measurement an aluminum cover is placed over both the focal plane and the cryostat window. The temperature of the detectors are monitored with a Lakeshore Germanium Resistance Thermometer (GRT) attached to the copper focal plane unit. A 10 kΩ heater — also attached to the focal plane unit and controlled by an SRS SIM 960 Analog PID controller — is used to maintain the temperature at the desired value for data points above base.

The dark temperature sweep data for a single detector is shown in the upper panels of Figure 3.2. We fit the IQ sweeps using the procedure outlined in the previous section. From these fits we extract the frequency $f_{\rm res}(T)$ and inverse quality factor $Q_i^{-1}(T)$ of the resonance as a function of temperature. Since the optical loading is negligible, these trajectories are completely determined by changes in the surface impedance of the Al absorptive section due to changes in the population of thermally generated quasi-particles. The explicit relationships are given by Equations (2.59), (2.60), (2.43), (2.44), and (2.37). We fit the frequency and quality factor trajectories separately using a Markov Chain Monte Carlo (MCMC) algorithm, which is described in detail in Appendix A. The free parameters of the fit are

$$\boldsymbol{\theta}_{\rm dark,\,f} \;=\; \left[\Delta_{0,f},\; \alpha_f,\; f_0\right] \qquad\qquad \boldsymbol{\theta}_{\rm dark,\,Q} \;=\; \left[\Delta_{0,Q},\; \alpha_Q,\; 1/Q_{i,0}\right] \;.$$

The best-fit parameters and uncertainties are estimated as the mean and covariance of the joint posterior distribution sampled by the MCMC. The parameters α and Δ_0 are highly degenerate, so the uncertainty estimates have a significant, positive off-diagonal term. In theory, there is a single gap energy Δ_0 and kinetic

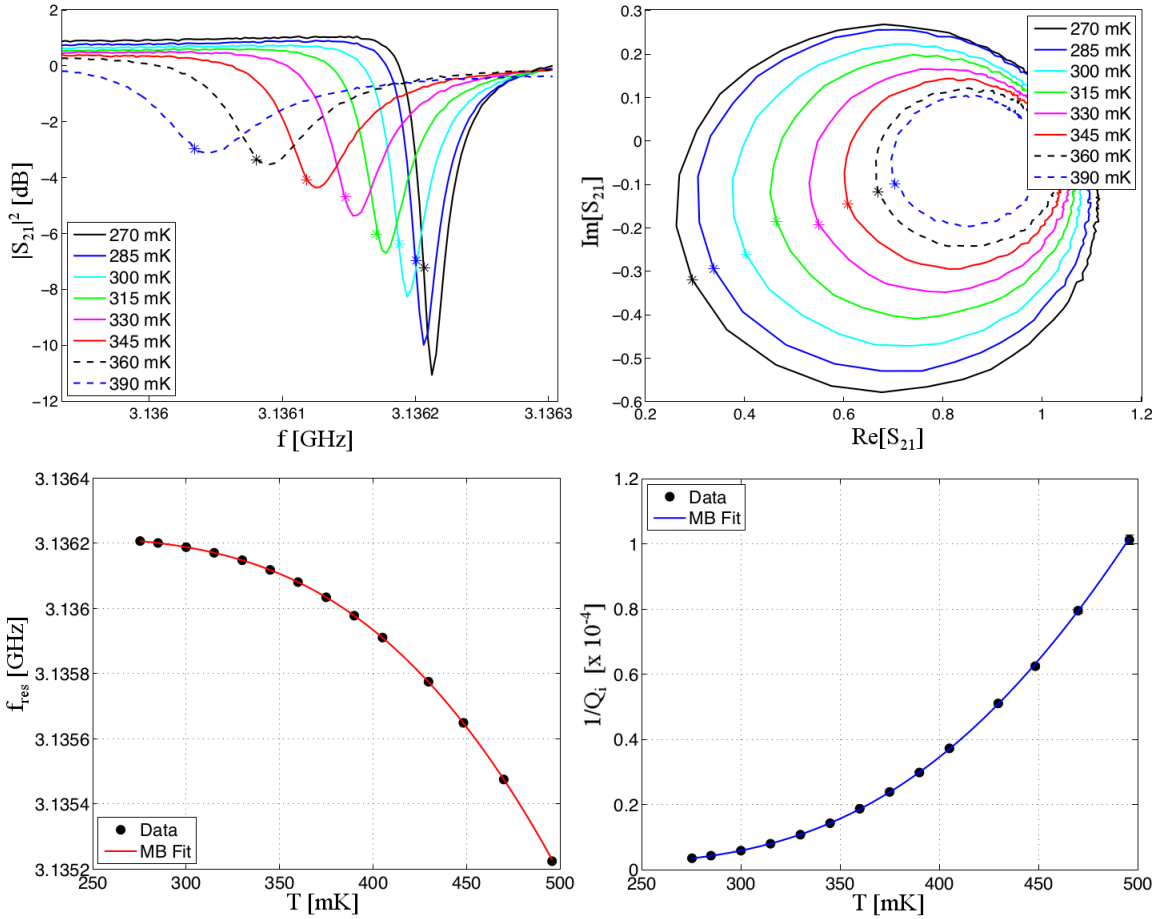

Figure 3.2: Example of a dark temperature sweep. IQ sweeps are collected at several temperatures, shown as different colors in the top row of plots. The top left panel displays the squared magnitude of the transmission near resonance and the the top right panel displays the transmission near resonance in the complex plane. As the temperature is increased, the resonator shifts to lower frequencies and the internal quality factor degrades, which results in a broadening and shallowing of the Lorentzian line shape and a shrinking in the diameter of the resonance circle. Each IQ sweep is fit to Equation (3.2) to extract $f_{\rm res}(T)$ and $Q_i^{-1}(T)$, which are shown as black circles in the bottom left panel and bottom right panel, respectively. The error bars on the measurements are less than the size of the symbols. The temperature trajectories are fit separately using the first order approximations for the Mattis-Bardeen integrals. The best-fit models are denoted by the red and blue lines.

inductance fraction α that appear in the equations for both the frequency and dissipation of the resonator. However, we have found empirically that the overall normalization of the dark trajectories differ by some factor not explained by our model (see Figure 3.3). The magnitude of the discrepancy is $\alpha_Q/\alpha_f \simeq 1.3$ and $\Delta_{0,Q}/\Delta_{0,f} \simeq 1.03$ when one assumes the first order approximation. There is better agreement if the model is calculated using the full integrals given in Equations (2.26) and (2.27), with $\alpha_Q/\alpha_f \simeq 1.075$. A possible explanation is that our detectors fall into a regime where the relation between the surface impedance of the superconductor and the quasiparticle density is more complicated than the theory described in Section 2.2.4.

In any case, the thermal response of the resonator is completely characterized by $\theta_{\rm dark,\,f}$ and $\theta_{\rm dark,\,Q}$. The

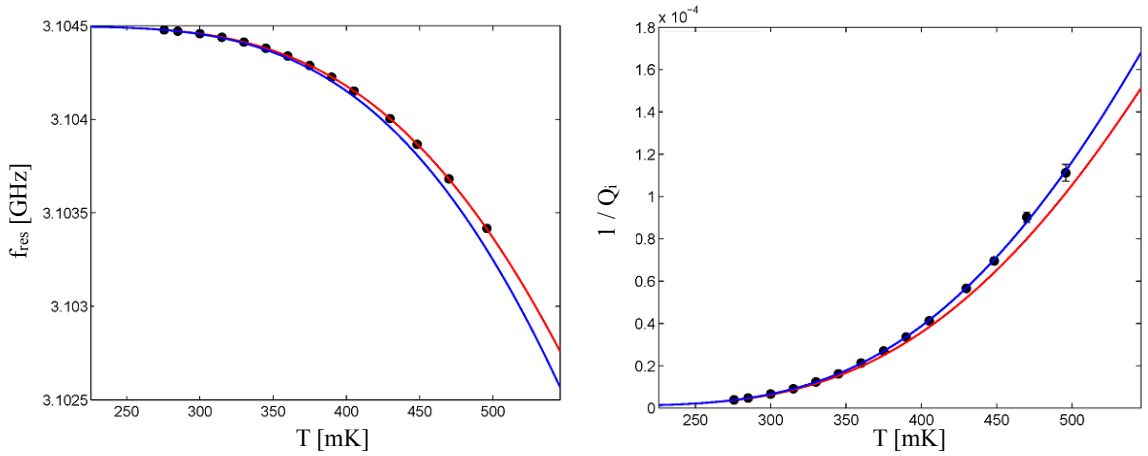

Figure 3.3: Example dark temperature sweep data and best-fit model. The black circles denote the measured frequency (left) and dissipation (right) as a function of temperature. The red line denotes the model prediction based on the fit to the frequency data. The blue line denotes the model prediction based on the fit to the dissipation data. The full Mattis-Bardeen integrals were used to make the model prediction. The discrepancy between frequency and dissipation is larger if the first order approximation is used.

purpose of the dark data set is to determine the best-fit values of these parameters for each resonance so that the thermal response can be accounted for appropriately when fitting the hot/cold data. In addition, due to the assumed equivalence of thermally and optically generated quasi-particles, $\theta_{\text{dark, f}}$ and $\theta_{\text{dark, Q}}$ calibrate the conversion between changes in quasi-particle density and changes in the frequency and dissipation of the resonator.

3.2.3 Hot/Cold

The second calibration measurement is similar to the first in that we collect IQ sweeps at 12-15 temperatures between base and 455 mK. However, for this measurement the aluminum covers are removed and we alternate between an ambient temperature (hot) and liquid nitrogen temperature (cold) beam-filling, blackbody load in front of the cryostat window. We use large pieces of Eccosorb® for the loads; a microwave absorbing material that has an approximately blackbody spectrum at sub/millimeter wavelengths [156, 157]. The Eccosorb® is fully submerged in a styrofoam container of LN_2 for the cold measurement.

The transparent portion of the MUSIC window is 300 mm in diameter. We use an $\sim$ 1 m square piece of Eccosorb® placed 300 mm from the window. This requires a large LN_2 bath that must be refilled often due to evaporation from the significant exposed surface area. The IQ sweep takes approximately 15 minutes to complete. We refill the bath before the start of the measurement and then top it off every 5 minutes.

Another difficulty in the LN_2 measurement is the formation of condensation on the cryostat window. Even a thin layer of condensation has high opacity at sub/millimeter wavelengths, which will result in an underestimation of the effective load temperature. In order to prevent condensation, we employ a nitrogen purge window, pictured in Figure 3.4. The purge window consists of a plexiglass ring that is mounted to

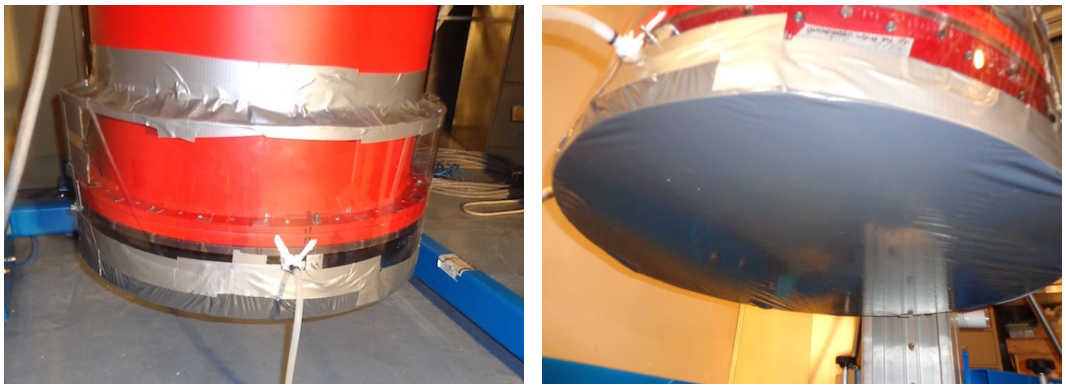

Figure 3.4: N_2 purge window mounted on the bottom of the MUSIC cryostat.

the lip of the cryostat and extends 4 inches past the cryostat window. Low-density polyethylene (LDPE) is stretched over the plexiglass ring forming a thin, air-tight membrane. N_2 gas is pumped into a $1/8$ inch diameter hole in the plexiglass ring and is vented from an exhaust hole of the same diameter on the opposite side. The pressure of the tank supplying the N_2 is increased until the membrane becomes slightly inflated. The purge window ensures that the region between the membrane and the cryostat window is void of water vapor. However, water vapor can still condense on the outside of the membrane. We use fans to limit conductive cooling by improving air flow in the region between the LN_2bath and the membrane. Even with these precautions, condensation still forms on the membrane when the humidity is high. We find that we are only able to collect hot/cold data when the relative humidity is $\lesssim 30\%$. We are also careful to check that the membrane is dry after each LN_2measurement.

We control and monitor the array temperature in the same way as the dark measurement. All of the hot/cold results presented in this work were collected on the third floor of the CSO. The CSO measures the temperature, humidity, and pressure using a thermometer and hygrometer mounted inside the dome. These values are updated every 5 minutes. We use the average value of the temperature as our estimate of $T_{\rm amb}$ for the hot measurements. We calculate the temperature of the liquid nitrogen load as

$$T_{\rm LN2} = 77.25\ {\rm K} - 0.00825\ \frac{\rm mb}{\rm K} \times (1013.25\ {\rm mb} - P_{\rm atm})\ , \tag{3.4}$$

where $T_{\rm LN2}$ has units of K and $P_{\rm atm}$ is the atmospheric pressure in units of millibar. The atmospheric pressure at the summit of Mauna Kea is $P_{\rm atm} \approx 625$ mb and so $T_{\rm LN2} \approx 74$ K.

Let $f_{\rm res}(T_{\rm bath},\ T_{\rm load})$ and $Q_i^{-1}(T_{\rm bath},\ T_{\rm load})$ denote the frequency and dissipation extracted from the IQ sweep collected at temperature $T_{\rm bath}$ with a load of temperature $T_{\rm load}$ at the cryostat window. The model prediction for these quantities is given by Equations (2.59), (2.60), (2.43), (2.44), (2.21), (2.37), and (2.7). The purpose of the hot/cold data set is to determine the efficiency $\eta = \eta_{\rm ph}\eta_{\rm opt}$ and excess loading. The basic idea is illustrated in Figure 3.5. The dark calibration can be used to convert either the measured frequency shift or the measured dissipation into a quasi-particle density. The difference between the quasi-particle density under the hot and

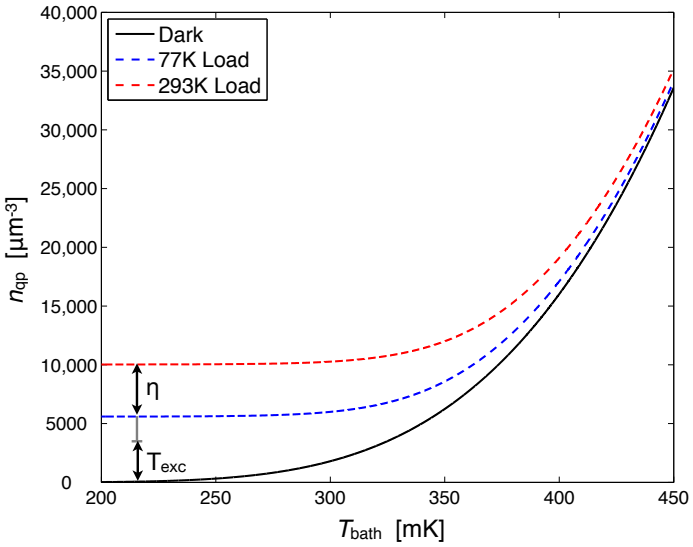

Figure 3.5: Idea behind the hot/cold measurement. All curves shown are theoretical predictions based on typical MUSIC detector parameters. The black line denotes the thermal quasi-particle density or the quasi-particle density in the absence of optical loading. The blue and red dashed line denote the quasi-particle density with a 77 K and 293 K temperature beam-filling, blackbody load in front of the cryostat window.

cold load places a constraint on the optical efficiency. One can then extrapolate to $T_{\rm load} = 0$ K at the cryostat window to infer the excess loading due to beam terminating on the interior of the cryostat.

There are several complications to this simple picture. First of all, examining Equations (2.21) and (2.7) it is clear that the sensitivity of the hot/cold data to η is completely degenerate with a number of parameters: the gap energy Δ, the single spin density of states N_0, the recombination coefficient R, the volume of the aluminum section V, and the bandwidth of the detector $\Delta\nu_{\rm mm}$. In order to extract the efficiency, we must supplement the hot/cold data with independent measurements of these degenerate parameters. We determine the gap energy from the dark data set as discussed in the previous section. We assume literature values for the single-spin density of states and rely on a combination of theoretical predictions and measurements in order to determine the recombination coefficient; we will discuss this further in Section 3.2.3.1 and Section 3.2.3.2. We measure the bandwidth individually for each resonator via Fourier transform spectroscopy, which will be discussed in Section 3.2.4. Finally, we express the volume as $V = Ad$ with area $A = 6\ \mu\text{m} \times 350\ \mu\text{m} = 2100\ \mu\text{m}^2$ and thickness d. While the area of the thin film is known, there is some uncertainty in the thickness: 60 nm of Al is deposited; however, an unknown amount is unintentionally etched away during processing. In all analysis that follows we will assume that 15 nm is etched away so that $d \equiv 45$ nm and then add a systematic error to our efficiency estimate that corresponds to the thickness varying between 30 and 60 nm.

For the analysis of the hot/cold data set, it is useful to lump several of the degenerate parameters into a single parameter

$$C \equiv \frac{\eta_{\rm opt}\eta_{\rm ph}\Delta\nu_{\rm mm}}{d}\ , \tag{3.5}$$

which has units of GHz nm^{-1}. The equation for the frequency and dissipation are then given by

$$f_{\rm res}(T_{\rm bath},\ T_{\rm load}) = f_{\rm res,0} - \frac{1}{2} f_{\rm res,0}\alpha_f \kappa_2\left(T,\omega,\Delta_{0,f}\right)\left\{\left[\frac{Ck_B\left(T_{\rm load}+T_{\rm exc}\right)}{RA\Delta} + \frac{1}{R\tau_{\rm max}}\left(n_{\rm qp,th}\left(T,\Delta_{0,f}\right)+\frac{1}{4R\tau_{\rm max}}\right)\right]^{1/2} - \frac{1}{2R\tau_{\rm max}}\right\} \quad (3.6)$$

$$Q_i^{-1}(T_{\rm bath},\ T_{\rm load}) = \frac{1}{Q_{i,0}} + \alpha_Q \kappa_1(T,\omega,\Delta_{0,Q})\left\{\left[\frac{Ck_B\left(T_{\rm load}+T_{\rm exc}\right)}{RA\Delta} + \frac{1}{R\tau_{\rm max}}\left(n_{\rm qp,th}(T,\Delta_{0,Q})+\frac{1}{4R\tau_{\rm max}}\right)\right]^{1/2} - \frac{1}{2R\tau_{\rm max}}\right\}, \quad (3.7)$$

where the temperature T is related to the bath temperature $T_{\rm bath}$ by Equation (2.111), which accounts for quasi-particle heating. The thermal quasi-particle density is given by Equation (2.37).

We construct the following quantities:

$$\Delta f_{\rm res}(T) = f_{\rm res}(T_{\rm bath},\ T_{\rm amb}) - f_{\rm res}(T_{\rm bath},\ T_{\rm LN2}) \quad (3.8)$$

$$T_{\rm exc}^{\rm\ naive}(T) = \frac{T_{\rm amb}\ Q_i^{-2}(T_{\rm bath},\ T_{\rm LN2}) - T_{\rm LN2}\ Q_i^{-2}(T_{\rm bath},\ T_{\rm amb})}{Q_i^{-2}(T_{\rm bath},\ T_{\rm amb}) - Q_i^{-2}(T_{\rm bath},\ T_{\rm LN2})}\ , \quad (3.9)$$

which we refer to as the frequency shift and naive excess load. We simultaneously fit these two quantities to the model given by Equations (3.6) and (3.7). There are several reasons why we choose to fit the frequency shift and naive excess load rather than fit $f_{\rm res}(T,T_{\rm load})$ and $Q_i^{-1}(T,T_{\rm load})$ directly. Fitting the frequency shift removes the primary dependence on $f_{\rm res,0}$, which can change between the dark and optical cool down due to flux trapping in the niobium. As was mentioned in Section 3.2.2, there is disagreement in the normalization of the dark frequency and dissipation trajectories. The naive excess load is a ratio of resonator quality factors at the same temperature, and therefore the exact conversion between δQ_i^{-1} and $n_{\rm qp}$ drops out. In the optical quasi-particle dominated, recombination limited regime, the naive excess load is equal to $T_{\rm exc}$. Effectively, we use the quality factor data to constrain the excess loading and the frequency shift data to constrain optical efficiency.

The free parameters of the fit are

$$\boldsymbol{\theta}_{\rm hot/cold} \ = \ \left[C,\ T_{\rm exc},\ \tau_{\rm max},\ n,\ \eta_{\rm e},\ Q_{i,0}^{-1},\ \Delta_{0,f},\ \alpha_f,\ \Delta_{0,Q},\alpha_Q\right]\ . \quad (3.10)$$

The gap energies and kinetic inductance fractions are well constrained by the dark data set. We have implemented a Markov Chain Monte Carlo (MCMC) that uses the Metropolis-Hastings Algorithm and simulated annealing to efficiently explore the multi-dimensional parameter space and search for global minimum of the likelihood function (see Appendix A). This enables us to include the results of the dark data set properly as a

prior on $[\Delta_{0,f},\ \alpha_f]$ and $[\Delta_{0,Q},\ \alpha_Q]$, taking into account the large off-diagonal elements in the uncertainty on each pair of parameters. It also enables us to include uncertainties in bath temperature and loading conditions.

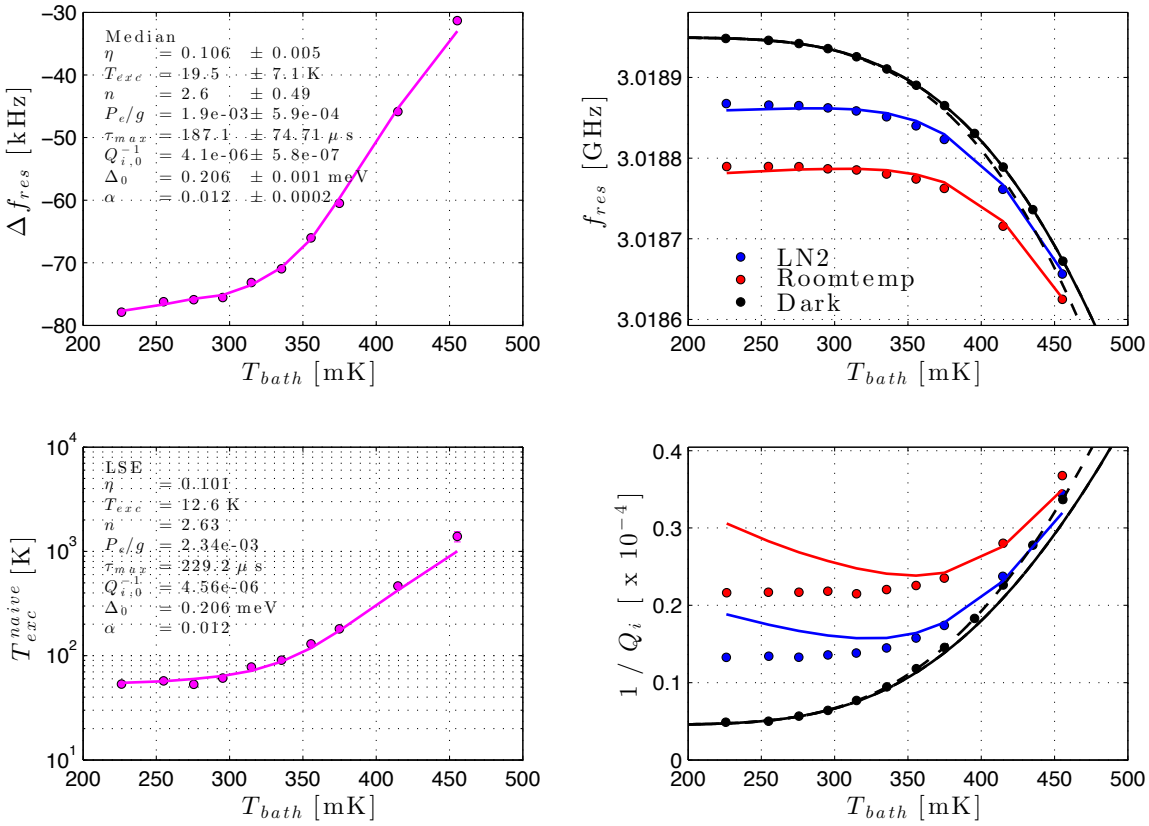

Figure 3.6: Example hot/cold data and best-fit model. *Left:* The frequency shift (top panel) and naive excess load (bottom panel) as a function of bath temperature. Data are denoted with circles and best-fit model predictions are denoted with solid lines. The best-fit parameter values are annotated in the upper left corner of the bottom panel. The (median) ± (median absolute deviation) of the marginalized posterior distributions are annotated in the upper left corner of the top panel. *Right:* The raw measurements of the resonant frequency (top panel) and internal quality factor (bottom panel) as a function of bath temperature under the hot (red) and cold (blue) loads. Shown in black are the dark temperature sweep measurements collected for this resonator during a previous cooldown. The solid black line is calculated using $[\Delta_{0,f},\ \alpha_f]$ and the dashed black line is calculated using $[\Delta_{0,Q},\ \alpha_Q]$.

Figure 3.6 shows example hot/cold data for a Band 1 resonator. It is important to note that, while the quality of fit to the frequency shift and naive excess load is excellent, as demonstrated in the panels on the left, the best-fit model predictions for the resonant frequency and internal quality factor are poor, as evidenced by the panels on the right. In general, the best-fit model reproduces the measured $f_{\rm res}(T_{\rm bath},\ T_{\rm load})$ better than the measured $Q_i^{-1}(T_{\rm bath},\ T_{\rm load})$. We have tried to fit the frequency and internal quality factor data directly, but find that our model cannot describe them both simultaneously. This is because the fractional change in κ_1 with temperature is larger than κ_2. Since the measured frequency and internal quality factor temperature trajectories are both constant at low temperature, this means that the internal quality factor data requires greater quasi-particle heating and a higher effective quasi-particle temperature than the frequency data (see

Section 2.2.9).

After fitting the hot/cold data for all detectors on a given device half-band, we examine a plot of the best-fit value of C as a function of resonant frequency. The observing band of each detector is extracted from this plot. This is possible because detectors of the same band are grouped together in resonant frequency and because the differences in C between bands are larger than the intrinsic scatter between detectors of the same band. Identifying the bands in this way is necessary because not all of the detectors have FTS data available, and even if they did, resonant frequencies shift between cooldowns due to flux trapping in the Nb and it is not always possible to retrieve the FTS data for a particular resonator.

Since the dark resonators exhibit much lower values of C than the antenna-coupled resonators, a simple cut on C is used to identify the dark resonators. We estimate $C_{\rm dir}$ and $T_{\rm exc,dir}$ as the mean value of C and $T_{\rm exc}$ over all dark resonators on a given device half-band. We then correct the values of C and $T_{\rm exc}$ for the antenna-coupled resonators on that device half-band using the following equations:

$$C_{\rm ant} = C - C_{\rm dir} \tag{3.11}$$

$$T_{\rm exc,ant} = \frac{C T_{\rm exc} - C_{\rm dir} T_{\rm exc,dir}}{C_{\rm ant}} \ . \tag{3.12}$$

In this way the dark resonators are used to measure and account for the effects of direct absorption.

3.2.3.1 Single-Spin Density of Electron States at the Fermi Energy Level

The value of N_0 for aluminum is reported in the literature as 1.2×10^{10} μm^{-3} eV^{-1} [158] and 1.72×10^{10} μm^{-3} eV^{-1} [103, 93, 159]. Throughout this thesis we assume $N_0 = 1.72 \times 10^{10}$ μm^{-3} eV^{-1}.

3.2.3.2 Recombination Coefficient

The recombination coefficient is given by the equation [160]

$$R = \frac{(2\Delta)^2}{2\left(k_B T_c\right)^3 N_0 \tau_0} \ , \tag{3.13}$$

where τ_0 is the material dependent timescale for the electron-phonon interaction. Kaplan et al. [160] perform a theoretical calculation to obtain $\tau_0 = 438$ ns for aluminum. If we assume that $\Delta_0 \approx 1.76 k_B T_c$ and use the average value $\Delta_0 = 0.205$ meV observed in our detectors, then this corresponds to a recombination coefficient $R = 7.1$ μm^3 sec^{-1}. Optical pulse measurements of the quasi-particle lifetime by Barends et al. [89] suggest that τ_0 may depend on both the device thickness and substrate. They find $\tau_0 = 687$ ns for 150 nm-thick aluminum on silicon and $\tau_0 = 430$ ns for 100 nm-thick aluminum on silicon, corresponding to $R = 4.5$ μm^3 sec^{-1} and $R = 7.2$ μm^3 sec^{-1}, respectively. Schlaerth [161] used third harmonic pulse measurements of the quasi-particle lifetime to infer a value $R \simeq 7.5$ μm^3 sec^{-1} for three detectors in an early DemoCam array (Device 1). These detectors were aluminum-niobium hybrid CPW resonators on a silicon

substrate with a 6 μm center strip, 2 μm gap, and a designed thickness of 60 nm.

Throughout this thesis we assume a value $R = 9.4$ μm^3 sec^{-1}. This is based on third harmonic pulse measurements of the quasi-particle lifetime collected in a dark scenario using three test devices on a MUSIC engineering-grade detector array (Device 9a). The test devices were all-aluminum CPW resonators on a silicon substrate with center strip/gap dimensions of 3/1, 6/2, and 9/3 (in units of μm) and a designed thickness of 60 nm. Schlaerth [161] gives a detailed description of the third harmonic pulse technique and its caveats. To briefly summarize, a "probe" and "pump" carrier tone are tuned to the resonant frequency and its third harmonic, respectively. A microwave switch is used to pulse the pump signal at a frequency around 1 kHz. The large microwave pump power generates an excess population of quasi-particle, which then recombine to the quiescent thermal population after termination of the pulse. Read out of the probe signal is triggered on pulse termination. The average decay profile over many pulses is used to determine the quasi-particle lifetime. This procedure is repeated at multiple bath temperatures. The measurements $[\tau_{qp}^{eff}(n_{qp,th})]^{-1}$ are then fit to the linear relationship given by Equation (2.24) to extract the slope R and intercept τ_{max}^{-1}. Note that this requires conversion of bath temperature to quiescent quasi-particle density, which acts as the independent variable in the linear fit. This is accomplished using Equation (2.37) with the value of Δ_0 determined from a Mattis-Bardeen fit to dark temperature sweep, resonant frequency data. The third harmonic pulsing measurements were collected with the test devices, instead of the antenna-coupled devices, because the test devices were designed to have a resonant frequency ~ 9 GHz, as opposed to $3-4$ GHz. As a result, the energy of a single pump photon is a larger fraction of the aluminum gap energy and is therefore able to generate quasi-particles more easily via heating. This is the same reason that the third harmonic is used as the pump frequency instead of the fundamental.

Measurements of the quasi-particle lifetime were collected at eight temperatures between $240-345$ mK. The resulting $[\tau_{qp}^{eff}(n_{qp,th})]^{-1}$ trajectories showed a clear linear trend. The 9/3 and 6/2 devices yielded consistent results of $R = 9.4 \pm 0.6$ μm^3 sec^{-1}. This is higher than, but still loosely consistent with, the set of values presented in the first paragraph of this section. We fix $R = 9.4$ μm^3 sec^{-1} for all analysis. We note that there is a large systematic uncertainty in extrapolating the test device measurement to our antenna coupled devices. Specifically, in the test device measurement, quasi-particles are generated along the third harmonic current distribution over the entire length of the CPW. In our detectors, quasi-particles are only generated in the aluminum portion at the shorted end of the MKID by optical power coupled through the antenna. The excess quasi-particle distribution is therefore considerably different between the two cases. We will address this uncertainty in the recombination coefficient in our interpretation of relevant results. Based on the set of values presented in the first paragraph of this section, a reasonable prior on the recombination coefficient is $7.1-9.4$ μm^3 sec^{-1}.

3.2.3.3 Nonuniform Absorption

In Section 2.2.10 we showed that, under reasonable assumptions, the effects of nonuniform absorption of optical power are completely characterized by a single parameter ζ (Equation (2.122)). Golwala [98] carried out the following procedure in order to determine ζ for the MUSIC detectors. First, hot/cold data were fit using the methodology outlined in Section 3.2.3 and assuming a uniform distribution of quasi-particles (i.e., $\zeta = 1$). This resulted in an initial estimate of the model parameters. The power absorption profile $\psi(z)$ was computed assuming a sheet resistance of 0.22 $\Omega/\square$, which is based on measurements made at 4 K. The quasi-particle density profile $\phi(z)$ was then obtained by numerically solving the diffusion equation (Equation (2.116)). In order to get the numerical solver to converge, the diffusion constant had to be reduced to $5-10\%$ of the theoretical value, or $D = 3-12$ cm^2 sec^{-1}. Note that these values are reasonably consistent with observed values [162]. The resulting quasi-particle density profile was used to calculate ζ, and the input model parameters were corrected. This process was repeated until ζ converged.

We employed a 1 mm long aluminum section for several generations of engineering-grade detector arrays. In order to reduce direct pick-up, which scales as the area of the aluminum section, we reduced the length to 0.35 mm for the science-grade detector arrays. Calculations showed that loss of power due to reflection became significant at lengths shorter than this. The diffusion equation was solved for both 1 mm and 0.35 mm. It was found that $\zeta_{1\text{mm}} = 1.10$ and $\zeta_{0.35\text{mm}} = 1.01-1.02$. These results were not a strong function of optical loading or bath temperature. This thesis is concerned with the analysis of the science-grade arrays. Since nonuniform absorption amounts to at most a 2% correction, we do not address it in our analysis.

3.2.4 FTS

The spectral response of the MUSIC detectors is set by the on-chip lumped element filters. We measure the bandpass of these filters using a Fourier Transform Spectrometer (FTS) that was originally built for the SPIDER experiment by Jon Gudmundsson [163]. The apparatus is essentially a polarized Michelson interferometer with a moving mirror that is contained in a lightweight, movable enclosure. Light from a LN_2blackbody source is collimated by a parabolic mirror and then split into two beams by a wire grid. The first beam travels a path of fixed length, in which it reflects of a rooftop mirror and then returns. The second beam travels a path of variable length, in which it reflects of a rooftop mirror attached to a carriage on a linear stage and then returns. The rooftop mirrors are made of polished aluminum and consist of two plane mirrors attached orthogonally at an edge. The beams recombine at the wire grid and then reflect off a $\sim 45^\circ$ mirror directed upward into the window of the MUSIC cryostat, where they are measured by the detectors. The beams interfere when they recombine due to phase differences introduced by differences in path length. By moving the carriage along the stage at a constant speed v_{stage}, differences in path length are mapped to differences in time, which turns each detector timestream into an interferogram. The Fourier transform of the interferogram yields the spectral response of the entire system between beam splitter and detector.

The length of the stage is 300 mm, which results in a frequency resolution of 1 GHz. The conversion between temporal frequency ν and millimeter-wave frequency $\nu_{\rm mm}$ is given by

$$\nu_{\rm mm} = \frac{c}{2\mathrm{v}_{\rm stage}}\nu \,, \tag{3.14}$$

where c is the speed of light and the factor of two arises because the change in path length is twice the change in the position of the stage. The MUSIC bandpass measurements were collected with a stage velocity of 8.75 mm/sec in order to place the spectra at a temporal frequency ν well above the $1/f$ and drift-type multiplicative electronics noise. Ideally we would like to measure the band centers of our detectors to sub-percent level accuracy, which requires that the stage move the carriage at an average velocity that deviates by less than 1% from the velocity requested. The TIME-Pilot experiment has calibrated the SPIDER FTS using a local oscillator as reference. The results are presented in Figure 3.7. They find that there are systematic offsets between the requested and achieved velocity of the stage, and that the size of the offset is dependent on the velocity requested. They performed a calibration measurement at 8.5 mm/sec, which is approximately equal to the velocity used for our measurement, and found that the true band center is 1.0261 times larger than the measured band center. We multiply the frequency scale $\nu_{\rm mm}$ by a correction factor of 1.0261 for all FTS results presented in this work.

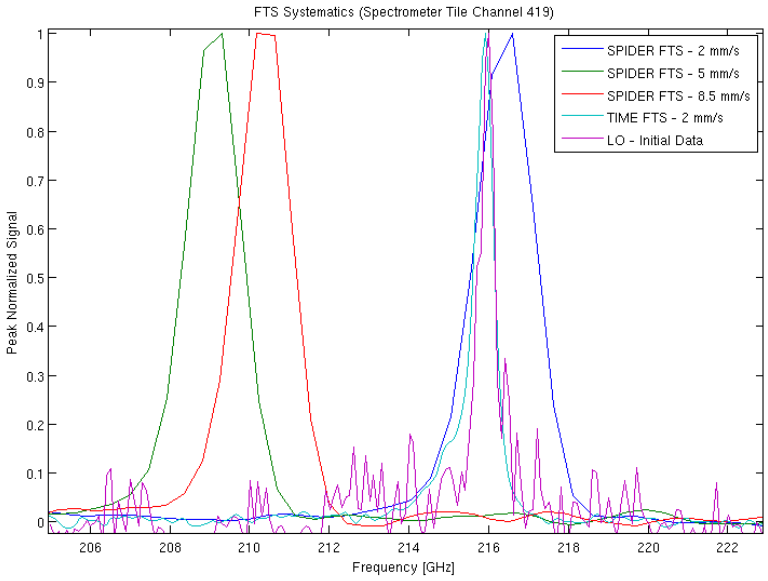

Figure 3.7: Calibration of the velocity of the linear stage on the SPIDER FTS. All data was collected with a single channel on the TIME-Pilot spectrometer. The LO was tuned to 216 GHz and measures the true bandpass, and therefore sets the frequency scale. The TIME-Pilot FTS reproduces the true bandpass with high accuracy. The SPIDER FTS reproduces the bandpass to varying degrees of accuracy depending on the velocity of stage. We used a velocity of approximately 8.5 mm/s for the measurements of the MUSIC bandpasses. Plot courtesy of Jonathon Hunacek.

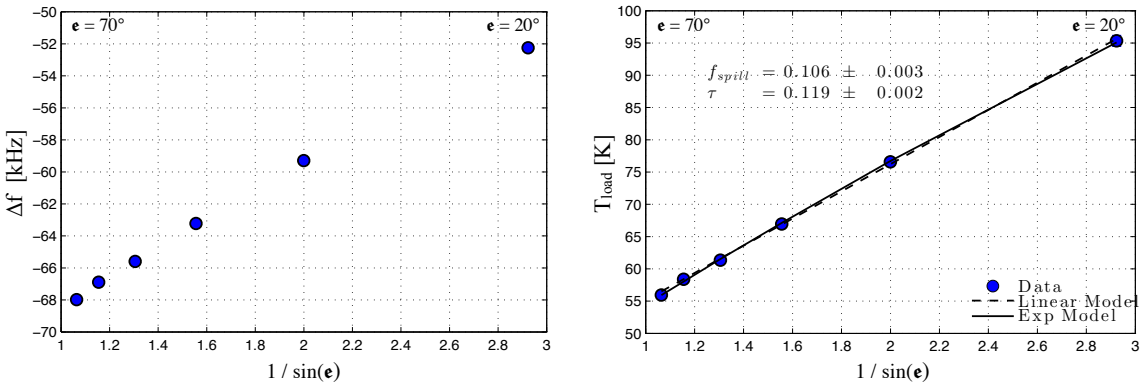

Figure 3.8: Example skydip data from a Band 1 resonator on Device A2. Left: Frequency shift relative to the value under room-temperature loading as a function of $1/\sin\mathfrak{e}$. The leftmost data point corresponds to an elevation $\mathfrak{e} = 70^\circ$ and the rightmost data point to $\mathfrak{e} = 20^\circ$. Right: The best fit parameters from the hot/cold are effectively used to convert Δf into a load temperature at the cryostat window. The solid black line denotes the best fit of the data to Equation (2.8). The dashed black line denotes the best fit using the approximation $e^{-\tau/\sin\mathfrak{e}} = 1 - \tau/\sin\mathfrak{e}$.

We describe in detail the reduction of the FTS dataset and present the resulting bandpasses, band centers, and effective band widths in Section 4.2.2. The effective band widths are used to convert the values of C measured with the hot/cold data to an optical efficiency.

3.2.5 Skydips

The final calibration measurement consists of collecting IQ sweeps at base temperature ($T_{\rm bath}^{\rm base} = 240$ mK) with the telescope pointed at empty sky at several elevation angles between $20^\circ - 70^\circ$. From these sweeps we extract the resonant frequency as a function of elevation angle $f_{\rm res}(\mathfrak{e})$ and calculate the shift relative to the resonant frequency under room-temperature loading

$$\Delta f_{\rm res}^{\rm sky}(\mathfrak{e}) = f_{\rm res}(T_{\rm bath}^{\rm base},\ T_{\rm amb}) - f_{\rm res}(T_{\rm bath}^{\rm base},\ T_{\rm load}(\mathfrak{e}))\ . \tag{3.15}$$

We fit this quantity to the model presented in Section 2.2. The relevant equations are (2.59), (2.60), (2.43), (2.44), (2.37), (2.21), (2.7), and (2.8). The load temperature is given by

$$\begin{aligned} T_{\rm load}(\mathfrak{e}) &= \left[C_{\rm ant}T_{\rm load,ant}(\mathfrak{e}) + C_{\rm dir}T_{\rm load,dir}(\mathfrak{e})\right]/C \\ &= \frac{C_{\rm ant}}{C}\left[f_{\rm spill,ant}T_{\rm amb} + (1-f_{\rm spill,ant})e^{-\tau_{\rm ant}/\sin\mathfrak{e}}\right] + \frac{C_{\rm dir}}{C}\left[f_{\rm spill,dir}T_{\rm amb} + (1-f_{\rm spill,dir})e^{-\tau_{\rm dir}/\sin\mathfrak{e}}\right]\ . \end{aligned} \tag{3.16}$$

The free parameters of the fit are

$$\boldsymbol{\theta}_{\rm sky} = \left[f_{\rm spill,ant},\ \tau_{\rm ant},\ f_{\rm spill,dir},\ \tau_{\rm dir},\ \boldsymbol{\theta}_{\rm hot/cold}\right]\ , \tag{3.17}$$

where $\theta_{\text{hot/cold}}$ are well constrained by the hot/cold data. Again, we use an MCMC to fit the data, including the results of the hot/cold as a prior. We assume that $T_{\text{atm}} = 250$ K and use the dome temperature reported at the time of the observation for T_{amb} (typically between 0–10° C).

Since $T_{\text{load,ant}}(\mathfrak{e}) = 0$ for the dark resonators, they are examined first and used to determine $f_{\text{spill,dir}}$ and τ_{dir}. The results are then included as a prior in the analysis of the skydip data for the antenna coupled resonators. Specifically, at each iteration of the MCMC the parameters $[f_{\text{spill,dir}},\ \tau_{\text{dir}}]$ are drawn randomly from the joint posterior distribution of a random dark resonator.

3.3 Noise

3.3.1 Additive Electronics

We have made precise measurements of the effective noise temperatures of the HEMTs employed in MUSIC at their operating temperature of 4 K in a test cryostat using a heated attenuator stage as a variable noise source [164]. We find that in the 3–5 GHz frequency range, $T_{\text{HEMT}} = 2$–6 K for the entire set of eight HEMTs (see Table 3.1). However, translating this effective noise temperature into a white noise level in the timestreams is difficult because it requires an accurate measurement of the gain between the input of the HEMT and the ADC. Instead of trying to dead reckon the white noise level of the electronics in this way, we measure it directly using the off-resonance carriers. After removal of the multiplicative electronics noise, the off-resonance data has a spectrum that is white at frequencies above 1 Hz. Since we have off-resonance carriers interspersed over our bandwidth, the white noise level of the electronics as a function of carrier frequency is directly measured.

Because the white noise floor of the electronics is designed to be dominated by the HEMT amplifier, we can then use the measured noise floor and the HEMT noise temperature to infer the gain between the HEMT and the ADC. Since we know the carrier power received at the ADC, we can back out the absolute power

Table 3.1: The ideal bias settings of the eight HEMT amplifiers, and the gain, noise temperature, and susceptibility to drain and gate voltage fluctuations measured at the ideal bias settings. The $\min\{T_{\text{HEMT}}\}$ and $\max\{T_{\text{HEMT}}\}$ refer to the minimum and maximum value between $3-5$ GHz.

HEMT	V_{drain} [V]	V_{gate} [V]	I_{drain} [mA]	$\partial G/\partial V_{\text{drain}}$ [V^{-1}]	$\partial G/\partial V_{\text{gate}}$ [V^{-1}]	G [dB]	$\min\{T_{\text{HEMT}}\}$ [K]	$\max\{T_{\text{HEMT}}\}$ [K]
248D	1.8	3.0	36	407	297	39.8	5.1	5.8
255D	1.6	0.9	30	2990	1000	38.0	2.0	2.8
256D	1.5	1.2	30	584	362	38.0	3.0	4.2
258D	1.3	0.8	31	497	101	37.0	3.6	4.3
263D	1.6	1.4	34	209	259	37.0	3.0	3.8
266D	1.5	2.1	30	1090	1040	40.0	3.3	4.0
289D	1.5	2.0	35	394	345	39.0	2.9	3.9
321D	1.5	0.6	30	–	–	37.0	2.0	3.5

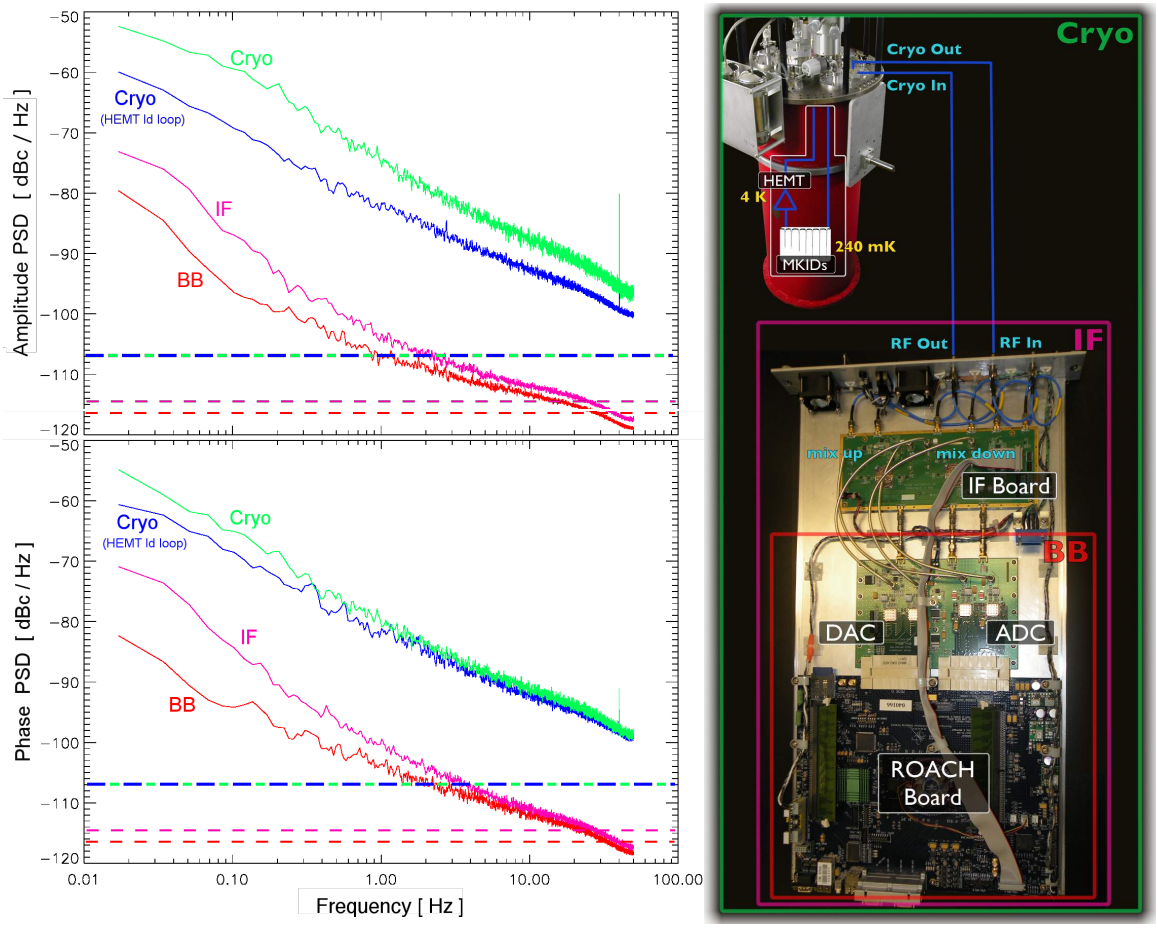

Figure 3.9: Left: Power spectral density in the amplitude and phase direction in units of dBc / Hz for the base-band (BB), intermediate-frequency (IF), and cryostat (Cyro) subsystems. Solid lines denote the median PSD over approximately 100 off-resonance carriers measured with one readout board. Dashed lines denote the white noise floor. Right: Cartoon of the readout electronics corresponding to one readout board. The various subsystems are outlined and labeled.

reaching the HEMT, and accurately determine the power reaching each resonator. This is important because knowledge of the carrier power at the resonator is required to predict the amplitude of the TLS noise.

3.3.2 Multiplicative Electronics

In this section we present several empirical facts regarding the multiplicative electronics noise that will be used to inform the removal algorithm. All of these results followed from the study of off-resonance carrier timestreams measured with the MUSIC readout electronics. The fact that the noise is multiplicative was easily confirmed by examining the power spectral density as a function of carrier power at the ADC. In the limit of zero carrier power the measured power spectral density is constant and coincides with the expected value of the electronics white noise floor. As the carrier power is increased we observe $1/f$ and drift type noise rise above this white noise floor, and find that the normalization of these components scale as A^2.

The MUSIC readout board is equipped with two switches that place the board in different "loopback modes" wherein the output signal is sent directly to the input, bypassing certain segments of the receiver chain. These switches enable us to study the contribution of various subsystems to the total noise. The base-band (BB) loopback mode sends the output of the DAC directly to the ADC, bypassing the entire process of up-converting to microwave frequencies and then down-converting to base band. The intermediate-frequency (IF) loopback mode sends the output of the IF board to the third IF amplifier (labeled IF-Amp-2 in Table 2.2), bypassing the cryostat and the first two room-temperature amplifiers. Finally, an external (Ext) loopback mode can be implemented by connecting the output of the readout board to the input with an SMA cable, bypassing the cryostat but including all room temperature electronics.

Figure 3.9 presents the noise power spectral density measured in BB loopback mode, IF loopback mode, and standard operations (Cryo). The carrier power at the ADC was maintained at a fixed value for all measurements, approximately equal to that used during observing. The dashed lines denotes the white noise floor of each of the subsystems. We find that in all cases $1/f$ and drift type noise dominate over the additive white noise across the frequency range of interest. We also find that in all cases the noise in the amplitude direction is comparable in magnitude to the noise in the phase direction. In switching from BB to IF loopback we have added up-conversion, down-conversion, and two stages of amplification. Somewhat surprisingly this introduces very little noise at short timescales. It does, however, introduce significant drift type noise resulting in a noticeable degradation in the long timescale stability. In switching from IF to Cryo we see an approximately 20 dB increase in the noise level at high frequencies and a 10-20 dB increase at low frequencies; the timestreams are entirely dominated by the noise from the cryogenic components.

It was not always the case that the noise from the room temperature components was subdominant to the noise from the cryogenic components. The two were comparable in magnitude throughout most of the development of the MUSIC readout. In the final version of the readout boards we did a better job heat sinking the ADC, DAC, and IF board, and also improved air flow by placing the boards in a ventilated crate. This reduced the drift noise from the room temperature electronics by two orders of magnitude. As a result, the total noise from the room temperature electronics is below the white noise floor of the system at high frequencies (> 1 Hz) and below the cryogenic $1/f$ and drift type noise at low frequencies. It is still large enough, however, that it must be removed in order to achieve a white spectrum at frequencies below 1 Hz.

The blue and green lines in Figure 3.9 were collected with setups that differ only in the method used to stabilize the bias power being supplied to the HEMT. For the green line we have set the power supply to provide a specific gate and drain voltage and done nothing else. For the blue line we have set the gate and drain voltage to the same values, but have also implemented a feedback loop that varies the gate voltage in order to keep the drain current constant. This results in a fairly significant decrease in the magnitude of the amplitude noise, presumably because the gain of the HEMT is more sensitive to fluctuations in the drain current than the gate voltage. The feedback loop also decreases the magnitude of the phase noise, although the improvement is not as noticeable as that seen in the amplitude direction.

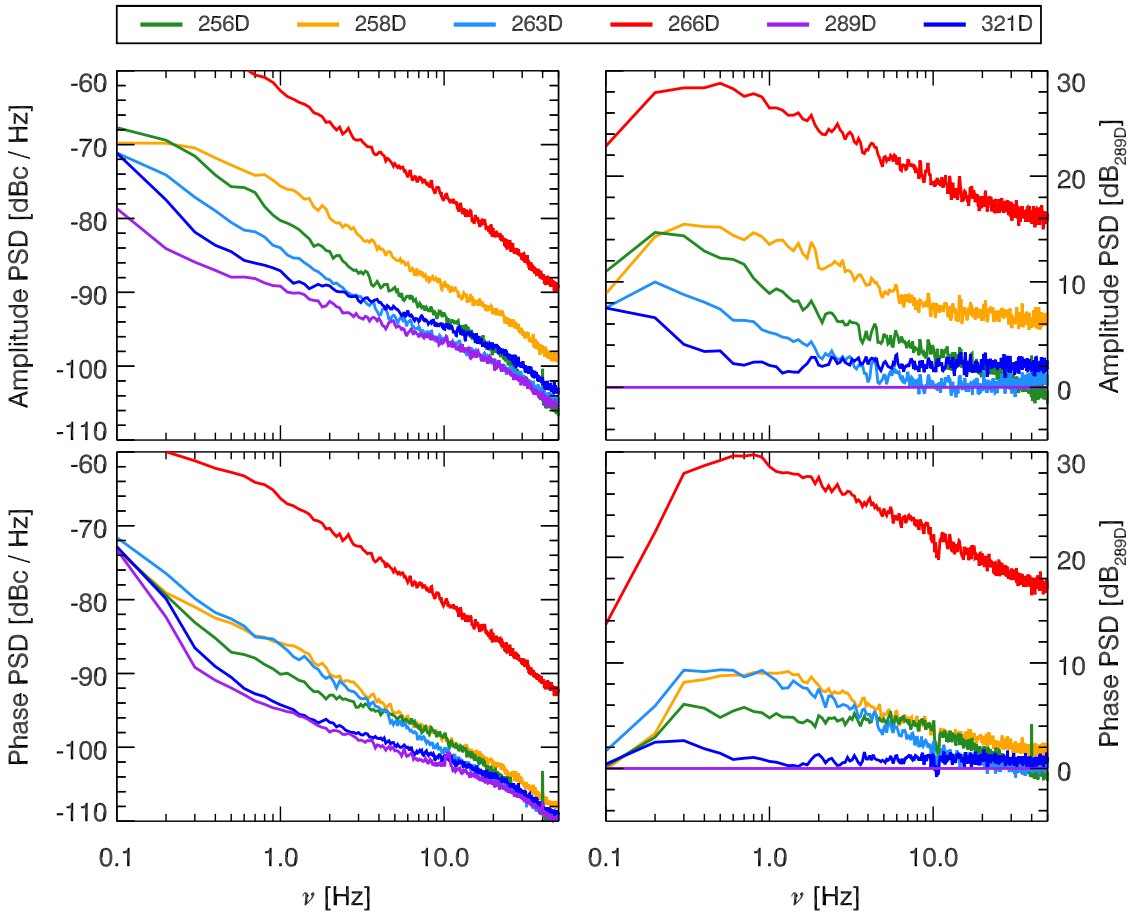

Figure 3.10: *Left:* The median power spectral density in the amplitude and phase direction in units of dBc / Hz. The median was taken over approximately 200 off-resonance carriers across two readout boards. The different colors denote different HEMT amplifiers. *Right:* The median power spectral density in the amplitude and phase direction relative to HEMT 289D, which has the best noise performance.

We attribute the large increase in $1/f$ and drift type noise between the IF and Cryo measurement primarily to the HEMT. Figure 3.10 compares the median off-resonance noise power spectral density collected during an actual observation for six of the readout channels. There is significant variation across the readout channels in both the magnitude of the noise and its spectral shape (due to differences in the relative contribution of $1/f$ and drift). The noise from the room temperature electronics is approximately uniform for the different readout boards, and the variation seen is entirely due to differences in HEMT noise performance. This variability can only partially be explained by the susceptibility of the HEMTs to fluctuations in bias voltage. Table 3.1 gives the measured susceptibility $\partial G/\partial V_{\text{drain}}$ and $\partial G/\partial V_{\text{gate}}$ of the gain of the HEMTs to fluctuations in the drain and gate voltage at their operating bias. We see that the HEMT that has the worst noise performance (266D) is also extremely susceptible to voltage fluctuations. In general, however, we do not observe the expected scaling in the magnitude of the HEMT noise with susceptibility. This suggests the presence of an additional source of noise internal to the amplifier. The large variation in HEMT noise performance means that the

multiplicative electronics noise will be prevalent in some detector arrays and entirely subdominant in others. If we exclude the outlier 266D, then at 1.0 Hz we see roughly 14 dB variation in the amplitude direction and 9 dB variation in the phase direction. We note that in the phase direction (and to a lesser extent the amplitude direction) at frequencies less than 0.1 Hz, the drift noise from room temperature electronics starts to become appreciable, which results in the noise power spectral density for the different detector arrays converging at low frequencies in Figure 3.10.

We claimed in Section 2.3.1.2 that the amplitude and phase fluctuations measured by carriers at different microwave frequencies are correlated. Our ability to remove the multiplicative electronics noise will depend on the degree to which this is true. Let $\boldsymbol{x}$ and $\boldsymbol{y}$ denote the time ordered data for two different carriers in a particular direction in the complex plane. We calculate the Pearson correlation coefficient between $\boldsymbol{x}$ and $\boldsymbol{y}$ in the Fourier domain as

$$\rho_{x,y} = \frac{\tilde{\boldsymbol{x}} \cdot \tilde{\boldsymbol{y}}}{\sqrt{(\tilde{\boldsymbol{x}} \cdot \tilde{\boldsymbol{x}})\,(\tilde{\boldsymbol{y}} \cdot \tilde{\boldsymbol{y}})}} \ , \tag{3.18}$$

where $\tilde{\boldsymbol{x}}$ and $\tilde{\boldsymbol{y}}$ denote the Fast Fourier Transform (FFT) of $\boldsymbol{x}$ and $\boldsymbol{y}$. The dot product is given by

$$\tilde{\boldsymbol{x}} \cdot \tilde{\boldsymbol{y}} = \sum_k \tilde{x}_k^* \, \tilde{y}_k \ , \tag{3.19}$$

where the summation runs over the frequency bins of interest. The Pearson correlation coefficient is a measure of the linear correlation between $\boldsymbol{x}$ and $\boldsymbol{y}$. By definition $\rho_{x,y} \in [-1, 1]$, with 1 indicating perfect correlation, 0 indicating no correlation, and -1 indicating perfect anti-correlation. If $|\rho_{x,y}| = 1$, then the relationship between x and y is perfectly described by a linear model.

Figure 3.11 shows the Pearson correlation coefficient between every pair of off-resonance carriers across four readout boards (and two readout channels) during a twenty-minute-long observation. We find that the time ordered data in both the amplitude direction and the phase direction is highly correlated between off-resonance carriers on the same readout board. This high degree of correlation persists between off-resonance carriers on different readout boards but the same readout channel (i.e., same detector array and same HEMT amplifier). This is not surprising since our previous considerations suggested that noise from the HEMT amplifier dominates in both the amplitude and phase direction. Finally, data collected with off-resonance carriers on different readout channels is completely uncorrelated. This is not surprising either since different readout channels do not share any electronic components, besides a common frequency reference.

There is additional structure in the correlation matrices beyond this simple picture. This is evident in the bottom row of Figure 3.11, which show the same data as the top row, but with a compressed color scale that highlights these secondary variations. In general, the high degree of correlation across each readout channel is more uniform in the amplitude direction than the phase direction. In the phase direction, the correlation degrades as one moves away from the diagonal of the matrix, which corresponds to moving toward pairs of

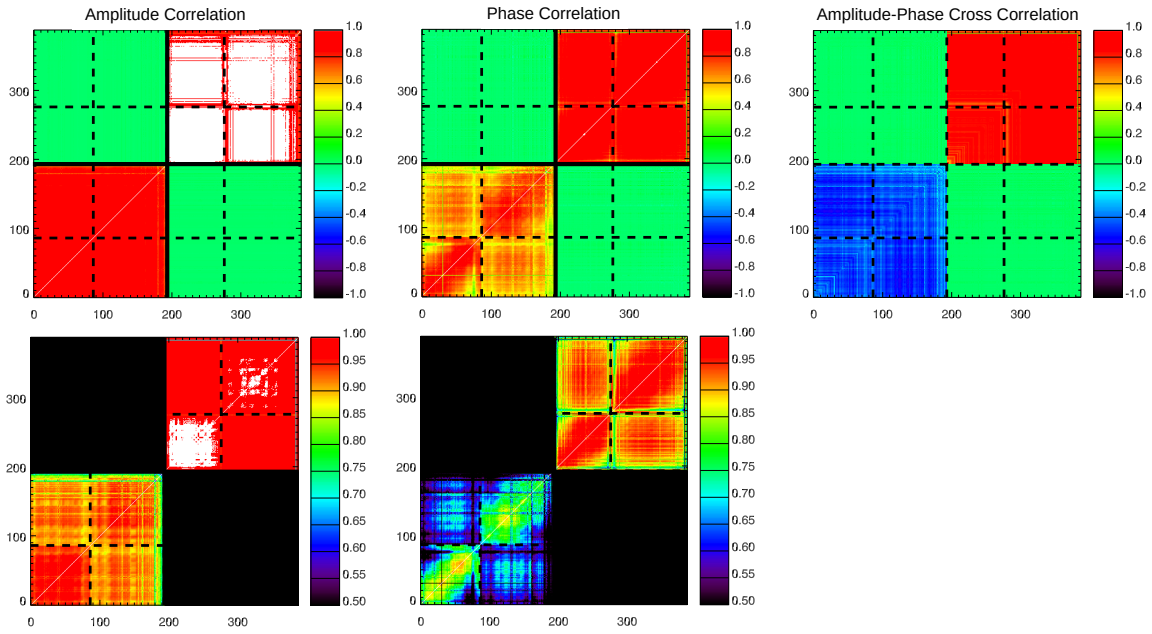

Figure 3.11: Pearson correlation coefficients between the 388 off-resonance carriers probing L120210.2R and L120210.2L. The correlation coefficients were calculated using Equation (3.18). The left, middle, and right column show the amplitude correlations, phase correlations, and amplitude-phase cross correlations, respectively. Dashed black lines separate the different readout boards. Solid black lines separate the different detector arrays: L120210.2R (connected to HEMT 289D) corresponds to carriers numbered 0-193, and L120210.2L (connected to HEMT 258D) corresponds to carriers numbered 194-387. For a given detector array, the carriers are numbered in order of increasing carrier frequency. The correlation coefficients were calculated in the Fourier domain using only temporal frequencies between 0.2 Hz and 20.0 Hz. The bottom row is identical to the top row, but with a compressed color scale, so that variations in the correlation coefficient between carriers on the same readout board are visible. Note that the white color corresponds to a correlation coefficient $\rho_{x,y} \approx 1$.

carriers with larger frequency separations. This suggests that the phase fluctuations are somewhat local in microwave frequency.

The lower left corner of each matrix corresponds to the off-resonance carriers that probe detector array L120210.2R and HEMT 289D. The upper right corner corresponds to the off-resonance carriers that probe detector array L120210.2L and HEMT 258D. 289D has the best noise performance, while 258D has the second worst noise performance (see Figure 3.10). We note several differences in the correlation matrices between these two readout channels. The third column in Figure 3.11 shows the cross-correlation between the amplitude and phase direction. In the case of 258D, amplitude and phase noise are completely correlated. This suggest a similar underlying cause, some source of low frequency noise internal to the HEMT amplifier that results in fluctuations in both its gain and phase delay. In the case of 289D, the HEMT noise is not as dominant. Indeed, in the phase direction it appears that the room temperature electronic noise is comparable, as evidenced by the reduced correlation between off-resonance carriers on separate readout boards. Interestingly, the amplitude and phase noise from 289D appear to be highly anti-correlated. We currently do not have a compelling physical explanation for the HEMT phase noise. It is either highly correlated or highly anti-correlated with the amplitude noise, depending on the amplifier.

3.3.3 Fundamental

The fundamental sources of noise include photon noise, recombination noise, and thermal generation noise. We predict the fundamental noise using Equation (2.176). The center frequency $\nu_{\rm mm}$ and bandwidth $\Delta\nu_{\rm mm}$ are determined from the FTS measurements. The thermal quasi-particle density $n_{\rm qp,th}$, quasi-particle density $n_{\rm qp}$, and optical power $P_{\rm opt}$ are determined from our calibrated response model using Equations (2.37), (2.124), and (2.105), respectively. We assume that the detectors have perfect quantum efficiency $\eta_{\rm qe} = 1$ and use the values of R and V presented earlier in this chapter. The lower bound on $\tau_{\rm max}$ obtained from the hot/cold data suggests that its effect on the fundamental noise will be negligible.

Accurately predicting the fundamental noise requires a good understanding of the optical loading. Examining Equation (2.105) we see that thermal radiation from the interior of the cryostat, room temperatures surfaces, and the sky all contribute to the total optical loading. The contribution from the interior of the cryostat is represented by the parameters $T_{\rm exc,ant}$ and $T_{\rm exc,dir}$, which have been measured for each resonator using the hot/cold dataset. The contribution from room temperature surfaces is given by $(f_{\rm spill,\,ant} + f_{\rm spill,dir})T_{\rm amb}$. The spillover fraction has been measured for each resonator using the skydip dataset. We use the median ambient temperature reported by the CSO over the course of the observation as our estimate of $T_{\rm amb}$. Finally, the contribution from the sky will depend on the atmospheric temperature $T_{\rm atm}$ and opacity τ. We assume $T_{\rm atm} = 250$ K. We take the median value of τ_{225} reported by the CSO tipping radiometer over the course of the observation and convert it to $\tau_{\rm ant}$ for each resonator using the ATM model for the atmospheric transmission and the bandpass measured via FTS. Since we do not have measurements of the direct pick-up spectral response we cannot predict $\tau_{\rm dir}$. As a result, we do not include the contribution from the direct pick-up beam in the

calculation of the total loading.

We currently do not have a solid measurement of the fundamental noise to confirm the predictions of the model. While the model is theoretically sound, there are a number of parameters that go into it that are not well known — specifically, the recombination constant R, the volume V due to uncertainty in the film thickness, and the maximum quasi-particle lifetime $\tau_{\max}$. We should be able to measure this noise directly in the frequency direction by simply sampling at a much higher frequency. Currently the MUSIC readout electronics sample at a $f_s = 100$ Hz, which restricts our attention to $\nu < 50$ Hz. At these frequencies the contamination from multiplicative electronics noise and TLS noise is significant. However, both of these noise sources have a declining spectrum, so if we pushed to higher frequencies eventually we would observe a white noise floor. All reasonable considerations suggest that the floor due to fundamental noise should be larger than electronics white noise floor in the frequency direction, so measuring this white noise floor would enable confirmation of the model. In addition, since the quasi-particle bandwidth should be less than the resonator bandwidth, the location of the roll-off in the noise would also provide a measurement of the quasi-particle lifetime. Unfortunately, changing the sampling frequency would require a modification of the FPGA firmware, and is outside the scope of this thesis.

3.3.4 Two-Level Systems

In February 2013 we collected noise data at multiple carrier powers with the detectors dark in order to isolate and measure the TLS noise. The dark configuration ensured that photon and atmospheric noise would not confuse or overwhelm the TLS signal. Examining the power spectral density of the on-resonance noise as a function of carrier power enabled identification of the TLS signal through the expected $P^{-1/2}$ dependence expressed in Equation (2.184). This scaling with power is unique to TLS noise. Relative to the carrier, additive electronics noise scales as P^{-1}, multiplicative electronics noise is independent of power, and sources of noise transduced via changes in the quasi-particle density — such as generation-recombination noise — are also independent of power assuming that the effect of the microwave power on the quasi-particle population is negligible.

We collected noise data at seven carrier powers spanning 14 dB for each of the detectors on six of the eight arrays (two of the arrays L120309.4R and L120423.1L were non-operational during this cooldown). In addition, we collected a second redundant dataset for the detectors on L120210.2R and L120210.2L. The data was collected with the MUSIC readout electronics. At each carrier power, we sampled $\hat{V}(t)$ for 15 minutes at $f_s = 100$ Hz. The highest carrier power was different for each resonator and was chosen to be the maximum power that could be delivered by the readout electronics and did not cause that resonator to bifurcate. The carrier power at the resonator was then decreased from this maximum value in steps of 2 dB by increasing the amount of output attenuation using the variable attenuator on the output side of the IF board. Each time the output attenuation was increased, the input attenuation was decreased by the same amount using the variable attenuator on the input side of the IF board. This varied the carrier power at the resonator but kept the carrier

power at the ADC constant. All data was collected at base temperature corresponding to $T_{\rm bath} = 237$ mK.

Many of the resonators entered the nonlinear regime at the higher carrier powers, and as a result their resonant frequencies shifted as we varied the carrier power. In order to ensure that all data was collected on resonance, each time we changed the attenuation we performed two IQ sweeps before collecting the timestream. The first IQ sweep was used to determine the frequency where the derivative $|d\hat{V}(f)/df|$ was at a maximum, which was used as an estimate of the resonant frequency. A set of buffers were generated that placed the on-resonance carriers at the newly determined resonant frequencies. These buffers were loaded on the readout boards and the second IQ sweep was performed in order to measure the transmission through the system near resonance. The second IQ sweep is necessary for two reasons. The process of generating a new buffer randomizes the phases of the carrier tones. Since we would like to determine the frequency direction from the IQ sweep, the phase information is crucial. Even if we are careful to maintain the phase of each carrier tone through buffer generation, changing the base-band frequency $f_{\rm BB}$ of the carrier tone in order to place it at the resonant frequency will change the base-band transmission $S_{21}^{\rm BB}(f_{\rm BB})$. Examining Equation (2.61) we see that this will result in values of $\hat{V}(f)$ that differ between the first and second IQ sweep. For the first IQ sweep, the LO was swept over $N = 81$ points with a frequency spacing $\Delta f = 7.5$ kHz. For the second IQ sweep, the LO was swept over $N = 81$ points with a frequency spacing $\Delta f = 2.5$ kHz. After the second IQ sweep, the LO was set to its nominal frequency and the timestream was collected.

We use the second IQ sweep to estimate both the frequency direction and the factor that converts from volts at the ADC to the equivalent $\delta f_{\rm res}/f_{\rm res}$. Let f_0 denote the frequency of an on-resonance carrier and let $\hat{V}(f_i)$ denote the complex carrier amplitude measured during the second IQ sweep with $i = -N/2, \ldots, 0, \ldots, N/2$. The derivative of $\hat{V}(f)$ is estimated using the symmetric difference quotient

$$\begin{aligned}\hat{V}'(f_i) &\approx \frac{\hat{V}(f_{i+1}) - \hat{V}(f_{i-1})}{2\Delta f} \\ &= \frac{\mathrm{I}(f_{i+1}) - \mathrm{I}(f_{i-1})}{2\Delta f} + j\frac{\mathrm{Q}(f_{i+1}) - \mathrm{Q}(f_{i-1})}{2\Delta f} \ . \end{aligned} \tag{3.20}$$

The frequency direction and conversion factor are then estimated as

$$\hat{\theta}_{\rm freq} = \arg\left(\hat{V}'(f_0)\right) \qquad\qquad \hat{A}_{\rm freq} = \frac{1}{f_0}\left|\hat{V}'(f_0)\right| \ . \tag{3.21}$$

We have confirmed that the estimates of $\theta_{\rm freq}$ and $A_{\rm freq}$ determined from the numerical derivative are on average equal to those obtained from fitting the complex $\hat{V}(f)$ data to the model given by Equation (3.1) and evaluating the derivative of the analytical model at the carrier frequency. The RMS scatter between the estimates obtained from the numerical derivative and those obtained from derivative of the analytical model is approximately 5%.

Reduction and analysis of the dark noise data proceeds as follows for each on-resonance carrier at each carrier power. We start by filtering a large number of spectral lines that are observed in the on-resonance data.

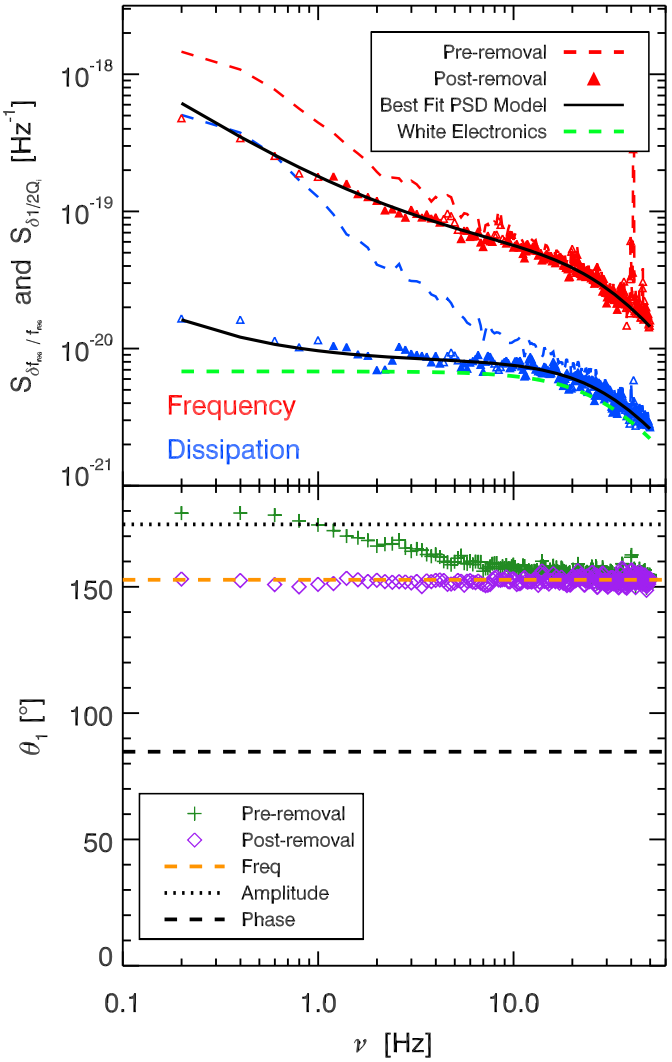

Figure 3.12: *Top:* The measured power spectral density in the frequency (red) and dissipation (blue) direction for an antenna coupled resonator on Device L120210.2L with frequency $f_{\rm res} = 3.089243$ GHz, quality factor $Q = 68,000$, and coupling quality factor $Q_c = 99,000$. The data was collected at a temperature of 237 mK and the highest achievable readout power, corresponding to $P = -87$ dBm or $P_{\rm int} = -38$ dBm. The timestreams were converted to the equivalent resonator frequency fluctuations $\frac{\delta f_{\rm res}}{f_{\rm res}}$ and resonator dissipation fluctuations $\frac{1}{2}\delta\frac{1}{Q_i}$ prior to calculating the PSDs. Dashed lines denote the PSDs before electronics noise removal and triangles denote the PSDs after electronics noise removal. Solid black lines denote the best fit of the PSDs after noise removal to Equation (3.24) for the frequency direction and Equation (3.25) for the dissipation direction. The electronics white noise floor inferred from nearby off-resonance carrier tones is denoted by the green dashed line. *Bottom:* The angle of the largest eigenvalue obtained from diagonalizing the I-Q cross power-spectral density before electronics noise removal (green +) and after electronics noise removal (purple $\diamond$). The frequency direction — determined independently from an IQ sweep — is denoted by the dashed yellow line. The amplitude and phase directions — determined from the mean value of the timestreams — are denoted by the black dotted and black dashed line, respectively.

These lines are narrow with FWHM less than 20 mHz. Most occur at harmonics of the pulse tube frequency $f_{\rm pt} = 1.41$ Hz, but there are others whose origins are unknown. We apply a series of forward-backward recursive notch-filters, with each filter designed to match the center frequency and width of a particular line [165]. The same series of filters is applied to the I and Q data of all carriers on a given board.

Next, we remove the multiplicative electronics noise. Essentially, the algorithm constructs templates for the amplitude and phase fluctuations from the off-resonance data, and then subtracts these templates from both the off-resonance and on-resonance data. We are able to remove down to the white noise floor at frequencies $\gtrsim 1$ Hz in the off-resonance timestreams. Residual $1/f$ noise is present at frequencies $\lesssim 1$ Hz

After filtering and noise removal, we apply the transformation

$$\delta X(t) + j\delta Y(t) = \frac{1}{\hat{A}_{\rm freq}} \left(\delta {\rm I}(t) + j\delta {\rm Q}(t)\right) e^{-j\hat{\theta}_{\rm freq}} \,, \tag{3.22}$$

which rotates the data to the frequency and dissipation direction and converts the timestreams into the equivalent fractional resonant frequency fluctuations $\delta X(t) \approx -\frac{\delta f_{\rm res}(t)}{f_{\rm res}}$ and dissipation fluctuations $\delta Y(t) \approx \frac{1}{2}\delta \frac{1}{Q_i}(t)$.

We break the 15 minute long timestreams into approximately 180 distinct 5 second long blocks, thereby restricting our attention to temporal frequencies between 0.2 Hz and 50 Hz. For each block we mean subtract and Hanning window both $\delta X(t)$ and $\delta Y(t)$. We then calculate the power spectral densities $S_{\delta X}(\nu)$ and $S_{\delta Y}(\nu)$, as well as the cross power spectral density $S_{\delta X,\delta Y}(\nu)$. We flag any blocks that contain outlier time samples. We also flag blocks whose total noise power in either the frequency or dissipation direction is an outlier. We then take the mean of the unflagged blocks as our final estimate of $S_{\delta X}(\nu)$, $S_{\delta Y}(\nu)$, and $S_{\delta X,\delta Y}(\nu)$. We use the standard error of the mean calculated using the unflagged blocks to estimate the uncertainty on these (cross) power spectral density estimates.

We construct the cross power spectral density matrix

$$C_{\delta X,\delta Y}(\nu) = \begin{bmatrix} S_{\delta X}(\nu) & S_{\delta X,\delta Y}(\nu) \\ S_{\delta X,\delta Y}(\nu) & S_{\delta Y}(\nu) \end{bmatrix} \tag{3.23}$$

and determine the eigenvectors and eigenvalues of this matrix at each frequency sampled. We then examine the direction of the eigenvector corresponding to the largest eigenvalue in the complex plane $\theta_1(\nu)$. The purpose of the dark dataset is to measure amplitude of the TLS noise for the MUSIC detectors. There is significant empirical evidence that the TLS noise is restricted to the frequency direction. Hence, $\theta_1(\nu)$ should correspond to the frequency direction for the temporal frequencies where TLS noise dominates. We find that indeed $\theta_1(\nu) \approx \hat{\theta}_{\rm freq}$ for the majority of resonators, carrier powers, and temporal frequencies. In the analysis that follows we only consider carrier powers where the mean value of the θ_1 between 4 Hz and 30 Hz is within 5° of $\theta_{\rm freq}$. We also require that the standard deviation of θ_1 over the same frequency range be less than 5°. This particular range was chosen because after applying the removal algorithm the multiplicative electronics noise is negligible at these frequencies in the off-resonance carriers. We apply a final requirement

that no more than 50% of the time blocks are flagged as bad.

We fit the following model to the power spectral densities

$$S_{\delta X}(\nu) = \frac{x_0 \, + \, x_{1/2}\nu^{-1/2} \, + \, x_1\nu^{-1}}{1 \, + \, (\nu/\nu_{\rm cutoff})^2} \tag{3.24}$$

$$S_{\delta Y}(\nu) = \frac{y_0 \, + \, y_1\nu^{-1}}{1 \, + \, (\nu/\nu_{\rm cutoff})^2} \, , \tag{3.25}$$

where $\nu_{\rm cutoff} = 34.54$ Hz is the cutoff frequency of our anti-aliasing filter and $\boldsymbol{\theta}_x = [x_0, \, x_{1/2}, \, x_1]$ and $\boldsymbol{\theta}_y = [y_0, \, y_1]$ are the free parameters of the fit. Here x_0 and y_0 represent the white noise floor, x_1 and y_1 represent the amplitude of residual $1/f$ type noise, and $x_{1/2}$ represents the amplitude of the TLS noise. The fit is performed in IDL with the MPFIT routine. The model provides a good fit in almost all cases.

The data reduction described in the preceding paragraphs is illustrated in Figure 3.12 for a typical detector operated at its highest carrier power. The top panel displays $S_{\delta X}$ and $S_{\delta Y}$ before and after electronics noise removal. Before removal, the multiplicative electronics noise is significant in both the frequency and dissipation direction. After removal, the noise in the dissipation direction is consistent with the white noise floor of the electronics at high ν and a small residual $1/f$ component is evident at low ν. The noise in the frequency direction is at least an order of magnitude larger than the noise in the dissipation direction at all ν. The black lines denote the best fit to the model given by Equations (3.24) and (3.25). In the bottom panel we display the rotation angle of the eigenvector corresponding to the largest eigenvalue, again both before and after electronics noise removal. Before removal, the angle is pulled towards the amplitude direction especially at low ν where the multiplicative electronics noise dominates. After removal, the angle collapses to the frequency direction — which is determined independently from the second IQ sweep — for all values of ν.

We directly measure the white noise floor of the electronics as a function of microwave frequency using the off-resonance carriers. We find that the best fit value of y_0 is approximately equal to the white noise floor of the electronics for all detectors at all carrier powers. However, we find that an excess white noise is necessary to explain the best fit value of x_0 on several of the detector arrays. When converted to $\frac{\delta f_{\rm res}}{f_{\rm res}}$ and $\frac{1}{2}\delta\frac{1}{Q_i}$, the white noise floor of the electronics scales as P^{-1}. We find that the value of x_0 follows the electronics noise floor at low carrier power but saturates at high carrier power. The measured values are consistent with $x_0(P) = x_0^{\rm elec}(P) + x_0^{\rm exc}$, so we assume this particular relation and fit all of the $S_{\delta X}$ data simultaneously with a single white noise parameter $x_0^{\rm exc}$. The excess white noise is illustrated in the bottom left panel of Figure 3.13.

Thermal generation and recombination noise are perhaps the most likely explanations for the excess white noise. The G-R noise is given by

$$S^{\rm G\text{-}R}_{\delta f_{\rm res}/f_{\rm res}} = \frac{2}{V}\left(\alpha\kappa_2\tau_{\rm qp}^{\rm eff}\right)^2\left(Rn_{\rm qp,th}^2 + \frac{1}{\tau_{\rm max}}n_{\rm qp,th}\right) \, . \tag{3.26}$$

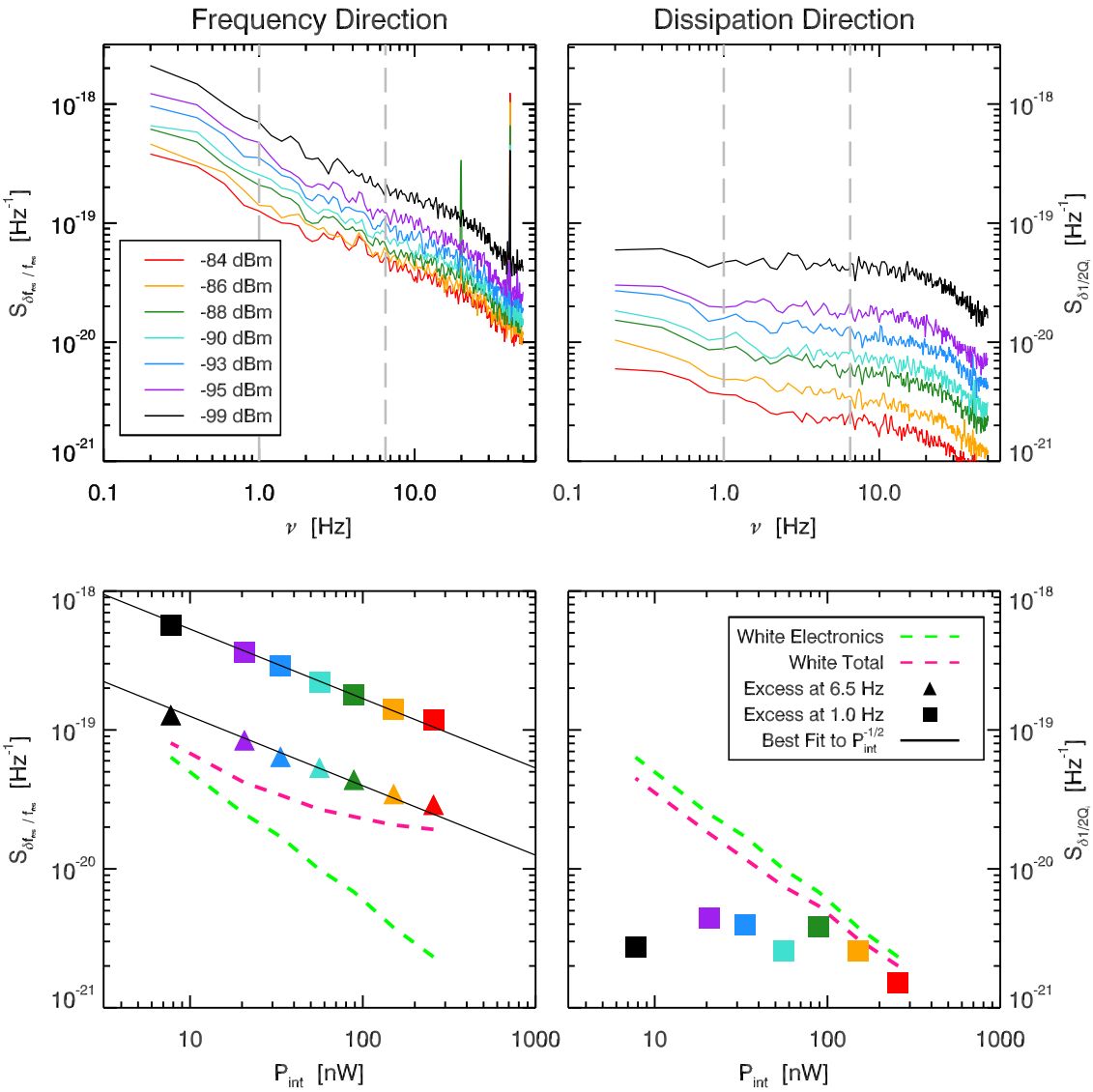

Figure 3.13: *Top:* The measured power spectral density after electronics noise removal in the frequency (left) and dissipation (right) direction for an antenna coupled resonator on Device L120210.2R with frequency $f_{\text{res}} = 3.134272$ GHz, quality factor $Q = 61{,}000$, and coupling quality factor $Q_c = 105{,}000$. The different colors denote different carrier powers on the feedline at the device ranging from $P = [-99, -84]$ dBm, which corresponds to $P_{\text{int}} = [-51, -36]$ dBm. The timestreams were converted to the equivalent resonator frequency fluctuations $\frac{\delta f_{\text{res}}}{f_{\text{res}}}$ and resonator dissipation fluctuations $\frac{1}{2}\delta\frac{1}{Q_i}$ prior to calculating the PSDs. *Bottom:* Measured power spectral density as a function of internal resonator power. The green dashed lines denote the electronics white noise floor inferred from nearby off-resonance carriers. The pink dashed lines denote the white noise floor determined from a fit to the PSDs. The triangles and squares denote the excess noise at 6.5 Hz and 1.0 Hz respectively after subtracting the white noise floor. The solid black lines denote the best fit of the excess noise in the frequency direction to the $P_{\text{int}}^{-1/2}$ scaling characteristic of TLS noise.

This equation is obtained by considering Equation (2.176) in the limit of zero optical loading. We can make predictions for the expected G-R noise using the values of α and Δ_0 obtained from Mattis-Bardeen fits to dark temperature sweeps that were collected during this same cooldown. However, this prediction is sensitive to the value of the intrinsic lifetime $\tau_{\rm max}$, for which we do not have a precise estimate. Results from the analysis of hot/cold data place a lower bound $\tau_{\rm max} \gtrsim 50\ \mu$s. If $\tau_{\rm max} = 50\ \mu$s then the measured values of $x_0^{\rm exc}$ are a factor of 6 times larger than the prediction for G-R noise. In the limit that $\tau_{\rm max}$ is very long ($\tau_{\rm max} \gtrsim 400\ \mu$s), then the measured values of $x_0^{\rm exc}$ are only a factor of 2 times larger than the prediction for G-R noise. We allow this excess white noise since it is necessary to yield reasonable fits to $S_{\delta X}$.

In order to extract the TLS noise amplitude, we examine the quantity

$$S^{\rm TLS}_{\delta f_{\rm res}/f_{\rm res}}(\nu) \equiv x_{1/2}\nu^{-1/2} + x_1\nu^{-1} \tag{3.27}$$

as a function of internal resonator power. In doing so, we are assuming that after subtracting the measured white noise floor the entirety of the noise that remains in the frequency direction is due to TLS. The internal resonator power is calculated using Equation (2.182); Q and Q_c are determined from a fit to the first IQ sweep collected at the lowest carrier power and P is accurately determined using the technique discussed in Section 3.3.1. We present $S^{\rm TLS}_{\delta f_{\rm res}/f_{\rm res}}$ at 1 Hz and 6.5 Hz for a typical MUSIC detector in the bottom left panel of Figure 3.13. We unambiguously observe the $P_{\rm int}^{-1/2}$ dependence on microwave readout power over a 14 dB range at both frequencies. That our measurements reveal this unique scaling with power combined with the fact that the dominant source of noise occurs in the frequency direction is strong evidence that we are seeing the TLS noise observed by other groups and described by the semi-empirical model presented in Section 2.3.2.2.

For each resonator, we fit the measured values of $S^{\rm TLS}_{\delta f_{\rm res}/f_{\rm res}}$ to the following relationship based on Equation (2.184)

$$S^{\rm TLS}_{\delta f_{\rm res}/f_{\rm res}}(P_{\rm int}, T_{\rm bath}, \nu) = B^2_{\rm TLS}\ \left(\frac{P_{\rm int}}{1\ \mu{\rm W}}\right)^{-1/2}\ \left(\frac{T_{\rm bath}}{250\ {\rm mK}}\right)^{-1.7}\ \left(\frac{\nu}{1\ {\rm Hz}}\right)^{-1/2}, \tag{3.28}$$

where $T_{\rm bath} = 237$ mK, $\nu = 6.5$ Hz, and $B^2_{\rm TLS}$ is the only free parameter of the fit. We stress that even though we are defining $B^2_{\rm TLS}$ with respect to 1 Hz for simplicity, we constrain its value using only the measurements at $\nu = 6.5$ Hz. We chose 6.5 Hz because it is free of spectral lines, it is high enough that the contamination from residual multiplicative electronics noise is negligible, and it is low enough that the TLS noise is still larger than the measured white noise floor. We fit only those carrier power measurements that passed all of the quality requirements specified above. Figure 3.14 shows the resulting best fit values of $B^2_{\rm TLS}$ as a function of resonant frequency for the six detector arrays studied during this cooldown. Noroozian et al. [126] (henceforth N09) measured $B^2_{\rm TLS} = 3.0 \times 10^{-20}$ for a nearly identical interdigitated capacitor (IDC) geometry as that used in the MUSIC resonators. The geometry has 19 fingers on each side, with a gap and center strip width $w_{\rm gap} = s_{\rm gap} = 10\ \mu$m. We display the N09 measurement as a blue dashed lined in Figure 3.14 for comparison.

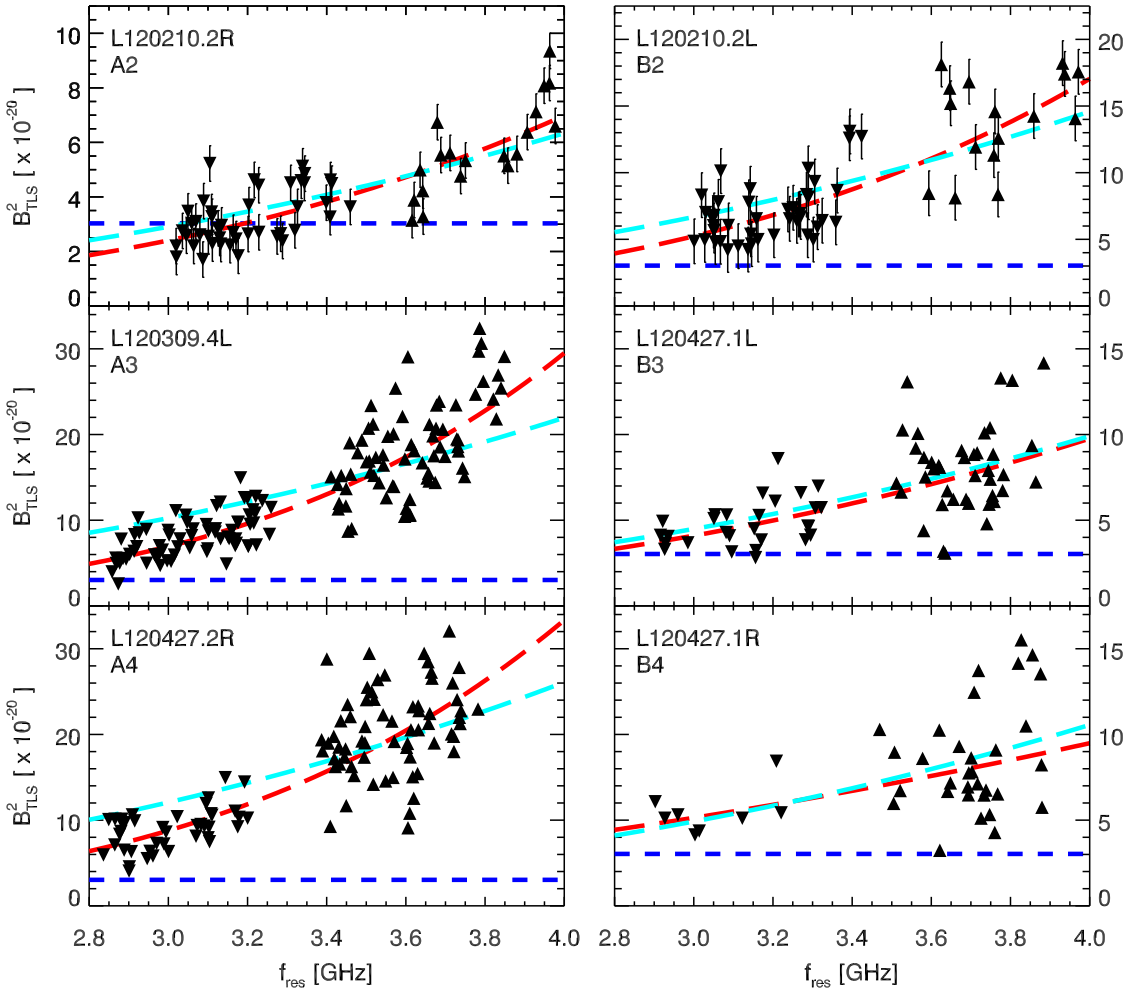

Figure 3.14: The TLS noise amplitude B^2_{TLS} as a function of resonant frequency for detectors on six of the MUSIC detector arrays. The error bars for the L120210.2R and L120210.2L arrays were determined by calculating half the average difference between estimates derived independently from two redundant data sets. The red dashed line is the best fit to a powerlaw. The dashed cyan line is the best fit to a power law with the exponent fixed at γ_{theory}. The blue dashed line is the value from Noroozian et al. [126]. Note that the y-axis range is different for the different detector arrays.

Table 3.2: The best-fit of Equation (3.29) to the measured values of $B^2_{\rm TLS}(f_{\rm res})$ for six MUSIC detector arrays.

Device ID	**Position**	$f_{\rm res,min}$ **[GHz]**	$\gamma_{\rm theory}$	γ	$A^2_{\rm TLS}$ $[\times 10^{-20}]$	$A_{\rm TLS}/A^{\rm Noroozian}_{\rm TLS}$
L120210.2R	A2	2.990125	2.71	3.7	2.37	0.89
L120210.2L	B2	3.000385	2.72	4.1	5.24	1.31
L120309.4L	A3	2.857985	2.65	5.0	5.44	1.34
L120427.1L	B3	2.915765	2.75	3.0	3.76	1.11
L120427.2R	A4	2.836008	2.68	4.6	6.77	1.49
L120427.1R	B4	2.883808	2.65	2.1	4.72	1.25

We find that $B^2_{\rm TLS}$ has a strong dependence on resonant frequency. For each detector array, we fit a power-law relationship

$$B^2_{\rm TLS}(f_{\rm res}) = A^2_{\rm TLS}\left(\frac{f_{\rm res}}{f_{\rm res,min}}\right)^{\gamma}, \tag{3.29}$$

where $f_{\rm res,min}$ is the minimum resonant frequency observed on the array. The best-fit parameters are presented in Table 3.2. We measure γ between 2.1 and 4.1 across the six detector arrays tested. The majority of this dependence is now understood as an unintended consequence of how we chose to vary the resonant frequencies. The MUSIC resonators have been scaled down to ~ 3.0 GHz from the 5.65 GHz resonator studied in N09 by increasing the length of the meandered inductor. The resonant frequency was then varied by decreasing the length/number of the fingers of the IDC. In total, the length was decreased by a factor of 2.2 in order to produce resonators that ranged from 3.0 to 4.0 GHz. The TLS noise amplitude varies inversely with the capacitor length, due to the fact that the TLS are spatially independent fluctuators whose noise adds incoherently. This inverse scaling with length results in an approximately $f_{\rm res}^{2.7}$ scaling with resonator frequency, which is not inconsistent with the best fit power laws for four out of the six detector array given the uncertainty in our measurement, as one can see from Figure 3.14. We can make a direct comparison between the lowest frequency MUSIC resonators and the resonator studied in N09, since the capacitor finger lengths are identical. We find that the ratio of the $A_{\rm TLS}$ that we measure to that measured by N09 varies between 0.9 and 1.5 across the six MUSIC detector arrays studied. Therefore, our results are consistent with those of N09, given the scatter we see between arrays.

We will use the value of $A_{\rm TLS}$ and γ calibrated with the dark dataset along with the semi-empirical model given in Equation (3.28) to predict the expected TLS noise on sky for each detector. One possible concern is that we have not confirmed the scaling with $T_{\rm bath}$ or ν. For our purpose it is not necessary to confirm the scaling with temperature because all on-sky data will be collected at approximately the same temperature as the dark dataset. However, we do need to confirm the $\nu^{-1/2}$ scaling with temporal frequency. To do so, we examine the square root of the ratio of $S^{\rm TLS}_{\delta f_{\rm res}/f_{\rm res}}$ measured at $\nu = [6.5, 1.0]$ Hz to that predicted by the model expressed in Equation (3.28) using the best fit value of $B^2_{\rm TLS}$ that we determined for each resonator. Figure 3.15 presents a histogram of this ratio for all resonators at all carrier powers. We see that at 6.5 Hz the ratio is tightly clustered around 1, as it should be since the model was calibrated using these exact measurements.

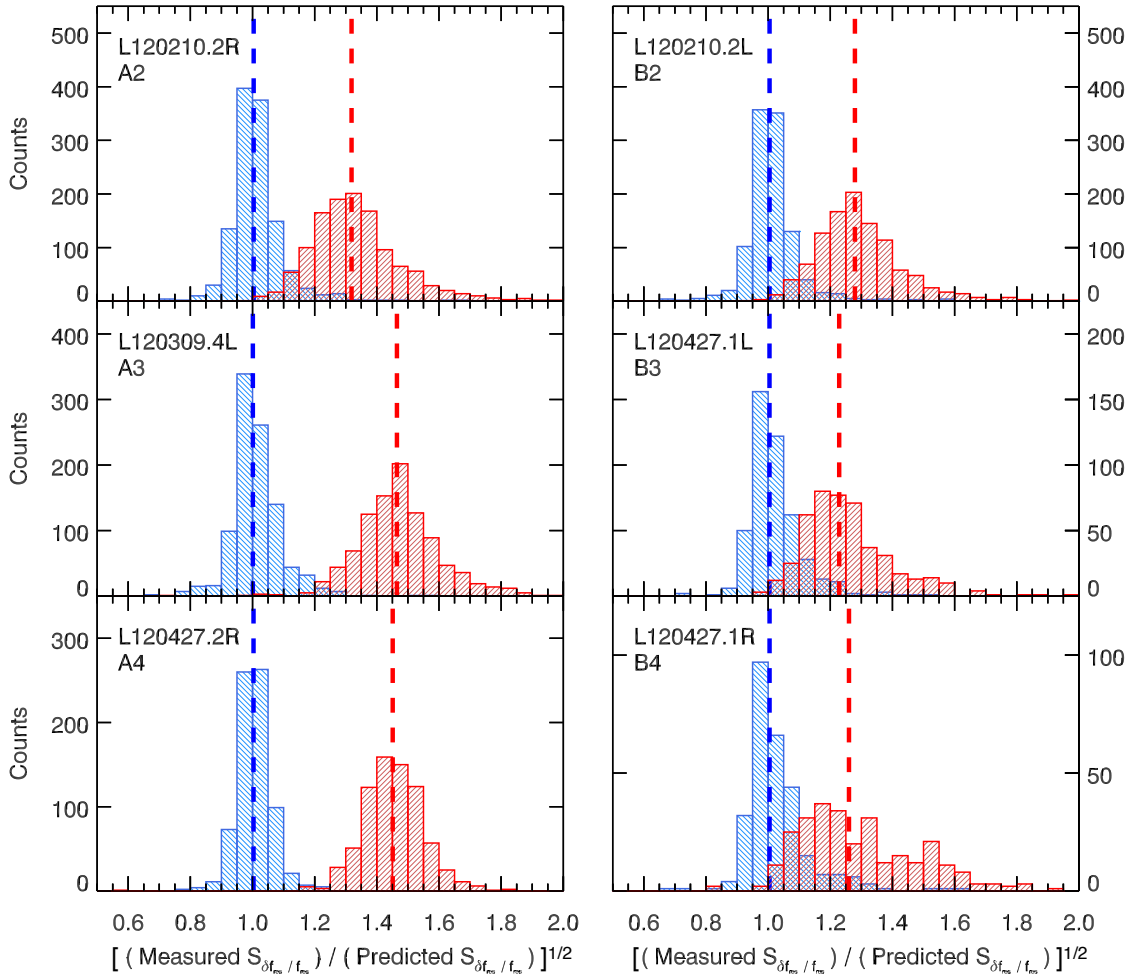

Figure 3.15: The square root of the measured value of $S_{\delta f_{\rm res}/f_{\rm res}}$ divided by the predicted value of $S_{\delta f_{\rm res}/f_{\rm res}}$ at 6.5 Hz (blue) and 1.0 Hz (red). The measured value is from the dark dataset, which we have discussed throughout this section. The predicted value is based on the TLS noise model given by Equation (3.28), which was calibrated individually for each resonator using the 6.5 Hz measurements. The histogram contains a count for each resonator at each carrier power. Only resonators that have a calibrated $B_{\rm TLS}^2$ are included in the histogram. The dashed line denotes the median value. This figure suggests a steepening of the TLS noise spectrum from the $\nu^{-1/2}$ behavior assumed by the model.

However, at 1.0 Hz the measured values are approximately 20-45% larger than that predicted assuming the $\nu^{-1/2}$ scaling. This is because at low frequencies the measured noise power spectral density transitions to a steeper ν^{-1} scaling. The transition frequency at which the $\nu^{-1/2}$ term is equal to the ν^{-1} term varies from resonator to resonator and array to array; in general we are not able to determine it precisely as the two components are degenerate. We can say that for L120427.1L and L120427.1R, which show a median ratio of 1.25, the transition frequency is less than 2 Hz. For L120210.2R and L120210.2L, which have a median ratio of 1.30, the transition frequency is less than 4 Hz. Finally, for L120309.4L and L120427.2R, which have a median ratio of 1.45, there does not appear to be a $\nu^{-1/2}$ component, and the scaling is entirely ν^{-1}.

The question then arises: does TLS noise transition to a ν^{-1} spectrum at low frequencies or is our measurement of $S^{\mathrm{TLS}}_{\delta f_{\mathrm{res}}/f_{\mathrm{res}}}$ contaminated by some other source of noise at low frequencies? The most likely source of contamination in a dark scenario is residual multiplicative electronics noise. Recall, however, that our measurements at 1.0 Hz clearly show a $P_{\mathrm{int}}^{-1/2}$ scaling, whereas multiplicative electronics noise is independent of power in these units. It is possible that the effectiveness of the noise removal algorithm is dependent on the level of uncorrelated noise present in the timestreams. In other words, it may be the case that as we increase the carrier power and decrease the TLS noise, we remove the electronics noise better, forcing a power dependence on the residual $1/f$ component. This is unlikely for several reasons. First, the electronics noise removal relies very little on the on-resonance data. The templates for the amplitude and phase fluctuations are determined entirely from the off-resonance data. The on-resonance data is only used to determine the mean carrier amplitude and phase. Second, this type of behavior is not observed in the dissipation direction, as evident in Figure 3.13. Third and perhaps most convincing, the raw electronics noise *before removal* — as measured by the off-resonance carriers — is below the excess low-frequency noise in question for the detector arrays connected to less noisy HEMTs. Finally, the excess low-frequency noise is uncorrelated between the different on-resonance carriers, whereas if the electronics noise removal was failing, we would expect some residual correlation between detectors.

There is no particular theoretical motivation for the $\nu^{-1/2}$ scaling. It is entirely empirical, and often measurements of the TLS noise are made at frequencies between 10 Hz and a few kHz. So, it is certainly possible that the TLS noise might transition to a steeper spectrum at low frequencies. There are, in fact, examples in the literature of deviations from the $\nu^{-1/2}$ scaling. Gao [93] notes that measurements of the power spectral density in the frequency direction transition from a $\nu^{-1/2}$ scaling to a ν^{-1} scaling below 10 Hz for niobium on silicon resonators. Burnett et al. [166] use a Pound locking technique to perform long timescale measurements of the resonant frequency of niobium on sapphire resonators, and measure TLS noise that has an entirely ν^{-1} spectrum. There is also theoretical motivation for a ν^{-1} scaling; Faoro and Ioffe [167] and Burnett et al. [128] develop a model for interacting TLS that predicts exactly this type of noise spectrum.

To end, we note anomalous behavior observed in two of the detector arrays, L120309.4L and L120427.2R, which have the largest values of A^2_{TLS} and the largest values of γ. The TLS noise definitely exhibits a stronger

dependence on resonant frequency than γ_{theory} for detectors on these two arrays. In addition, while the other four detector arrays have a $\nu^{-1/2}$ component to the TLS noise spectrum, these two detector arrays have a purely ν^{-1} TLS noise spectrum over the frequency range that we are able to examine ($\nu < 50$ Hz). Lastly, the detectors on these two array have large TLS-induced loss tangents. The loss tangents were extracted from dark temperature sweep measurements of $f_{\text{res}}(T)$. Normally, at the temperatures under consideration, the TLS-induced frequency shift is negligible compared to the quasi-particle-induced frequency shift. However, for the detectors on these two arrays, at low temperatures, as the temperature is increased we see a clear increase in resonant frequency. We fit the dark temperature sweep data to the sum of Equation (2.179) and Equation (2.59), and extract $F\delta^0_{\text{TLS}} \simeq 6.0 \times 10^{-5}$ for L120309.4L and $F\delta^0_{\text{TLS}} \simeq 7.8 \times 10^{-5}$ for L120427.2R. In the other four detector arrays, we are only able to place an upper bound of $F\delta^0_{\text{TLS}} \lesssim 8.0 \times 10^{-6}$.

3.3.5 Atmospheric

We now examine data collected on the telescope during the October 2012 engineering run in order to characterize the atmospheric noise. Figure 3.16 shows the power spectral density calculated from the timestream $\hat{V}(t)$ of an on-resonance carrier centered on a representative Band 1 resonator. Note that this is the raw data without filtering or noise removal. The timestream was collected during a 20-minute-long observation in which the telescope performed raster scans across a very faint source. The impact of the source on the individual resonator PSDs is negligible. Prior to calculating the PSD we rotated the timestream to the amplitude and phase basis and divided by the carrier amplitude. For comparison, Figure 3.16 also shows the PSD of the off-resonance carrier that is closest in microwave frequency to the on-resonance carrier. If multiplicative electronics noise dominated then in these units the on-resonance and off-resonance PSDs would be identical, and this does indeed appear to be the case at intermediate temporal frequencies in the amplitude direction. However, there is clearly excess noise present in the on-resonance data. We know that the noise that dominates at higher frequencies is due to TLS based on our results from the previous section. But at low frequencies, the PSDs clearly transition to a much steeper spectrum that has a slope consistent with $\nu^{-8/3}$. In Section 2.3.2.3 we showed that the K-T thin screen model for atmospheric noise predicts exactly a $\nu^{-8/3}$ scaling in the 2D regime, which holds if $\nu \ll \frac{h_{\text{avg}}|\boldsymbol{w}|}{2\Delta h \sin \mathfrak{e}}$.

In addition, the noise fluctuations that exhibit this steep $\nu^{-8/3}$ spectrum occur in a well-defined direction in the complex plane. We examined the angle $\theta_1(\nu)$ of the eigenvector corresponding to the largest eigenvalue of the cross-power spectral density matrix for the on-resonance data. This technique was introduced in Section 3.3.4 where we employed it to the study of TLS noise. At low frequencies $\theta_1(\nu)$ converges to a fixed value that is slightly rotated from the frequency direction. This is exactly what one would expect for atmospheric noise, which would lie in the quasi-particle direction.

We have shown that the noise fluctuations that dominate the on-resonance timestreams at low frequencies have a $\nu^{-8/3}$ spectrum and appear in a direction in the complex plane that is roughly consistent with the quasi-particle direction. One final expectation of atmospheric noise discussed in Section 2.3.2.3 is that it

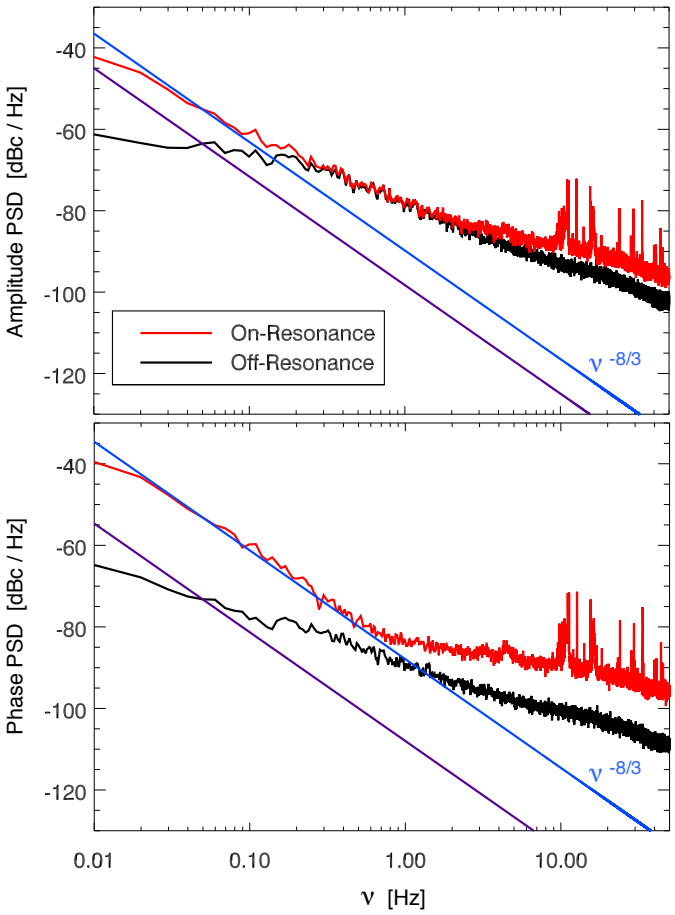

Figure 3.16: Power spectral density of the noise affecting an on-resonance carrier (red) and off-resonance carrier (black) in the amplitude (top) and phase (bottom) direction in units of dBc/Hz. The on-resonance carrier was centered on a Band 1 resonator on L120210.2L with a resonant frequency $f_{\rm res} = 3.06174$ GHz. The off-resonance carrier was separated by approximately 4 MHz from the on-resonance carrier. The data was collected during a 20-minute-long observation in which the telescope performed raster scans across a faint source. The elevation angle of the telescope was $\mathfrak{e} = 70^{\circ}$ and the atmospheric opacity at 225 GHz was $\tau_{225} = 0.075$. The blue and purple lines denote a $\nu^{-8/3}$ scaling with temporal frequency normalized to the value of the PSD at 50 mHz.

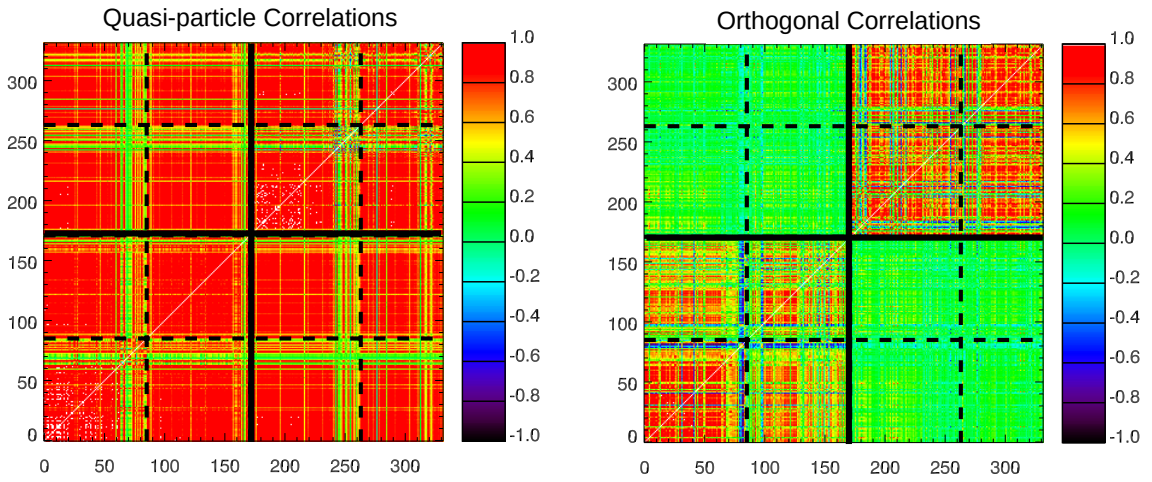

Figure 3.17: Pearson correlation coefficients between the 327 on-resonance carriers probing L120210.2R and L120210.2L. Only the carriers centered on antenna coupled resonators are shown. The quasi-particle direction is shown on the left and the orthogonal direction is shown on the right. Dashed black lines separate the different readout boards. Solid black lines separate the different detector arrays: L120210.2R corresponds to carriers numbered 0-161, and L120210.2L corresponds to carriers numbered 162-326. The correlation coefficients were calculated in the Fourier domain using only temporal frequencies between 0.02 Hz and 0.20 Hz. The data was collected during a 20-minute-long observation in which the telescope performed raster scans across a faint source. The elevation angle of the telescope was $\mathfrak{e} = 35^\circ$ and the atmospheric opacity at 225 GHz was $\tau_{225} = 0.12$.

should be correlated across detectors. In order to investigate whether the steep low-frequency noise is correlated, we use the weighted mean of $\theta_1(\nu)$ at low frequencies as an estimate of the quasi-particle direction $\hat{\theta}_{\rm qp}$. We rotate the timestreams to the quasi-particle and orthogonal basis. We then calculate the Pearson correlation coefficients between all on-resonance carriers in this basis. The correlation coefficients are calculated in the Fourier domain using only frequencies between 0.02 Hz and 0.20 Hz where the noise of interest dominates. The results are presented in Figure 3.17. Directing our attention first to the quasi-particle direction we find that the majority of detectors are almost perfectly correlated with each other. Apart from a handful of anomalous detectors, this high degree of correlation persists across observing band, readout board, and detector array. Next, examining the orthogonal direction, we see that it looks similar to the correlation matrices for the off-resonance carriers presented in Figure 3.11. The crucial piece of evidence is that detectors on different arrays are highly correlated in the quasi-particle direction, but almost completely uncorrelated in the orthogonal direction (as is the case for off-resonance carriers). This means that the low-frequency noise appearing in the quasi-particle direction cannot be multiplicative electronics noise.

We have shown that noise due to fluctuations in atmospheric emission dominates at low frequencies and appears in a well-defined direction in the complex plane. The high degree of correlation over the focal plane and between different observing bands bodes well for the atmospheric noise removal.

Chapter 4

MUSIC Detector Characterization

4.1 Introduction

We have calibrated the full instrument model described in Chapter 2 using the procedure outlined in Chapter 3 for the detectors on the science-grade MUSIC arrays. This chapter presents the results of the calibration procedure. The science-grade arrays were fabricated in 2012. The yield from the initial fabrication run was lower than expected, with many of the arrays suffering from feedline discontinuities. These discontinuities were, for the most part, eliminated in subsequent fabrication runs by improving the cleaning process between fabrication steps. In total, six arrays were produced that have both feedline continuity and high resonator yield. Recall that a single array is 6×12 pixels, with each pixel sensitive to four bands, for a total of 288 resonators. Approximately 95% of the designed resonators are identified in network analyzer sweeps for each of the six arrays. The arrays are subdivided into two half-bands, with 144 resonators per half-band. The lower half-band contains resonators between approximately $3 - 3.4$ GHz and the upper half-band contains resonators between approximately $3.6 - 4.0$ GHz. The two half-bands share a HEMT and coaxial cable, but are read-out using different electronic boards. The division is a result of the approximately 450 MHz bandwidth of the readout electronics, which is set by the sampling rate of the ADC.

The detector arrays are identified by a name of the format L[DATE].[WAFER#][L/R], where [DATE] is the date that the array was fabricated, [WAFER#] is an integer that differentiates between wafers produced on that date, and [L/R] indicates whether the array was on the left/right side of the wafer. The position of the detector arrays in the focal plane unit (FPU) has not changed since September 20, 2012. All results presented in this thesis were collected after that date, so we will often refer to the arrays by their position in the FPU, which has two rows (A-B) and four columns (1-4). In most cases, we will quote separate results for the lower and upper half band. As an example, A2L and A2U refer to the lower and upper half band of the detector array in row A, column 2.

4.2 Science-grade Arrays

4.2.1 ε Test Devices

Each detector array contains six ε test devices. These are lumped-element LC resonators that are inductively coupled to the feedline. They use parallel-plate capacitors that are fabricated from the same dielectric layer that is used for the antennas and bandpass filters. The capacitors are large enough that edge effects are negligible. As a result, the resonant frequencies of the test devices are given by

$$f_{\text{res}} = \frac{1}{2\pi\sqrt{LC}} = \frac{1}{2\pi}\sqrt{\frac{d}{LA\varepsilon}}\,, \tag{4.1}$$

where L is the inductance, A and d are the area and thickness of the capacitor, ε is the dielectric constant, and $C = A\varepsilon/d$ is the capacitance. Note that we have good control over the area of the capacitor. Assuming that the inductance does not vary appreciably between fabrication runs, a comparison of the resonant frequencies of the test devices on different detector arrays yields a measurement of the relative change in the ratio ε/d of the dielectric. In addition, the internal quality factor Q_i of the test devices yields a measurement of the dielectric loss tangent.

The ε test devices are designed to have resonant frequencies between $5-8$ GHz, which places them above the detectors and below the α test devices. In order to vary the resonant frequencies of the six test devices, the area of the capacitor is scaled according to Table 4.1. We were able to identify a subset of the test devices in vector network analyzer measurements of the forward transmission through the science-grade detector arrays. The expected frequency spacing was used to distinguish the test devices from spurious niobium resonances. Three of the six arrays had at least two resonators in the designed frequency range with approximately the correct frequency spacing.

In July 2012, we measured the complex transmission near the resonant frequencies of the ε test devices with a vector network analyzer at six temperatures between 240 and 470 mK. The output power was set to -55 dBm, corresponding to approximately -95 dBm on the feedline at the resonator. The squared magnitude of the transmission is fit to the skewed Lorentzian profile given by Equation (3.2), and the frequency, internal

Table 4.1: Designed area, area ratio, and frequency ratio of the ε test devices.

ε ID	Capacitor Dimension [μm $\times$ μm]	Area Ratio	Frequency Ratio
1	140 x 156	1.20	0.91
2	140 x 143	1.10	0.95
3	140 x 130	1.00	1.00
4	140 x 94	0.72	1.18
5	140 x 86	0.66	1.23
6	140 x 78	0.60	1.29

Table 4.2: Results from analysis of the ε test device temperature sweeps. The quantities $f_{\text{res},0}$ and $F\delta^0_{\text{TLS}}$ are obtained by fitting the measured $f_{\text{res}}(T_{\text{bath}})$ curve to the TLS model given by Equation (2.179). The quantities Q_c, Q_i, and $1/Q_i$ are approximately independent of temperature, and the quoted values are the inverse variance weighted mean of the measurements at six different temperatures.

Device ID	**Position**	**ε ID**	**$f_{\text{res},0}$ [GHz]**	**$f_{\text{res},0}$ Ratio**	**Q_c**	**Q_i**	**$1/Q_i$**	**$F\delta^0_{\text{TLS}}$**
Xa		1	5.765990	0.919	13,870	10,430	9.58e-5	8.83e-4
		2	6.030539	0.961	9,577	26,060	3.84e-5	8.82e-4
		3	6.277488	1.000	18,200	9,250	1.08e-4	8.69e-4
L120210.2R	A2	1	5.574707	0.914	21,473	6,680	1.50e-4	1.13e-3
		2	5.843750	0.958	27,025	13,680	7.31e-5	1.18e-3
		3	6.102553	1.000	13,600	7,540	1.33e-4	1.15e-3
L120427.1L	B3	2	5.875316		10,420	15,120	6.61e-5	1.11e-3
		3	6.127498		6,375	4,540	2.20e-4	1.03e-3
L120427.1R	B4	2	5.820225		12,854	15,000	6.61e-5	1.10e-3
		4	7.457972		13,910	8,060	1.24e-4	1.07e-3

quality factor, and coupling quality factor are extracted. Since the test devices are entirely niobium, the quasi-particle density is negligible at the bath temperatures examined, and the resonant frequency is set by the resonant response of TLS. We fit the $f_{\text{res}}(T_{\text{bath}})$ curve to the TLS model given by Equation (2.179) to obtain the resonant frequency $f_{\text{res},0}$ and the quantity $F\delta^0_{\text{TLS}}$, which is the product of the dielectric filling factor F and the TLS-induced loss tangent δ^0_{TLS}. Note that for the test devices the aspect ratio of the capacitor is large enough that $F = 1$ is an excellent approximation. We show an example of the data and best-fit TLS model for a single test device on L120210.2R in Figure 4.1. The other test devices show similar behavior. We summarize the results for all test devices found on the MUSIC detector arrays in Table 4.2. To provide a point of comparison, we also summarize the results from an identical analysis of the test devices on an engineering grade detector array, Device Xa. The Device Xa data was collected in March 2011.

Device Xa also employed a Si_3N_4 dielectric. The measured band centers of the detectors on Device Xa implied $\varepsilon = 7.0$ assuming the designed thickness $d = 400$ nm [102]. We find that the resonant frequencies on the test devices have decreased by 3% between Device Xa and L120210.2R. This suggests a 6% increase in the dielectric constant to $\varepsilon = 7.42$ (or, alternatively, a 6% decrease in the dielectric thickness to $d = 376$ nm, or some combination of the two). The bandpass filter design for the detectors on the science-grade arrays was adjusted based on the observed Device Xa bandpasses. As a result, the change in the ratio of ε/d implied by the ε test device measurement will result in a shift in the L120210.2R band centers from the desired values. We confirm that the L120210.2R band centers have shifted using FTS and discuss the implications in Section 4.2.2. We also measure a 30% increase in the TLS-induced loss tangent δ^0_{TLS} between Device Xa and the science-grade detector arrays.

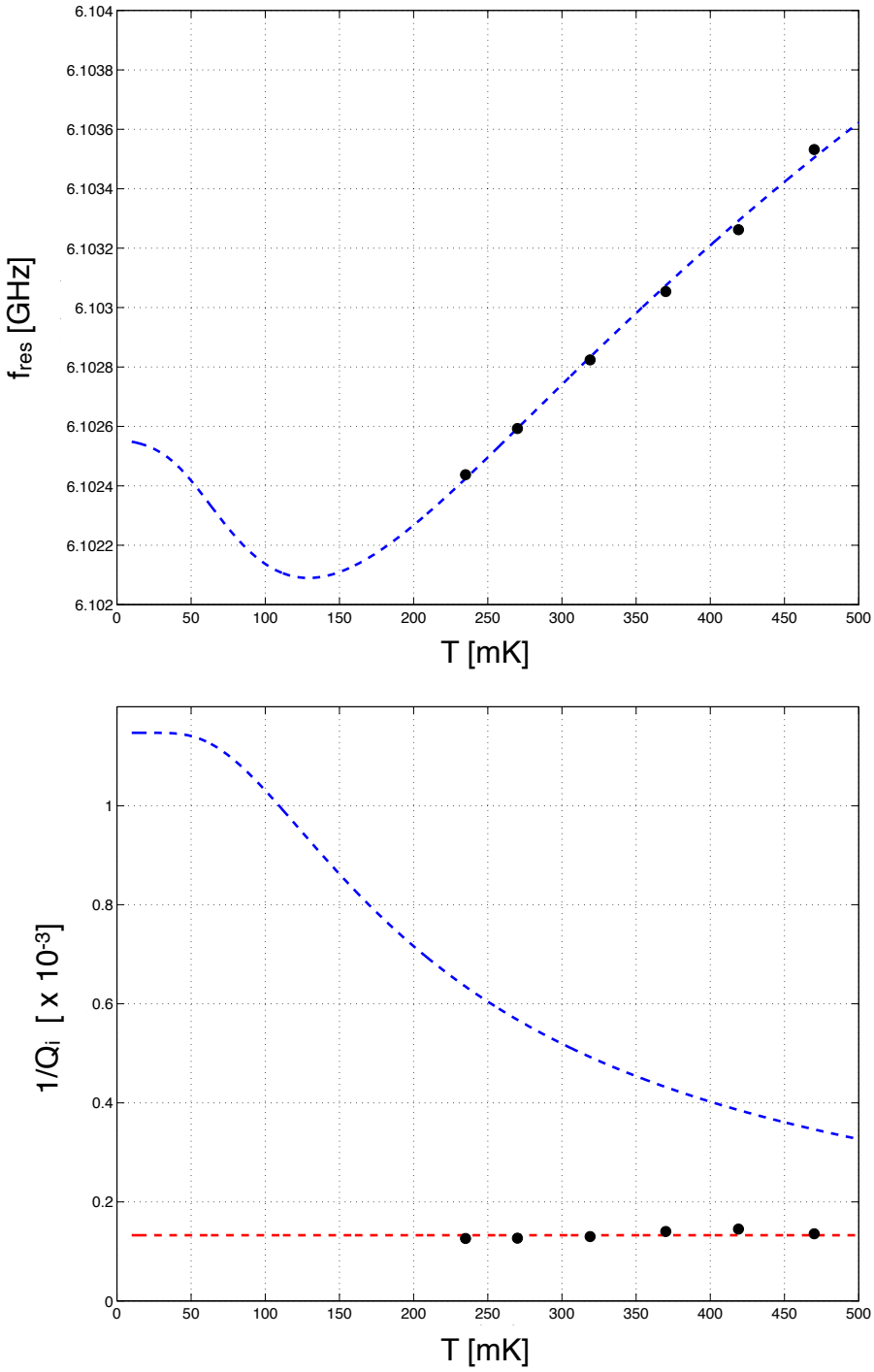

Figure 4.1: *Top:* Resonant frequency as a function of temperature for ε test device number 3 on L120210.2R. The black circles denote the measured values. Error bars are smaller than the radius of the circle. The blue dashed line denotes the best fit of the data to Equation (2.179). Over the temperature range that we are able to probe, the resonant response of the TLS results in an approximately linear increase in the resonant frequency with temperature. *Bottom:* Internal resonator loss as a function of temperature for the same test device. We measures an internal resonator loss that is constant with temperature. This is in contradiction with our expectation based on the frequency shift data, the TLS model, and our assumption of low carrier power, which is shown as the blue dashed line. The red dashed line is the inverse variance weighted mean of the measured data points.

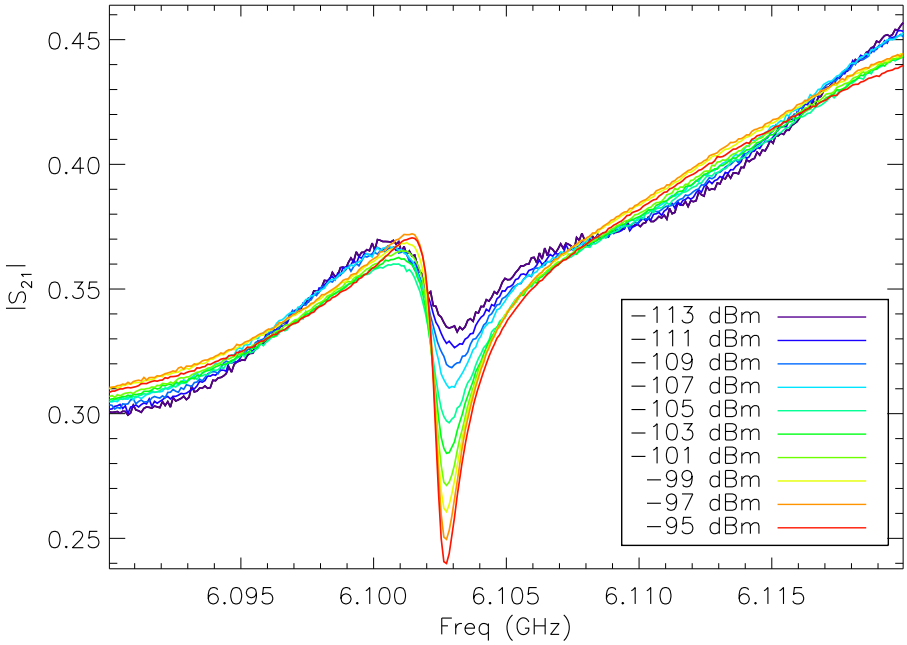

Figure 4.2: The magnitude of the transmission as a function of frequency for ε test device number 3 on L120210.2R. The different colors denote different powers on the feedline at the device.

4.2.1.1 Power Dependence

The ε test devices have internal quality factors that are constant with temperature. If we use the best-fit value of $F\delta_{\rm TLS}^0$ determined from the frequency shift data to predict the TLS-induced dielectric loss using Equation (2.178) and assuming low carrier power so that $(|\boldsymbol{E}|/E_c)^2 \ll 1$, we find that our prediction is larger than what is measured and also has significant temperature dependence. This is illustrated in Figure 4.1. The TLS-induced loss is expected to saturate with electric field strength, as discussed in Section 2.3.2.2. The observed behavior could be explained if $(|\boldsymbol{E}|/E_c)^2 \gg 1$. In this case, we have fully saturated the TLS-induced loss and are dominated by some other temperature independent source of loss inherent to the test devices. In order to test this hypothesis, we used a vector network analyzer to measure the complex transmission near the resonant frequencies of the three test devices on L120210.2R as a function of power at base temperature (240 mK). We collected measurements at 10 powers between -113 dBm and -95 dBm on the feedline at the resonator. The results are consistent for the three test devices. We show the magnitude of the transmission near resonance as a function of power for one of the test devices in Figure 4.2. Note that the measurements at low power require a long integration time and many averages due to a low signal-to-noise ratio. We find that the internal quality factor does indeed decrease with power, presumably due to an increase in the TLS-induced loss, whereas both the resonant frequency and coupling quality factor are approximately independent of power. These results are illustrated in Figure 4.3. Unfortunately, we are unable to collect measurements at the low carrier powers required to satisfy $(|\boldsymbol{E}|/E_c) \ll 1$. As a result, we do not see the loss-tangent inferred from the quality factor data converge to the loss-tangent inferred from the frequency shift data.

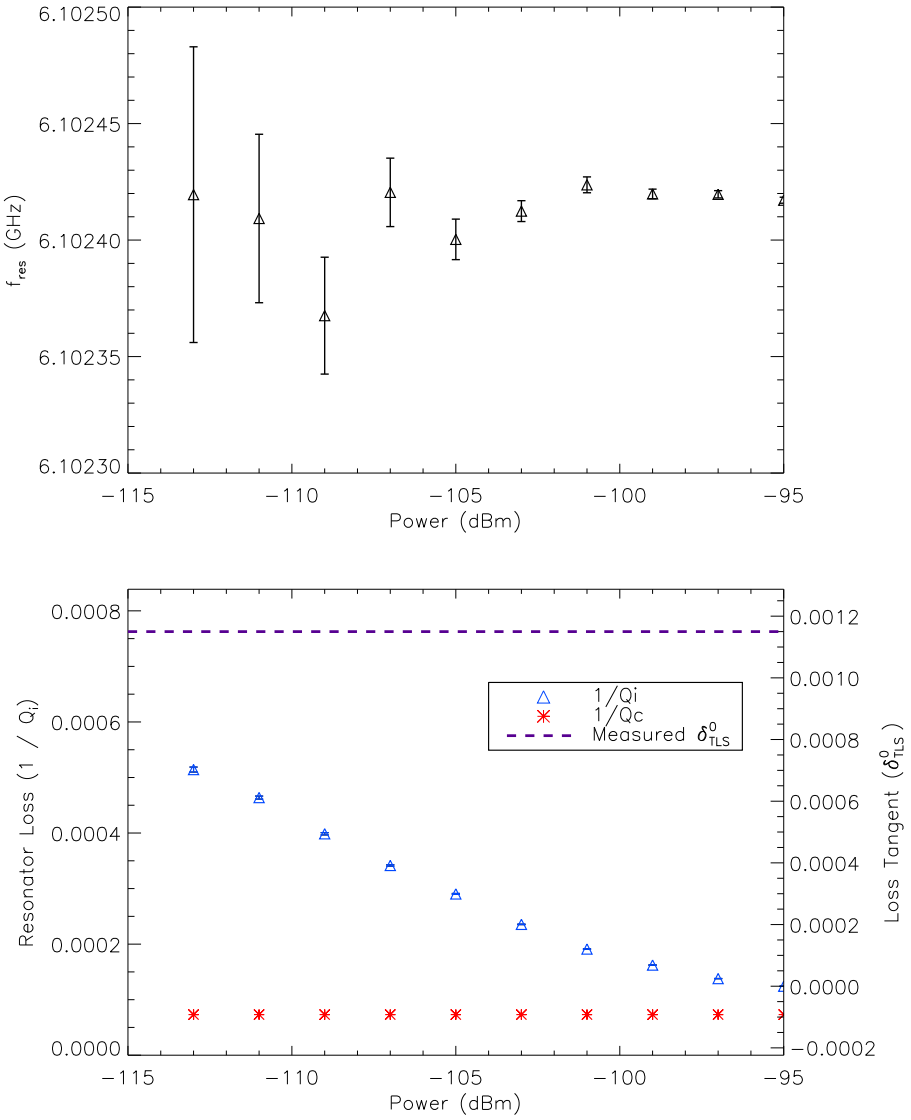

Figure 4.3: *Top:* Resonant frequency as a function of carrier power on the feedline at the device for ε test device number 3 on L120210.2R. *Bottom:* Resonator loss as a function of carrier power on the feedline at the device for the same test device. Blue triangles denote the internal resonator loss. Red asterisks denote the loss due to coupling to the feedline, which is approximately independent of power. The purple dashed line denotes the expectation for the TLS-induced loss in the low power limit based on analysis of the frequency shift data.

4.2.2 FTS

We collected FTS data over the course of three days, between 2013/07/27 and 2013/07/29. We obtained 22 datasets in total, varying the position of the SPIDER FTS apparatus with respect to the cryostat window. We collected an IQ sweep and re-centered the carriers on-resonance approximately every other dataset. For each dataset, the carriage carrying the mirror was set to scan the central 280 mm of the 300 mm long stage, and then return. This was repeated $N_{\text{cycle}} = 8 - 12$ times, so that each dataset contained $N_{\text{scan}} = 16 - 24$ interferograms. For each scan, the carriage followed a trapezoidal velocity profile in which it accelerated at 2.5 mm/sec/sec to a maximum velocity of 8.75 mm/sec/sec, traveled at constant velocity for approximately 250 mm, and then decelerated at 2.5 mm/sec/sec. There was no difference in the resulting spectra between forward and backward scans.

The FTS was only capable of illuminating a small fraction of the detectors at once (roughly one device half-band). In an attempt to obtain bandpasses for all detectors, we collected 22 datasets over a grid of positions relative to the center of cryostat window. Our control over the position of the apparatus was fairly crude and not entirely repeatable, so the following alignment process was carried out before collecting each dataset. We set the carriage to the center of the stage, where the two paths of the FTS have equal lengths. This is the location where constructive interference is maximum and is commonly referred to as the white light fringe. We began collecting data and monitored it in real time for a subset of detectors that were evenly spaced over the particular device half-band that we hoped to illuminate at that particular apparatus position. We then waved a room temperature Eccosorb® wand back-and-forth in front of the FTS LN_2 load. If the detectors were well coupled to the LN_2 load, then the difference in temperature between the room temperature wand and the LN_2 load created a noticeable signal in the detector timestreams. We fine tuned the position of the apparatus so that the room-temperature-wand signal was maximized in a significant number of the detector timestreams. The central part of the focal plane unit was much easier to illuminate than the edges. The lower half-bands of A2, A3, B2, and B3 were easily aligned and have high-quality spectra. In order to align the upper half-bands of these four detector arrays, we had to direct the FTS beam into the cryostat at an angle. This was accomplished by rotating the cryostat slightly with respect to vertical. After doing so, we were able to obtain high-quality spectra for the upper half-bands of A2, A3, B2, and B3. In order to align the A4 and B4 detector arrays, we had to direct the FTS beam into the cryostat at an angle orthogonal to the rotational freedom of the cryostat. This was achieved by adjusting the angle of the last mirror with respect to horizontal from 45° to 50°. While the room-temperature-wand signal was observed in the detector timestreams for these two arrays, few interferograms were detected, and we were only able to obtain spectra for a handful of detectors. The number of detectors on each device half-band that measured at least one interferogram is presented in the top panel of Figure 4.4.

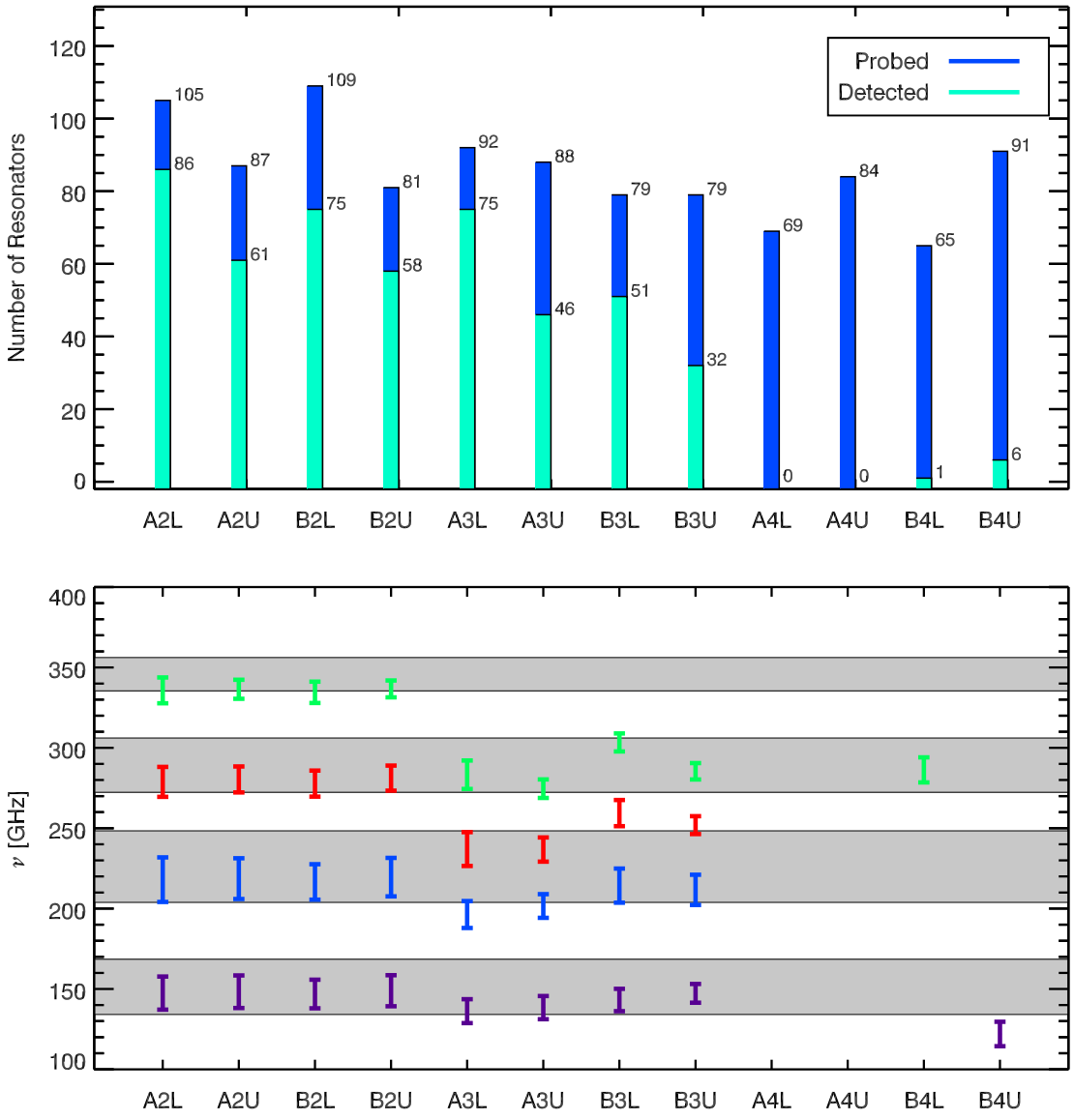

Figure 4.4: *Top:* The number of resonators on each device half-band that were probed during the FTS measurements (blue) and measured at least one interferogram (green). *Bottom:* The median band center and effective band width for the resonators on each device half-band. The different colors denote the four MUSIC observing bands. The gray boxes denote the designed bandpasses.

We focus on datasets that have a white light fringe clearly visible in at least one detector timestream. Of the 22 datasets, 15 satisfy this criteria. Analysis of each dataset proceeds as follows:

- We determine the frequency direction $\widehat{\theta}_{\text{freq}}$ and conversion factor $\widehat{A}_{\text{freq}}$ for each resonator from the most recent IQ sweep using the technique outlined in Section 3.3.4. We rotate the data to the frequency direction and convert to fractional resonant frequency fluctuations. We apply all further analysis to the frequency component alone.
- We examine the half-band-averaged timestreams by eye in order to determine the location of the N_{scan} white light fringes.
- We extract a 28.5 second block of time centered on each white light fringe from the timestream. This corresponds to the 250 mm where the carriage was traveling at its maximum velocity (8.75 mm/sec).
- We fit a polynomial to each block of time and then subtracted it to remove the large scale features caused by changes in loading as the mirror moved across the stage.
- We apply a Hanning window to each block of time and then calculated the PSD. We average the PSDs for the N_{scan} blocks of time together to obtain a final estimate of the PSD for each resonator for each dataset.
- We run a peak finding algorithm on the PSDs. We apply a cut on the peak-height-to-continuum ratio, peak width, and peak location to find the actual spectra.
- We take the square root of the PSD.
- We mask the peaks and fit the continuum noise level to the model given by Equation (3.24). We subtract the best fit model and then normalize by the maximum value to obtain an estimate of the transmission.
- We use Equation (3.14) to convert from temporal frequency to millimeter-wave frequency. We then multiply the millimeter-wave frequency by a factor of 1.0261 to correct for velocity miscalibration (see Section 3.2.4).

If a resonator has spectra in multiple datasets, then we average them together, weighting by the peak-height-to-continuum ratio.

We calculate the band center and effective bandwidth for each resonator as

$$\nu_{\text{mm,ant}} = \frac{\int \text{FTS}(\nu)\ \nu\ d\nu}{\int \text{FTS}(\nu)\ d\nu} \qquad\qquad \Delta\nu_{\text{mm,ant}} = \int \text{FTS}(\nu)\ d\nu\ , \tag{4.2}$$

where $\text{FTS}(\nu)$ denotes the measured bandpass. The median values of these two quantities are illustrated in Figure 4.4 and presented in Table 4.3 for each device half-band. We also display the average bandpass in Figures 4.5-4.6. In both the figures and the table we compare the measured bandpasses to the designed bandpasses.

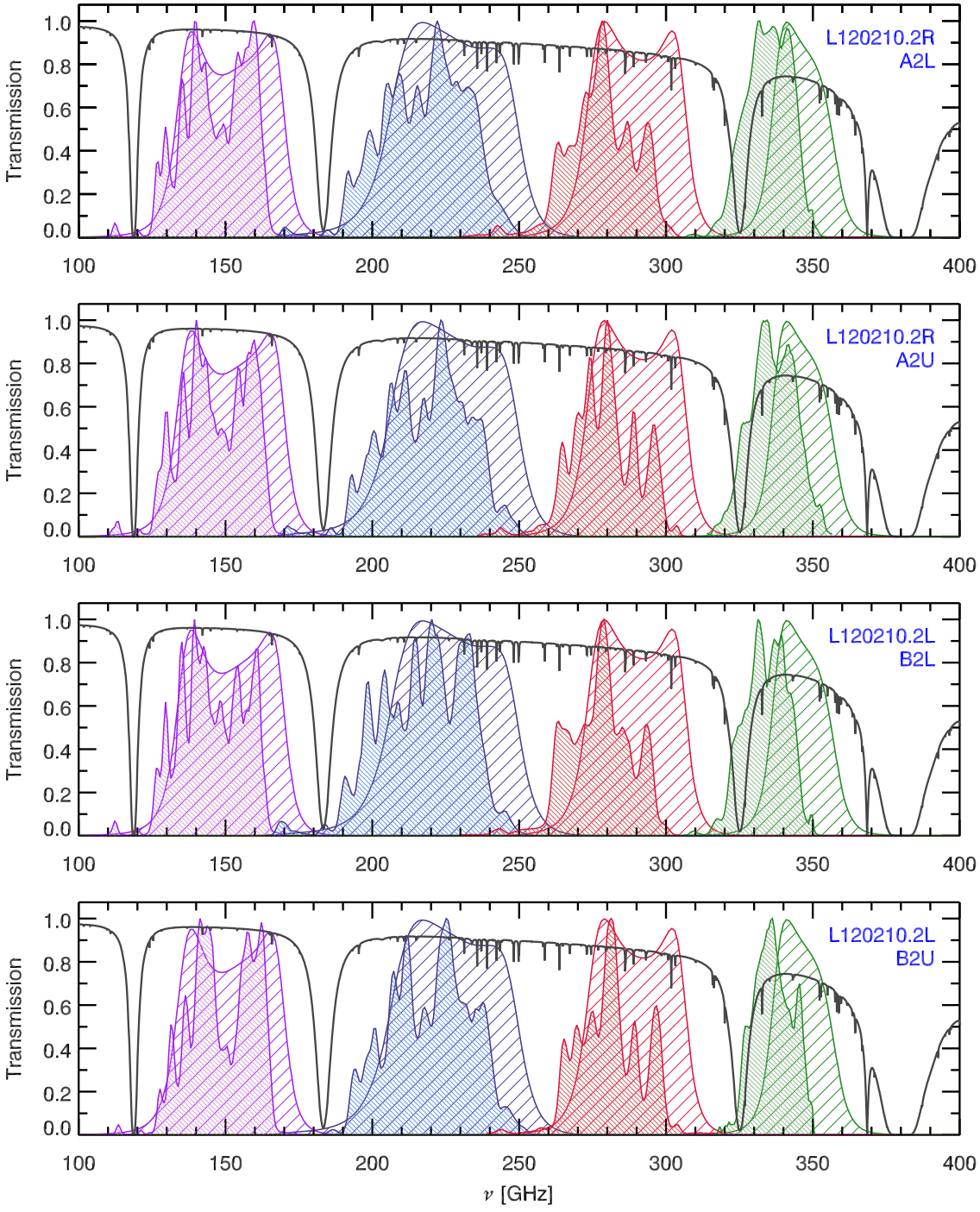

Figure 4.5: MUSIC bandpasses for the L120210.2R and L120210.2L detector arrays. The different colors denote the four observing bands. The solid-filled regions show the measured bandpasses and the hashed-filled regions show the designed bandpasses. Overlaid on each plot is the atmospheric transmission spectrum at the CSO for 1.68 mm precipitable water vapor (historical median). The measured bandpasses were obtained by averaging over all detectors on the specified device half-band.

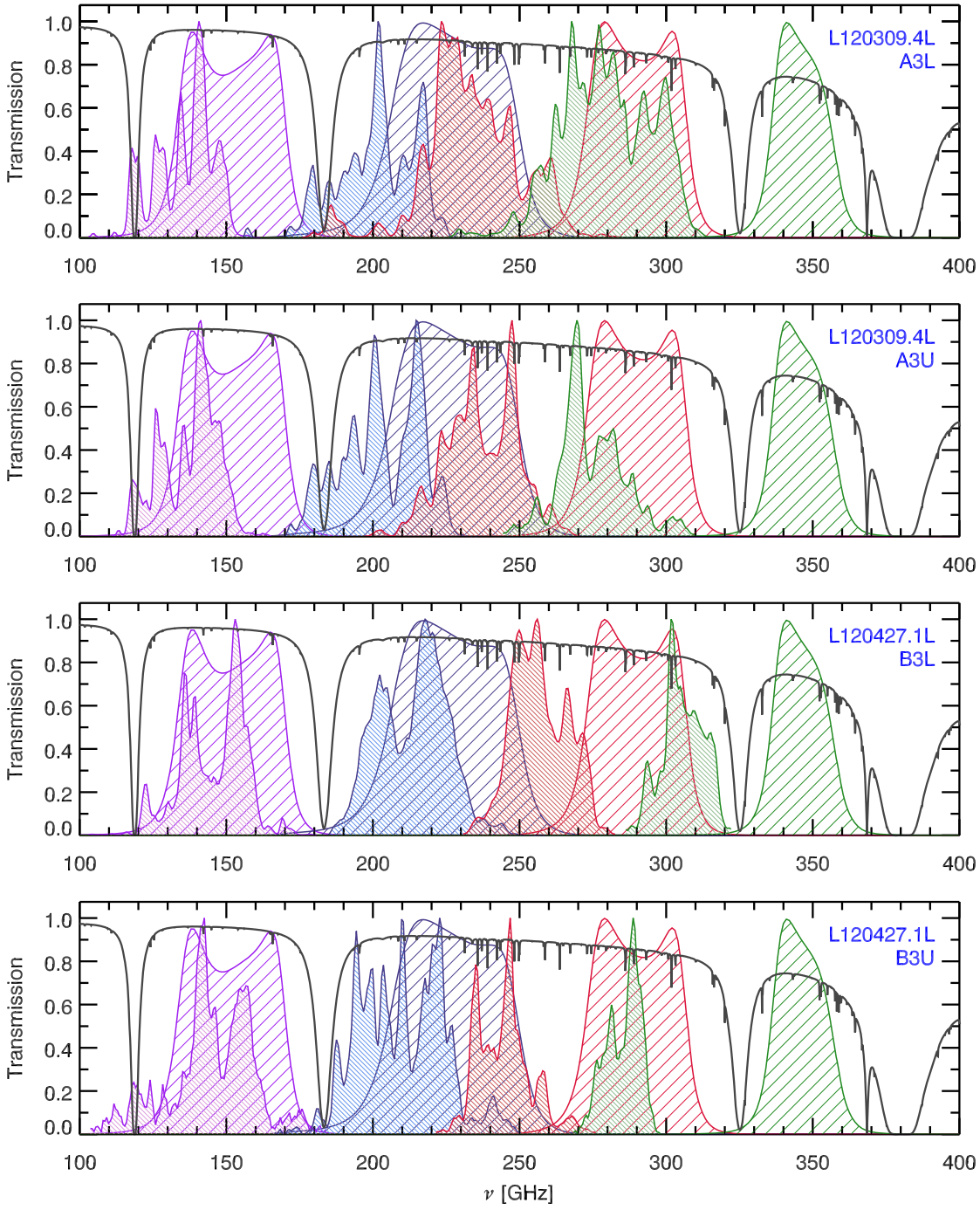

Figure 4.6: MUSIC bandpasses for the L120309.4L and L120427.1L detector arrays. The different colors denote the four observing bands. The solid-filled regions show the measured bandpasses and the hashed-filled regions show the designed bandpasses. Overlaid on each plot is the atmospheric transmission spectrum at the CSO for 1.68 mm precipitable water vapor (historical median). The measured bandpasses were obtained by averaging over all detectors on the specified device half-band.

Table 4.3: The median band centers and effective band widths for four of the MUSIC detector arrays.

		$\nu_{\mathrm{mm,ant}}$ [GHz]			
Device ID	Position	Band 0	Band 1	Band 2	Band 3
Designed		151.3	226.1	289.3	345.8
L120210.2R	A2	147.6	218.2	279.3	335.9
L120210.2L	B2	148.3	217.8	280.2	334.7
L120309.4L	A3	137.1	198.2	237.0	278.9
L120427.1L	B3	144.2	212.8	257.2	303.1

		$\nu_{\mathrm{mm,ant}}$ [Measured / Designed]			
Device ID	Position	Band 0	Band 1	Band 2	Band 3
L120210.2R	A2	0.98	0.96	0.97	0.97
L120210.2L	B2	0.98	0.96	0.97	0.97
L120309.4L	A3	0.91	0.88	0.82	0.81
L120427.1L	B3	0.95	0.94	0.89	0.88

		$\Delta\nu_{\mathrm{mm,ant}}$ [GHz]			
Device ID	Position	Band 0	Band 1	Band 2	Band 3
Designed		34.3	44.5	33.8	20.7
L120210.2R	A2	20.5	26.5	17.6	13.6
L120210.2L	B2	18.0	23.5	16.0	12.4
L120309.4L	A3	14.5	16.0	17.1	14.2
L120427.1L	B3	11.7	20.0	14.1	10.7

		$\Delta\nu_{\mathrm{mm,ant}}$ [Measured / Designed]			
Device ID	Position	Band 0	Band 1	Band 2	Band 3
L120210.2R	A2	0.60	0.60	0.52	0.66
L120210.2L	B2	0.53	0.53	0.47	0.60
L120309.4L	A3	0.42	0.36	0.51	0.68
L120427.1L	B3	0.34	0.45	0.42	0.52

We find that the measured band centers shifted downward in frequency by $\simeq 3\%$ from the designed band centers for the A2 and B2 array. This downward shift was caused by an increase in the ratio of the dielectric constant ε to the thickness d of the Si_3N_4 dielectric used for the science-grade detector array. Measurements of the ε test devices on the A2 detector array confirm this explanation, showing an increase of 6% in ε/d between the final engineering-grade tiles and the science-grade tiles, as discussed in Section 4.2.1. The impact of this shift on the 150, 225, and 290 GHz observing bands is minimal; however, the 345 GHz band shifted far enough that it has significant overlap with a water absorption line at $\simeq 325$ GHz. As a result, the sensitivity of the 345 GHz observing band is noticeably degraded.

Clearly something more insidious is affecting the A3 and B3 band centers. We find that for these two detector arrays, the ratio of the measured to designed band center is band dependent. This results in the 150 and 225 GHz band spilling into each other, and the 345 GHz band being far from the desired location.

This variation in the location of the band centers makes analysis of science data collected with these arrays difficult. Although we were unable to obtain FTS measurements for a significant number of detectors on the A4 and B4 arrays, measurements of the response to hot and cold loads suggest that the bandpasses for these arrays exhibit similar behavior to that seen in A3 and B3. Because of this, we have chosen to pursue science observations with the A2 and B2 arrays only. *The remainder of this thesis will focus on calibration of the detectors on the A2 and B2 arrays.*

The effective bandwidth ranges from 47% to 66% of the designed bandwidth for the A2 and B2 detectors. The is due to modest fringing, clearly visible in Figures 4.5-4.6. Simulations of the bandpass filter, which are also shown in Figures 4.5-4.6, do not display fringes. Vector network analyzer measurements at microwave frequencies of a scaled version of the bandpass filter design are also free of fringes [102]. This suggests that the source is not the actual filter, but rather the optical chain. Based on the frequency separation of adjacent fringes, we suspect that the fringing originates from standing waves in the dielectric filters.

4.2.3 Yield

The MUSIC readout electronics are used to collect network analyzer (NA) sweeps of each detector array. NA sweeps are measurements of the complex transmission through the system over the entire range of microwave frequencies where we expect to find resonances (approximately $3-4$ GHz). They are simply IQ sweeps with the carrier tones distributed approximately uniformly across the readout bandwidth and the number of points in the sweep chosen such that the range of frequencies each carrier tone sweeps out overlaps slightly with its two neighbors. They are typically collected with a resolution of 7.5 kHz. This is the first measurement made during both the dark and optical cooldowns. A peak finding algorithm is applied to the NA sweep to identify the location of the resonances. The NA sweep is then scanned by eye to ensure that no resonances were missed by the peak finding algorithm. NA sweeps of the A2 and B2 detector arrays are shown in Figure 4.7.

Table 4.4 presents the detector yield of the A2 and B2 arrays. Each array is designed to have 288 resonators. We find $\simeq 95\%$ of the designed resonances in the NA sweeps. We place an initial cut to remove collisions: pairs of resonances that are too close to each other. We use a < 200 kHz cut on frequency separation to identify a collision, which on average corresponds to $\lesssim 2.5$ FWHM. The remaining $\simeq 80\%$ of the designed resonances are read out during observations; however, additional cuts are used to determine which resonances will be used for map making. We cut resonances that deviate from the skewed Lorentzian shape, have low quality factors, or bifurcate at low readout powers, resulting in 66% of the number designed. We then cut resonances that are outliers in terms of their noise and response performance. This leaves approximately 57% of the number designed. However, some fraction of these correspond to dark resonators; the number of antenna coupled resonators that pass all cuts is approximately 49% of the number designed.

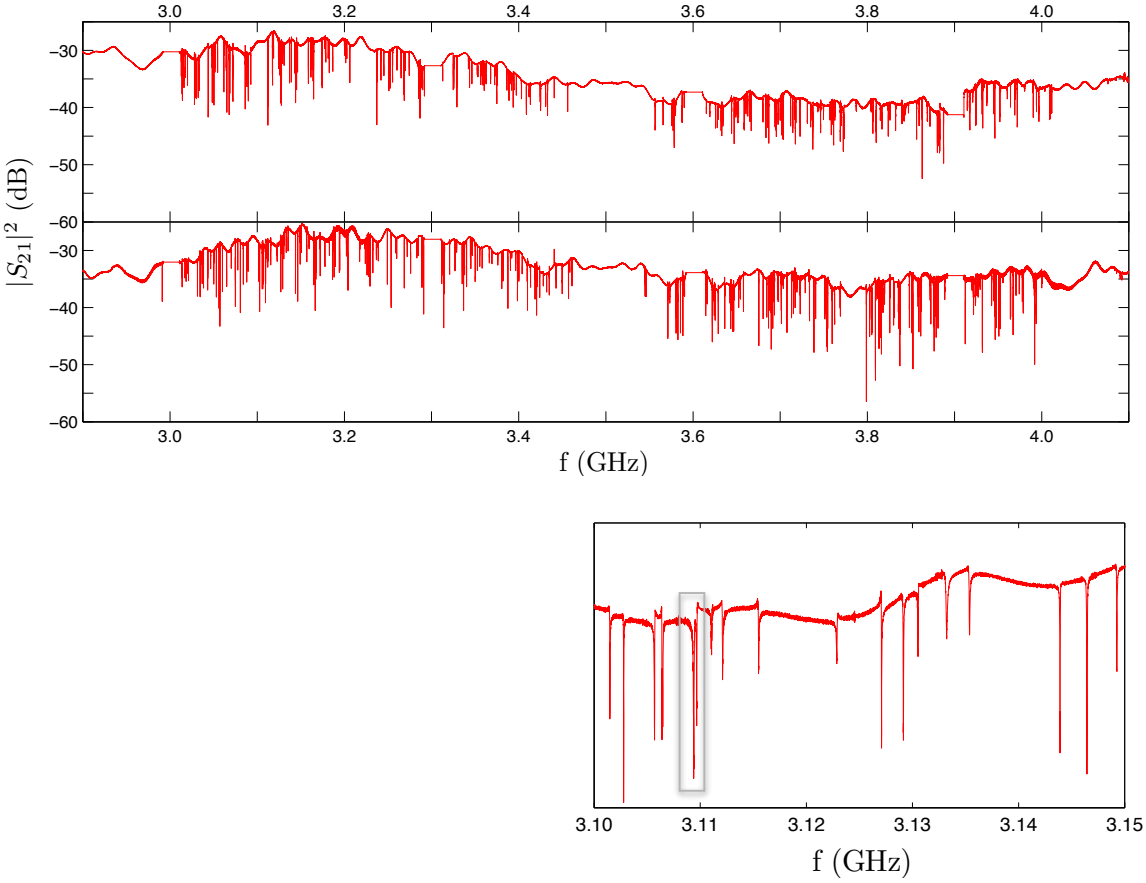

Figure 4.7: *Top:* Network analyzer sweeps of the detector arrays in the A2 (upper panel) and B2 (lower panel) positions. Shown is the squared magnitude of the transmission through the system as a function of microwave frequency. The large scale variations in the transmission should be ignored as they are an artifact of the technique used to collect network analyzer sweeps with the MUSIC readout electronics. The small scale features are accurately measured. *Bottom:* A zoom-in on the network analyzer sweep of the B2 detector array. Here individual resonances can be identified. The gray box denotes a pair of resonances that are classified as a collision.

Table 4.4: Detector yield of the A2 and B2 arrays. The first two columns list the number of detectors designed and the number of detectors found in network analyzer sweeps. Then, moving from left to right, the columns list the number of resonators that remain after placing additional quality cuts. For a description of each cut see the text. The top two rows are in units of number of resonators. The bottom two rows are in units of percentage of resonators with respect to the number designed. Taken from Sayers et al. [168].

Device	Designed	Found	Collisions	Distorted / Low-Q / Power	Noise/Response	Optical
A2	288	277	227	190	166	143
B2	288	272	237	190	159	138
A2	100%	96%	79%	66%	58%	50%
B2	100%	94%	82%	66%	55%	48%

4.2.4 Dark Temperature Sweeps

We collected dark temperature sweep data for all of the MUSIC detectors in January 2013. The dataset consists of IQ sweeps at 15 temperatures between 230 mK and 450 mK. The dataset is analyzed according to the procedure outlined in Section 3.2. We present histograms of the resulting best-fit parameters for all of the detectors on the A2 and B2 arrays in Figure 4.8. When fitting the resonant frequency data, we find that the median value of the kinetic inductance fraction for our detectors is $\alpha_f = 0.011$ and the median value of the gap energy at zero temperature for our detectors is $\Delta_{0,f} = 0.204$ meV. When fitting the dissipation data, we find that the median value of the kinetic inductance fraction is $\alpha_Q = 0.014$ and the median value of the gap energy at zero temperature is $\Delta_{0,Q} = 0.21$ meV. Hence, the $Q_i^{-1}(T_{\rm bath})$ dark trajectories imply kinetic inductance fractions that are 30% larger and gap energies that are 3% larger than those implied by the $f_{\rm res}(T_{\rm bath})$ dark trajectories. There is evidence that this discrepancy is largely a result of using the first-order approximation to the Mattis-Bardeen integrals. When the full integral is employed in the fitting procedure, there is better agreement in the parameter values derived from the resonant frequency and dissipation data. This appears to be due to the fact that at high temperatures the first-order analytical expressions provide a better approximation to the full-integral prediction for σ_2 than σ_1. This is a relatively recent development, and we have not yet implemented a full-integral analysis of the hot/cold and skydip data. Therefore, for the remainder of this thesis we will use the first-order approximation and assume different values of $[\alpha,\ \Delta_0]$ when predicting the resonant frequency and internal quality factor, as outlined in Chapter 3.

We observe variations in both the kinetic inductance fraction and the gap energy at zero temperature across each detector array. This is illustrated in Figure 4.9, which shows α_f and $\Delta_{0,f}$ as a function of resonant frequency for the detectors on the B2 array. The patterns that emerge when these parameters are plotted as a function of resonant frequency are the result of trends with both the azimuth and elevation offset of the pixels. We will present direct evidence for this in Section 4.3.1. One possible explanation is variation in the thickness of the Al section due to a gradient in the amount of Al that is etched away during fabrication. Recall that the best-fit parameters from the dark analysis act as input to the hot/cold analysis. Because of the variation in α and Δ_0 across the detector array, it is important to match the dark results to the hot/cold data

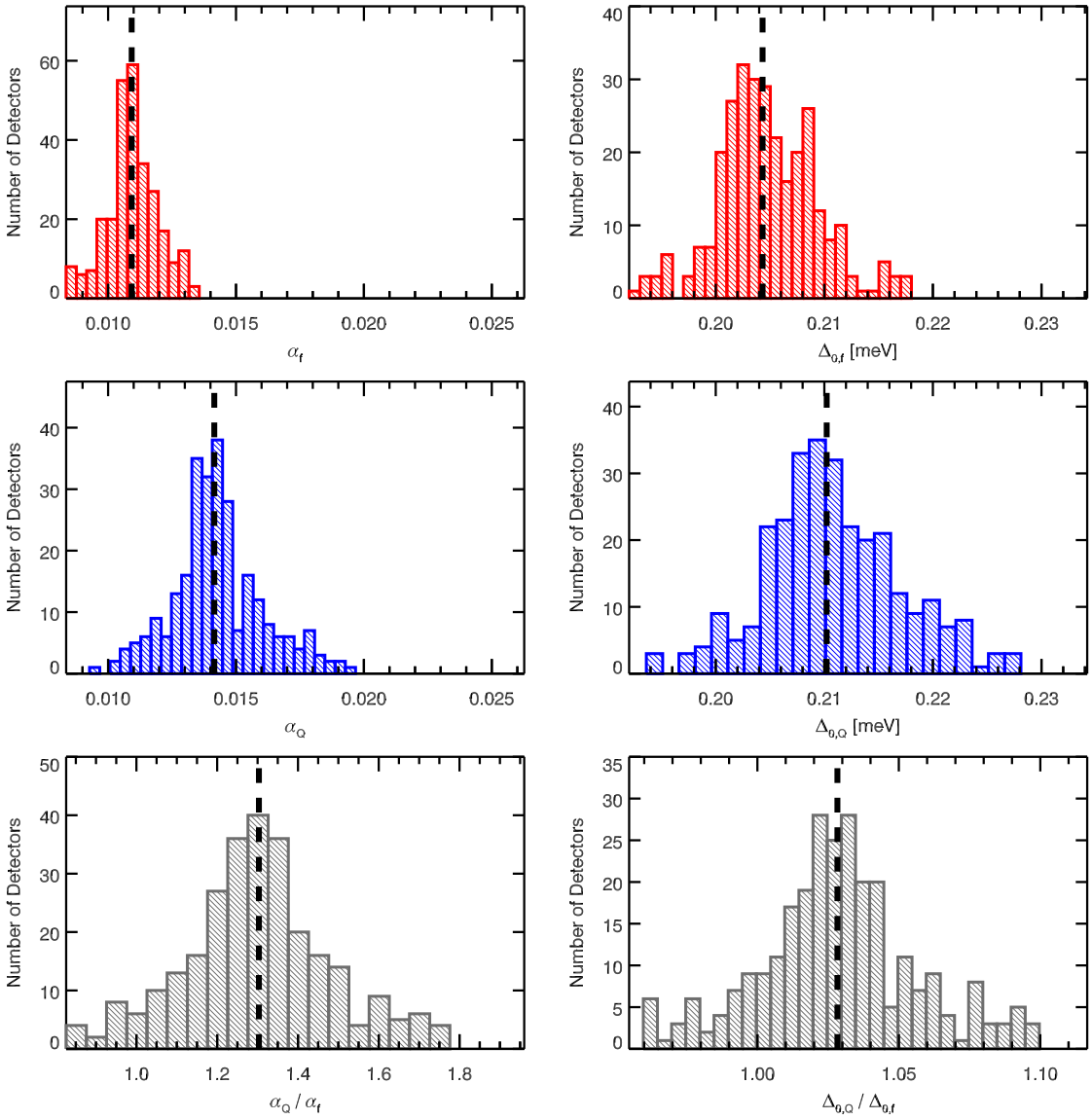

Figure 4.8: Parameter estimates obtained from fitting Mattis-Bardeen theory to dark temperature sweep data. Histograms contain the results for all detectors on the A2 and B2 arrays. Dashed black lines denote median values. The left column shows the kinetic inductance fraction α. The right column shows the gap energy at zero temperature Δ_0. The upper panels (red) show the results of fitting the resonant frequency data $f_{\rm res}(T_{\rm bath})$. The middle panels (blue) show the results of fitting the dissipation data $Q_i^{-1}(T_{\rm bath})$. The bottom panels (gray) show the ratio of the dissipation results to the frequency results.

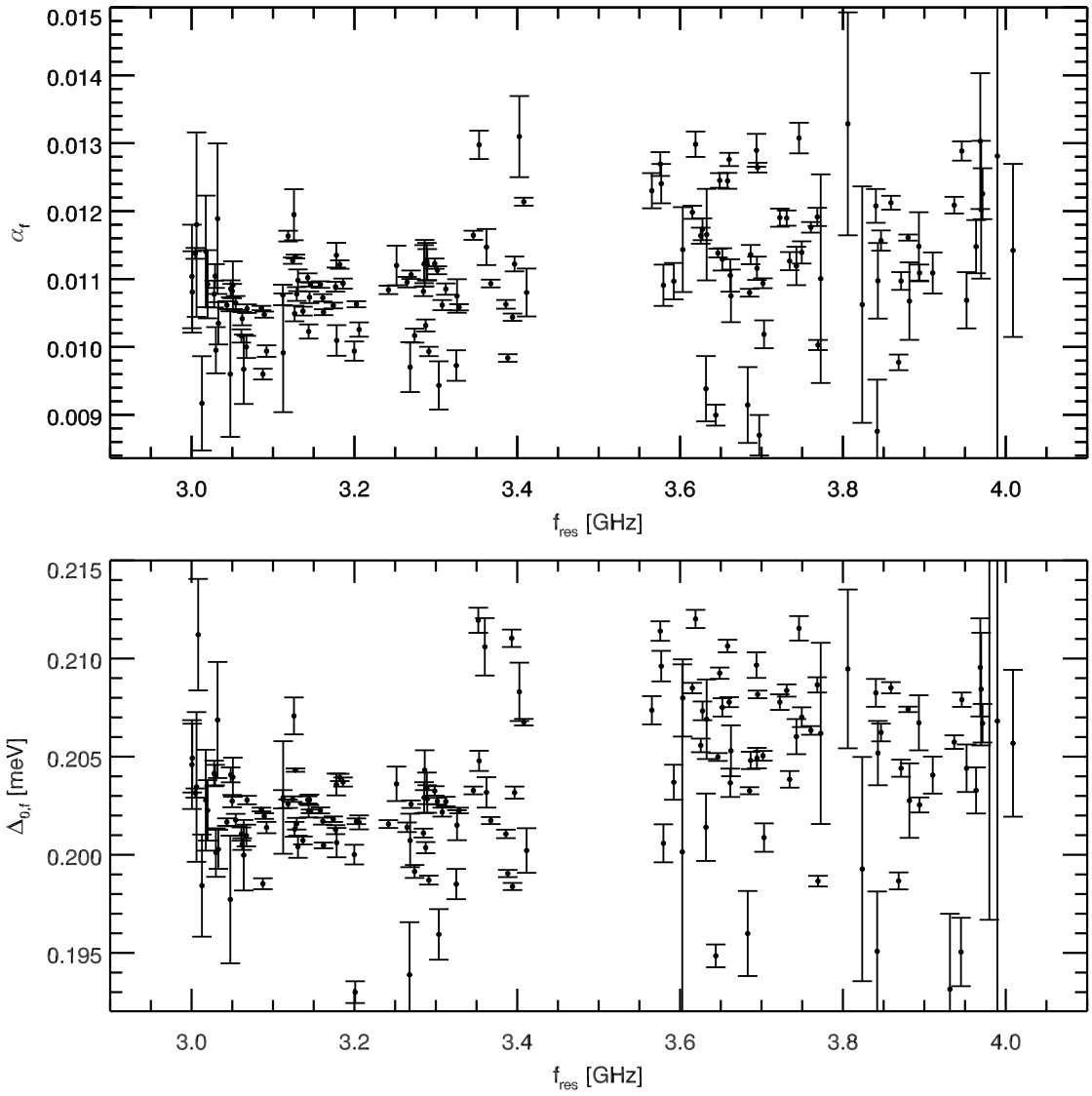

Figure 4.9: The kinetic inductance fraction α_f and gap energy at zero temperature $\Delta_{0,f}$ as a function of resonant frequency for the detectors on the B2 array.

for each resonator individually.

4.2.5 Hot/Cold

We collected hot/cold data for all of the A2 and B2 detectors on October 10, 2013. The dataset consists of IQ sweeps measured with the MUSIC readout electronics at 10 temperatures between 240 mK and 445 mK under both an ambient temperature and liquid nitrogen beam-filling, blackbody load. The ambient temperature was $T_{\rm amb} = 283 \pm 2$ K. The dataset is analyzed according to the procedure outlined in Section 3.2.3. The results of the analysis are presented in Tables 4.5-4.6. Table 4.5 presents the median and median absolute deviation of the parameters of interest, taken over all detectors of the specified band on the specified device half band. Table 4.6 is identical to Table 4.5 except that the median and median absolute deviation are taken over all detectors of the specified band on the A2 and B2 arrays. We use the median and median absolute deviation to quantify the center and dispersion of the distribution of values because these statistics are outlier resistant. Note that we multiply the median absolute deviation by a factor of 1.4826 so that it is equal to the standard deviation for normally distributed values.

The model used to describe the hot/cold data includes several nuisance parameters, which are not presented in Tables 4.5-4.6. We are not sensitive enough to the $\tau_{\rm max}$ parameter to fully constrain it, but we do obtain a lower limit $\tau_{\rm max} \gtrsim 50$ μs. We are able to constrain $1/Q_{i,0}$ for each resonator and find values that are consistent with the best-fit values from the dark temperature sweep, suggesting that $1/Q_{i,0}$ does not vary between cooldowns (note that unlike α and Δ_0, we do not use the results of the dark temperature sweeps to place a prior on $1/Q_{i,0}$). Finally, the nuisance parameters used to model the elevated quasi-particle temperature — n and $\tilde{\eta}_e$ — are highly degenerate, but we are sensitive to the difference in the temperature of the quasi-particle population and the temperature of the bath. We find that at 240 mK the temperature of the quasi-particle population is elevated by ≈ 3 mK from the bath temperature under the LN_2 load and is elevated by ≈ 10 mK from the bath temperature under the ambient temperature load. As the bath temperature increases, the quasi-particle population quickly returns to bath temperature.

We find that the small-signal response due to direct absorption is $[10\%,\ 5\%,\ 9\%,\ 15\%]$ of the total small-signal response for the four observing bands (determined using the dark resonators, specifically $C^{\rm dark}/C$). Note that this refers to the response to a beam-filling load at the cryostat window. The excess loading due to direct absorption is $[30\%,\ 20\%,\ 30\%,\ 25\%]$ of the total excess loading (determined using the dark resonators, specifically $P_{\rm exc}^{\rm dark}/P_{\rm exc}$). This represents a considerable reduction in the amount of direct absorption compared to what was seen in the engineering-grade detector arrays. These reductions were achieved through two modifications to the instrument. First, the direct absorption was found to scale as approximately the area of the Al section, so we reduced the length of Al section from 1 mm to 0.35 mm. We did not reduce the length further because we wanted to maintain a high absorption efficiency to radiation coupled through the antenna. Second, the direct absorption should be sensitive to both polarizations while the antennas are only sensitive to a single polarization, so we installed a polarizing wire grid in the optical path in late 2012. This reduced

Table 4.5: Hot/Cold results. The quoted values are the (median) ± (median absolute deviation), calculated using the detectors of the specified band on the specified device half-band.

Band	Device	N_{res}	$\Delta\nu_{\mathrm{mm,ant}}$ [GHz]	T_{exc} [K]	P_{exc} [pW]	$P_{\mathrm{exc,ant}}$ [pW]	C [GHz/nm]	C_{ant} [GHz/nm]	η_{ant}
Dark	A2L	5	–	68±36	0.2±0.1	–	0.006±0.002	–	–
	A2U	4	–	70±38	0.2±0.1	–	0.004±0.001	–	–
	B2L	6	–	149±22	0.3±0.1	–	0.003±0.000	–	–
	B2U	3	–	91±58	0.2±0.1	–	0.004±0.000	–	–
0	A2L	4	20	36±23	0.8±0.4	0.6±0.4	0.038±0.008	0.033±0.008	0.072±0.017
	A2U	10	20	28±16	0.7±0.3	0.5±0.3	0.046±0.006	0.041±0.006	0.091±0.014
	B2L	6	17	34±16	0.9±0.5	0.6±0.5	0.035±0.008	0.032±0.008	0.080±0.020
	B2U	6	19	24±10	0.7±0.2	0.5±0.2	0.042±0.006	0.038±0.006	0.089±0.014
1	A2L	18	27	23±15	1.1±0.7	0.9±0.7	0.078±0.005	0.073±0.005	0.118±0.009
	A2U	3	25	21±3	1.1±0.3	0.9±0.3	0.079±0.004	0.075±0.004	0.133±0.007
	B2L	11	22	14±11	0.6±0.4	0.3±0.4	0.066±0.004	0.063±0.004	0.128±0.009
	B2U	10	23	19±4	1.0±0.2	0.7±0.2	0.078±0.009	0.073±0.009	0.138±0.018
2	A2L	20	18	25±6	0.7±0.3	0.6±0.3	0.045±0.004	0.040±0.004	0.097±0.011
	A2U	11	16	35±23	0.9±0.7	0.7±0.7	0.043±0.008	0.039±0.008	0.109±0.023
	B2L	20	16	16±9	0.4±0.2	0.1±0.2	0.042±0.004	0.039±0.004	0.109±0.010
	B2U	12	15	26±7	0.8±0.5	0.6±0.5	0.048±0.008	0.043±0.008	0.125±0.023
3	A2L	8	16	50±9	0.8±0.1	0.7±0.1	0.028±0.006	0.022±0.006	0.063±0.016
	A2U	12	11	38±14	0.7±0.3	0.5±0.3	0.032±0.010	0.027±0.010	0.103±0.036
	B2L	12	13	46±17	0.7±0.4	0.5±0.4	0.025±0.003	0.022±0.003	0.073±0.011
	B2U	3	10	33±3	0.3±0.1	0.1±0.1	0.018±0.005	0.014±0.005	0.059±0.021

Table 4.6: Hot/Cold results. The quoted values are the (median) ± (median absolute deviation), calculated using all detectors of the specified band.

Band	N_{res}	$\Delta\nu_{\mathrm{mm,ant}}$ [GHz]	T_{exc} [K]	P_{exc} [pW]	$P_{\mathrm{exc,ant}}$ [pW]	C [GHz/nm]	C_{ant} [GHz/nm]	η_{ant}
Dark	18	–	84±64	0.2±0.1	–	0.004±0.001	–	–
0	26	20	29±13	0.7±0.3	0.5±0.3	0.042±0.008	0.038±0.008	0.083±0.013
1	42	24	20±10	1.0±0.5	0.7±0.5	0.076±0.009	0.071±0.008	0.125±0.015
2	63	16	24±10	0.6±0.3	0.4±0.3	0.044±0.004	0.040±0.004	0.108±0.014
3	35	13	47±14	0.8±0.3	0.6±0.2	0.026±0.007	0.022±0.007	0.074±0.022

Table 4.7: Comparison of the expected and measured single-polarization optical efficiency. See the text for a description of how the different contributions to the expected efficiency are determined. The values quoted for the measured efficiency are the median and median absolute deviations over resonators of a given band on the detector arrays in the A2 and B2 positions.

	Expected Efficiency							Measured Efficiency	Measured / Expected
Band	Phonon	Absorption	Microstrip	Antenna	Lyot Stop	Filters	Total	$(\eta_{\mathrm{ph}} \times \eta_{\mathrm{opt,ant}})$	
0	0.60	0.88	0.88	0.74	0.28	0.74	0.071	0.083 ± 0.013	1.17 ± 0.18
1	0.50	0.88	0.83	0.70	0.51	0.76	0.099	0.125 ± 0.015	1.26 ± 0.15
2	0.46	0.88	0.79	0.78	0.68	0.69	0.117	0.108 ± 0.014	0.92 ± 0.12
3	0.43	0.88	0.75	0.71	0.76	0.61	0.093	0.074 ± 0.022	0.79 ± 0.24

the direct absorption by a factor of $\simeq 1.6$, which is less than the expected factor of 2, but still represents a significant improvement. The hot/cold results for the dark resonators are used to correct the hot/cold results for the antenna coupled resonators using the procedure outlined in Section 3.2.3. This enables extraction of the optical efficiency and excess loading of the antenna.

We now compare the measured optical efficiency to the expected optical efficiency based on the known sources of loss in the MUSIC instrument. Table 4.7 tabulates the known sources of loss. We associate an expected efficiency to each, which is estimated from either a direct measurement, analytical calculation, or simulation:

Phonon Refers to $\eta_{\rm ph}$. The quoted values are taken from the simulation of Guruswamy et al. [87]. The origin of $\eta_{\rm ph}$ and a description of the simulation are given in Section 2.2.2.

Absorption Refers to the fraction of the power incident on the MKID that is absorbed by the MKID. The quoted values are the result of an analytical calculation [161]. This calculation accounts for two effects, which have opposing dependencies on the resistivity of the Al section. First, as the resistivity of the Al section increases, the length scale for absorption of light from the overlapping Nb/Si_3N_4 microstrip becomes smaller, resulting in an improved absorption efficiency. Second, as the resistivity of the Al section increases, the impedance mismatch between the Al section and the Nb portion of the microstrip increases, resulting in reflection and a reduced absorption efficiency. The calculation assumes that the Al has a sheet resistance of 0.22 $\Omega/\square$, which is based on direct measurements made at 4 K.

Microstrip Refers to dielectric loss of the microstrip that carries the light collected by the antenna to the MKID. The loss tangent of the Si_3N_4 dielectric at millimeter-wave frequencies was measured using a set of "loss test devices" on an engineering-grade detector array, Device 9a. The loss test device is designed as follows. Light collected by an antenna is sent through a 3 dB microstrip splitter; half of the power is sent directly to a "reference" MKID and the other half is sent over a long run of microstrip before terminating in a "loss" MKID. The difference in the length of microstrip between the loss and reference MKID is 41.4 mm. The hot/cold analysis is carried out on both the loss and reference MKID. The ratio of the optical efficiency of the loss MKID to that of the reference MKID yield an estimate of the dielectric loss in the excess run of microstrip, which can then be converted into a dielectric loss tangent. We find that on average the loss MKID has an optical efficiency that is 0.26 times that of the reference MKID. We have measured the band center of the loss test devices to be 330 GHz via FTS. Hence, the loss tangent of Si_3N_4 is 1.6×10^{-3}. This results in the microstrip efficiencies quoted in Table 4.7 for the 8.4 mm length of microstrip used in the actual detectors.

Antenna Refers to the efficiency of the phased array of slot dipole antennas. It is calculated by applying the method of moments to an infinite array of infinite long slots. This accounts for feed efficiency, radiation efficiency, and transmission through the silicon and AR coating. It does not account for losses

to substrate modes, which is expected to be an $\sim 10\%$ effect. It also does not account for inefficiency due to the fact that the actual slots have finite length and the impedance varies near the ends, which is expected to be another $\sim 10\%$ effect that will be largest for the lower frequency bands.

Lyot Accounts for the loss due to the truncation of the beam at the Lyot stop. It is estimated using Zemax simulations of the MUSIC optics [138].

Filters Accounts for the loss and reflections of the dielectric, metal-mesh, and infrared shader filters. The loss of each filter is estimated using the methods and references outlined in Sayers et al. [138]. The reflections at the interface of each filter is estimated via simulation. [1]

The product of these efficiencies is presented in the **Total** column of Table 4.7. We expect that the MUSIC instrument will have single-polarization optical efficiencies between 7% and 12%, depending on the observing band.

In general, the optical efficiencies inferred from hot/cold are in good agreement with the expected optical efficiencies. There does appear to be a slight band dependent discrepancy. In Band 0 and Band 1 the measured efficiency is larger than expected, whereas in Band 2 and Band 3 the measured efficiency is smaller than expected. The quoted uncertainties are simply the dispersion observed across the detectors of a given band. There is also systematic uncertainty in the measured values that arise from our uncertainty in the assumed values of the recombination coefficient and the thickness of the Al section. This systematic uncertainty is not included in the quoted uncertainties. However, it should effect all bands approximately equally, and therefore would not explain the band dependent discrepancy. The true efficiencies would be 30% greater than the quoted values if zero Al is etched away during fabrication instead of the assumed 15 nm. The true efficiencies would be 50% less than the quoted values if 30 nm of Al is etched away instead of the assumed 15 nm and if the recombination coefficient is 7.1 μm^3 sec^{-1} instead of the assumed 9.4 μm^3 sec^{-1}. Note that the $^{+30\%}_{-50\%}$ systematic errors correspond to the absolute boundaries of what we believe are reasonable values for the recombination coefficient and thickness. Without independent measurements of the recombination coefficient and thickness of the MKIDs employed in MUSIC, it is difficult to determine the overall normalization of the band dependent optical efficiency to better than approximately 50% accuracy.

4.2.6 Skydips

Skydip data was collected for all detectors on the A2 and B2 arrays on the night of September 25, 2013. The dataset consists of IQ sweeps collected with the dome open and the telescope pointed at 6 elevation angles between 20° and 70°; specifically $\mathfrak{e} = [20^\circ,\ 30^\circ,\ 40^\circ,\ 50^\circ,\ 60^\circ,\ 70^\circ]$. The ambient temperature over the course of the skydip measurement was $T_{\rm amb} = 277.7 \pm 0.1$ K. The CSO tipping radiometer measures the optical depth at 225 GHz every 10 minutes. The tipping radiometer reported $\tau_{225} = 0.1036 \pm 0.003$ over the course of the skydip measurement (which corresponds to $\mathcal{C}_{\rm PW} = 1.94 \pm 0.06$ mm). The following morning the

[1] `http://www.luxpop.com/`

opening in the hex plate of the telescope was covered with a large piece of Eccosorb® and a final IQ sweep was collected to act as the room-temperature load reference measurement. The ambient temperature during the reference measurement was $T_{\rm amb} = 285.5$ K. The dataset is analyzed according to the procedure outlined in Section 3.2.5.

Analysis of the dark resonator skydip data yields a measurement of the direct absorption spillover fraction. We find that the median spillover fraction for the dark resonators is $f_{\rm spill,dir} = 0.28$. However, there is significant variation among the dark resonators, with spillover fractions ranging from 0.20 to 0.36. This is much larger than the ~ 0.01 measurement uncertainty on the individual measurements, and is most likely due to a dependence on focal plane position. In other words, the direct absorption spillover fraction is most likely larger for resonators positioned near the edge of the focal plane than for those positioned near the center. However, we cannot confirm this hypothesis, because it is difficult to extract a beam location for the dark resonators. When fitting the skydip data for the antenna coupled resonators, we place a prior on the direct absorption spillover fraction that accounts for this large variation. We also measure $\tau_{\rm dir} = 0.18 \pm 0.05$ for the dark resonators.

The best fit antenna spillover fractions $f_{\rm spill,ant}$ are presented in Figure 4.10 as a function of the azimuthal offset of the detector from the center of the focal plane. We observe a clear increase in the antenna spillover fractions for detectors situated towards the edge of the focal plane. This increase is largest in the lower frequency bands. The black dashed line denotes the expected spillover fraction due to the expected inefficiencies of the MUSIC optics. It assumes 1% absorption for each of the five mirrors in the optics chain and Ruze scattering from the primary mirror. In the central region of the focal plane we measure an excess antenna spillover fraction of [0.08, 0.04, 0.02, 0.10] for the four observing bands.

We use the Atmospheric Transmission at Microwaves (ATM) model by Pardo et al. [129] to infer the atmospheric transmission spectrum $\mathrm{ATM}(\nu)$ from the value of τ_{225} measured by the CSO tipping radiometer. The optical depth in band is then predicted as

$$\tau_{\rm ant} = -\ln\left(\frac{\int \mathrm{FTS}(\nu)\mathrm{ATM}(\nu)d\nu}{\int \mathrm{FTS}(\nu)d\nu}\right), \tag{4.3}$$

where $\mathrm{FTS}(\nu)$ denotes the bandpass measured via FTS. We compare this prediction to the resulting best-fit estimate of $\tau_{\rm ant}$ from the skydips. We find excellent agreement in Bands 0, 1, and 2. This gives us confidence that for the three lowest frequency bands we can use τ_{225} and the ATM model to infer the sky loading for any given observation. In Band 3, the predicted $\tau_{\rm ant}$ is approximately 30% larger than the value measured via skydip. Recall that the bandpasses for the MUSIC detectors are shifted by 3% to lower frequency due to an increase in the ratio ε/d of the Si_3N_4 dielectric relative to the engineering-grade tiles used to calibrate the filter geometry. Because of this shift, Band 3 overlaps with the waterline at 325 GHz, which makes the predicted $\tau_{\rm ant}$ very sensitive to both the ATM model and the bandpass measured via FTS. Therefore, we do not believe that we can accurately predict the loading and responsivity for the Band 3 resonators at this time.

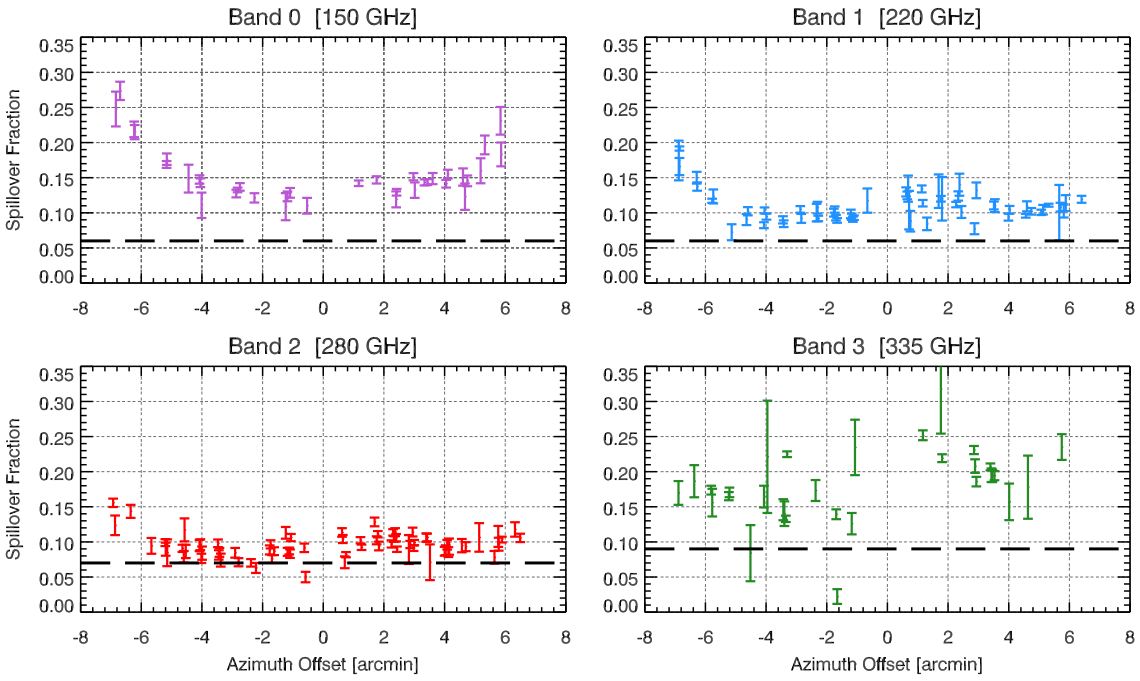

Figure 4.10: Spillover fraction $f_{\mathrm{spill,ant}}$ as a function of the azimuthal offset of the detector from the center of the focal plane. Each panel corresponds to a different observing band. The black dashed line denotes the expected spillover fraction based on the expected inefficiencies of the MUSIC optics (see text).

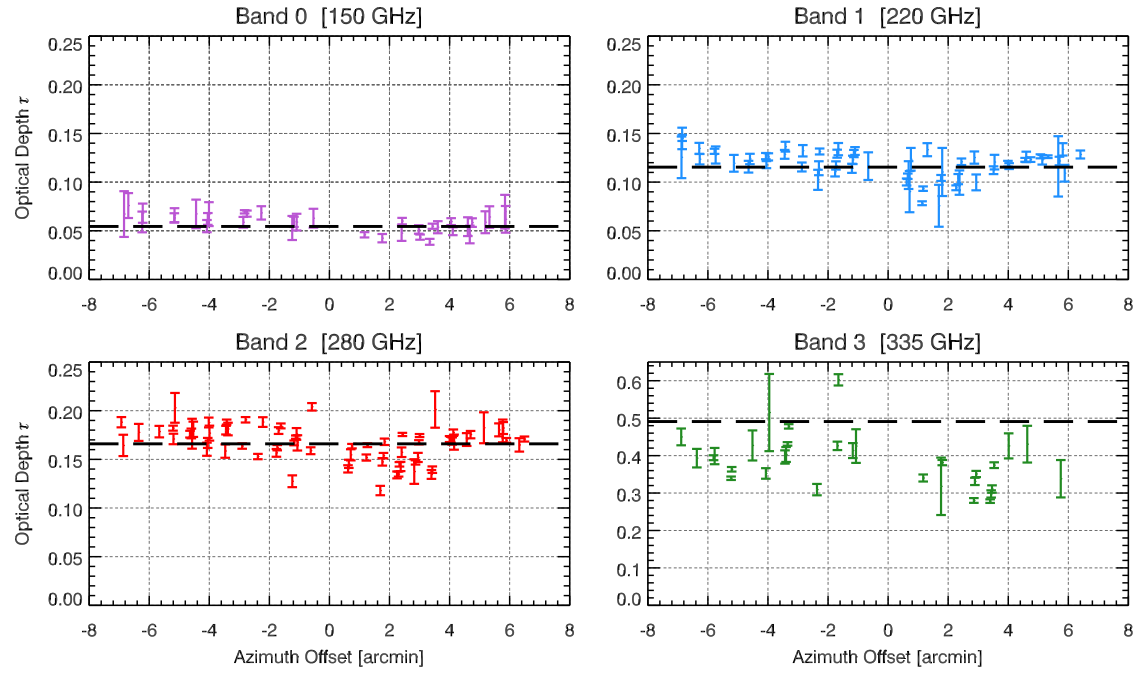

Figure 4.11: Optical depth τ_{ant} as a function of the azimuthal offset of the detector from the center of the focal plane. Each panel corresponds to a different observing band. The black dashed line denotes the expected optical depth based on the average $\tau_{225} = 0.1036$ reported by the CSO over the course of the skydip measurement, the ATM model for the atmospheric transmission, and the detector bandpasses measured via FTS.

Table 4.8: Median background loading, calculated using detectors of the specified band on the A2 and B2 arrays. All temperatures are referred to the cryostat window. $T_{\rm exc}$ is determined from the hot/cold data, $T_{\rm spill}$ is determined from the skydip data, and $T_{\rm sky}$ is determined from the FTS bandpass measurements and the ATM model assuming $\mathcal{C}_{\rm PW} = 1.3$ mm. These three temperatures sum to give the total loading $T_{\rm load}$. $P_{\rm opt}$ is the equivalent optical power incident on the MKID.

Band	**T_{exc} [K]**	**T_{spill} [K]**	**T_{sky} [K]**	**T_{load} [K]**	**P_{opt} [pW]**
0	30	45	10	**85**	**3.3**
1	20	30	20	**70**	**5.5**
2	25	30	25	**80**	**3.9**
3	40	55	70	**165**	**4.9**

4.2.7 Loading

Table 4.8 breaks down the total detector loading $T_{\rm load}$ into contributions from spillover onto the interior of the cryostat $T_{\rm exc}$, spillover onto room temperature surfaces $T_{\rm spill} = f_{\rm spill} T_{\rm amb}$, and emission from the atmosphere $T_{\rm sky} = (1 - e^{-\tau/\sin\epsilon}) T_{\rm atm}$. All temperatures are referred to the cryostat window so that they can be compared directly. For Bands 0-2 spillover onto room temperature surfaces is the dominant contribution to the loading. Spillover onto the interior of the cryostat is also appreciable, and is only slightly smaller than spillover onto room temperature surfaces. The contribution from atmospheric emission increases with observing band center frequency, such that it is negligible in Band 0 and dominates in Band 3. Note that the quoted numbers include the contributions from both the antenna and direct absorption.

4.2.8 Responsivity

We test that the calibrated model fully describes the small-signal responsivity of our detectors by comparing the measured and predicted response to an unresolved astronomical source. We use Uranus for this analysis because it is a well-studied, stable blackbody that is bright enough to detect at high signal-to-noise in individual detector timestreams, but not so bright that it causes non-linear response.

The measured response is obtained by taking the peak height of Uranus in the individual detector timestreams (in units of fractional frequency fluctuations $\delta f_{\rm res}/f_{\rm res}$) and dividing by the known flux of Uranus. We assume the following empirical model from Griffin and Orton [39] for the brightness temperature of Uranus:

$$T_b(x) = 0.931 \times \left(-795.694 + 845.179x - 288.946x^2 + 35.200x^3\right) , \tag{4.4}$$

where $x = \log_{10}\lambda$ with the wavelength λ in units of μm. The factor of 0.931 is a correction presented in Sayers et al. [41] based on WMAP measurements of the brightness temperature of Uranus at 94 GHz [40]. Assuming we are in the Rayleigh-Jeans limit ($h\nu \ll k_B T_b$) the intensity $I(\nu)$ is given by

$$I(\nu) = \frac{2k_B\nu^2 T_b}{c^2} . \tag{4.5}$$

The flux of the source is then calculated as

$$S = \Omega_{\rm source} \frac{\int \mathrm{FTS}(\nu)\mathrm{ATM}(\nu,\mathfrak{e})I(\nu)d\nu}{\int \mathrm{FTS}(\nu)\mathrm{ATM}(\nu,\mathfrak{e})d\nu} \ , \tag{4.6}$$

where $\mathrm{FTS}(\nu)$ denotes the measured bandpass and $\mathrm{ATM}(\nu,\mathfrak{e})$ is the atmospheric transmission at the CSO at elevation $\mathfrak{e}$. The atmospheric transmission at zenith is calculated using the ATM model with the mm of precipitable water vapor determined from the tipper measurement of τ_{225} at the time of the observation. The zenith transmission is then scaled to elevation $\mathfrak{e}$ using the relationship $\mathrm{ATM}(\nu,\mathfrak{e}) = [\mathrm{ATM}(\nu,90^\circ)]^{1/\sin\mathfrak{e}}$. Since the solid angle of Uranus varies with observation epoch, we calculate $\Omega_{\rm source}$ at the time of the observation using the JCMT FLUXES software.

The predicted response is given by

$$\begin{aligned} r_{\rm src} &= \left| \frac{\partial\left(\delta f_{\rm res}/f_{\rm res}\right)}{\partial S} \right| \\ &= \left| \frac{\partial\left(\delta f_{\rm res}/f_{\rm res}\right)}{\partial n_{\rm qp}} \right| \left| \frac{\partial n_{\rm qp}}{\partial P_{\rm opt,ant}} \right| \left| \frac{\partial P_{\rm opt,ant}}{\partial T_{\rm load,ant}} \right| \left| \frac{\partial T_{\rm src}}{\partial S} \right| \ , \end{aligned} \tag{4.7}$$

where the terms on the second line are obtained by taking the appropriate partial derivative of Equations (2.59), (2.131), (2.105), and (2.9) from left to right. Doing so results in the following expression:

$$r_{\rm src} = \frac{\alpha\kappa_2\eta_{\rm ph}\eta_{\rm opt,ant}\left(1-f_{\rm spill,ant}\right)e^{-\tau_{\rm ant}/\sin\mathfrak{e}}A_{\rm eff}\,\Delta\nu_{\rm mm,ant}}{4V\Delta\left(2Rn_{\rm qp}+\tau_{\rm max}^{-1}\right)} \ , \tag{4.8}$$

which we can evaluate directly using the best fit model parameters for each resonator. We determine $\tau_{\rm ant}$ from Equation (4.3) using the value of τ_{225} reported by the CSO at the time of the observation to infer the atmospheric transmission. From $\tau_{\rm ant}$ we can determine the background loading which sets the quasi-particle density $n_{\rm qp}$ in the above equation.

We have collected 55 observations of Uranus for flux calibration purposes over the course of our August/September 2013 observing run. The median value of the column density of precipitable water vapor for this set of observations is $\mathcal{C}_{\rm PW} = 1.66$ mm, which is approximately equal to the historical median. We calculate the median ratio of measured to predicted response for each resonator over the 55 observations. This is shown in Figure 4.12 as a function of the microwave power $P_{\rm g}$ used to probe each resonator relative to the critical power $P^{\rm crit}$ at which that resonator bifurcates. Note that the ratio $P/P^{\rm crit} = a$ was estimated by fitting the pre-observation IQ sweep to a model for the transmission near resonance that includes a nonlinear kinetic inductance. We expect to see a slight degradation in detector responsivity with increasing power due to the nonlinear kinetic inductance and also (possible) microwave heating of the quasi-particle population. Since all of the calibration measurements are collected at low readout power, this effect is not included in our model and hence not included in the predicted response. We do indeed see a degradation in the ratio of measured to predicted response as we move to larger values of $P_{\rm g}/P_{\rm g}^{\rm crit}$, decreasing by $\sim 35\%$ between the low power

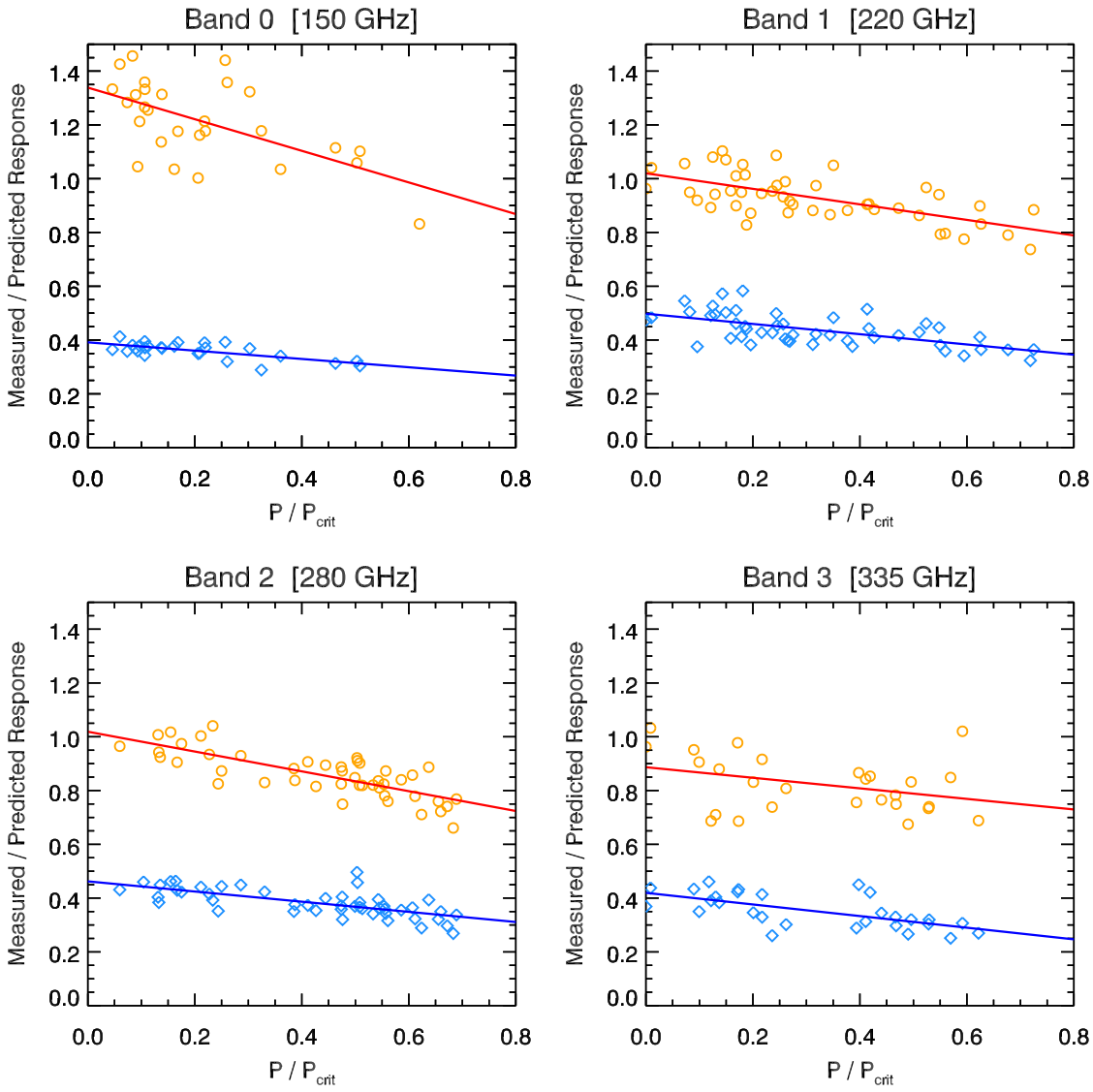

Figure 4.12: Response comparison. Light blue diamonds denote the ratio of measured to predicted response to an unresolved astronomical source (in this case Uranus). Orange circles denote the ratio of measured to predicted response to small changes in airmass. Blue and red lines are linear fits to the data.

limit and the critical power. These values are consistent with more direct measurements of the degradation in frequency response with readout power for detectors on our engineering-grade arrays [161].

In the low power limit — where we expect our model to hold — we measure a response to Uranus that is a factor of [0.40, 0.50, 0.45, 0.40] times the predicted response for the four observing bands. One possible cause for this discrepancy is that a significant portion of our beam is making it to the sky but is not part of the main beam (i.e., sidelobes or a diffuse wide-angle beam). Another possibility is that we have an incomplete understanding of the detector physics. The instrument model is constrained using only large signal response: for the hot/cold measurements we use the difference between a 77 K and room temperature load and for the sky dip measurements we use the difference between a sky load and room temperature load. Perhaps the large signal response does not translate into small signal response in the way described by the instrument model presented in Chapter 2.

In order to distinguish between these two possibilities, we examined the detector response to small changes in elevation. As the telescope scans in elevation there is a small change in the airmass, which in turn causes a small change in the background loading. The majority of our science observations are collected using a lissajous scan strategy, where the azimuth and elevation of the telescope are modulated with sine waves of different periods. This places the signal due to changing airmass at the specific frequency with which we are driving the telescope in the elevation direction. By examining the correlation coefficient between the detector timestreams and the elevation track of the telescope in a narrow window centered on the fundamental scan frequency, we are able to detect this small signal response to a beam-filling calibrator.

Specifically we examine

$$\begin{aligned} r_{\mathfrak{e}} &= \left| \frac{\partial \left(\delta f_{\rm res} / f_{\rm res} \right)}{\partial \mathfrak{e}} \right| \\ &= \left| \frac{\partial \left(\delta f_{\rm res} / f_{\rm res} \right)}{\partial n_{\rm qp}} \right| \left| \frac{\partial n_{\rm qp}}{\partial P_{\rm opt}} \right| \left| \frac{\partial P_{\rm opt}}{\partial T_{\rm load}} \right| \left| \frac{\partial T_{\rm load}}{\partial \mathfrak{e}} \right| \\ &= \left| \frac{\partial \left(\delta f_{\rm res} / f_{\rm res} \right)}{\partial n_{\rm qp}} \right| \left| \frac{\partial n_{\rm qp}}{\partial P_{\rm opt}} \right| \left| \frac{\partial P_{\rm opt}}{\partial T_{\rm load}} \right| \left(1 - f_{\rm spill,ant} \right) \tau_{\rm ant} T_{\rm atm} e^{-\tau_{\rm ant} / \sin \mathfrak{e}} \frac{\cos \left(\mathfrak{e} \right)}{\sin^2 \left(\mathfrak{e} \right)} , \end{aligned} \tag{4.9}$$

where the terms on the second line are obtained by taking the appropriate partial derivative of Equations (2.59), (2.131), (2.105), and (2.9), from left to right. The ratio of the measured to predicted value of $r_{\mathfrak{e}}$ is presented in Figure 4.12. This was determined from over 400 observations of faint sources. In Band 1 and Band 2, the measured and predicted response are in good agreement in the low-power regime. However, in Band 0 the measured response is 35% larger than predicted and in Band 3 the measured response is 10% smaller than predicted. The agreement of Band 1 and Band 2 strongly suggest that our understanding of the MKID small-signal response is correct and the discrepancy for unresolved sources is due to a significant fraction of the beam being dispersed to wide angles. We discount Band 3 because of the systematics in the model discussed earlier. The excess response in Band 0 is not currently understood, but points in the same direction

as the implications of the Band 1 and Band 2 analysis. The measured Band 0 values are noisy due to the fact that the atmosphere is relatively transparent at these frequencies, and hence the response to changes in elevation is small.

4.3 Optics Reconfiguration

The MUSIC optics were reconfigured in early 2014 in order to couple the A2 and B2 detector arrays to the sky with maximum per-pixel optical efficiency. Specifically, the location and geometry of the cryogenic lens was changed in order to speed up the system to an average focal ratio of 2.19 over the focal plane [168]. This reduced the overall footprint of the focal plane from eight arrays to two arrays and reduced the field of view from a 14 arcmin diameter circle to an 11.5 arcmin square. Zemax simulations predict that the reconfiguration will improve the optical efficiency $\eta_{\mathrm{opt,ant}}$ by a factor of $[2.0,\ 1.55,\ 1.25,\ 1.12]$ for the four observing bands. This gain in optical efficiency is due to a reduction in the amount of beam terminating at the Lyot stop. As we will see in the following chapter, the sensitivity of the MUSIC detectors is limited by TLS noise. Equations (2.214) and (2.212) suggest that the NEFD due to TLS noise scales as $\eta_{\mathrm{opt,ant}}^{-1/2}$, so naively we expect the optics reconfiguration to result in a factor of $[1.41,\ 1.24,\ 1.12,\ 1.06]$ improvement in NEFD. However, Zemax simulations also predict that the optics reconfiguration will result in a moderate increase in the size of the PSF, which will degrade the NEFD and point source sensitivity. Accounting for this, we still expect a factor of $[1.41,\ 1.17,\ 0.90,\ 0.82]$ improvement in NEFD, and therefore better sensitivity in the two lowest frequency observing bands [168].

A series of baffles were installed on the underside of the Lyot stop at the same time as the optics reconfiguration. These baffles are motivated by a model in which, in a time-reverse sense, 5–10% of the beam scatters off of the flat underside of the Lyot stop, scatters off of the region near the focal plane, and then exits the cryostat at large angles. This model explains the larger than expected spillover fraction and the increase in spillover fraction towards the edge of the focal plane (see Section 4.2.6). If the model is correct, the baffles will eliminate the excess spillover.

Unfortunately, the detector array in the A2 position (L120210.2R) was damaged during the optics reconfiguration and is no longer capable of collecting data. This leaves us with the single detector array in the B2 position (L120210.2L). The resulting field of view is 11.5 arcmin $\times$ 5.8 arcmin.

After the optics reconfiguration, we repeated the full suite of calibration measurements for the B2 array (with the exception of FTS). The results are presented below. For each calibration measurement, we compare the results obtained after the optics reconfiguration to those obtained before the optics reconfiguration. The two analysis were performed in an identical manner. Many of the plots and tables shown in the sections below will be similar to those shown in the sections above.

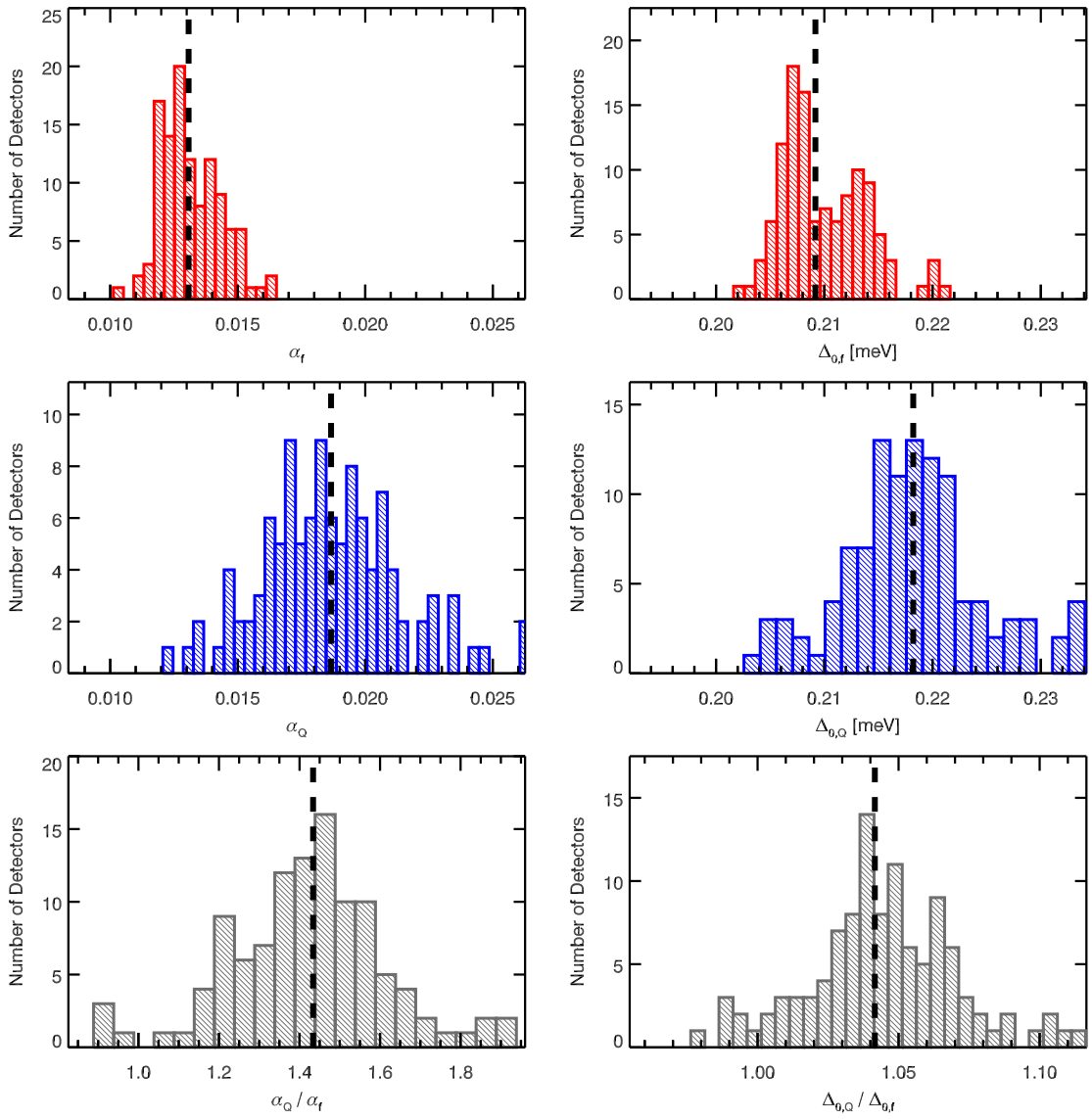

Figure 4.13: Parameter estimates obtained from fitting Mattis-Bardeen theory to dark temperature sweep data. Histograms contain the results for all detectors on the B2 array. Dashed black lines denote median values. The left column shows the kinetic inductance fraction α. The right column shows the gap energy at zero temperature Δ_0. The upper panels (red) show the results of fitting the resonant frequency data $f_{\rm res}(T_{\rm bath})$. The middle panels (blue) show the results of fitting the dissipation data $Q_i^{-1}(T_{\rm bath})$. The bottom panels (gray) show the ratio of the dissipation results to the frequency results.

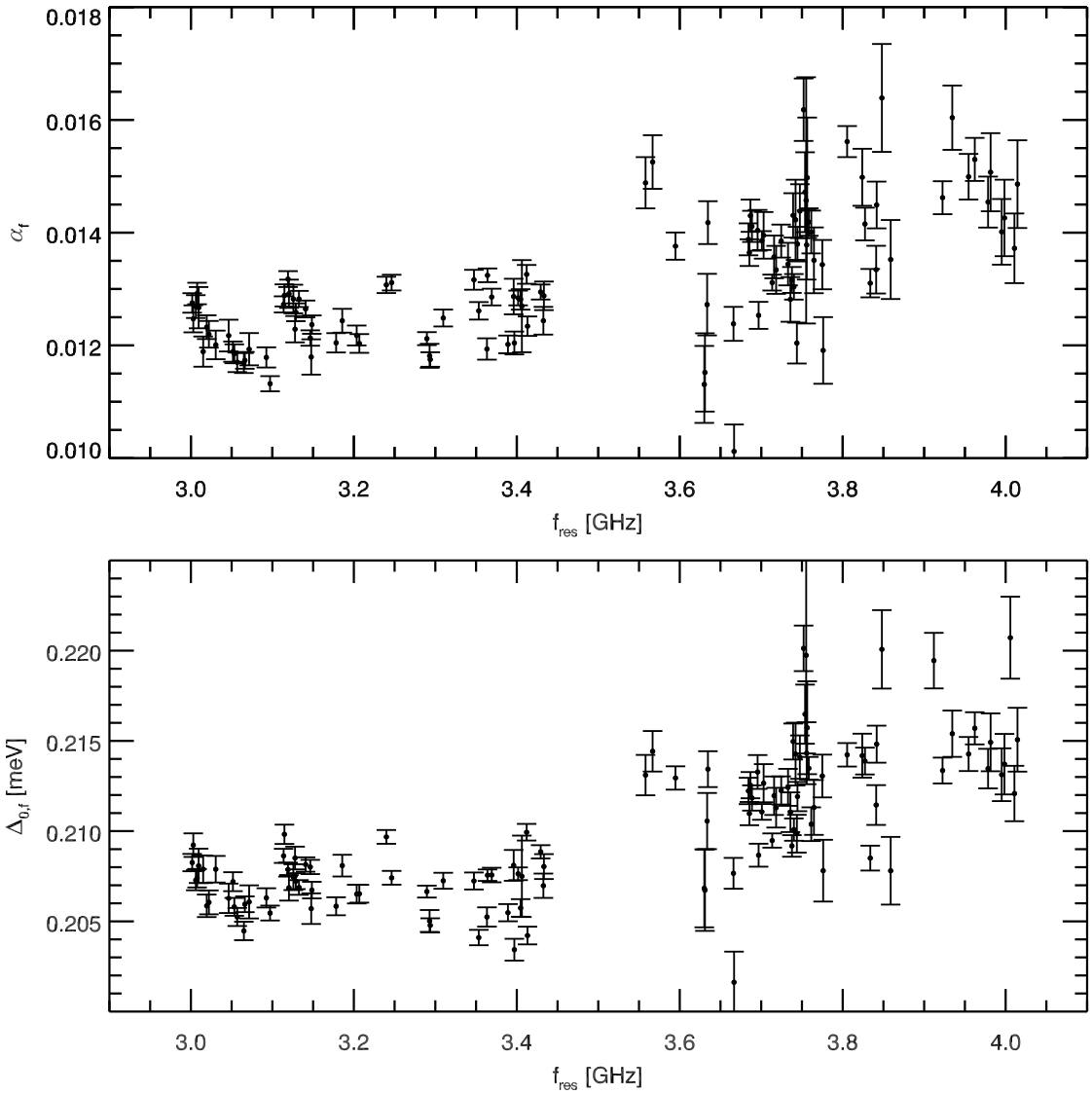

Figure 4.14: The kinetic inductance fraction α_f and gap energy at zero temperature $\Delta_{0,f}$ as a function of resonant frequency for the detectors on the B2 array.

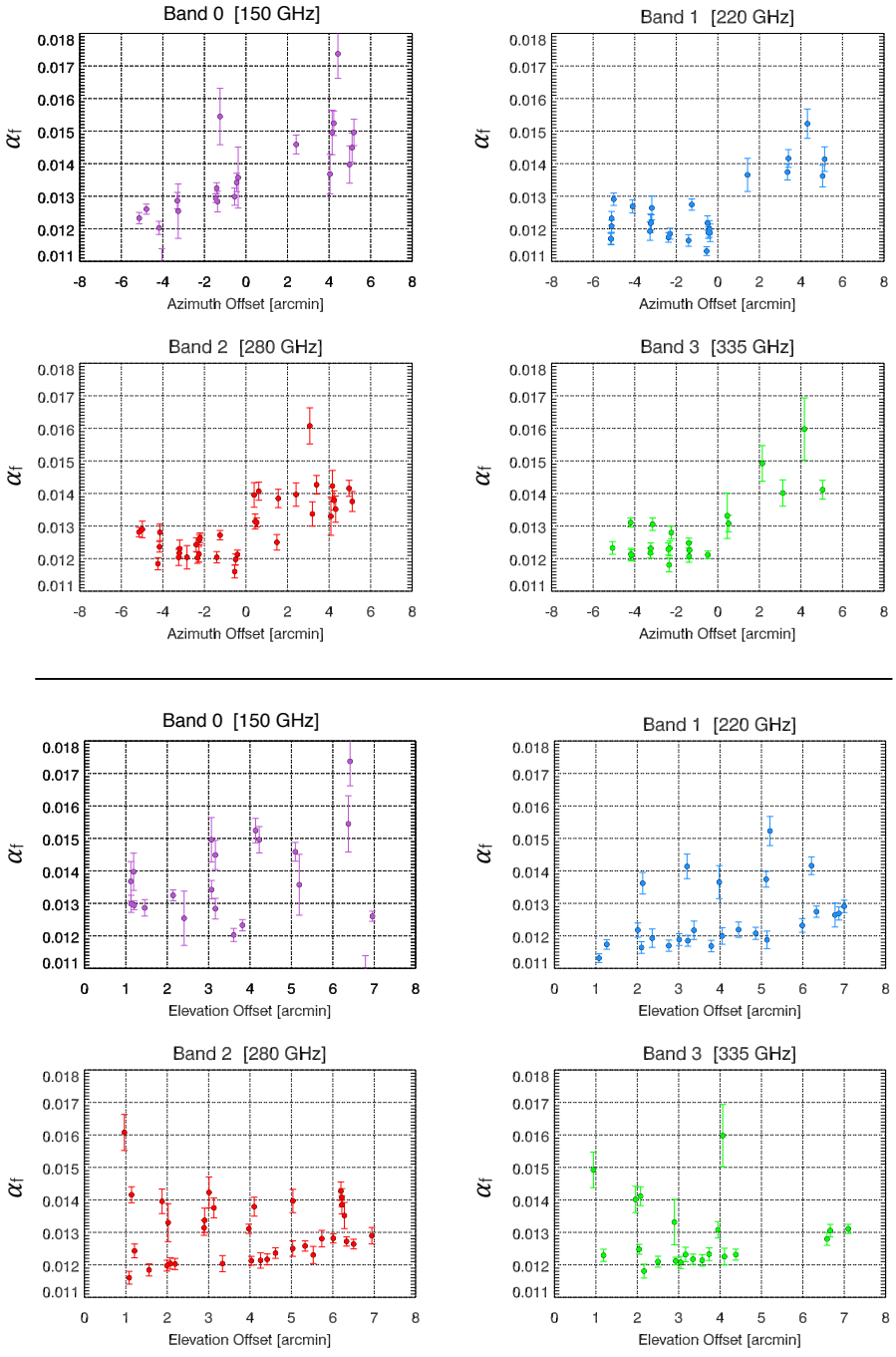

Figure 4.15: The kinetic inductance fraction α_f as a function of the offset in azimuth (top four panels) and the offset in elevation (bottom four panels) of the detector from the center of the focal plane for detectors on the B2 array.

4.3.1 Dark Temperature Sweeps

We collected dark temperature sweep data for detectors on the B2 array on June 27, 2014. The dataset consists of IQ sweeps at 12 temperatures between 225 mK and 455 mK. The dataset is analyzed according to the procedure outlined in Section 3.2. Figure 4.13 shows histograms of the resulting best-fit parameters. When fitting the resonant frequency data, we find that the median value of the kinetic inductance fraction is $\alpha_f = 0.013$ and the median value of the gap energy at zero temperature is $\Delta_{0,f} = 0.209$ meV. When fitting the dissipation data, we find that the median value of the kinetic inductance fraction is $\alpha_Q = 0.019$ and the median value of the gap energy at zero temperature is $\Delta_{0,Q} = 0.218$ meV. Hence, the $Q_i^{-1}(T_{\text{bath}})$ dark trajectories imply kinetic inductance fractions that are 40% larger and gap energies that are 4% larger than those implied by the $f_{\text{res}}(T_{\text{bath}})$ dark trajectories. Interestingly, both the kinetic inductance fraction and the gap energy at zero temperature increased after the optics reconfiguration. The kinetic inductance fraction α_f increased by $\sim 15\%$ and the gap energy at zero temperature $\Delta_{0,f}$ increased by $\sim 3\%$. The magnetic shielding was improved during the optics reconfiguration. This change in the magnetic environment of the MKIDs may be the cause of the observed changes in the dark behavior.

Figure 4.14 displays α_f and $\Delta_{0,f}$ as a function of resonant frequency for the detectors on the B2 array. This can be directly compared to Figure 4.9. The patterns with resonant frequency are even more obvious after the optics reconfiguration. In order to demonstrate that these patterns are the result of trends across the focal plane, we plot α_f as a function of the azimuth and elevation offset of the pixel from the center of the focal plane in Figure 4.15. The azimuth and elevation offset of each pixel were obtained from beam maps of Uranus collected during the subsequent optical run. We find that the kinetic inductance fraction is roughly 15% larger for pixels on the upper half-band (positive azimuth offset) than the lower half-band (negative azimuth offset). We also find that there is a positive correlation between the kinetic inductance fraction and the elevation offset of the pixel for both half-bands.

4.3.2 Hot/Cold

We collected hot/cold data for all of the B2 detectors on July 23, 2014. The dataset consists of IQ sweeps at 10 temperatures between 225 mK and 455 mK under both an ambient temperature and liquid nitrogen beam-filling, blackbody load. The ambient temperature was $T_{\text{amb}} = 287 \pm 1.5$ K. The dataset is analyzed according to the procedure outlined in Section 3.2.3. The results of the analysis are presented in Tables 4.9-4.10. These tables can be compared directly to Tables 4.5-4.6, which display the results before the optics reconfiguration.

Figure 4.16 shows histograms of the measured optical efficiency η_{ant} for each observing band both before and after the optics reconfiguration. The optics reconfiguration did indeed result in a significant increase in the optical efficiency of the detectors. On average, η_{ant} improved by a factor of $[1.50,\ 1.33,\ 1.33,\ 1.18]$ for the four observing bands. However, this differs from the expected improvement factors of $[2.0,\ 1.55,\ 1.25,\ 1.12]$, particularly in Band 0 where we anticipated the largest gain. Table 4.11 compares the measured and expected

efficiency after the optics reconfiguration. In general, the measured efficiency is still in good agreement with the expected efficiency.

Figure 4.17 shows histograms of the excess loading from the cryostat $P_{\mathrm{exc,ant}}$ for each observing band both before and after the optics reconfiguration. We expect a small decrease in the excess loading after the optics reconfiguration because less of the beam is coupled to the Lyot stop. The measurement uncertainty on $P_{\mathrm{exc,ant}}$ is large, and — with the exception of Band 3 — it is difficult to say whether or not we actually observe a decrease.

Unfortunately the small-signal response due to direct absorption increased by a factor of $\simeq 2$ after the optics reconfiguration, as evidenced by the analysis of the dark resonators. This is likely because a significant portion of the direct absorption beam was being terminated at the Lyot stop prior to the optics reconfiguration. This brings the fractional small-signal response due to direct absorption to $[12\%,\ 8\%,\ 12\%, 23\%]$ of the total small-signal response for the four observing bands (computed as C^{dark}/C). Note that this is the response to a beam-filling load at the cryostat window. Given our uncertainties, the excess loading due to direct absorption remains unchanged after the optics reconfiguration. The direct absorption contributes approximately $[50\%,\ 30\%,\ 40\%,\ 75\%]$ of the total excess loading for the four observing bands (computed as $P_{\mathrm{exc}}^{\mathrm{dark}}/P_{\mathrm{exc}}$).

Table 4.9: Hot/Cold results after the optics reconfiguration. The quoted values are the (median) ± (median absolute deviation), calculated using the detectors of the specified band on the specified device half-band.

Band	Device	N_{res}	$\Delta\nu$ [GHz]	T_{exc} [K]	P_{exc} [pW]	$P_{\mathrm{exc,ant}}$ [pW]	C [GHz/nm]	C_{ant} [GHz/nm]	η_{ant}
Dark	B2L	15	–	76±17	0.3±0.1	–	0.006±0.001	–	–
	B2U	7	–	37±11	0.2±0.0	–	0.007±0.001	–	–
0	B2L	13	17	16±7	0.5±0.3	0.3±0.3	0.055±0.004	0.049±0.004	0.123±0.009
	B2U	8	19	16±5	0.6±0.2	0.4±0.2	0.059±0.005	0.052±0.005	0.120±0.011
1	B2L	19	22	17±8	1.0±0.5	0.7±0.5	0.088±0.004	0.082±0.004	0.167±0.008
	B2U	6	23	23±3	1.4±0.4	1.2±0.4	0.099±0.010	0.092±0.010	0.173±0.019
2	B2L	21	16	20±2	0.7±0.1	0.4±0.1	0.056±0.004	0.050±0.004	0.140±0.010
	B2U	19	15	17±6	0.6±0.3	0.5±0.3	0.060±0.004	0.052±0.004	0.151±0.012
3	B2L	17	13	25±5	0.5±0.1	0.2±0.1	0.031±0.002	0.025±0.002	0.085±0.008
	B2U	9	10	18±3	0.4±0.1	0.2±0.1	0.032±0.002	0.025±0.002	0.107±0.007

Table 4.10: Hot/Cold results after the optics reconfiguration. The quoted values are the (median) ± (median absolute deviation), calculated using all detectors of the specified band.

Band	N_{res}	$\Delta\nu$ [GHz]	T_{exc} [K]	P_{exc} [pW]	$P_{\mathrm{exc,ant}}$ [pW]	C [GHz/nm]	C_{ant} [GHz/nm]	η_{ant}
Dark	22	–	60±33	0.3±0.1	–	0.007±0.001	–	–
0	21	17	16±7	0.6±0.3	0.4±0.3	0.057±0.005	0.050±0.005	0.123±0.011
1	25	22	19±9	1.1±0.6	0.8±0.6	0.089±0.006	0.082±0.006	0.167±0.016
2	40	16	19±4	0.7±0.2	0.4±0.2	0.058±0.006	0.051±0.005	0.144±0.017
3	26	13	21±6	0.4±0.1	0.2±0.1	0.031±0.002	0.025±0.002	0.087±0.013

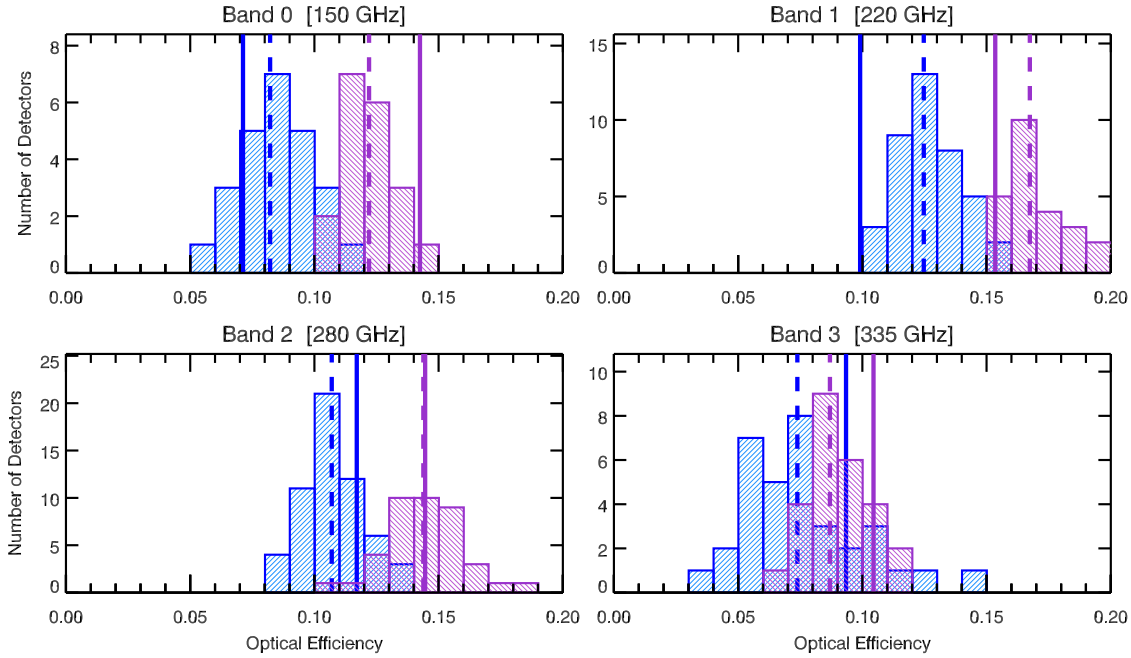

Figure 4.16: The measured optical efficiency $\eta_{\rm ant} = \eta_{\rm ph}\eta_{\rm opt,ant}$ before (blue) and after (red) the optics reconfiguration. All detectors with well-behaved hot/cold data are included in the histograms. We include detectors on the A2 and B2 arrays in the before histogram and detectors on the B2 array in the after histogram.

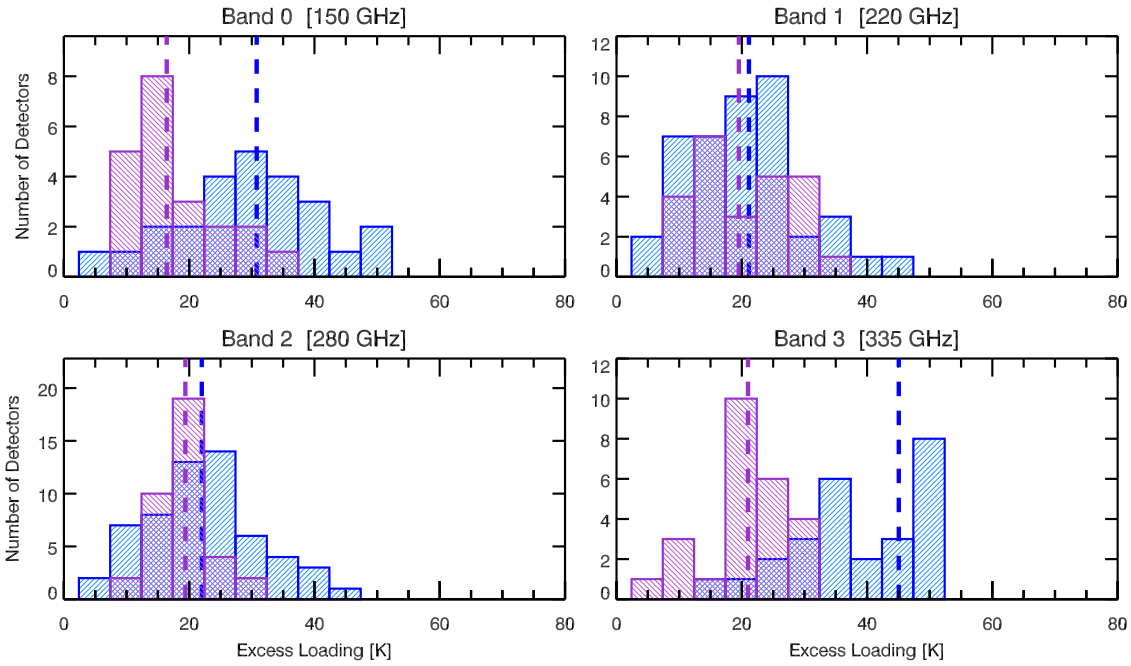

Figure 4.17: The measured excess loading $T_{\rm exc}$ before (blue) and after (red) the optics reconfiguration.

Table 4.11: Comparison of the expected and measured single-polarization optical efficiency. See Section 4.2.5 for a description of how the different contributions to the expected efficiency are determined. The optics reconfiguration altered the Lyot stop efficiency only, all other expected efficiencies are identical to those presented in Table 4.7. The values quoted for the measured efficiency are the median and median absolute deviations over resonators of the specified band on the B2 detector array.

	Expected Efficiency							Measured Efficiency	Measured / Expected
Band	**Phonon**	**Reflection**	**Microstrip**	**Antenna**	**Lyot Stop**	**Filters**	**Total**	**($\eta_{\rm ph} \times \eta_{\rm opt,ant}$)**	
0	0.60	0.88	0.88	0.74	0.56	0.74	0.142	0.123 ± 0.011	0.86 ± 0.08
1	0.50	0.88	0.83	0.70	0.79	0.76	0.153	0.167 ± 0.016	1.09 ± 0.10
2	0.46	0.88	0.79	0.78	0.84	0.69	0.145	0.144 ± 0.017	1.00 ± 0.12
3	0.43	0.88	0.75	0.71	0.85	0.61	0.104	0.087 ± 0.013	0.83 ± 0.12

4.3.3 Skydips

We collected skydip data for all of the detectors on the B2 array on the night of July 31, 2014. The dataset consists of IQ sweeps collected with the dome open and the telescope pointed at 6 elevation angles between 20° and 70°; specifically $\mathfrak{e} = [20^\circ,\ 30^\circ,\ 40^\circ,\ 50^\circ,\ 60^\circ,\ 70^\circ]$. The ambient temperature over the course of the skydip measurement was $T_{\rm amb} = 275.2 \pm 0.3$ K. The CSO tipping radiometer measures the optical depth at 225 GHz every 10 minutes. The tipping radiometer reported $\tau_{225} = 0.119 \pm 0.008$ over the course of the skydip measurement (which corresponds to $\mathcal{C}_{\rm PW} = 2.25 \pm 0.16$ mm). The following morning the opening in the hex plate of the telescope was covered with a large piece of Eccosorb® and a final IQ sweep was collected to act as the room-temperature load reference measurement. The ambient temperature during the reference measurement was $T_{\rm amb} = 276.9$ K. The dataset is analyzed according to the procedure outlined in Section 3.2.5.

We find that the spillover fraction for the dark resonators is $f_{\rm spill,dir} = 0.31 \pm 0.02$. We also measure $\tau_{\rm dir} = 0.24 \pm 0.02$. The mean value of these two quantities did not change appreciably with the optics reconfiguration. However, the scatter in these two quantities across the different dark resonators decreased significantly and is now roughly consistent with the measurement uncertainty.

The best fit antenna spillover fractions $f_{\rm spill,ant}$ are presented in Figure 4.18 as a function of the azimuthal offset of the detector from the center of the focal plane. We no longer observe a large increase in spillover at the edge of the focal plane. It appears that either the optics reconfiguration or the improved baffling at the Lyot stop was successful in this regard. However, the spillover is still in excess of the expectation based on the inefficiencies of the MUSIC optics. Indeed, the measured spillover fraction in the central region of the focal plane is almost identical to the values measured before the optics reconfiguration.

Finally, Figure 4.19 compares the best-fit optical depth $\tau_{\rm ant}$ with our prediction based on the average value of τ_{225} reported by the CSO over the course of the measurement, the ATM model, and the measured bandpasses. The figure reconfirms that that we can reliably predict the optical depth for Band 0, 1, and 2. In addition, the predictions for the Band 3 resonators are much closer to the measured values than was seen in

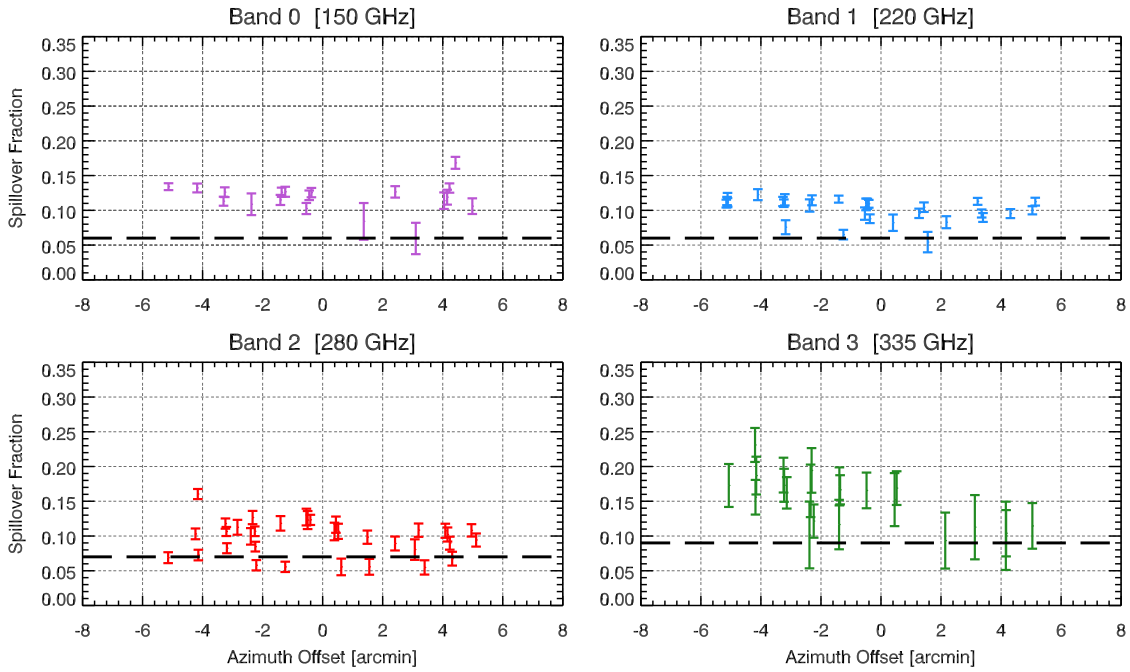

Figure 4.18: Spillover fraction as a function of the azimuthal offset of the detector from the center of the focal plane after the optics reconfiguration. Each panel corresponds to a different band. The black dashed line denotes the expected spillover fraction based on the inefficiencies of the telescope.

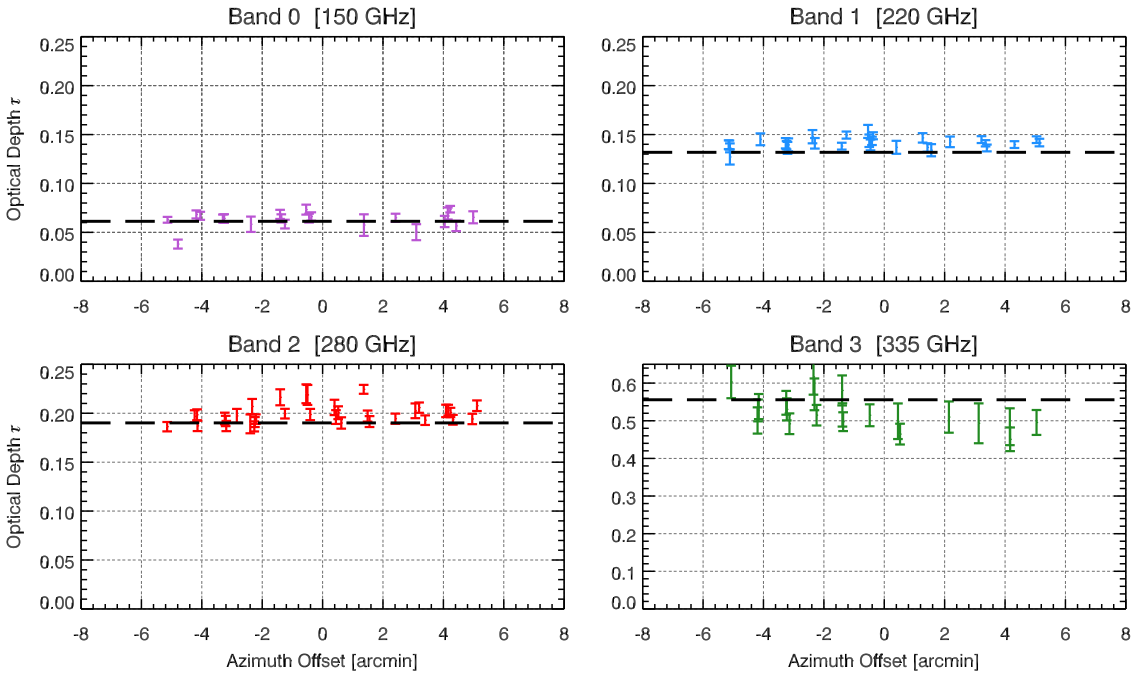

Figure 4.19: Optical depth τ as a function of the azimuthal offset of the detector from the center of the focal plane. Each panel corresponds to a different band. The black dashed line denotes the expected optical depth based on the average $\tau_{225} = 0.119$ reported by the CSO over the course of the skydip measurement, the ATM model for the atmospheric transmission, and the measured detector bandpasses.

Section 4.2.6.

4.3.4 Sleeve Test

We performed a calibration measurement that we call the sleeve test in order to determine the source of the excess spillover discussed in Section 4.2.6 and Section 4.3.3. The measurement and analysis can be summarized as follows:

- The cryostat is taken off the telescope/optics box. A LN_2 load is placed in front of the cryostat window.
- A cylindrical sleeve (20 inches in diameter) is placed between the cryostat window and the LN_2 load. The interior of the sleeve is lined with Eccosorb®. The sleeve sits at room temperature. An example sleeve is pictured in Figure 4.20.
- IQ sweeps are collected with the cryostat at several heights. As the height increases, the solid angle of the room temperature sleeve increases and the solid angle of the LN_2 load decreases.
- The LN_2 load is replaced with a room temperature, beam filling Eccosorb® load. An IQ sweep is collected. This acts as the reference measurement.
- The IQ sweeps are fit to Equation (3.2) and the resonant frequencies extracted. The quantity

$$\Delta f_{\text{res}}^{\text{sleeve}}(h) = f_{\text{res}}(T_{\text{bath}}^{\text{base}},\ T_{\text{amb}}) - f_{\text{res}}(T_{\text{bath}}^{\text{base}},\ T_{\text{load}}(h)) \tag{4.10}$$

  is constructed, which is the frequency shift between the room temperature reference measurement and the sleeve measurement at height h. We fit this quantity to the model presented in Section 2.2. The relevant equations are (2.59), (2.44), (2.37), (2.21), and (2.7). The load temperature is given by

$$\begin{aligned} T_{\text{load}}(h) &= \left[C_{\text{ant}} T_{\text{load,ant}}(h) + C_{\text{dir}} T_{\text{load,dir}}(h)\right]/C \\ &= \frac{C_{\text{ant}}}{C}\left[f_{\text{spill,ant}}(h) T_{\text{amb}} + (1 - f_{\text{spill,ant}}(h)) T_{\text{LN}_2}\right] + \frac{C_{\text{dir}}}{C}\left[f_{\text{spill,dir}}(h) T_{\text{amb}} + (1 - f_{\text{spill,dir}}(h)) T_{\text{LN}_2}\right] . \end{aligned} \tag{4.11}$$

  The free parameters of the fit are

$$\boldsymbol{\theta}_{\text{sleeve}} = \left[f_{\text{spill,ant}}(\boldsymbol{h}),\ f_{\text{spill,dir}}(\boldsymbol{h}),\ \boldsymbol{\theta}_{\text{hot/cold}}\right] . \tag{4.12}$$

  where $\boldsymbol{\theta}_{\text{hot/cold}}$ is well constrained by the hot/cold data. Note that we do not assume a parametric model for the spillover fractions; there is a separate direct absorption and antenna spillover fraction for each height.

- Since $T_{\text{load,ant}}(\boldsymbol{h}) = 0$ for the dark resonators, they are examined first and used to determine $f_{\text{spill,dir}}(\boldsymbol{h})$. All of the parameters of the model other than $f_{\text{spill,dir}}(\boldsymbol{h})$ are well constrained by the hot/cold analysis. There

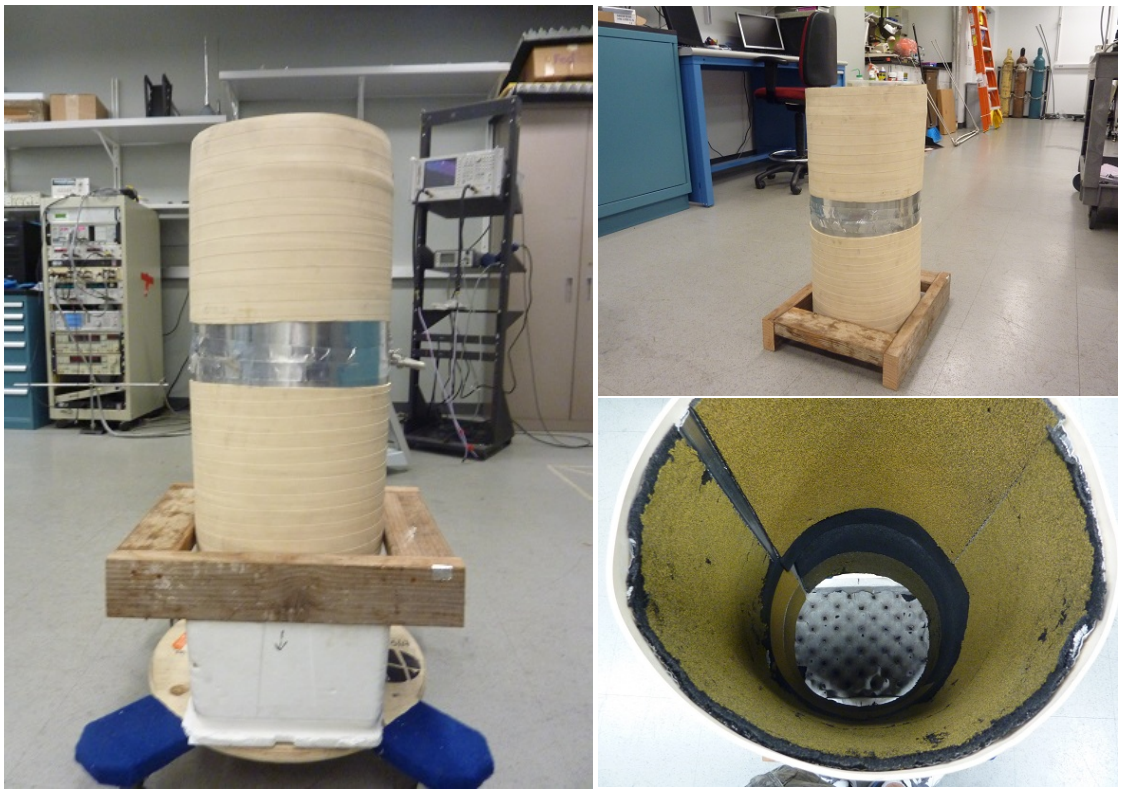

Figure 4.20: Example of an Eccosorb® sleeve. The white styrofoam container is filled with LN_2 during the measurement. The cryostat is lowered down into the sleeve. The sleeve pictured here was built for a test dewar at Caltech. The actual sleeve used for the measurement described in this section is wider. It is constructed out of a rubber trash can that has the bottom removed and the interior lined with a thin layer of Eccosorb®.

are N_h measurements $\Delta f_{\rm res}^{\rm sleeve}(\boldsymbol{h})$, but N_h unknowns $f_{\rm spill,dir}(\boldsymbol{h})$. Thus, we are not truly performing a fit but rather solving our model for the direct absorption spillover fraction. This is accomplished with a root finding algorithm. The procedure is repeated many times. For each sample, $\Delta f_{\rm res}^{\rm sleeve}(h)$ is randomly perturbed by its measurement error and $\boldsymbol{\theta}_{\rm hot/cold}$ is randomly drawn from the hot/cold joint posterior distribution. This propagates the uncertainty on the measurement and the other model parameters to the quantity of interest, $f_{\rm spill,dir}(\boldsymbol{h})$.

- The procedure is repeated for the antenna coupled resonators to determine $f_{\rm spill,ant}(\boldsymbol{h})$. The only difference is that for each sample we also draw $f_{\rm spill,dir}(\boldsymbol{h})$ randomly from the joint posterior distribution (determined in the previous step) of a random dark resonator.

The purpose of the sleeve test is to measure the fraction of the beam that is terminating on the room temperature load as a function of distance from the cryostat window.

In total we collected IQ sweeps at 8 heights between 4 inches and 34 inches. Here we define h as the distance between the cryostat window and the surface of the LN_2 load. The temperature of the room drifted from $T_{\rm amb} = 290$ K to $T_{\rm amb} = 277$ K over the course of the sleeve test. We record the temperature reported by

the CSO throughout the sleeve test and use the appropriate temperature to model the frequency shift at each height.

The direct absorption spillover fraction and antenna spillover fraction are plotted as a function of height in Figure 4.21 and Figure 4.22, respectively. The behavior is fairly uniform for detectors of a given band. There are several detectors that show a large increase in the antenna spillover fraction at large sleeve heights; we have confirmed that these detectors are located near the edge of the focal plane. For the majority of the detectors, the antenna spillover is less than 10% at all sleeve heights examined. The direct absorption, on the other hand, has a broad beam and a significant fraction of it terminates on the sleeve.

When the sleeve has a height of $\simeq 19$ inches, the LN_2 load occupies the same solid angle as the elliptical mirror when the cryostat is on the optics box. Therefore, we can interpolate the $f_{\rm spill,ant}(\boldsymbol{h})$ curve to 19 inches to determine the fraction of the antenna beam that will exit the cryostat at large angles and terminate in the optics box instead of reflecting off of the elliptical mirror. Note that this is only valid for detectors located near the center of the focal plane. The large-angle spillover fraction is shown in Figure 4.23 as a function of the radial offset of the detector from the center of the focal plane. We measure 4% for Band 0 and $1-2\%$ for Bands $1-3$. This will result in an additional 10 K of loading (referred to the cryostat window) for Band 0 and $2.5-5$ K of loading for Band $1-3$, which is a small fraction of the total loading. While it may be possible to reduce the large-angle spillover with improved baffling, it is likely that we have reached the point of diminishing returns.

We can subtract the large-angle spillover fraction measured with the sleeve test from the spillover fraction $f_{\rm spill,ant}$ measured with skydips in Section 4.3.3 to obtain an estimate of the spillover due to the optics, which we call the CSO spillover fraction. This quantity is shown in Figure 4.24. Remember that our assumptions are only valid for detectors near the center of the focal plane (small radial offset). For Band 0 and Band 1 the measured CSO spillover fraction is equal to our expectation assuming 1% absorption for each of the five mirrors and Ruze scattering from the primary. For Band 2 and Band 3 there is an excess spillover of approximately $3-5\%$.

4.3.5 Loading

Table 4.12 breaks down the total detector loading $T_{\rm load}$ into contributions from spillover onto the interior of the cryostat $T_{\rm exc}$, spillover onto room temperature surfaces $T_{\rm spill} = f_{\rm spill} T_{\rm amb}$, and emission from the atmosphere $T_{\rm sky} = (1 - e^{-\tau/\sin\epsilon}) T_{\rm atm}$. All temperatures are referred to the cryostat window so that they can be compared directly. For Bands 0-2 spillover onto room temperature surfaces is the dominant contribution to the loading. Spillover onto the interior of the cryostat is also appreciable, and is only slightly smaller than spillover onto room temperature surfaces. The contribution from atmospheric emission increases with observing band center frequency, such that it is negligible in Band 0 and dominates in Band 3. Note that the quoted numbers include the contributions from both the antenna and direct absorption.

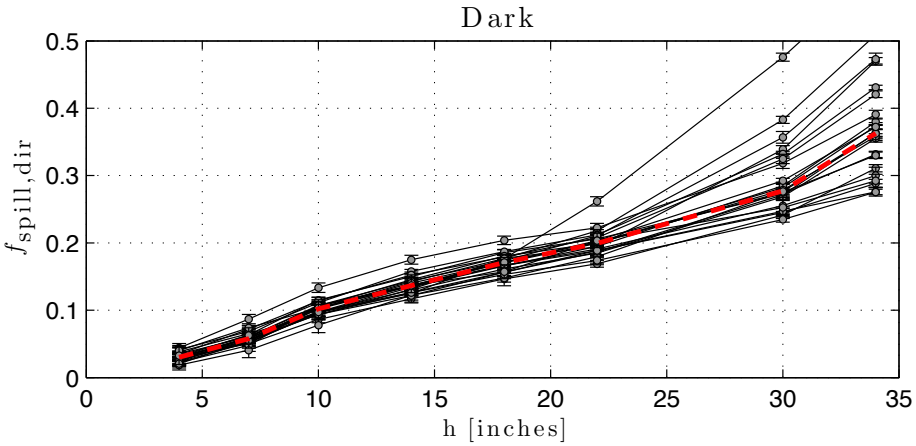

Figure 4.21: Direct absorption spillover fraction as a function of sleeve height. Each line corresponds to a different dark resonator on the B2 array. The gray circles denote the measured data points. The red line denotes the median behavior.

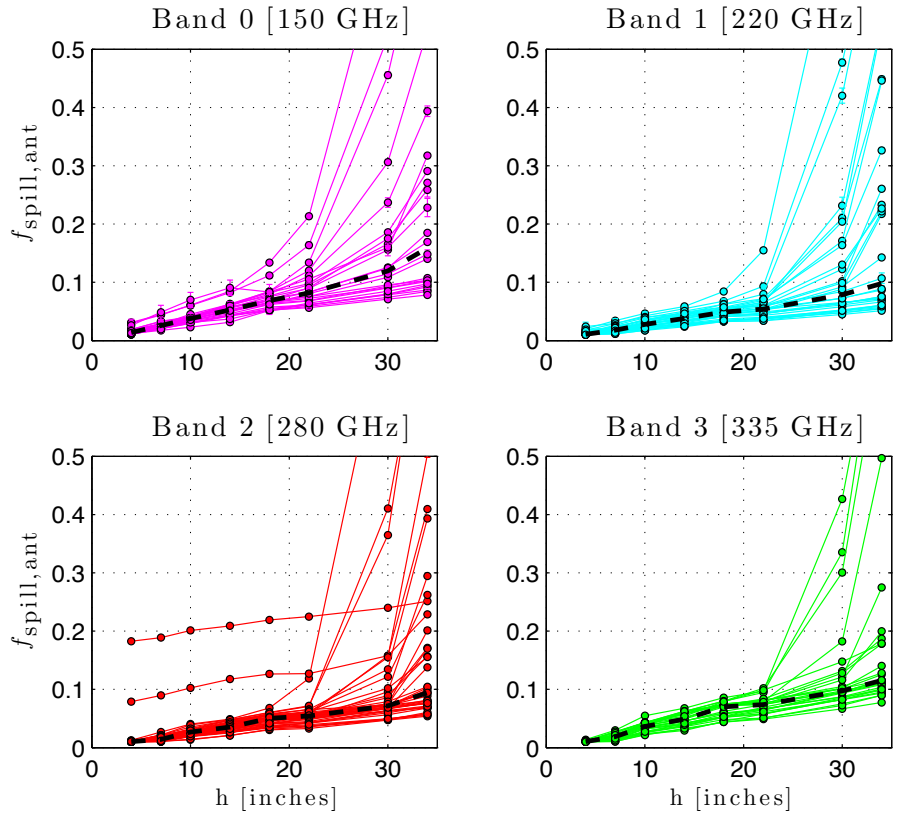

Figure 4.22: Antenna spillover fraction as a function of sleeve height. Each line corresponds to a different resonator on the B2 array. Circles denote the measured data points. The black dashed lines denote the median behavior.

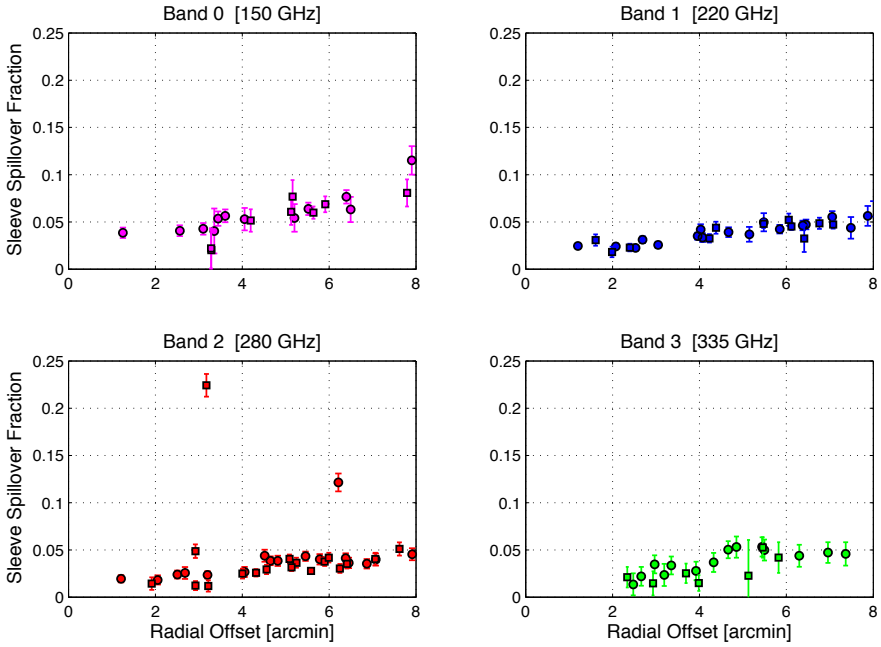

Figure 4.23: Antenna spillover fraction measured with the sleeve at a height of 19 inches as a function of the radial offset of the detector from the center of the focal plane. At small radial offsets, the values shown are equal to the fraction of the beam that exits the cryostat at large angle and terminates in the optics box prior to reaching the elliptical mirror.

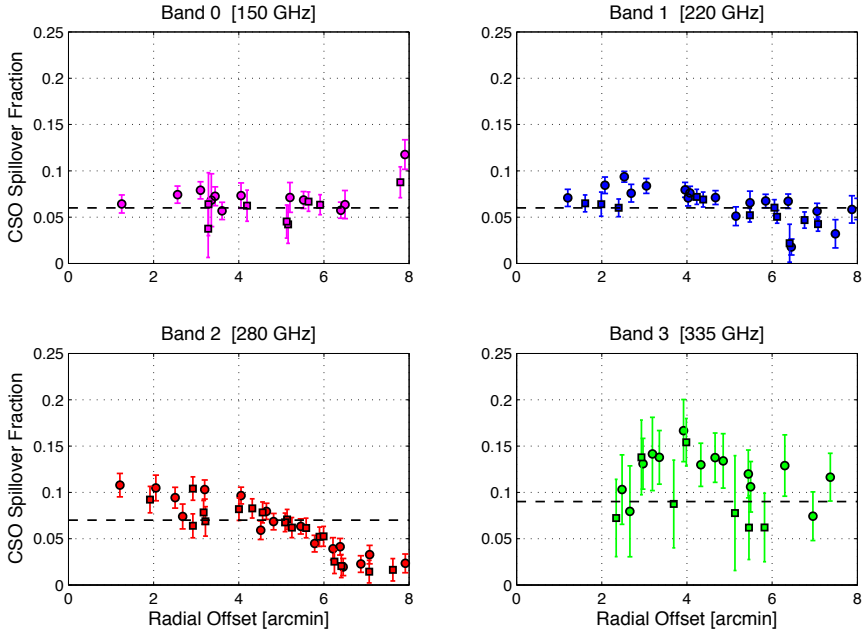

Figure 4.24: CSO antenna spillover fraction as a function of the radial offset of the detector from the center of the focal plane. The values shown are obtained by subtracting the 19 inch sleeve test spillover fraction (see Figure 4.23) from the $f_{\mathrm{spill,ant}}$ measured with skydips (see Figure 4.18). The black dashed line denotes the expected value. The CSO antenna spillover fraction includes the loss due to absorption by the ambient temperature mirrors in the MUSIC optical chain and the spillover past the elliptical mirror.

Table 4.12: Median optical loading after optics reconfiguration, calculated using all detectors of the specified band. $T_{\rm exc}$ is determined from the hot/cold data. $T_{\rm spill}$ is determined from the skydip data. $T_{\rm sky}$ is determined by convolving FTS measurements of the bandpass with the atmospheric transmission spectrum corresponding to τ_{225}.

Band	**T_{exc} [K]**	**T_{spill} [K]**	**T_{sky} [K]**	**T_{load} [K]**	**P_{opt} [pW]**
0	15	40	10	**70**	**3.5**
1	20	35	25	**80**	**7.8**
2	20	35	35	**90**	**5.6**
3	20	55	95	**165**	**5.4**

4.3.6 Responsivity

We again test that the calibrated model describes the small-signal responsivity of our detectors by comparing the measured and predicted response to Uranus. We employ 20 observations of Uranus that were collected for flux calibration purposes over the course of our August/September 2014 observing run. The median value of the column density of precipitable water vapor for this set of observations is $\mathcal{C}_{\rm PW} = 1.66$ mm, which is approximately equal to the historical median and the original analysis. We calculate the median ratio of measured to predicted response for each resonator over the 20 observations. The analysis is identical to that outlined in Section 4.2.8. The results are presented in Figure 4.25. There was some hope that the optics reconfiguration — specifically the reduction in the amount of beam terminating on the Lyot stop and the additional baffles — would reduce the (suspected) wide-angle beam response. We find that at low carrier powers where our calibrated model is valid, the measured response to an unresolved astronomical source is a factor of [0.48, 0.60, 0.55, 0.65] times the predicted response. Recall that before the optics reconfiguration the measured response was a factor of [0.40, 0.50, 0.45, 0.40] times the predicted response, so there was a slight improvement on the order of 10%. However, a significant fraction of our beam remains unaccounted for.

Figure 4.25 also compares the measured and predicted response to small changes in elevation. The values shown were determined from hundreds of observations of faint sources using the same technique outlined in Section 4.2.8. We find that the measured small-signal response to a beam-filling calibrator is still approximately equal to the predicted response for the four observing bands. We carry out two tests to investigate the source of the missing beam.

4.3.6.1 Secondary Collar Test

If the MUSIC optics are either misaligned or out of focus, then some fraction of the beam could bypass the secondary mirror and spillover onto the sky. In order to test this hypothesis we collected skydips with Eccosorb® collars attached to the secondary mirror. The CSO staff constructed three Eccosorb® collars of increasing diameter. The intermediate collar is 33 inches in diameter and is pictured in Figure 4.26. The

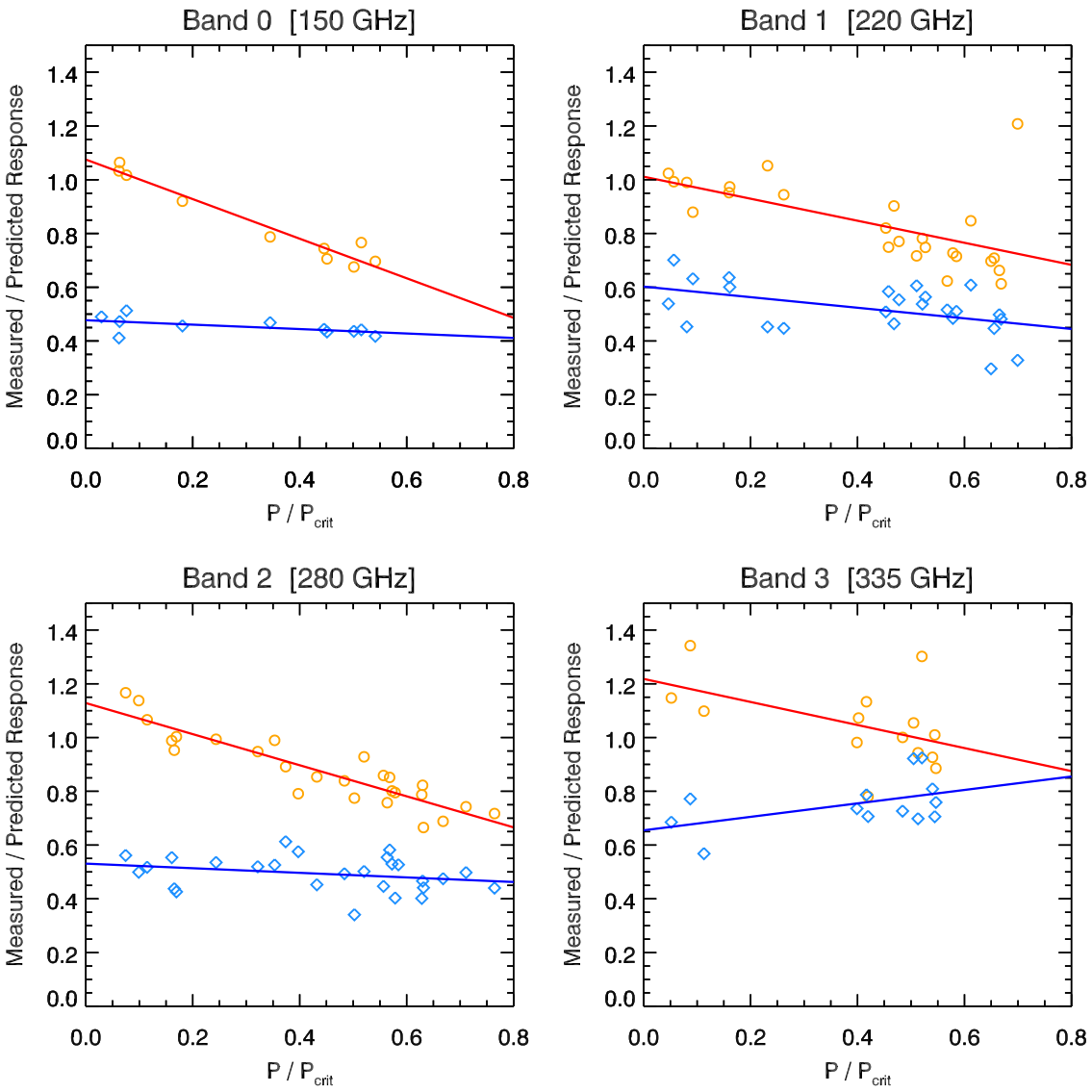

Figure 4.25: Response comparison after the optics reconfiguration. Light blue diamonds denote the ratio of measured to predicted response to an unresolved astronomical source (in this case Uranus). Orange circles denote the ratio of measured to predicted response to small changes in airmass. Blue and red lines are linear fits to the data.

Figure 4.26: *Left:* The intermediate size (100%) Eccosorb® collar. *Right:* Steve Baca showing the Eccosorb® collar attached to the secondary mirror of the CSO. Photos taken by Simon Radford.

secondary mirror is 23 inches in diameter, so the area of the intermediate collar is approximately equal to the area of the secondary. The other two collars are 28 inches and 40 inches in diameter, which correspond to 50% and 200% the area of the secondary, respectively.

Multiple skydips are collected:

1. Two redundant skydips without a collar attached to the secondary.
2. Skydips with the 50%, 100%, and 200% collar attached to the secondary.
3. Skydips with each of the four quadrants of the 200% collar attached to the secondary.

The entire dataset was collected on the night of January 23, 2015. Each skydip measurement consists of IQ sweeps taken with the dome open and the telescope pointed at 6 elevation angles between 20° and 70°. From these sweeps we extract the resonant frequency as a function of elevation angle $f_{\rm res}(\mathfrak{e})$ and calculate the shift relative to the resonant frequency under room-temperature loading. The room-temperature loading reference measurement was obtained by placing a large piece of Eccosorb® over the opening in the hex plate and was collected on the same night as the skydips. The same room-temperature reference measurement was used for all of the skydips.

The top panels of Figure 4.27 compare the skydips collected with the full collars of varying sizes. On the left, we have a detector located towards the center of the focal plane. On the right, we have a detector located towards the edge of the focal plane. Focusing first on the right, we find that the frequency shift relative to the

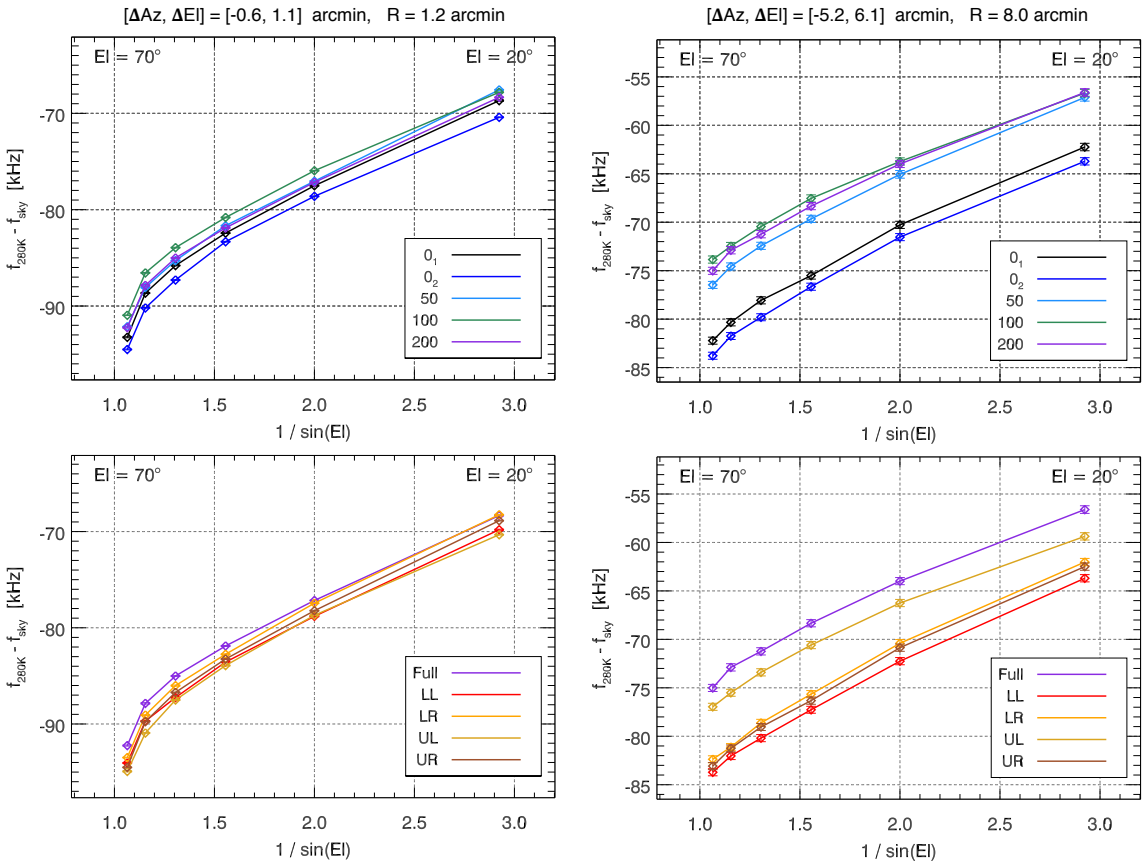

Figure 4.27: Skydips collected with various secondary collar configurations. 0_1 and 0_2 refer to the two redundant measurements without a collar. 50, 100, and 200 refer to the measurements with full collars of increasing radial size. LL, LR, UL, and UL are the lower-left, lower-right, upper-left, and upper-right quadrant measurements with the largest (200) collar. The left and right columns show two Band 1 detectors on the lower half-band of the B2 array that are located near the center and edge of the focal plane, respectively. The azimuthal, elevation, and radial offset of the detectors from the center of the focal plane are quoted in the title.

warm load is larger without a collar than with a collar of any size. The frequency shift either gets slightly smaller or stays the same as you increase the collar size from 50% to 100% to 200%, suggesting that most of the spillover occurs within a radius of 14 inches. The two redundant skydips without a collar were collected four hours apart. They show similar results, suggesting that the systematics due to changing conditions throughout the night are small. Now, focusing on the left, we find that the skydip is almost identical whether or not we have a collar (of any size). This suggests that the detectors located in the center of the focal plane do not see the secondary collar. We find that the majority of the resonators have behavior similar to that shown on the left; it is only the detectors located at the edge of the focal plane that the collar has a noticeable effect on the skydips. Since the large discrepancy in the measured and predicted response to an unresolved astronomical source is observed in all detectors, secondary spillover cannot be the explanation.

The bottom panels of Figure 4.27 compare the skydips obtained with each of the four quadrants of the 200% collar attached to the secondary. The results corroborate the story presented in the previous paragraph. The skydips are identical for detectors located in the center of the focal plane. For detectors located at the edge, the spillover past the secondary is clearly localized to a specific quadrant.

Even for the detectors located at the edge, the frequency response between sky and room-temperature collar is $\lesssim 15\%$ of the frequency response between sky and room-temperature beam-filling load. This suggests that the secondary spillover is a small effect.

4.3.6.2 Large-Angle Beammaps

Knowledge of the effective area of the CSO is necessary to predict the response to an unresolved astronomical source. We calculate A_{eff} using the throughput theorem: $A_{\text{eff}} = \lambda^2/\Omega_{\text{beam}}$. The beam solid-angle Ω_{beam} is determined by fitting a two-dimensional Gaussian to a beammap of Uranus, taking the average value of the FWHM in the two directions, and employing the equation

$$\Omega_{\text{beam}} = \frac{\pi \ \text{FWHM}^2}{4\ln(2)} \ . \tag{4.13}$$

Note that the FWHM in the two directions are approximately equal and a Gaussian shape provides a good fit to the main beam. If there is wide-angle response outside of the main beam, then this will result in an underestimation of Ω_{beam} and overestimation of the response to an unresolved astronomical source. Hence, wide-angle response is a possible explanation for the observed discrepancy between the measured and predicted response to Uranus. In order to test this hypothesis we have made precise measurements of the beams of our detectors. This analysis is primarily the work of Jordan Wheeler; however, the results bring some resolution to the aforementioned discrepancy, so we briefly summarize them in this section.

The flux density of Jupiter is two orders of magnitude larger than Uranus, and enables a study of the beams at very large angles. It also drives the detectors into a nonlinear regime at small angles and distorts the beammap within the central arcmin. We use Uranus to measure the beam at small angles and Jupiter

to measure the beam and large angles. By splicing the Uranus and Jupiter beammaps together in this way we are able to measure the beams out to approximately 10 arcmin. Multiple wide-angle beammaps of both Uranus and Jupiter were collected. For each source we compute the inverse-variance weighted average of the beammaps of all detectors of a given observing band. We find that indeed there are significant sidelobes and diffuse wide angle response outside of the main beam. The fraction of the total power outside of the main beam is [0.77, 0.75, 0.73, 0.52] for the four observing band. This explains more than half of the observed discrepancy between our measured and predicted response to an unresolved astronomical source.

We have compiled a list of the wide-angle response of millimeter and submillimeter instruments that are similar to MUSIC in order to determine if our measured values are reasonable. The Atacama Cosmology Telescope (ACT) measures approximately 20% of the beam solid angle outside of a Gaussian fit to the main beam at 148 and 218 GHz [169]. These measurements extend out to $15-20$ arcmin. The APEX-SZ experiment measures 30% of the beam solid angle outside of the main beam at 150 GHz [170]. This measurement extends out to 4 arcmin. The SCUBA-2 instrument measures 24% of the beam solid angle outside of the main beam at 350 GHz and 39% at 660 GHz [171]. These measurements extend out to 3.33 arcmin and 2.1 arcmin, respectively, but note that the SCUBA-2 beams are much smaller than the other experiments and MUSIC. Finally, the South Pole Telescope (SPT) measures that 15% of the beam solid angle is *outside of 15 arcmin* at 150 and 220 GHz [172]. Our results are consistent with all of these measurements, and suggest that millimeter and submillimeter instruments on ~ 10 meter telescopes can expect to find $20-30$% of their beam solid angle outside of the main beam. We are unable to probe our beams beyond 10 arcmin due to atmospheric noise combined with the relatively slow scan speed of the CSO. But if the measurements made by SPT also hold for MUSIC, which is not unreasonable given the similarities between the two instruments, then we can expect to find an additional 15% of the beam at these very large angles. This would bring the measured and predicted response into agreement at the 10% level.

4.4 Conclusions

In this chapter we presented calibration results for the detectors on the science-grade arrays. These results can be combined with the model outlined in Chapter 2 to understand the propagation of both signal and noise throughout the instrument. To summarize:

- The measured optical efficiency of the detectors is in fairly good agreement with our expectations. There is a slight band dependent discrepancy. Without independent measurements of the recombination coefficient and Al thickness there is a systematic uncertainty of 50% on the overall normalization of the band dependent optical efficiency.

- A small fraction of the beam exits the cryostat at large angles and terminates in the room temperature optics box. This large angle spillover fraction is 4% for Band 0 and $1-2$% for Band 1-3. It does not

contribute significantly to the total loading.

- The spillover due to the MUSIC optics is equal to our expectation for Band 0 and Band 1, and slightly larger than expected in Band 2 and Band 3.
- During observations there is $3-8$ pW of loading at the input to the MKID, depending on observing band.
- The response to an unresolved astronomical source is approximately $40-50\%$ smaller than our expectation based on the calibrated model of our instrument or the measured response to a beam-filling calibrator. Sidelobes and wide-angle diffuse response explain a large fraction of this discrepancy.

Chapter 5

MUSIC Sensitivity

5.1 Introduction

We now examine the noise present in the MUSIC detector timestreams during science observations collected in August and September of 2013. The algorithm used to remove the electronics and atmospheric noise is described, and the quality of the removal quantified. The residual noise is compared to our expectations based on the known sources of intrinsic detector noise, which were calibrated in Chapter 3. We quote the MUSIC single detector sensitivity as a function of observing band and temporal frequency. We conclude by comparing the measured sensitivity to background-limited sensitivity.

All of the data presented in this chapter was collected during the August/September 2013 observing run. Note that this is before the optics reconfiguration. There was a small improvement in the detector sensitivity after the optics reconfiguration, but we have chosen to focus on the pre-optics reconfiguration data because it has been studied in much greater detail. For the most part, we focus on the noise in the frequency direction and neglect the dissipation direction. Since the quasi-particle direction is rotated $\simeq 6^{\circ}$ from the frequency direction for the MUSIC detectors, very little astronomical signal lies in the dissipation direction. As a result, the sensitivity in the dissipation direction is comparatively poor.

5.2 Electronics Noise Removal

Approximately 40% of the carrier tones read out during observations are centered off-resonance. We use the off-resonance carriers to monitor and correct for the $1/f$ and drift type amplitude and phase fluctuations sourced by the electronic components. We now describe this procedure in detail.

Consider the case where we have n off-resonance carriers and we sample the complex amplitude of each m times at frequency $f_s = 100$ Hz. The resulting data set is labeled $\{\mathrm{I},\mathrm{Q}\}_{ij}$, where $i = 1, \ldots, n$ and $j = 1, \ldots, m$. If we assume that the amplitude and phase fluctuations are multiplicative and coherent across microwave frequency, then we obtain the following model for the in-phase and quadrature-phase components

of carrier i at time sample j:

$$\begin{aligned}\widehat{\mathrm{I}}_{ij} &= A_i\left[(1+\delta A_j)\cos\phi_i - \delta\phi_j \sin\phi_i\right] + \delta w_{\mathrm{I}} \\ \widehat{\mathrm{Q}}_{ij} &= A_i\left[(1+\delta A_j)\sin\phi_i + \delta\phi_j \cos\phi_i\right] + \delta w_{\mathrm{Q}}\ .\end{aligned} \tag{5.1}$$

These equations were originally presented in Section 2.3.1.2. Recall that $A = g_{\mathrm{RF}} g_{\mathrm{BB}} A_0$ and $\phi = \phi_0 - 2\pi f \tau_{\mathrm{RF}} - 2\pi f_{\mathrm{BB}} \tau_{\mathrm{BB}}$ are the DC carrier amplitude and phase measured at the output of the system. The amplitude at the output A is related to the amplitude at the input A_0 by some overall voltage gain $g_{\mathrm{RF}} g_{\mathrm{BB}} = \sqrt{G_{\mathrm{RF}} G_{\mathrm{BB}}}$. Similarly the phase ϕ at the output is related to the phase at the input ϕ_0 by some overall baseband cable delay τ_{BB} and RF cable delay τ_{RF}. The $\delta w = \delta w_{\mathrm{I}} + j\delta w_{\mathrm{Q}}$ term denotes the additive white noise from the entire system referred to the ADC. Finally, δA and $\delta\phi$ denote the amplitude and phase fluctuations, respectively. The quantity δA is a linear combination of the amplitude fluctuations from the individual electronic components. Likewise the quantity $\delta\phi$ is a linear combination of the phase fluctuations from the individual electronic components.

We assume that the amplitude and phase fluctuations are common to all n resonators, and take $\boldsymbol{\delta A}$ and $\boldsymbol{\delta\phi}$ to be $2\times m$ free parameters of our model. We take the amplitudes $\boldsymbol{A}$ and phases $\boldsymbol{\phi}$ to be an additional $2\times n$ free parameters. Here the amplitude fluctuations $\boldsymbol{\delta A}$ and phase fluctuations $\boldsymbol{\delta\phi}$ vary with time but are common to all carriers. The amplitudes $\boldsymbol{A}$ and phases $\boldsymbol{\phi}$ are constant in time but vary between carriers; they are the carrier dependent normalization to the common mode fluctuations. We denote the set of all model parameters as

$$\boldsymbol{\theta} \quad = \quad \left[\boldsymbol{A},\ \boldsymbol{\phi},\ \boldsymbol{\delta A},\ \boldsymbol{\delta\phi}\right]^T\ . \tag{5.2}$$

Given the measured data, our problem amounts to finding estimates $\hat{\boldsymbol{\theta}} = \left[\hat{\boldsymbol{A}},\ \hat{\boldsymbol{\phi}},\ \boldsymbol{\delta}\hat{\boldsymbol{A}},\ \boldsymbol{\delta}\hat{\boldsymbol{\phi}}\right]^T$ of the $(2\times n + 2\times m)$ model parameters that maximize the likelihood function, or equivalently minimize the negative log-likelihood function

$$-\log\left[\mathcal{L}(\boldsymbol{\theta}|\{\mathrm{I},\mathrm{Q}\})\right] \quad = \quad \frac{1}{2}\sum_{i=1}^{n}\sum_{j=1}^{m}\frac{1}{\sigma_i^2}\left[(\mathrm{I}_{ij} - \widehat{\mathrm{I}}_{ij}(\boldsymbol{\theta}))^2 + (\mathrm{Q}_{ij} - \widehat{\mathrm{Q}}_{ij}(\boldsymbol{\theta}))^2\right]\ , \tag{5.3}$$

where σ_i^2 is the variance of the additive white noise referred to the ADC for carrier i. This equation assumes that the variance of the additive white noise is equal for the in-phase and quadrature-phase component of each carrier, which we expect theoretically and have confirmed experimentally. By taking the derivative of Equation (5.3) with respect to $\{\delta\phi_j,\ \delta A_j,\ \phi_i,\ A_i\}$ and setting it equal to zero, one can derive the following expressions for the maximum likelihood estimates:

$$\delta\hat{\phi}_j = \frac{\sum_{i=1}^{n} \sigma_i^{-2}\,\hat{A}_i\left[\mathrm{Q}_{ij}\cos\hat{\phi}_i - \mathrm{I}_{ij}\sin\hat{\phi}_i\right]}{\sum_{i=1}^{n} \sigma_i^{-2}\,\hat{A}_i^2} \tag{5.4}$$

$$\delta\hat{A}_j = \frac{\sum_{i=1}^{n} \sigma_i^{-2}\,\hat{A}_i\left[\mathrm{I}_{ij}\cos\hat{\phi}_i + \mathrm{Q}_{ij}\sin\hat{\phi}_i - \hat{A}_i\right]}{\sum_{i=1}^{n} \sigma_i^{-2}\,\hat{A}_i^2} \tag{5.5}$$

$$\hat{\phi}_i = \arctan\left(\frac{\sum_{j=1}^{m}\left[(1+\delta\hat{A}_j)\mathrm{Q}_{ij} - \delta\hat{\phi}_j\mathrm{I}_{ij}\right]}{\sum_{j=1}^{m}\left[(1+\delta\hat{A}_j)\mathrm{I}_{ij} + \delta\hat{\phi}_j\mathrm{Q}_{ij}\right]}\right) \tag{5.6}$$

$$\hat{A}_i = \frac{\cos\hat{\phi}_i\sum_{j=1}^{m}\left[(1+\delta\hat{A}_j)\mathrm{I}_{ij} + \delta\hat{\phi}_j\mathrm{Q}_{ij}\right] + \sin\hat{\phi}_i\sum_{j=1}^{m}\left[(1+\delta\hat{A}_j)\mathrm{Q}_{ij} - \delta\hat{\phi}_j\mathrm{I}_{ij}\right]}{m + \sum_{j=1}^{m}(2\delta\hat{A}_j + \delta\hat{A}_j^2 + \delta\hat{\phi}_j^2)}\,. \tag{5.7}$$

Note that, given the carrier-specific normalizations $\hat{A}_i$ and $\hat{\phi}_i$ one can analytically calculate the maximum likelihood estimates of the common mode fluctuations $\delta\hat{A}_j$ and $\delta\hat{\phi}_j$. Likewise, given $\delta\hat{A}_j$ and $\delta\hat{\phi}_j$, one can calculate $\hat{A}_i$ and $\hat{\phi}_i$. This naturally lends itself to an iterative method for finding the best solution. We start by using the sample mean of the data to inform a guess at the amplitude and phase of the carriers

$$\hat{\phi}_i^{(0)} = \arctan\left(\frac{\overline{\mathrm{Q}}_i}{\overline{\mathrm{I}}_i}\right) \tag{5.8}$$

$$\hat{A}_i^{(0)} = \sqrt{\overline{\mathrm{I}}_i^2 + \overline{\mathrm{Q}}_i^2} \tag{5.9}$$

and then calculate $\delta\hat{\phi}_j$ and $\delta\hat{A}_j$ using Equation (5.4) and Equation (5.5). We then re-calculate $\hat{\phi}_i$ and $\hat{A}_i$ using Equation (5.6) and Equation (5.7). This process is repeated until the change in the negative log-likelihood reaches some desired tolerance. Typically convergence occurs in $2-3$ iterations. We estimate the variance σ_i^2 from the Allan variance of the residuals after the first iteration.

We find that $\boldsymbol{\delta A}$ and $\boldsymbol{\delta\phi}$ have a mild dependence on microwave frequency, and that we improve the removal by fitting local groups of $5-10$ carriers. The choice of the number of carriers to use in the fit is a trade-off between improving sensitivity to possible decoherence of $\boldsymbol{\delta A}$ and $\boldsymbol{\delta\phi}$ with microwave frequency (fewer carriers), and averaging down on the additive white noise that is introduced in the $\boldsymbol{\delta\hat{A}}$ and $\boldsymbol{\delta\hat{\phi}}$ templates (more carriers).

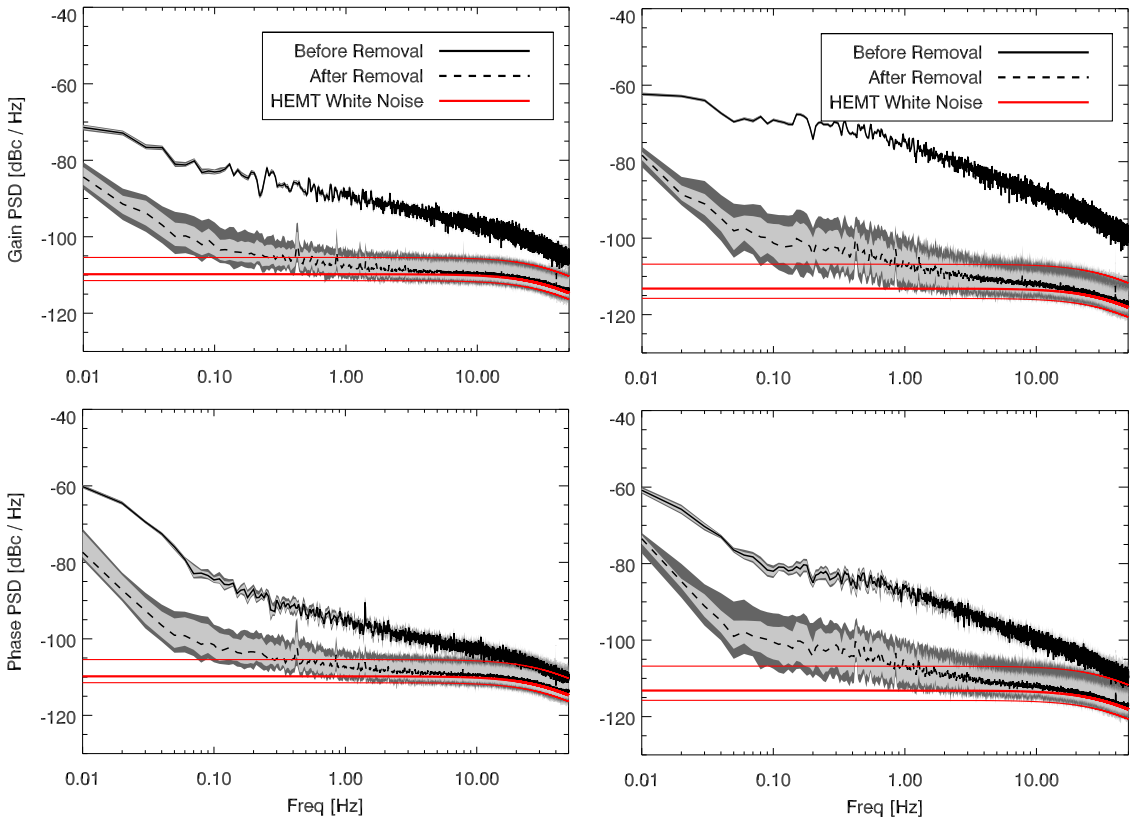

Figure 5.1: Power spectral density of the amplitude (*top*) and phase (*bottom*) fluctuations of off-resonance carriers probing Device A2 (*left*) and Device B2 (*right*). The black line, light grey contours, and dark grey contours denote, respectively, the median, inner 68%, and inner 95% of the values measured by the off-resonance carriers probing each device. The solid line denotes the raw data and the dashed line denotes the residuals after applying the electronics noise removal algorithm. The median and inner 95% of values of the additive electronics noise are denoted by the thick and thin solid red lines, respectively.

We also find that we improve the removal by fitting blocks of time that are shorter than the $10-20$ minute long observation. This could be due to non-stationary drift noise from the room temperature electronics. We calculate a different value $\hat{A}_{ij}$ and $\hat{\phi}_{ij}$ at each time sample j using the equivalent of a moving average with a width of ~ 100 seconds (still using Equation (5.6) and Equation (5.7)). This enables us to fit shorter blocks of time while avoiding discontinuities in the residual timestreams.

The performance of the electronics noise removal algorithm is illustrated in Figure 5.1, where we plot the power spectral density in the amplitude and phase direction before and after removal. The left column shows off-resonance carriers probing Device A2 and the right column shows off-resonance carriers probing Device B2. Recall that Device A2 was connected to the HEMT with the best $1/f$ noise performance, whereas Device B2 was connected to the HEMT with the second worst $1/f$ noise performance (see Section 3.3.2). In the case of Device A2, we are able to remove down to the additive white noise floor of the electronics at frequencies above 1 Hz. In the case of Device B2, we are able to remove down to the additive white noise floor at frequencies above 5 Hz. Even though we are unable to clean the multiplicative electronics noise entirely from our timestreams, we do remove an impressive 30 dB of noise in the gain direction and 20 dB of noise in the phase direction (in the case of Device B2).

5.3 On-Resonance Noise Removal

We now describe the algorithm used to remove electronics and atmospheric noise from the raw on-resonance data. Note that prior to running this algorithm, we determine the electronics noise templates ($\boldsymbol{\delta A}$ and $\boldsymbol{\delta\phi}$) from the off-resonance carriers using the algorithm described in the previous section.

1. For each on-resonance carrier we identify templates for the amplitude fluctuations $\boldsymbol{\delta A}$ and phase fluctuations $\boldsymbol{\delta\phi}$. Recall that we have constructed many versions of these templates using groups of $5-10$ off-resonance carriers with similar microwave frequencies. We associate to each on-resonance carrier the templates constructed from the nearest (i.e., closest in microwave frequency on the same electronics board) group of off-resonance carrier.

2. We subtract $\boldsymbol{\delta A}$ and $\boldsymbol{\delta\phi}$ from each on-resonance carrier, scaling by the mean amplitude A and phase ϕ of the on-resonance carrier in the way prescribed by Equation (5.1).

3. We create a template for the atmospheric fluctuations by averaging the frequency component of all on-resonance carriers of a given observing band. We use the frequency component because it contains the majority of the atmospheric signal and we are able to measure the frequency direction accurately for each resonator using a pre-observation IQ sweep.

4. We iteratively re-calculate the correlation coefficient that scales the template to the individual on-resonance carriers, using only temporal frequencies between $10-100$ mHz where the atmospheric noise is found to dominate.

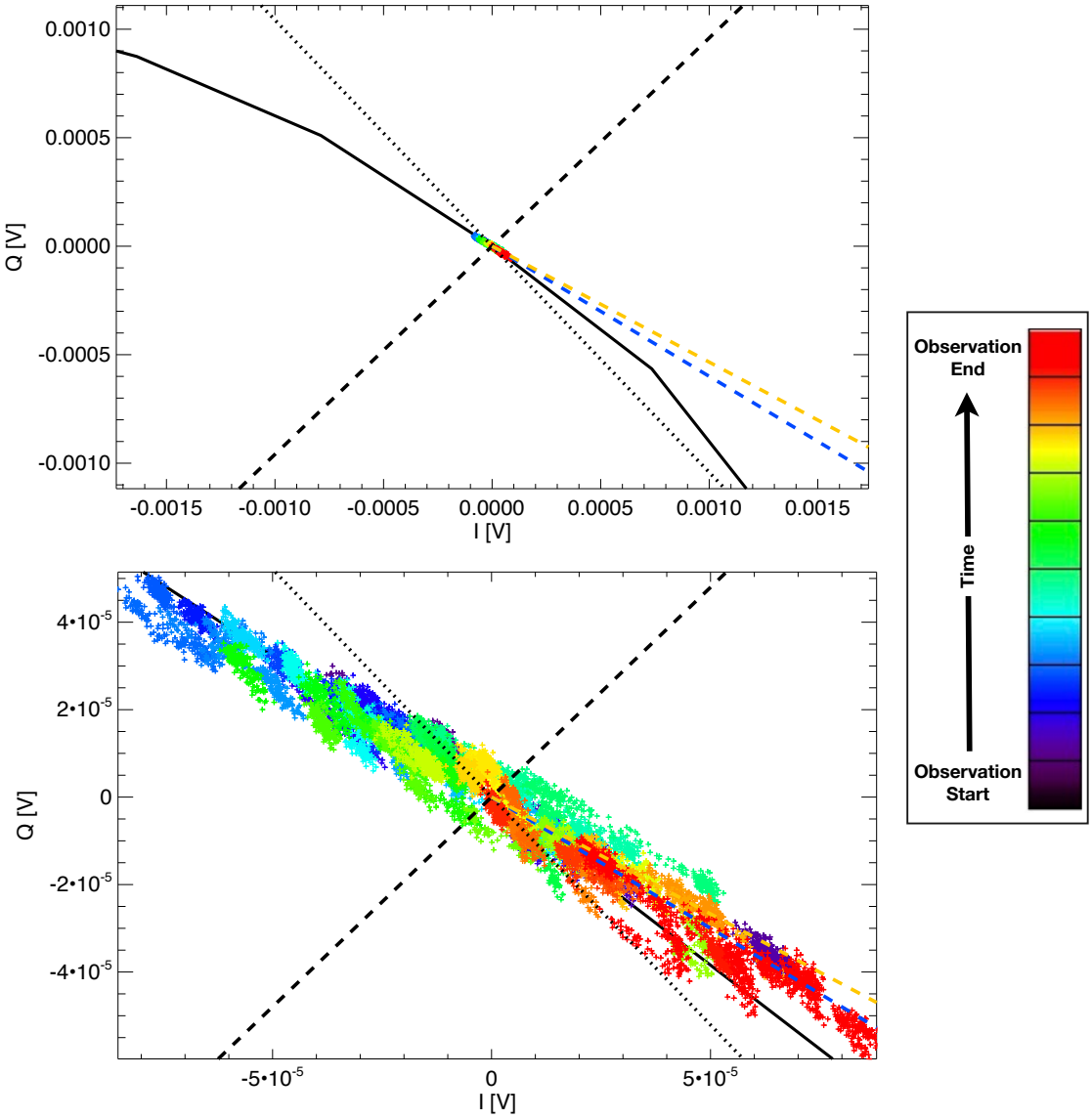

Figure 5.2: Raw on-resonance IQ data from a raster scan observation of a faint source. The scattered points show the data, with the colors indicating continuous 5 second long segments corresponding to scans across the source. The data collected in between each scan as the telescope turns around is not shown. The mean of the entire 20 minute long observation has been subtracted. The black dotted line denotes the amplitude direction and the black dashed line denotes the phase direction, both of which are determined from the mean value of the I and Q timestreams (approximately). The solid black line (top panel only) denotes the pre-observation IQ sweep. The yellow dashed line denotes the frequency direction determined from the tangent to the IQ sweep at the carrier frequency. The blue dashed line denotes the quasi-particle direction determined from the long timescale ($<$ 100 mHz) fluctuations in the data. *Top:* Zoom-out showing both the data and the pre-observation IQ sweep. Note that the pre-observation IQ sweep was collected with a step size of 2.5 kHz, which is large enough near the resonant frequency that the corresponding change in the complex transmission is non-linear. As a result the measured IQ sweep does not appear smooth. *Bottom:* Zoom-in on the data.

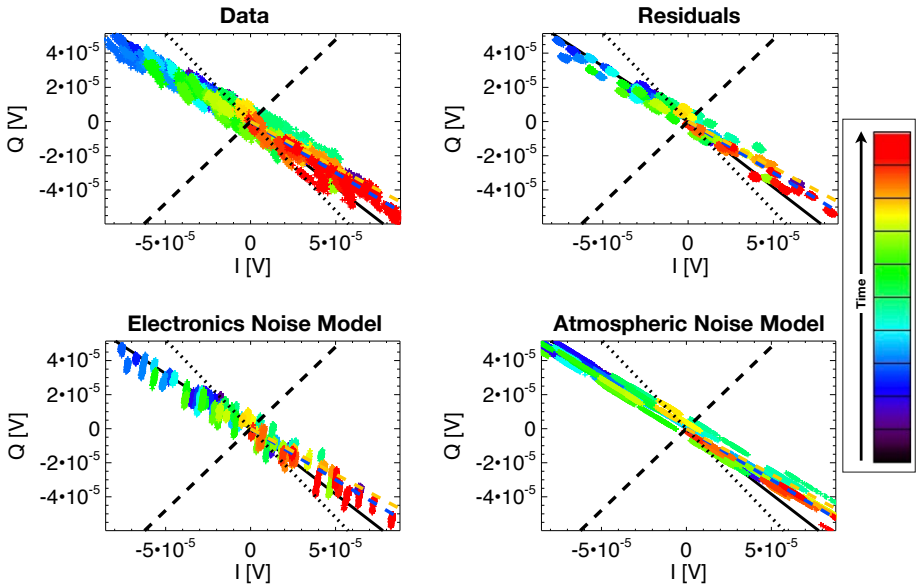

Figure 5.3: Illustration of the process of on-resonance noise removal. *Top left:* The same raw on-resonance IQ data that was shown in Figure 5.2. See the caption of Figure 5.2 for the legend. *Bottom left:* The model for the electronics noise, constructed from the off-resonance data using the algorithm described in Section 5.2. *Bottom right:* The model for the atmospheric noise, constructed from the on-resonance data using the algorithm described in Section 5.3. *Top right:* The residuals after subtracting the electronics and atmospheric noise model from the data. Note that we have retained the mean value of each scan to better illustrate the performance of the noise removal on all scans. In practice the mean value of each scan is subtracted, resulting in a collapse of the individual noise ellipses to the origin.

5. Once we have converged on a atmospheric noise template, we calculate the correlation coefficient between the template and the dissipation component, again using only temporal frequencies between $10 - 100$ mHz.

6. We subtract the appropriately scaled template for the atmospheric fluctuations from the frequency and dissipation component of each on-resonance carrier.

This process is illustrated in the time domain in Figure 5.3.

As mentioned above, we estimate the frequency direction for each resonator from a pre-observation IQ sweep. These IQ sweeps are collected approximately once every hour or whenever there is a change in astronomical source. We fit the IQ sweep to Equation (3.1). Note that the pre-observation IQ sweeps are collected at the same high carrier powers that are employed during observations to improve sensitivity. We let the nonlinearity parameter a float in the fit in order to describe the distortion of the IQ sweeps due to the high carrier powers. Equation (3.1) provides a good fit in nearly all cases. We evaluate the analytical expression for the derivative of this model at the resonant frequency to obtain an estimate of θ_{freq} and $|\partial V/\partial(\delta f_{\text{res}}/f_{\text{res}})|$. We use these quantities to rotate I and Q into the dissipation and frequency components and also to convert from volts at the ADC to dissipation shift and fractional frequency shift (see Section 2.4 for more information on this procedure). If desired, we can then use the model outlined in Chapter 2 and calibrated in Chapter 4

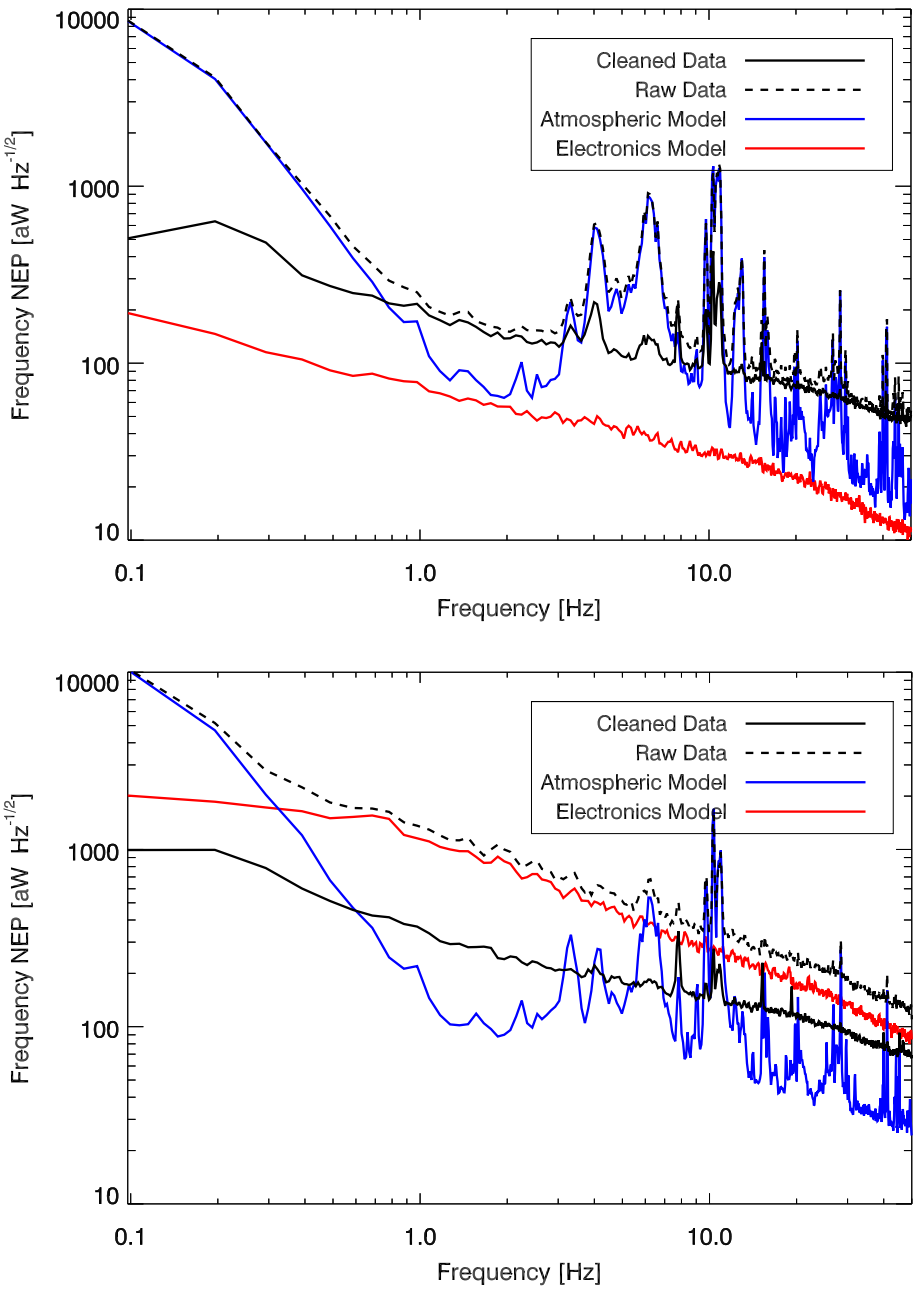

Figure 5.4: NEP in the frequency direction, determined from a single observation. The values in the plot are obtained by taking the median over all Band 1 resonators on the lower half-band of Device A2 (*top*) and the upper half-band of Device B2 (*bottom*). The dashed black line denotes the raw data. The solid red line denotes the model for the electronics noise. The solid blue line denotes the model for the atmospheric noise. The solid black line denotes the cleaned data, obtained by subtracting the electronics and atmospheric noise model from the raw data.

to convert the timestreams into changes in the optical power incident on the MKID, source temperature, or source flux.

Figure 5.4 shows the detector NEP in the frequency direction before and after noise removal. This figure was produced from a 10 minute long observation of a faint source collected using a lissajous scan strategy. The $\mathcal{C}_{\rm PW}$ at the time of the observation was 1.4 mm, which is close to the historical median at the CSO (1.68 mm). The quantities shown are obtained by taking the median over all of the Band 1 resonators on a given device half-band; the top panel using the resonators between $3.0-3.5$ GHz on Device A2 and the bottom panel using the resonators between $3.5-4.0$ GHz on Device B2.

The electronics noise in the bottom panel (Device B2U) is much larger than the electronics noise in the top panel (Device A2L); roughly 22 dB at 1 Hz. The majority of the electronics noise is due to fluctuations in the gain and phase delay of the HEMT amplifier. We see substantial variation in the amplitude of these gain fluctuations across the 8 HEMTs used in MUSIC, as discussed in detail in Section 3.3.2. The amplifier connected to A2 has the best performance, while the amplifier connected to B2 has the second poorest performance. The difference in the intrinsic amplitude of the gain fluctuations between the A2 and B2 HEMT accounts for 14 dB. The other 8 dB is due to differences in the factor $\partial S_{21}/\partial P_{\rm opt}$, which converts between complex transmission and optical power, primarily due to differences in the median resonator quality factor of the two samples. For A2 the electronics noise is subdominant to other sources of noise intrinsic to the detector, and the utility of the electronics noise removal algorithm is minimal. For B2 the electronics noise is the dominant source of noise. In this case, the electronics noise removal algorithm is absolutely necessary and results in significant improvements (>10 dB) in detector sensitivity.

The atmospheric noise dominates at frequencies $<0.5-1.0$ Hz and shows the expected $\mathrm{NEP}^{\rm atm} \propto f^{-4/3}$ scaling. We construct a separate template for the atmospheric noise for each observing band by averaging over all of the detectors of that band on the two detector arrays. A single template is able to describe the very low frequency noise of all detectors of a given observing band reasonably well, suggesting that the atmospheric noise is indeed a common mode signal across the focal plane. In addition, the templates obtained for the different observing bands are highly correlated, and it may be possible to improve the performance of the atmospheric noise removal by using the spectral information in more sophisticated algorithms (e.g., Adam et al. [144]).

At frequencies $\gtrsim 2$ Hz the raw data show a large number of lines and features above the continuum level. The narrow spectral lines occur at harmonics of the pulse tube frequency $f_{\rm pt} = 1.41$ Hz. The wider features are associated with the movement of the telescope; they are not observed when the telescope is idle, only when it is scanning, and their amplitudes increase by up to an order of magnitude during lissajous scans (compared to raster scans). The data from the off-resonance carriers is completely free of spectral lines, which suggests that the features in the on-resonance data are not caused by electrical pick-up. Most mechanisms by which the pulse tube cooler and the scanning of the telescope could influence the resonators are either thermal or optical in nature (e.g., temperature of filter stack fluctuating and changing resonator loading, or

mechanical vibrations producing thermal fluctuations that change resonator bath temperature). However, both thermal and optical mechanisms would place the spectral lines in the quasi-particle direction. We find strong evidence that the features are instead occurring in the frequency direction. This suggests that the underlying mechanism is magnetic in nature [173]. Whatever the origin, the spectral lines and noncontinuum features are highly correlated between detectors on a given device, as evidenced by the fact that they are "picked-up" in the atmospheric template (as seen in Figure 5.4) and, for the most part, removed. Further improvement in the removal of the spectral lines was obtained by correlating and regressing out the AZ and EL motion of the telescope from the frequency direction data prior to atmospheric noise removal [174]

5.4 Residual Noise

5.4.1 Comparison to Calibrated Model Predictions

We subtract the electronics and atmospheric noise from the raw data using the procedure outlined in the previous section. We then predict the residual or uncorrelated noise that we expect to see in *each individual* detector timestream using the technique described in Section 3.3.1 for additive electronics noise, Section 3.3.4 for TLS noise, and Section 3.3.3 for the fundamental noise due to photon, generation, and recombination noise. The measured noise is compared to the total predicted noise to determine how well we understand the sensitivity of our detectors.

Figure 5.5 shows the measured NEP in the frequency direction after electronics and atmospheric noise removal along with the predicted contribution from the various sources of intrinsic detector noise. This figure is produced from the same 10 minute long lissajous observation and the same Band 1 detectors as Figure 5.4. We see excellent agreement between the measured noise and the total predicted noise at frequencies $\gtrsim 2-3$ Hz. For now let's focus on these frequencies where the data and calibrated model agree. We find that for detectors in the upper half-bands the TLS noise dominates. For detectors in the lower half-bands the TLS noise is less than or equal to the fundamental noise of the MKID (quadrature sum of the photon, generation, and recombination noise). This is because the amplitude of the TLS noise is significantly larger for detectors in the upper half-bands ($f_{\rm res} = 3.5-4.0$ GHz) than for detectors in the lower half-bands ($f_{\rm res} = 3.0-3.5$ GHz), as discussed in Section 3.3.4. The contribution from the additive electronics noise is negligible.

Figure 5.5 is derived from a single observation using half of the Band 1 resonators. In order to form a more comprehensive idea of how well the measured noise matches the predicted noise, we examined a sample of 11 observations representative of the observing conditions encountered during the August/September 2013 run. Figure 5.6 presents histograms of the ratio of measured to predicted NEP at 6.5 Hz and 1.0 Hz. For reference, the half width at half maximum of the beams of our detectors correspond to [2.4, 3.4, 4.2, 4.6] Hz for the four observing bands at the scan speeds achieved at the CSO. Thus, 6.5 Hz can be considered an approximate upper bound on the temporal frequencies to which we are sensitive.

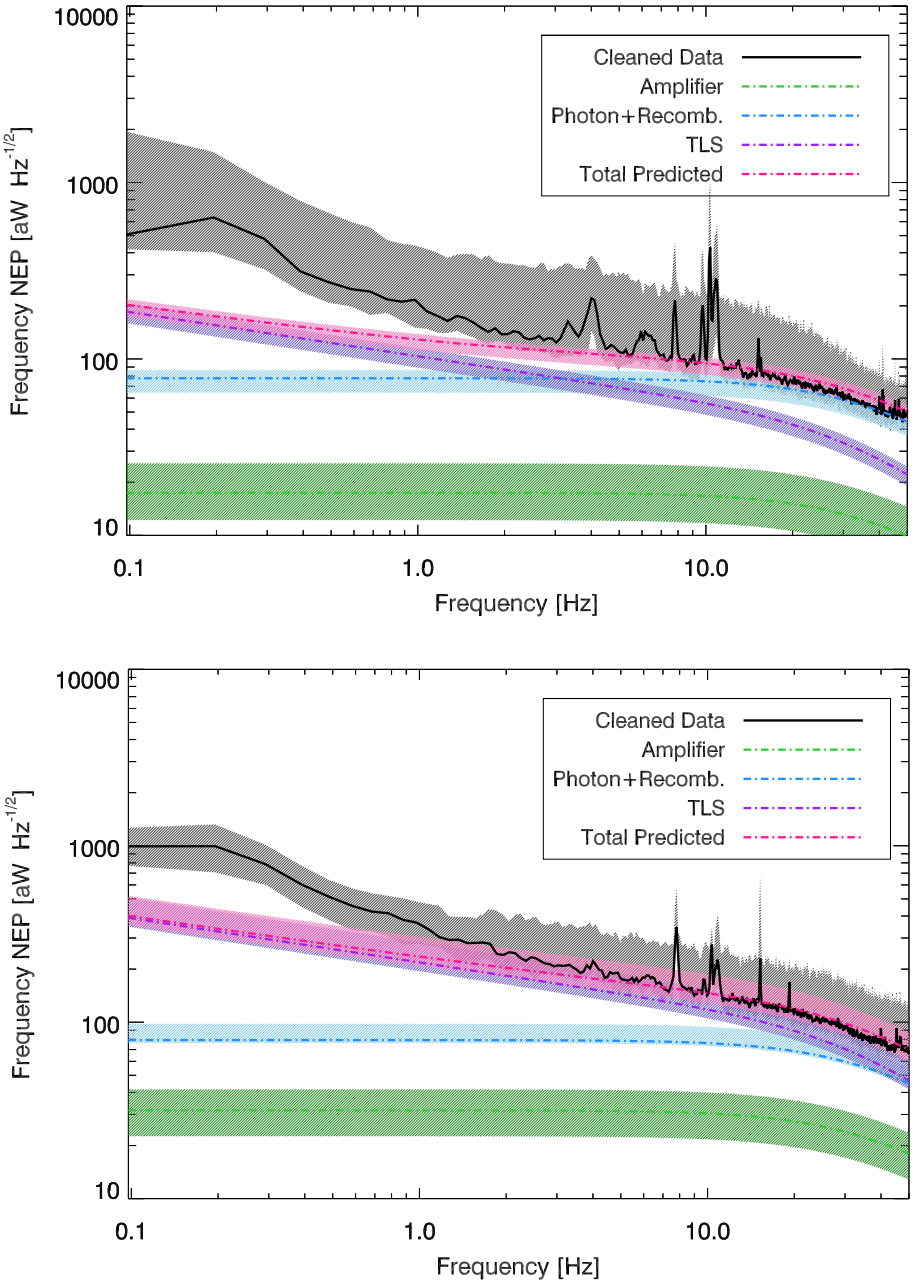

Figure 5.5: NEP in the frequency direction, determined from a single observation. The lines and contours are obtained by taking the median and inner 95% over all Band 1 resonators on the lower half-band of Device A2 (*top*) and the upper half-band of Device B2 (*bottom*). The solid black line denotes the cleaned data, obtained by subtracting the electronics and atmospheric noise model from the raw data. The dash-dotted lines denote predictions for the various uncorrelated noise sources that we expect in the cleaned data; additive electronics noise is shown in green, the quadrature sum of the photon, generation, and recombination noise is shown in light blue, TLS noise is shown in purple, and the total quadrature sum of all the noise sources is shown in pink.

On average we see excellent agreement between the measured and predicted noise at 6.5 Hz, with the exception of Band 0 where the measured noise is 30% larger than predicted. Note that these histograms cover all of the resonators on A2 and B2 over a wide range of loading conditions from 0.2 mm to 4.8 mm column depth of precipitable water vapor (median $\mathcal{C}_{\rm PW} = 1.3$ mm). This gives us confidence that the primary sources of noise are well characterized, that we understand how they scale with background loading, and that we are doing an effective job cleaning the atmospheric and electronics noise at high frequencies. The NEP due to each source of intrinsic detector noise is quoted at 6.5 Hz in Tables 5.1 and 5.2.

We observe degradation in the measured NEP relative to predicted as we move to lower frequencies. In Band 0 the measured NEP at 1.0 Hz is 60% larger than predicted, and in Bands 1, 2, and 3 it is 40% larger than predicted. However, the model prediction for the TLS noise is based on measurements made at 6.5 Hz and assumes the usual $\nu^{-1/2}$ scaling of $S_{\delta f_{\rm res}/f_{\rm res}}$ to extrapolate to 1.0 Hz. We presented strong evidence in Section 3.3.4 that the TLS noise spectrum steepens at low frequency. In fact, Figure 3.15 shows that for resonators on A2 and B2 the measured NEP due to TLS noise at 1.0 Hz is 30% larger than expected based on the measurement at 6.5 Hz and assuming the usual dependence on temporal frequency. Since TLSs are the dominant noise source at 1.0 Hz, this explains the majority of the discrepancy observed in Figure 5.6. Thus, for Bands 1, 2, and 3, the measured and predicted NEP in on-sky, science observations are equal at the 10% level at all frequencies $\gtrsim 1.0$ Hz. The remaining 10% discrepancy at 1.0 Hz is likely due to residual atmospheric or electronics noise. Band 0 detectors exhibit a 30% discrepancy between the measured and predicted noise at both 6.5 and 1.0 Hz that is currently unexplained. The discrepancy can be traced to detectors on the lower half-bands. The characteristics of this discrepancy suggest either a mischaracterization of the TLS noise or some source of excess noise, although it is not clear why either would effect only the Band 0 detectors on the lower half-band.

We present the measured NE($\delta f_{\rm res}/f_{\rm res}$), NEP, NET, and NEFD in the frequency direction at 6.5 Hz in Tables 5.3−5.4 and at 1.0 Hz in Tables 5.5−5.6. The quoted values are the median taken over various subsets of detectors and over our representative sample of 11 observations from the August/September 2013 observing run. See Equations (2.210), (2.215), and (2.214) for definitions of the NEP, NET, and NEFD, respectively. The NE($\delta f_{\rm res}/f_{\rm res}$) is the noise equivalent fractional frequency fluctuation. This is just the square root of the power spectral density converted to fractional frequency fluctuations of the resonator (i.e., NE($\delta f_{\rm res}/f_{\rm res}$) $= \sqrt{S_{\delta f_{\rm res}/f_{\rm res}}}$). Note that NEP is referred to the input of the MKID, while NET and NEFD are referred above the atmosphere. The quoted NET and NEFD take into account the $40-60$% unexplained loss thought to be due to sidelobes and wide-angle diffuse response.

5.4.2 Comparison to Background-Limited Performance

One of the goals of the MUSIC instrument was to demonstrate near-background-limited sensitivity using MKIDs in a large-format array [175]. Figure 5.7 compares the measured NEP to the model prediction for the background-limited NEP. We define the background-limited NEP for MKIDs as that due to photon shot

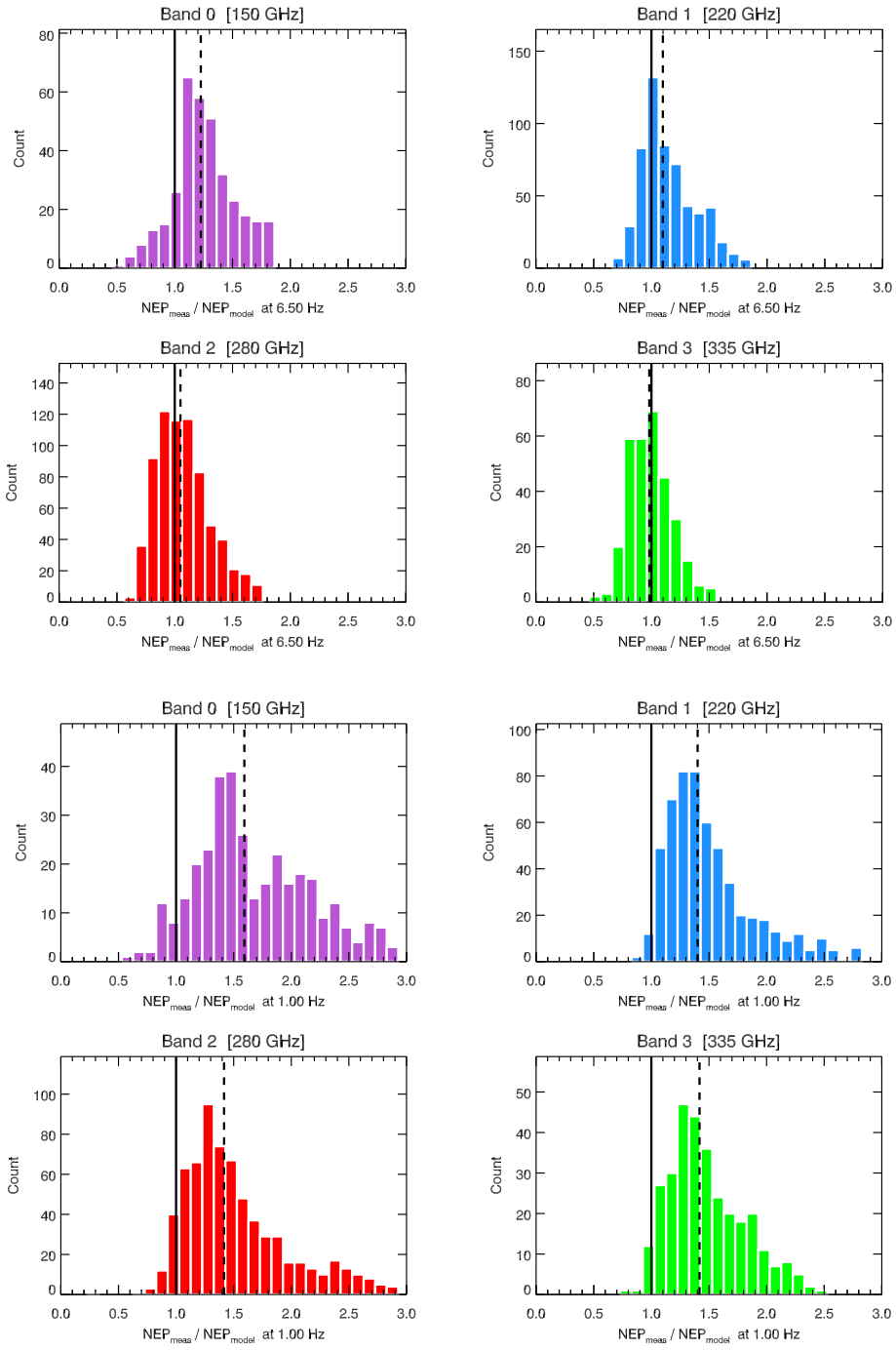

Figure 5.6: Ratio of measured to predicted NEP at 6.5 Hz (*top four panels*) and 1.0 Hz (*bottom four panels*). The dashed black lines denote median values. Each count in the histogram is a single detector during a single observation. All detectors on Devices A2 and B2 were used. In total 11 observations were used, spanning $\mathcal{C}_{\rm PW} = 0.2 - 4.8$ mm (median $\mathcal{C}_{\rm PW} = 1.3$ mm).

Table 5.1: NEP at 6.5 Hz in units of aW $Hz^{-1/2}$. The values listed are the median over the given band/device, calculated using the sample of 11 observations mentioned in the text. The "Fundamental" column is the quadrature sum of the GR, shot, and Bose noise. The "Total Predicted" column is the quadrature sum of the amplifier, fundamental, and TLS noise.

		Predicted							Measured	
Band	Device	Amplifier	*GR*	*Shot*	*Bose*	Fundamental	TLS	Total	Total	Ratio
0	A2L	29	26	26	32	50	65	**85**	**130**	1.5
	A2U	27	26	26	36	50	85	**110**	**135**	1.2
	B2L	13	24	24	32	45	70	**85**	**130**	1.6
	B2U	17	24	26	36	50	110	**125**	**125**	1.1
1	A2L	16	36	42	52	75	65	**100**	**110**	1.1
	A2U	44	38	44	64	85	125	**165**	**215**	1.3
	B2L	15	34	40	51	75	80	**110**	**120**	1.1
	B2U	32	38	44	64	85	145	**170**	**185**	1.1
2	A2L	13	32	44	56	80	65	**100**	**105**	1.1
	A2U	22	32	42	56	75	90	**125**	**135**	1.1
	B2L	9	28	38	46	65	70	**100**	**105**	1.0
	B2U	13	30	40	54	75	100	**125**	**125**	1.0
3	A2L	17	34	48	74	95	75	**120**	**115**	0.9
	A2U	29	32	46	68	90	95	**140**	**145**	1.1
	B2L	12	30	46	67	85	85	**125**	**115**	0.9
	B2U	35	28	42	56	75	140	**165**	**215**	1.2

Table 5.2: NEP at 6.5 Hz in units of aW $Hz^{-1/2}$. The values listed are the median over the given band/device, calculated using the sample of 11 observations mentioned in the text.

	Predicted							Measured	
Band	Amplifier	*GR*	*Shot*	*Bose*	Fundamental	TLS	Total	Total	Ratio
0	20	26	26	34	50	85	**100**	**130**	1.3
1	22	36	42	56	80	90	**125**	**150**	1.1
2	13	30	40	52	70	75	**110**	**115**	1.1
3	17	32	46	70	90	85	**130**	**125**	1.0

Table 5.3: Measured noise at 6.5 Hz. The values listed are the median over the given band and device half-band, calculated using the sample of 11 observations mentioned in the text.

Band	Device	NEDFF [$Hz^{-1/2}$]	NEP [aW $Hz^{-1/2}$]	NET [mK $s^{1/2}$]	NEFD [mJy $s^{1/2}$]
0	A2L	4.0e-10	130	8	280
	A2U	4.0e-10	135	7	250
	B2L	4.1e-10	130	8	300
	B2U	4.0e-10	125	6	230
1	A2L	2.1e-10	110	2	100
	A2U	4.4e-10	215	4	165
	B2L	2.5e-10	120	3	120
	B2U	3.7e-10	185	4	160
2	A2L	2.2e-10	105	4	180
	A2U	3.1e-10	135	5	220
	B2L	2.4e-10	105	4	200
	B2U	3.1e-10	125	5	230
3	A2L	2.3e-10	115	10	505
	A2U	3.4e-10	145	13	650
	B2L	2.6e-10	115	11	585
	B2U	4.7e-10	215	14	710

Table 5.4: Measured noise at 6.5 Hz. The values listed are the median over the given band, calculated using the sample of 11 observations mentioned in the text.

Band	NEDFF [$Hz^{-1/2}$]	NEP [aW $Hz^{-1/2}$]	NET [mK $s^{1/2}$]	NEFD [mJy $s^{1/2}$]
0	4.0e-10	130	7	250
1	2.9e-10	150	3	130
2	2.7e-10	115	5	210
3	2.8e-10	125	11	580

Table 5.5: Measured noise at 1.0 Hz. The values listed are the median over the given band and device half-band, calculated using the sample of 11 observations mentioned in the text.

Band	Device	NEDFF [$Hz^{-1/2}$]	NEP [aW $Hz^{-1/2}$]	NET [mK $s^{1/2}$]	NEFD [mJy $s^{1/2}$]
0	A2L	7.9e-10	260	16	555
	A2U	7.5e-10	245	13	480
	B2L	8.5e-10	280	17	600
	B2U	7.1e-10	215	11	410
1	A2L	3.6e-10	185	4	170
	A2U	8.7e-10	432	8	340
	B2L	4.3e-10	205	5	210
	B2U	7.0e-10	345	7	270
2	A2L	4.0e-10	180	8	330
	A2U	5.9e-10	260	11	450
	B2L	4.5e-10	185	9	380
	B2U	6.6e-10	250	11	470
3	A2L	4.2e-10	200	18	905
	A2U	7.3e-10	290	27	1360
	B2L	5.3e-10	245	25	1270
	B2U	9.1e-10	390	29	1435

Table 5.6: Measured noise at 1.0 Hz. The values listed are the median over the given band, calculated using the sample of 11 observations mentioned in the text.

Band	NEDFF [$Hz^{-1/2}$]	NEP [aW $Hz^{-1/2}$]	NET [mK $s^{1/2}$]	NEFD [mJy $s^{1/2}$]
0	7.6e-10	250	14	500
1	5.3e-10	270	6	230
2	5.3e-10	225	10	400
3	5.5e-10	245	24	1220

noise, photon Bose noise, thermal generation noise, and recombination noise, which we have collectively referred to as the fundamental noise throughout this thesis (see Section 2.3.2.1).

At 6.5 Hz, the median NEP is a factor of [2.6, 1.7, 1.5, 1.4] larger than $\mathrm{NEP}_{\mathrm{BLIP}}$ for the four observing bands. The majority of the spread observed in these distributions is due to an increase in the amplitude of the TLS noise with resonant frequency (see Section 3.3.4). The most sensitive detectors, or the detectors with the lowest resonant frequencies, are approximately background-limited in Band 1, 2, and 3. The median detectors have approximately equal contributions from TLS noise and fundamental noise in Band 1, 2, and 3. We measure noise in excess of our model prediction in Band 0, as discussed in the previous section. As a result, the performance of the Band 0 detectors relative to BLIP is significantly worse compared to the other three bands. The most sensitive Band 0 detectors are a factor of 1.4 above BLIP and the median Band 0 detectors are a factor of 2.6 above BLIP.

The fundamental noise is white, whereas the TLS noise is usually assumed to have a power spectral density that scales as $\nu^{-1/2}$, and in the case of the MUSIC detectors has somewhere between a $\nu^{-1/2}$ and ν^{-1} scaling. As a result, the measured NEP degrades significantly with respect to BLIP at 1.0 Hz. The median NEP is a factor of [5.0, 3.0, 2.8, 2.7] larger than $\mathrm{NEP}_{\mathrm{BLIP}}$ for the four observing bands, with the most sensitive detectors a factor of [2.0, 1.6, 1.3, 1.2] above BLIP. The resulting map space sensitivity lies in between the 1.0 Hz and 6.5 Hz timestream sensitivity, but tends to fall closer to the 1.0 Hz value.

5.5 Conclusions

We presented an analytical model for the responsivity and noise of microwave kinetic inductance detectors. We calibrated this model for each MKID employed in MUSIC using a variety of in-lab and on-sky measurements. We then compared the measured response of the detectors to a beam-filling calibrator to the model prediction. We also compared the measured on-sky noise to the model prediction for intrinsic detector noise. For the most part, we find excellent agreement for the majority of our detectors over a wide range of observing conditions. This gives us confidence that the model adequately describes the underlying physics. The calibrated model provides insight into the performance of our instrument, and also enables predictions for future instruments that employ MKIDs.

We did encounter a few discrepancies between the model and the measured detector properties. The largest being that the measured response to an unresolved astronomical source is $50-60\%$ smaller than either the model prediction or the response to a beam-filling calibrator ($40-50\%$ after the optics reconfiguration). We found that roughly half of the discrepancy is attributed to an underestimation of the beam solid angle due to the presence of sidelobes and diffuse wide-angle response. Since we were only able to probe the radial beam profile out to 10 arcmin, we may still be underestimating the beam solid angle. The South Pole Telescope (SPT) — an instrument that shares many similarities with MUSIC — measured 15% of their beam solid angle outside of 15 arcmin at similar wavelengths [172]. If this also holds for MUSIC, then it would

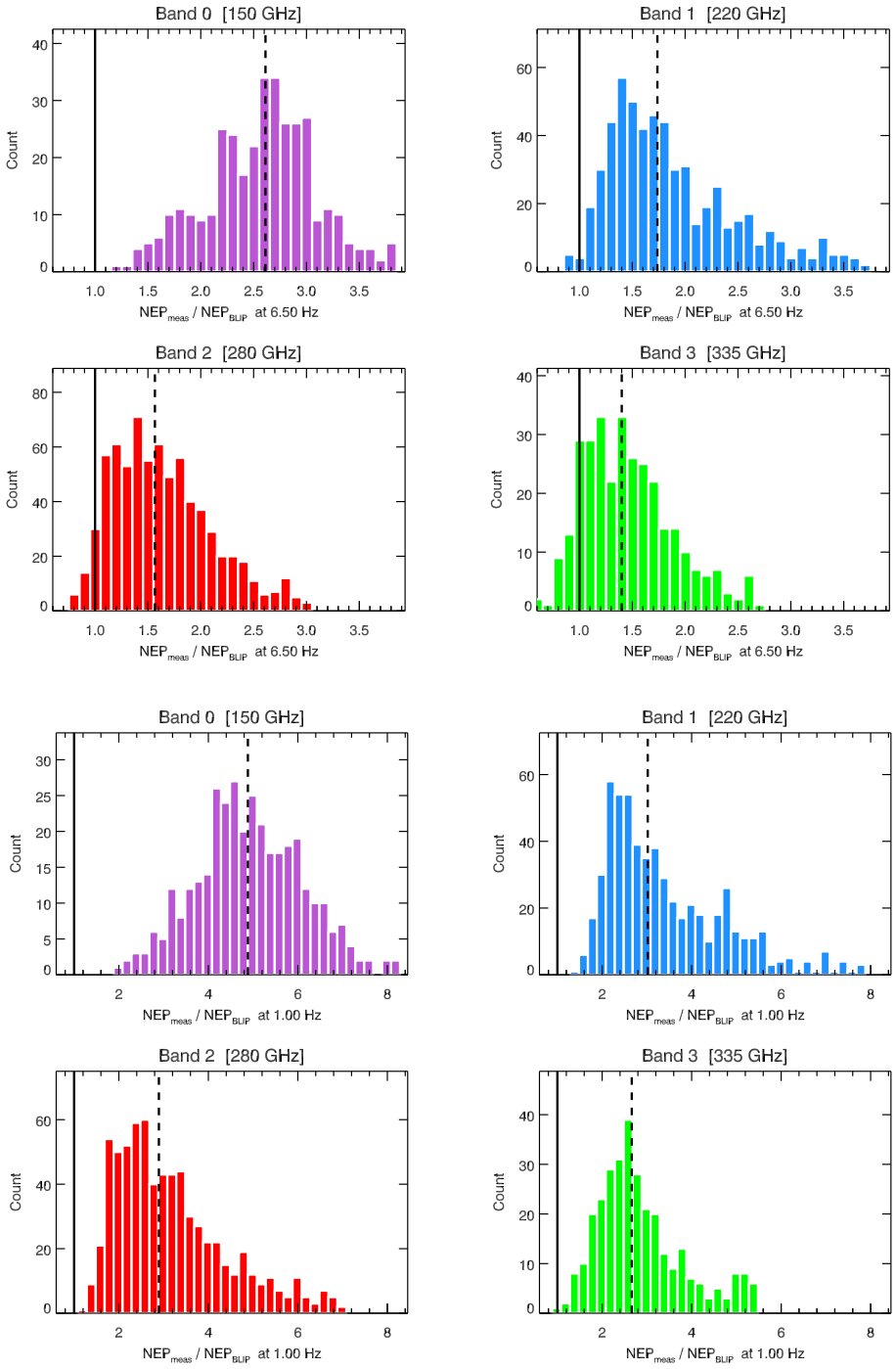

Figure 5.7: Ratio of measured NEP to predicted background-limited performance NEP (photon shot noise, photon Bose noise, thermal generation noise, and recombination noise) at 6.5 Hz (*top four panels*) and 1.0 Hz (*bottom four panels*). The dashed black lines denote median values. Each count in the histogram is a single resonator during a single observation. All detectors on Devices A2 and B2 were used. In total 11 observations were used, spanning $\mathcal{L}_{\rm PW} = 0.2 - 4.8$ mm (median $\mathcal{L}_{\rm PW} = 1.3$ mm).

bring the measured and predicted response to an unresolved astronomical source into rough agreement. The fact that the measured response to a beam-filling calibrator roughly matches the model prediction further supports the idea that the remaining discrepancy is sourced by the optics rather than the detectors.

We find that the power spectral density of the TLS noise steepens at low frequency from the often assumed $\nu^{-1/2}$ scaling. This results in a fairly significant degradation in the final map space sensitivity. Future instruments should be conservative in their predictions for the spectral shape of the TLS noise. This is especially relevant for CMB polarization experiments concerned with signal on large angular scales.

We measure an increase in the overall amplitude of the TLS noise with resonant frequency. This is an unintended consequence of the fact that the resonant frequency of the detectors was increased by decreasing the size of the capacitor. It is easily remedied in future detector arrays by instead decreasing the length of the inductor. This would significantly reduce the variability in detector sensitivity, and in principle bring the majority of detectors in line with the best performing detectors. Recall that currently the best performing detectors are approximately background limited at 6.5 Hz and have equal contributions from TLS noise and fundamental noise at 1.0 Hz.

The theoretical advantage of MKIDs over well-established technologies such as Transition Edge Sensors (TES) is the ease at which they are multiplexed in the frequency domain. However, in order for MKIDs to be truly scalable their fabrication has to be cost efficient and reliable. The fabrication of the MUSIC detectors proved challenging, so much so that we were only able to populate one quarter of the focal plane. Progress will be made on this front with the gradual refinement of fabrication techniques and a move towards simpler mask designs. Obtaining the full benefits of the impressive multiplexing factors that can be achieved with MKIDs also requires background-limited pixels. The main impediment to achieving BLIP with MKIDs is TLS noise, which was shown to be the limiting factor in the sensitivity of the MUSIC detectors. There are a number of designs currently being pursued that are promising for reducing the TLS NEP. These include operating at lower resonant frequencies [151, 152, 153] and employing high-resistivity superconducting thin films such as titanium nitride [146, 147, 148, 149, 150].

To conclude, we list some of MUSIC's achievements. MUSIC successfully demonstrated several new detector technologies: MKIDs, phased-arrays of slot-dipole antennas, and lumped-element on-chip bandpass filters. The flux calibration of the instrument is accurate to $5-10\%$ RMS, which is comparable to the best results obtained from similar instruments at millimeter and submillimeter wavelengths. The pointing is accurate to 3 arcsec RMS, which is thought to be limited by the CSO itself [168]. The readout electronics are capable of performing fast measurements of the complex transmission through thousands of MKIDs [102]. The multiplicative noise sourced by these electronics can be adequately removed using off-resonance carriers. Both the MUSIC readout electronics and cryostat are robust and efficient. This enabled a relatively small team to observe with MUSIC at the CSO for a total of 210 nights between 2013 and 2015. One of the science results that came out of these observations was a multi-band measurement of the Sunyaev-Zel'dovich Effect towards the galaxy cluster RX J1347.5 − 1145. This measurement is pictured in Figure 5.8 and was

used to place a constraint on the peculiar velocity of the cluster [174]. The extended observing run also helped to establish a comprehensive understanding of the instrument and its detectors, as demonstrated in this thesis.

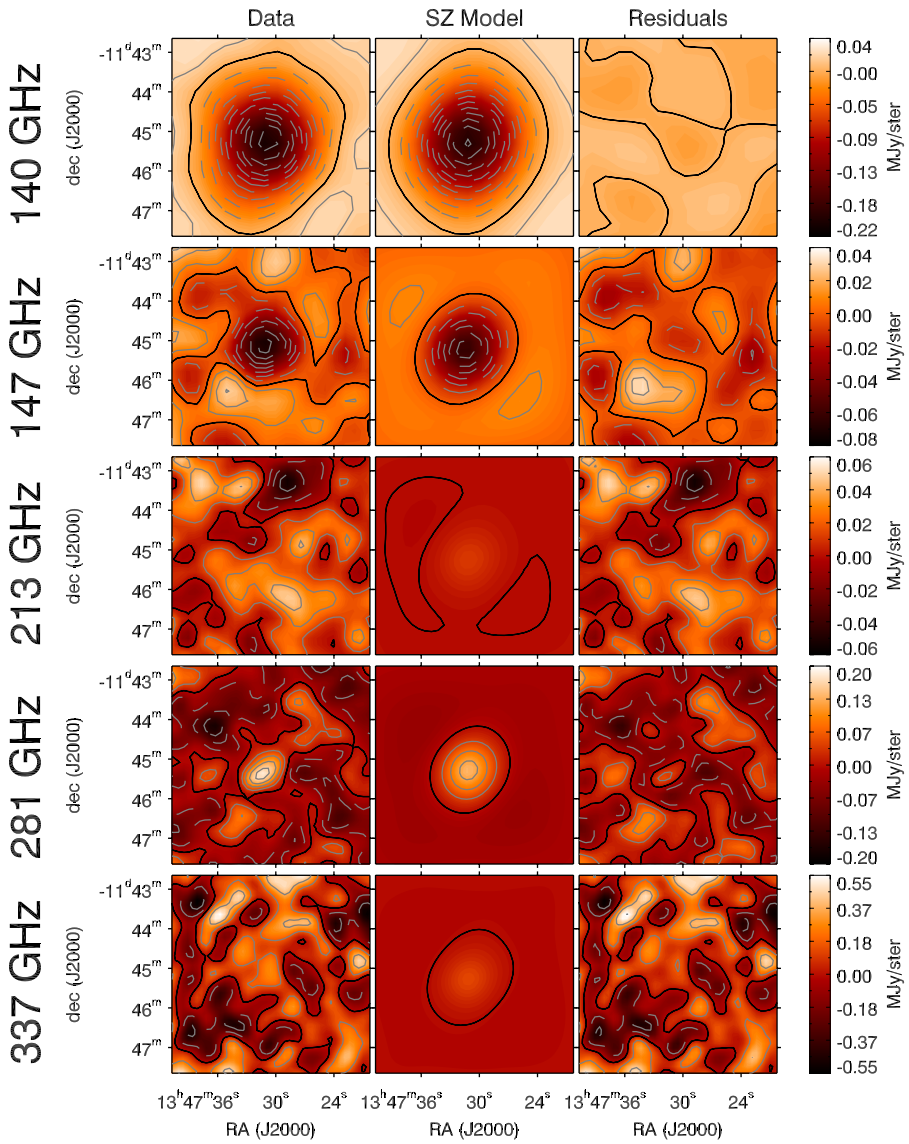

Figure 5.8: Five band measurement of the Sunyaev-Zel'dovich Effect towards the galaxy cluster RX J1347.5 − 1145. The columns show from left to right the image measured with Bolocam (*top row*) and MUSIC (*bottom four rows*), the best-fit model, and the residuals after subtracting the best-fit model from the image. The model is an elliptical gNFW spatial profile taken from Czakon et al. [35] with the overall normalization allowed to float independently for each band. The model provides a good fit in all cases. The solid gray lines show positive S/N in steps of 1 and the dashed gray lines show negative S/N in steps of 1 (Bolocam is ±3). The solid black line corresponds to 0. All of the images have been filtered and models for the central AGN and the brightest dusty star-forming galaxies have been subtracted. The high-pass filter applied to the MUSIC images was more aggressive than that applied to the Bolocam image, resulting in a more compact SZ signal. The lack of signal at 213 GHz is due to the fact that the band is near the null of the thermal SZ spectrum. Taken from Sayers et al. [174].

Appendix A

MCMC Fits to Calibration Data

In this appendix we describe the Markov Chain Monte Carlo (MCMC) algorithm used to fit the model described in Chapter 2 to dark temperature sweep data, hot/cold data, skydip data, and a variety of other calibration measurements. We present the algorithm in the context of fitting hot/cold data since it was originally developed for this problem.

For a given detector, the hot/cold data consists of measurements of the resonant frequency $f_{\rm res}(T_{\rm bath},\ T_{\rm load})$ and the inverse internal quality factor $Q_i^{-1}(T_{\rm bath},\ T_{\rm load})$ at N_T bath temperatures and $N_{\rm load} = 2$ loading conditions (liquid nitrogen and room temperature). Let us denote this data set as

$$\boldsymbol{y} = \left[\boldsymbol{f}_{\rm res},\ \boldsymbol{Q_i^{-1}}\right] , \tag{A.1}$$

where $\boldsymbol{y}$ contains $N = 2 \times N_{\rm T} \times N_{\rm load}$ measurements total.

Denote the set of parameters describing the model as $\boldsymbol{\theta}$. We will partition these parameters into two groups, $\boldsymbol{\theta} = [\boldsymbol{\theta}_1,\ \boldsymbol{\theta}_2]$, where $\boldsymbol{\theta}_1$ contains all parameters for which we have no prior information and $\boldsymbol{\theta}_2$ contains all parameters for which we have some prior information. The prior information might come from theoretical considerations, direct measurement, or a previous analysis. For example, when fitting the hot/cold data we use the results of Mattis-Bardeen fits to the dark temperature sweep data to place a prior on two of the parameters: the kinetic inductance fraction α and gap energy at zero temperature Δ_0.

We would like to implement a MCMC that – in the limit of a large number of iterations – draws samples from the joint posterior distribution $p(\boldsymbol{\theta}|\boldsymbol{y})$. The joint posterior distribution is the probability that the parameters take on a particular set of values given the known model and the measured data. According to Bayes' theorem the posterior distribution is given by

$$p(\boldsymbol{\theta}|\boldsymbol{y}) = \frac{\mathcal{L}(y|\boldsymbol{\theta})p(\boldsymbol{\theta})}{p(\boldsymbol{y})} . \tag{A.2}$$

The likelihood function $\mathcal{L}(y|\boldsymbol{\theta})$ is the probability of observing the measured data given the known model and a particular set of model parameters. The prior distribution $p(\boldsymbol{\theta})$ is the probability that the model parameters

take on a particular set of values. The marginal likelihood $p(\boldsymbol{y})$ (also known as the evidence) is the probability of observing the measured data; it is a normalization that ensures that the joint posterior distribution integrates to 1.

Assume that our measurements have Gaussian errors so that

$$y_j = h_j(\boldsymbol{\theta}) + \varepsilon_j \ , \tag{A.3}$$

where $h_j(\boldsymbol{\theta})$ is the model prediction and $\varepsilon_j \sim N(0, \sigma_j)$ with the uncertainty σ_j known from fits to the IQ sweeps. Then the likelihood function is given by

$$\mathcal{L}(\boldsymbol{y}|\boldsymbol{\theta}) \propto \exp\left(-\frac{1}{2}\chi^2\right) \ , \tag{A.4}$$

where

$$\chi^2 = \sum_j \frac{(y_j - h_j(\boldsymbol{\theta}))^2}{\sigma_j^2} \ . \tag{A.5}$$

In order to sample from the joint posterior distribution we use the Metropolis-Hastings algorithm. In theory, implementation of the Metropolis-Hastings algorithm is very simple, just follow these steps:

1. At iteration t randomly draw a set of parameters $\boldsymbol{\theta}^{(t)}$ from a proposal distribution $g(\boldsymbol{\theta}^{(t)}|\boldsymbol{\theta}^{(t-1)})$.
2. Evaluate the likelihood function $\mathcal{L}(\boldsymbol{y}|\boldsymbol{\theta}^{(t)})$ and $\mathcal{L}(\boldsymbol{y}|\boldsymbol{\theta}^{(t-1)})$.
3. Form the likelihood ratio $r = \mathcal{L}(\boldsymbol{y}|\boldsymbol{\theta}^{(t)}) / \mathcal{L}(\boldsymbol{y}|\boldsymbol{\theta}^{(t-1)})$.
4. Draw a uniform random number $u \sim U[0,1]$. If $u < r$, then accept the new set of parameters $\boldsymbol{\theta}^{(t)}$. Otherwise reject the new set of parameters and keep $\boldsymbol{\theta}^{(t-1)}$. Therefore, the algorithm will *always* move to regions in the parameter space with higher likelihood (or equivalently lower χ^2), and will *sometimes* move to regions with lower likelihood (higher χ^2).
5. Repeat steps $1-4$ many times.

In the limit that $t \to \infty$ the chain will reach a stationary distribution that can be shown to be equivalent to the joint posterior distribution, so long as the proposal distribution is symmetric or $g(\boldsymbol{\theta}^{(t)}|\boldsymbol{\theta}^{(t-1)}) = g(\boldsymbol{\theta}^{(t-1)}|\boldsymbol{\theta}^{(t)})$. The Metropolis-Hasting's algorithm enables one to draw samples from the joint posterior distribution without knowing the overall normalization (the marginal likelihood $p(\boldsymbol{y})$). It is then trivial to obtain samples from the marginal posterior distribution $p(\theta_i|\boldsymbol{y})$ for the i'th parameter of interest.

In practice, however, a number of complications immediately arise: What should we use for the proposal distribution? How many iterations should we perform? How do we know if the Markov Chain has converged to the stationary distribution? How do we determine parameter estimates from the set of samples drawn from

the joint posterior distribution? The literature contains a wide variety of techniques that can be used to answer these questions. Here we simply state what was found to work for our specific problem of fitting the MUSIC detector calibration data.

Regarding the choice of a proposal distribution: Draw $\boldsymbol{\theta}_1^{(t)}$ from a Gaussian centered on $\boldsymbol{\theta}_1^{(t-1)}$. As the chain progresses, calibrate the covariance of this Gaussian. Draw $\boldsymbol{\theta}_2^{(t)}$ from the prior distribution.

Regarding the covariance of the proposal distribution: Every n_{check} iterations, estimate the variance $\widehat{\text{Var}}$ of each parameter using the last n_{check} iterations. Update the variance of the proposal distribution for each parameter using the weighted average $\sigma^2_{\text{new}} = w\widehat{\text{Var}} + (1-w)\sigma^2_{\text{old}}$. In practice, we found $n_{\text{check}} = 10,000$ and $w = 0.15$ worked well. In principle, one could also update the off-diagonal elements of the covariance matrix to improve the efficiency with which the parameter space is sampled, however this was not employed in our analysis (the off-diagonal elements were fixed at 0).

Regarding convergence to the stationary distribution: Perform M Markov Chains simultaneously ($M = 10$ for all of the analysis presented in this dissertation). Randomize the starting location of these chains. For each parameter $\theta \in \boldsymbol{\theta}$, calculate the within-chain variance W and between-chain variance B every n_{check} iterations. The within-chain variance is given by the set of equations

$$\bar{\theta}_m = \frac{1}{n}\sum_{t=1}^{n}\theta_{mt} \tag{A.6}$$

$$s_m^2 = \frac{1}{n-1}\sum_{t=1}^{n}\left(\theta_{mt} - \bar{\theta}_m\right)^2 \tag{A.7}$$

$$W = \frac{1}{m}\sum_{m=1}^{M} s_m^2\,, \tag{A.8}$$

where $\bar{\theta}_m$ is the sample mean of chain m, s_m^2 is the sample variance of chain m, and W is the average value of the sample variance over all chains. The between-chain variance is given by the set of equations

$$\bar{\theta} = \frac{1}{m}\sum_{t=1}^{m}\bar{\theta}_m \tag{A.9}$$

$$B = \frac{n}{m-1}\sum_{t=1}^{n}\left(\bar{\theta}_m - \bar{\theta}\right)^2\,, \tag{A.10}$$

where $\bar{\theta}$ is the sample mean over all chains, and B is the sample variance of the sample means over all chains multiplied by n. The variance of the stationary distribution is estimated as a weighted average of W and B. Specifically

$$\widehat{\text{Var}} = \left(1 - \frac{1}{n}\right)W + \frac{1}{n}B\,. \tag{A.11}$$

The $\widehat{R}$ estimator [176] is then defined as the ratio of the total variance to the within-chain variance

$$\widehat{R} = \sqrt{\frac{\widehat{\mathrm{Var}}}{W}} \,. \tag{A.12}$$

At the beginning of the MCMC the chains are in random locations in parameter space, the between-chain variance is significant, and the total variance is much larger than the within-chain variance, i.e., $\widehat{R} \gg 1$. As the chains converge to the stationary distribution, the between-chain variance converges to the within-chain variance. As a result, the total variance converges to the within-chain variance and $\widehat{R} \to 1$. In practice, we iterate until the total number of iterations $>$ 1,000,000 and $\hat{R} < 1.1$ for all parameters. After convergence, a burn-in period is discarded for each of the M chains. The M chains are then concatenated.

Regarding convergence to the stationary distribution: One common failure mode is that a chain becomes trapped in a local minimum. In order to encourage the chains to explore the parameter space and find the global minimum, we perform simulated annealing; a technique in which all uncertainties σ_j^2 are multiplied by a factor $T_{\mathrm{sys}}^{(}t)$, which we refer to as the system temperature. At the beginning of the MCMC, we "melt" the system by setting $T_{\mathrm{sys}} \gg 1$. After this initial melting phase we "anneal" the system by lowering T_{sys} from its initial value down to 1. Simulated annealing encourages the chains to explore the parameter space during the melting phase and then freezes the chains at the global minimum during the annealing phase. The process is illustrated in . We employ a slow, linear annealing schedule. In our case, the melting phase lasts 100,000 iterations and the annealing phase lasts 400,000 iterations. We discard these first 500,000 iterations as burn-in. This gives us at least 500,000 remaining iterations for 10 chains, so more than 5 million draws from the joint posterior distribution in total.

Regarding boundaries: We enforce boundaries on the allowed values of $\boldsymbol{\theta}_1$. We try to choose nonrestrictive boundaries, i.e. the boundaries are placed where the likelihood function is already negligible. However, this is not always possible, especially for nuisance parameters. In these cases we choose physically motivated boundaries. During the MCMC, if a draw from the proposal distribution places a parameter beyond either boundary, then we "reflect" off of the boundary back into the allowed region. This ensures that the boundaries are equivalent to a uniform prior on the parameter.

Regarding parameter estimation: The final result is a chain containing draws from the joint posterior distribution. Each draw is a set of parameters $\boldsymbol{\theta}$. We can marginalize over the joint posterior distribution by simply restricting our focus to a single parameter of interest. We use the median and median absolute deviation of the draws from the marginalized posterior distribution as our best estimate of each parameter and its uncertainty. We save the chain, and if we are using the results of the MCMC as a prior in a future fit, then we draw a set of parameters randomly from the chains at each iteration of the future fit. This ensures that the parameter-parameter correlations are properly accounted for in the

propagation of uncertainty.

Figures A.2−A.3 show the Markov chains and posterior distributions for two model parameters, $C = \eta\Delta\nu_{\rm mm}/d$ and $\tau_{\rm max}$, that result from fitting the hot/cold data for a typical detector. The hot/cold data provides a fairly tight constraint on C. The nuisance parameter $\tau_{\rm max}$, on the other hand, is not well constrained, but we are able to place a lower bound on its value.

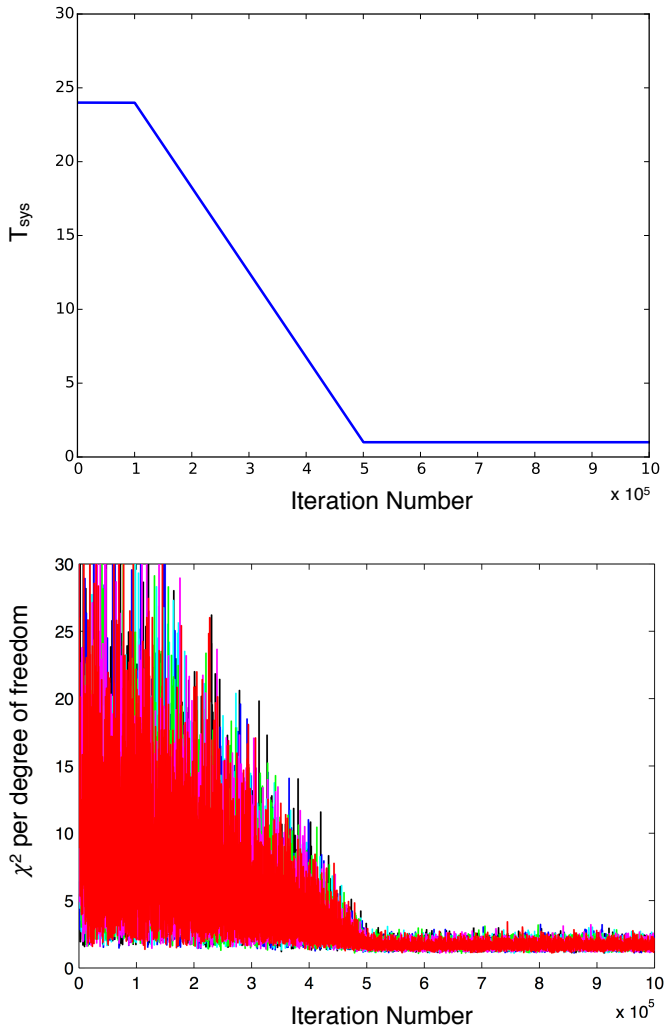

Figure A.1: *Top:* Annealing schedule, or the system temperature as a function of iteration number. The melting phase corresponds to the initial 100,000 iterations where $T_{\rm sys} = 24$. The annealing phase corresponds to the next 400,000 iterations where the system temperature decreases linearly from $T_{\rm sys} = 24$ to $T_{\rm sys} = 1$. The initial 500,000 iterations are discarded as burn-in, and the remaining iterations where $T_{\rm sys} = 1$ are assumed to be draws from the joint posterior distribution. *Bottom:* The χ^2 per degree of freedom as a function of iteration number. Each color denotes one of the ten chains that were run simultaneously. During the melting and annealing phases, the system is able to explore regions of parameter space with large χ^2 per degree of freedom and is unlikely to become trapped in local minima.

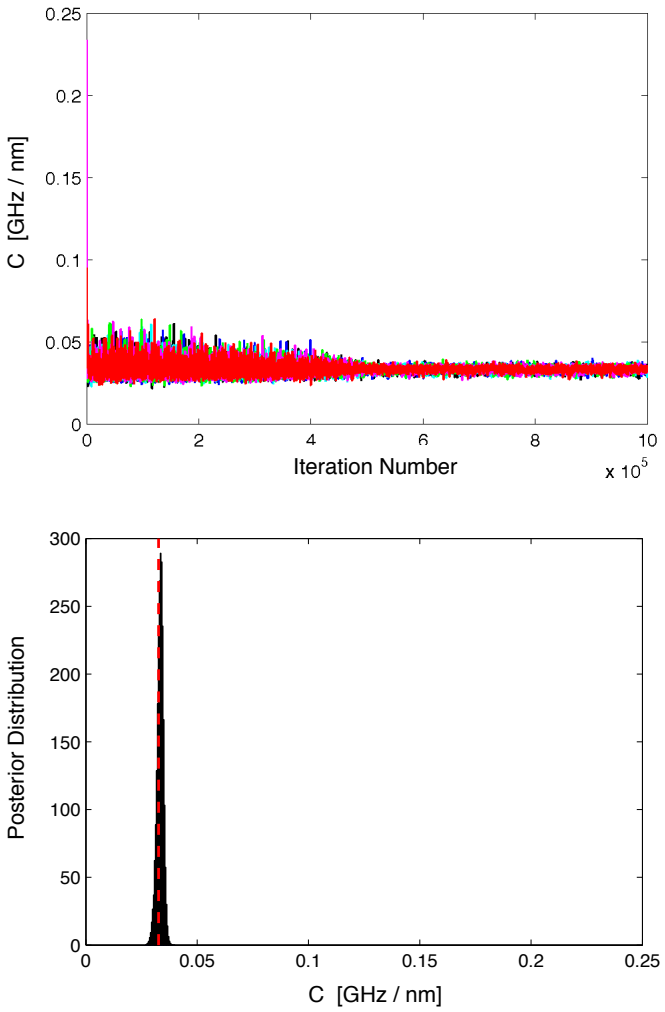

Figure A.2: Result of performing an MCMC fit to the hot/cold data for a typical detector. *Top:* The parameter $C = \eta d/\Delta\nu_{\text{mm}}$ as a function of iteration number. Each color denotes one of the ten chains that were run simultaneously. *Bottom:* The marginalized posterior distribution of C, obtained by concatenating the last 500,000 iterations of the ten chains shown above. The red-dashed line denotes the median value.

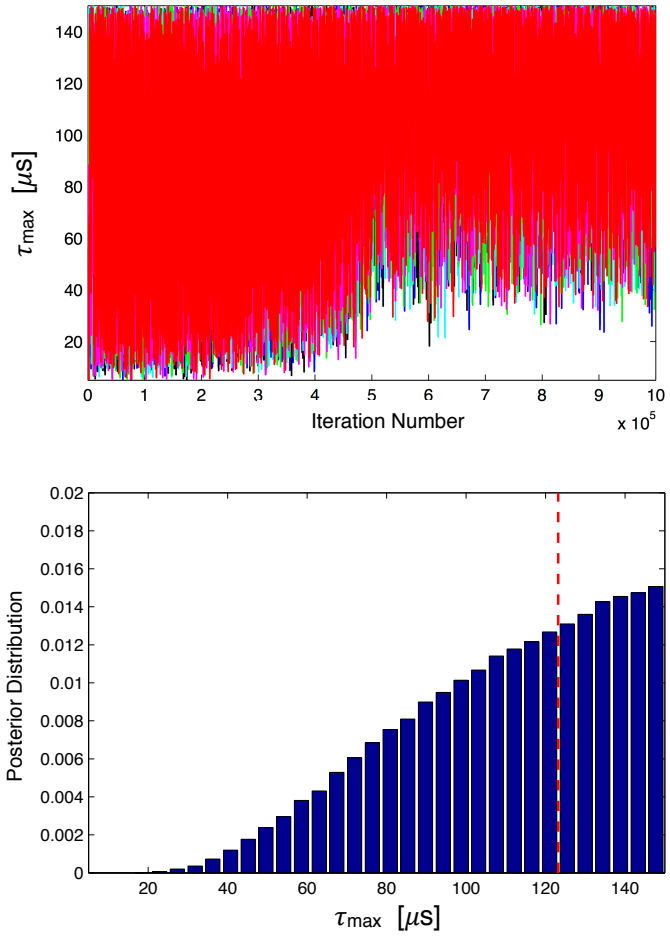

Figure A.3: Result of performing an MCMC fit to the hot/cold data for a typical detector. *Top:* The parameter τ_{max} as a function of iteration number. Each color denotes one of the ten chains that were run simultaneously. *Bottom:* The marginalized posterior distribution of τ_{max}, obtained by concatenating the last 500,000 iterations of the ten chains shown above. The red-dashed line denotes the median value.

Bibliography

[1] G. Holder, Z. Haiman, and J. J. Mohr. "Constraints on Ω_m, Ω_{Lambda}, and σ_8 from Galaxy Cluster Redshift Distributions". In: ApJ 560 (Oct. 2001), pp. L111–L114. DOI: 10.1086/324309. eprint: astro-ph/0105396 (cit. on p. 2).

[2] Z. Haiman, J. J. Mohr, and G. P. Holder. "Constraints on Cosmological Parameters from Future Galaxy Cluster Surveys". In: ApJ 553 (June 2001), pp. 545–561. DOI: 10.1086/320939. eprint: astro-ph/0002336 (cit. on p. 2).

[3] G. M. Voit, S. T. Kay, and G. L. Bryan. "The baseline intracluster entropy profile from gravitational structure formation". In: MNRAS 364 (Dec. 2005), pp. 909–916. DOI: 10.1111/j.1365-2966.2005.09621.x. eprint: astro-ph/0511252 (cit. on p. 2).

[4] C. L. Sarazin. *X-ray emission from clusters of galaxies*. 1988 (cit. on p. 2).

[5] R. A. Sunyaev and Y. B. Zeldovich. "The Observations of Relic Radiation as a Test of the Nature of X-Ray Radiation from the Clusters of Galaxies". In: *Comments on Astrophysics and Space Physics* 4 (Nov. 1972), p. 173 (cit. on p. 2).

[6] A. Cavaliere, A. Lapi, and R. Fusco-Femiano. "Nonthermal support for the outer intracluster medium". In: A&A 525, A110 (Jan. 2011), A110. DOI: 10.1051/0004-6361/201015390. arXiv: 1010.4415 [astro-ph.CO] (cit. on p. 3).

[7] E. T. Lau, A. V. Kravtsov, and D. Nagai. "Residual Gas Motions in the Intracluster Medium and Bias in Hydrostatic Measurements of Mass Profiles of Clusters". In: ApJ 705 (Nov. 2009), pp. 1129–1138. DOI: 10.1088/0004-637X/705/2/1129. arXiv: 0903.4895 [astro-ph.CO] (cit. on pp. 3, 4).

[8] N. Battaglia, J. R. Bond, C. Pfrommer, and J. L. Sievers. "On the Cluster Physics of Sunyaev-Zel'dovich and X-Ray Surveys. I. The Influence of Feedback, Non-thermal Pressure, and Cluster Shapes on Y-M Scaling Relations". In: ApJ 758, 74 (Oct. 2012), p. 74. DOI: 10.1088/0004-637X/758/2/74. arXiv: 1109.3709 [astro-ph.CO] (cit. on p. 3).

[9] K. Nelson, E. T. Lau, and D. Nagai. "Hydrodynamic Simulation of Non-thermal Pressure Profiles of Galaxy Clusters". In: ApJ 792, 25 (Sept. 2014), p. 25. DOI: 10.1088/0004-637X/792/1/25. arXiv: 1404.4636 (cit. on pp. 3, 6, 24).

[10] C. L. Reichardt, L. Shaw, O. Zahn, K. A. Aird, B. A. Benson, L. E. Bleem, J. E. Carlstrom, C. L. Chang, H. M. Cho, T. M. Crawford, A. T. Crites, T. de Haan, M. A. Dobbs, J. Dudley, E. M. George, N. W. Halverson, G. P. Holder, W. L. Holzapfel, S. Hoover, Z. Hou, J. D. Hrubes, M. Joy, R. Keisler, L. Knox, A. T. Lee, E. M. Leitch, M. Lueker, D. Luong-Van, J. J. McMahon, J. Mehl, S. S. Meyer, M. Millea, J. J. Mohr, T. E. Montroy, T. Natoli, S. Padin, T. Plagge, C. Pryke, J. E. Ruhl, K. K. Schaffer, E. Shirokoff, H. G. Spieler, Z. Staniszewski, A. A. Stark, K. Story, A. van Engelen, K. Vanderlinde, J. D. Vieira, and R. Williamson. "A Measurement of Secondary Cosmic Microwave Background Anisotropies with Two Years of South Pole Telescope Observations". In: ApJ 755, 70 (Aug. 2012), p. 70. DOI: 10.1088/0004-637X/755/1/70. arXiv: 1111.0932 [astro-ph.CO] (cit. on pp. 3, 11).

[11] L. D. Shaw, D. Nagai, S. Bhattacharya, and E. T. Lau. "Impact of Cluster Physics on the Sunyaev-Zel'dovich Power Spectrum". In: ApJ 725 (Dec. 2010), pp. 1452–1465. DOI: 10.1088/0004-637X/725/2/1452. arXiv: 1006.1945 [astro-ph.CO] (cit. on p. 3).

[12] A. Vikhlinin, A. V. Kravtsov, R. A. Burenin, H. Ebeling, W. R. Forman, A. Hornstrup, C. Jones, S. S. Murray, D. Nagai, H. Quintana, and A. Voevodkin. "Chandra Cluster Cosmology Project III: Cosmological Parameter Constraints". In: ApJ 692 (Feb. 2009), pp. 1060–1074. DOI: 10.1088/0004-637X/692/2/1060. arXiv: 0812.2720 (cit. on p. 3).

[13] A. B. Mantz, A. von der Linden, S. W. Allen, D. E. Applegate, P. L. Kelly, R. G. Morris, D. A. Rapetti, R. W. Schmidt, S. Adhikari, M. T. Allen, P. R. Burchat, D. L. Burke, M. Cataneo, D. Donovan, H. Ebeling, S. Shandera, and A. Wright. "Weighing the giants - IV. Cosmology and neutrino mass". In: MNRAS 446 (Jan. 2015), pp. 2205–2225. DOI: 10.1093/mnras/stu2096. arXiv: 1407.4516 (cit. on p. 3).

[14] D. Nagai, A. Vikhlinin, and A. V. Kravtsov. "Testing X-Ray Measurements of Galaxy Clusters with Cosmological Simulations". In: ApJ 655 (Jan. 2007), pp. 98–108. DOI: 10.1086/509868. eprint: astro-ph/0609247 (cit. on p. 4).

[15] B. A. Benson, T. de Haan, J. P. Dudley, C. L. Reichardt, K. A. Aird, K. Andersson, R. Armstrong, M. L. N. Ashby, M. Bautz, M. Bayliss, G. Bazin, L. E. Bleem, M. Brodwin, J. E. Carlstrom, C. L. Chang, H. M. Cho, A. Clocchiatti, T. M. Crawford, A. T. Crites, S. Desai, M. A. Dobbs, R. J. Foley, W. R. Forman, E. M. George, M. D. Gladders, A. H. Gonzalez, N. W. Halverson, N. Harrington, F. W. High, G. P. Holder, W. L. Holzapfel, S. Hoover, J. D. Hrubes, C. Jones, M. Joy, R. Keisler, L. Knox, A. T. Lee, E. M. Leitch, J. Liu, M. Lueker, D. Luong-Van, A. Mantz, D. P. Marrone, M. McDonald, J. J. McMahon, J. Mehl, S. S. Meyer, L. Mocanu, J. J. Mohr, T. E. Montroy, S. S. Murray, T. Natoli, S. Padin, T. Plagge, C. Pryke, A. Rest, J. Ruel, J. E. Ruhl, B. R. Saliwanchik, A. Saro, J. T. Sayre, K. K. Schaffer, L. Shaw, E. Shirokoff, J. Song, H. G. Spieler, B. Stalder, Z. Staniszewski, A. A. Stark, K. Story, C. W. Stubbs, R. Suhada, A. van Engelen, K. Vanderlinde, J. D. Vieira, A. Vikhlinin, R.

Williamson, O. Zahn, and A. Zenteno. “Cosmological Constraints from Sunyaev-Zel’dovich-selected Clusters with X-Ray Observations in the First 178 deg^2 of the South Pole Telescope Survey”. In: ApJ 763, 147 (Feb. 2013), p. 147. DOI: 10.1088/0004-637X/763/2/147. arXiv: 1112.5435 [astro-ph.CO] (cit. on p. 4).

[16] M. Postman, D. Coe, N. Benítez, L. Bradley, T. Broadhurst, M. Donahue, H. Ford, O. Graur, G. Graves, S. Jouvel, A. Koekemoer, D. Lemze, E. Medezinski, A. Molino, L. Moustakas, S. Ogaz, A. Riess, S. Rodney, P. Rosati, K. Umetsu, W. Zheng, A. Zitrin, M. Bartelmann, R. Bouwens, N. Czakon, S. Golwala, O. Host, L. Infante, S. Jha, Y. Jimenez-Teja, D. Kelson, O. Lahav, R. Lazkoz, D. Maoz, C. McCully, P. Melchior, M. Meneghetti, J. Merten, J. Moustakas, M. Nonino, B. Patel, E. Regös, J. Sayers, S. Seitz, and A. Van der Wel. “The Cluster Lensing and Supernova Survey with Hubble: An Overview”. In: ApJS 199, 25 (Apr. 2012), p. 25. DOI: 10.1088/0067-0049/199/2/25. arXiv: 1106.3328 [astro-ph.CO] (cit. on pp. 4, 28).

[17] J. F. Navarro, C. S. Frenk, and S. D. M. White. “A Universal Density Profile from Hierarchical Clustering”. In: ApJ 490 (Dec. 1997), pp. 493–508. eprint: astro-ph/9611107 (cit. on p. 5).

[18] A. Vikhlinin, A. Kravtsov, W. Forman, C. Jones, M. Markevitch, S. S. Murray, and L. Van Speybroeck. “Chandra Sample of Nearby Relaxed Galaxy Clusters: Mass, Gas Fraction, and Mass-Temperature Relation”. In: ApJ 640 (Apr. 2006), pp. 691–709. DOI: 10.1086/500288. eprint: astro-ph/0507092 (cit. on pp. 5, 6).

[19] A. Cavaliere and R. Fusco-Femiano. “The Distribution of Hot Gas in Clusters of Galaxies”. In: A&A 70 (Nov. 1978), p. 677 (cit. on p. 5).

[20] A. J. R. Sanderson and T. J. Ponman. “X-ray modelling of galaxy cluster gas and mass profiles”. In: MNRAS 402 (Feb. 2010), pp. 65–72. DOI: 10.1111/j.1365-2966.2009.15888.x. arXiv: 0910.3212 (cit. on pp. 5, 6).

[21] M. Roncarelli, S. Ettori, K. Dolag, L. Moscardini, S. Borgani, and G. Murante. “Simulated X-ray galaxy clusters at the virial radius: Slopes of the gas density, temperature and surface brightness profiles”. In: MNRAS 373 (Dec. 2006), pp. 1339–1350. DOI: 10.1111/j.1365-2966.2006.11143.x. eprint: astro-ph/0609824 (cit. on p. 6).

[22] A. Vikhlinin, W. Forman, and C. Jones. “Outer Regions of the Cluster Gaseous Atmospheres”. In: ApJ 525 (Nov. 1999), pp. 47–57. DOI: 10.1086/307876. eprint: astro-ph/9905200 (cit. on p. 6).

[23] D. M. Neumann. “Tracing the X-ray emitting intra-cluster medium of clusters of galaxies beyond r_{200}”. In: A&A 439 (Aug. 2005), pp. 465–477. DOI: 10.1051/0004-6361:20053015. eprint: astro-ph/0505049 (cit. on p. 6).

[24] J. H. Croston, G. W. Pratt, H. Böhringer, M. Arnaud, E. Pointecouteau, T. J. Ponman, A. J. R. Sanderson, R. F. Temple, R. G. Bower, and M. Donahue. "Galaxy-cluster gas-density distributions of the representative XMM-Newton cluster structure survey (REXCESS)". In: A&A 487 (Aug. 2008), pp. 431–443. DOI: 10.1051/0004-6361:20079154. arXiv: 0801.3430 (cit. on p. 6).

[25] A. Morandi, M. Sun, W. Forman, and C. Jones. "The galaxy cluster outskirts probed by Chandra". In: MNRAS 450 (July 2015), pp. 2261–2278. DOI: 10.1093/mnras/stv660. arXiv: 1501.04095 (cit. on p. 6).

[26] F. Pizzolato, S. Molendi, S. Ghizzardi, and S. De Grandi. "Smaug: A New Technique for the Deprojection of Galaxy Clusters". In: ApJ 592 (July 2003), pp. 62–78. DOI: 10.1086/375617. eprint: astro-ph/0304016 (cit. on p. 7).

[27] N. Grevesse and A. J. Sauval. "Standard Solar Composition". In: Space Sci. Rev. 85 (May 1998), pp. 161–174. DOI: 10.1023/A:1005161325181 (cit. on p. 7).

[28] N. Itoh, Y. Kohyama, and S. Nozawa. "Relativistic Corrections to the Sunyaev-Zeldovich Effect for Clusters of Galaxies". In: ApJ 502 (July 1998), pp. 7–15. DOI: 10.1086/305876. eprint: astro-ph/9712289 (cit. on p. 8).

[29] M. Donahue, G. M. Voit, A. Mahdavi, K. Umetsu, S. Ettori, J. Merten, M. Postman, A. Hoffer, A. Baldi, D. Coe, N. Czakon, M. Bartelmann, N. Benitez, R. Bouwens, L. Bradley, T. Broadhurst, H. Ford, F. Gastaldello, C. Grillo, L. Infante, S. Jouvel, A. Koekemoer, D. Kelson, O. Lahav, D. Lemze, E. Medezinski, P. Melchior, M. Meneghetti, A. Molino, J. Moustakas, L. A. Moustakas, M. Nonino, P. Rosati, J. Sayers, S. Seitz, A. Van der Wel, W. Zheng, and A. Zitrin. "CLASH-X: A Comparison of Lensing and X-Ray Techniques for Measuring the Mass Profiles of Galaxy Clusters". In: ApJ 794, 136 (Oct. 2014), p. 136. DOI: 10.1088/0004-637X/794/2/136. arXiv: 1405.7876 (cit. on pp. 10, 14, 27).

[30] R. C. Hickox and M. Markevitch. "Resolving the Unresolved Cosmic X-Ray Background in the Chandra Deep Fields". In: ApJ 661 (June 2007), pp. L117–L121. DOI: 10.1086/519003. eprint: astro-ph/0702556 (cit. on p. 10).

[31] M. Markevitch, M. W. Bautz, B. Biller, Y. Butt, R. Edgar, T. Gaetz, G. Garmire, C. E. Grant, P. Green, M. Juda, P. P. Plucinsky, D. Schwartz, R. Smith, A. Vikhlinin, S. Virani, B. J. Wargelin, and S. Wolk. "Chandra Spectra of the Soft X-Ray Diffuse Background". In: ApJ 583 (Jan. 2003), pp. 70–84. DOI: 10.1086/345347. eprint: astro-ph/0209441 (cit. on p. 10).

[32] J. Glenn, J. J. Bock, G. Chattopadhyay, S. F. Edgington, A. E. Lange, J. Zmuidzinas, P. D. Mauskopf, B. Rownd, L. Yuen, and P. A. Ade. "Bolocam: a millimeter-wave bolometric camera". In: *Advanced Technology MMW, Radio, and Terahertz Telescopes*. Ed. by T. G. Phillips. Vol. 3357. Society of Photo-Optical Instrumentation Engineers (SPIE) Conference Series. July 1998, pp. 326–334 (cit. on p. 11).

[33] D. J. Haig, P. A. R. Ade, J. E. Aguirre, J. J. Bock, S. F. Edgington, M. L. Enoch, J. Glenn, A. Goldin, S. Golwala, K. Heng, G. Laurent, P. R. Maloney, P. D. Mauskopf, P. Rossinot, J. Sayers, P. Stover, and C. Tucker. "Bolocam: status and observations". In: *Z-Spec: a broadband millimeter-wave grating spectrometer: design, construction, and first cryogenic measurements*. Ed. by C. M. Bradford, P. A. R. Ade, J. E. Aguirre, J. J. Bock, M. Dragovan, L. Duband, L. Earle, J. Glenn, H. Matsuhara, B. J. Naylor, H. T. Nguyen, M. Yun, and J. Zmuidzinas. Vol. 5498. Society of Photo-Optical Instrumentation Engineers (SPIE) Conference Series. Oct. 2004, pp. 78–94. DOI: 10.1117/12.553154 (cit. on p. 11).

[34] J. Sayers, T. Mroczkowski, N. G. Czakon, S. R. Golwala, A. Mantz, S. Ameglio, T. P. Downes, P. M. Koch, K.-Y. Lin, S. M. Molnar, L. Moustakas, S. J. C. Muchovej, E. Pierpaoli, J. A. Shitanishi, S. Siegel, and K. Umetsu. "The Contribution of Radio Galaxy Contamination to Measurements of the Sunyaev-Zel'dovich Decrement in Massive Galaxy Clusters at 140 GHz with Bolocam". In: ApJ 764, 152 (Feb. 2013), p. 152. DOI: 10.1088/0004-637X/764/2/152. arXiv: 1209.5129 [astro-ph.CO] (cit. on pp. 11, 12).

[35] N. G. Czakon, J. Sayers, A. Mantz, S. R. Golwala, T. P. Downes, P. M. Koch, K.-Y. Lin, S. M. Molnar, L. A. Moustakas, T. Mroczkowski, E. Pierpaoli, J. A. Shitanishi, S. Siegel, and K. Umetsu. "Galaxy Cluster Scaling Relations between Bolocam Sunyaev-Zel'dovich Effect and Chandra X-Ray Measurements". In: ApJ 806, 18 (June 2015), p. 18. DOI: 10.1088/0004-637X/806/1/18. arXiv: 1406.2800 (cit. on pp. 11, 17, 205).

[36] J. Sayers, S. R. Golwala, S. Ameglio, and E. Pierpaoli. "Cluster Morphologies and Model-independent Y_{SZ} Estimates from Bolocam Sunyaev-Zel'dovich Images". In: ApJ 728, 39 (Feb. 2011), p. 39. DOI: 10.1088/0004-637X/728/1/39. arXiv: 1010.1798 [astro-ph.CO] (cit. on pp. 11, 28).

[37] J. Sayers, S. R. Golwala, P. A. R. Ade, J. E. Aguirre, J. J. Bock, S. F. Edgington, J. Glenn, A. Goldin, D. Haig, A. E. Lange, G. T. Laurent, P. D. Mauskopf, H. T. Nguyen, P. Rossinot, and J. Schlaerth. "Studies of Millimeter-wave Atmospheric Noise above Mauna Kea". In: ApJ 708 (Jan. 2010), pp. 1674–1691. DOI: 10.1088/0004-637X/708/2/1674. arXiv: 0904.3943 [astro-ph.IM] (cit. on pp. 11, 89, 91–93).

[38] G. Sandell. "Secondary calibrators at submillimetre wvelengths." In: MNRAS 271 (Nov. 1994), pp. 75–80 (cit. on p. 11).

[39] M. J. Griffin and G. S. Orton. "The near-millimeter brightness temperature spectra of Uranus and Neptune". In: Icarus 105 (Oct. 1993), p. 537. DOI: 10.1006/icar.1993.1147 (cit. on pp. 11, 161).

[40] J. L. Weiland, N. Odegard, R. S. Hill, E. Wollack, G. Hinshaw, M. R. Greason, N. Jarosik, L. Page, C. L. Bennett, J. Dunkley, B. Gold, M. Halpern, A. Kogut, E. Komatsu, D. Larson, M. Limon, S. S. Meyer, M. R. Nolta, K. M. Smith, D. N. Spergel, G. S. Tucker, and E. L. Wright. "Seven-year Wilkinson Microwave Anisotropy Probe (WMAP) Observations: Planets and Celestial Calibration

Sources". In: ApJS 192, 19 (Feb. 2011), p. 19. DOI: 10.1088/0067-0049/192/2/19. arXiv: 1001.4731 [astro-ph.CO] (cit. on pp. 11, 161).

[41] J. Sayers, N. G. Czakon, and S. R. Golwala. "143 GHz Brightness Measurements of Uranus, Neptune, and Other Secondary Calibrators with Bolocam between 2003 and 2010". In: ApJ 744, 169 (Jan. 2012), p. 169. DOI: 10.1088/0004-637X/744/2/169. arXiv: 1110.3473 [astro-ph.IM] (cit. on pp. 11, 161).

[42] R. Keisler, C. L. Reichardt, K. A. Aird, B. A. Benson, L. E. Bleem, J. E. Carlstrom, C. L. Chang, H. M. Cho, T. M. Crawford, A. T. Crites, T. de Haan, M. A. Dobbs, J. Dudley, E. M. George, N. W. Halverson, G. P. Holder, W. L. Holzapfel, S. Hoover, Z. Hou, J. D. Hrubes, M. Joy, L. Knox, A. T. Lee, E. M. Leitch, M. Lueker, D. Luong-Van, J. J. McMahon, J. Mehl, S. S. Meyer, M. Millea, J. J. Mohr, T. E. Montroy, T. Natoli, S. Padin, T. Plagge, C. Pryke, J. E. Ruhl, K. K. Schaffer, L. Shaw, E. Shirokoff, H. G. Spieler, Z. Staniszewski, A. A. Stark, K. Story, A. van Engelen, K. Vanderlinde, J. D. Vieira, R. Williamson, and O. Zahn. "A Measurement of the Damping Tail of the Cosmic Microwave Background Power Spectrum with the South Pole Telescope". In: ApJ 743, 28 (Dec. 2011), p. 28. DOI: 10.1088/0004-637X/743/1/28. arXiv: 1105.3182 (cit. on p. 11).

[43] J. J. Condon, W. D. Cotton, E. W. Greisen, Q. F. Yin, R. A. Perley, G. B. Taylor, and J. J. Broderick. "The NRAO VLA Sky Survey". In: AJ 115 (May 1998), pp. 1693–1716. DOI: 10.1086/300337 (cit. on p. 11).

[44] J. Merten, M. Meneghetti, M. Postman, K. Umetsu, A. Zitrin, E. Medezinski, M. Nonino, A. Koekemoer, P. Melchior, D. Gruen, L. A. Moustakas, M. Bartelmann, O. Host, M. Donahue, D. Coe, A. Molino, S. Jouvel, A. Monna, S. Seitz, N. Czakon, D. Lemze, J. Sayers, I. Balestra, P. Rosati, N. Benítez, A. Biviano, R. Bouwens, L. Bradley, T. Broadhurst, M. Carrasco, H. Ford, C. Grillo, L. Infante, D. Kelson, O. Lahav, R. Massey, J. Moustakas, E. Rasia, J. Rhodes, J. Vega, and W. Zheng. "CLASH: The Concentration-Mass Relation of Galaxy Clusters". In: *ArXiv e-prints* (Apr. 2014). arXiv: 1404.1376 (cit. on pp. 12, 13, 26).

[45] A. Zitrin, T. Broadhurst, K. Umetsu, D. Coe, N. Benítez, B. Ascaso, L. Bradley, H. Ford, J. Jee, E. Medezinski, Y. Rephaeli, and W. Zheng. "New multiply-lensed galaxies identified in ACS/NIC3 observations of Cl0024+1654 using an improved mass model". In: MNRAS 396 (July 2009), pp. 1985–2002. DOI: 10.1111/j.1365-2966.2009.14899.x. arXiv: 0902.3971 [astro-ph.CO] (cit. on p. 12).

[46] I. Balestra, E. Vanzella, P. Rosati, A. Monna, C. Grillo, M. Nonino, A. Mercurio, A. Biviano, L. Bradley, D. Coe, A. Fritz, M. Postman, S. Seitz, M. Scodeggio, P. Tozzi, W. Zheng, B. Ziegler, A. Zitrin, M. Annunziatella, M. Bartelmann, N. Benitez, T. Broadhurst, R. Bouwens, O. Czoske, M. Donahue, H. Ford, M. Girardi, L. Infante, S. Jouvel, D. Kelson, A. Koekemoer, U. Kuchner, D. Lemze, M. Lombardi, C. Maier, E. Medezinski, P. Melchior, M. Meneghetti, J. Merten, A. Molino,

L. Moustakas, V. Presotto, R. Smit, and K. Umetsu. “CLASH-VLT: spectroscopic confirmation of a z = 6.11 quintuply lensed galaxy in the Frontier Fields cluster RXC J2248.7-4431”. In: A&A 559, L9 (Nov. 2013), p. L9. DOI: 10.1051/0004-6361/201322620. arXiv: 1309.1593 [astro-ph.CO] (cit. on p. 12).

[47] N. Benítez. “Bayesian Photometric Redshift Estimation”. In: ApJ 536 (June 2000), pp. 571–583. DOI: 10.1086/308947. eprint: astro-ph/9811189 (cit. on p. 12).

[48] J. Merten, M. Cacciato, M. Meneghetti, C. Mignone, and M. Bartelmann. “Combining weak and strong cluster lensing: applications to simulations and MS 2137”. In: A&A 500 (June 2009), pp. 681–691. DOI: 10.1051/0004-6361/200810372. arXiv: 0806.1967 (cit. on pp. 12, 13).

[49] K. Umetsu, E. Medezinski, M. Nonino, J. Merten, M. Postman, M. Meneghetti, M. Donahue, N. Czakon, A. Molino, S. Seitz, D. Gruen, D. Lemze, I. Balestra, N. Benítez, A. Biviano, T. Broadhurst, H. Ford, C. Grillo, A. Koekemoer, P. Melchior, A. Mercurio, J. Moustakas, P. Rosati, and A. Zitrin. “CLASH: Weak-lensing Shear-and-magnification Analysis of 20 Galaxy Clusters”. In: ApJ 795, 163 (Nov. 2014), p. 163. DOI: 10.1088/0004-637X/795/2/163. arXiv: 1404.1375 (cit. on p. 13).

[50] M. Meneghetti, E. Rasia, J. Merten, F. Bellagamba, S. Ettori, P. Mazzotta, K. Dolag, and S. Marri. “Weighing simulated galaxy clusters using lensing and X-ray”. In: A&A 514, A93 (May 2010), A93. DOI: 10.1051/0004-6361/200913222. arXiv: 0912.1343 [astro-ph.CO] (cit. on pp. 13, 28).

[51] A. Mahdavi, H. Hoekstra, A. Babul, J. Sievers, S. T. Myers, and J. P. Henry. “Joint Analysis of Cluster Observations. I. Mass Profile of Abell 478 from Combined X-Ray, Sunyaev-Zel’dovich, and Weak-Lensing Data”. In: ApJ 664 (July 2007), pp. 162–180. DOI: 10.1086/517958. eprint: astro-ph/0703372 (cit. on pp. 14, 15).

[52] A. Mahdavi, H. Hoekstra, A. Babul, C. Bildfell, T. Jeltema, and J. P. Henry. “Joint Analysis of Cluster Observations. II. Chandra/XMM-Newton X-Ray and Weak Lensing Scaling Relations for a Sample of 50 Rich Clusters of Galaxies”. In: ApJ 767, 116 (Apr. 2013), p. 116. DOI: 10.1088/0004-637X/767/2/116. arXiv: 1210.3689 [astro-ph.CO] (cit. on pp. 14, 15).

[53] D. Nagai, A. V. Kravtsov, and A. Vikhlinin. “Effects of Galaxy Formation on Thermodynamics of the Intracluster Medium”. In: ApJ 668 (Oct. 2007), pp. 1–14. DOI: 10.1086/521328. eprint: astro-ph/0703661 (cit. on p. 17).

[54] M. Arnaud, G. W. Pratt, R. Piffaretti, H. Böhringer, J. H. Croston, and E. Pointecouteau. “The universal galaxy cluster pressure profile from a representative sample of nearby systems (REXCESS) and the Y_{SZ} - M_{500} relation”. In: A&A 517, A92 (July 2010), A92. DOI: 10.1051/0004-6361/200913416. arXiv: 0910.1234 [astro-ph.CO] (cit. on p. 17).

[55] B. J. Maughan, C. Jones, W. Forman, and L. Van Speybroeck. “Images, Structural Properties, and Metal Abundances of Galaxy Clusters Observed with Chandra ACIS-I at 0.1 <z <1.3”. In: ApJS 174 (Jan. 2008), pp. 117–135. DOI: 10.1086/521225. eprint: astro-ph/0703156 (cit. on p. 17).

[56] B. J. Maughan, P. A. Giles, S. W. Randall, C. Jones, and W. R. Forman. “Self-similar scaling and evolution in the galaxy cluster X-ray luminosity-temperature relation”. In: MNRAS 421 (Apr. 2012), pp. 1583–1602. DOI: 10.1111/j.1365-2966.2012.20419.x. arXiv: 1108.1200 [astro-ph.CO] (cit. on p. 17).

[57] J. Sayers, N. G. Czakon, A. Mantz, S. R. Golwala, S. Ameglio, T. P. Downes, P. M. Koch, K.-Y. Lin, B. J. Maughan, S. M. Molnar, L. Moustakas, T. Mroczkowski, E. Pierpaoli, J. A. Shitanishi, S. Siegel, K. Umetsu, and N. Van der Pyl. “Sunyaev-Zel’dovich-measured Pressure Profiles from the Bolocam X-Ray/SZ Galaxy Cluster Sample”. In: ApJ 768, 177 (May 2013), p. 177. DOI: 10.1088/0004-637X/768/2/177. arXiv: 1211.1632 [astro-ph.CO] (cit. on p. 17).

[58] Gareth O. Roberts and Jeffrey S. Rosenthal. “Optimal scaling for various Metropolis-Hastings algorithms”. In: *Statist. Sci.* 16.4 (Nov. 2001), pp. 351–367. DOI: 10.1214/ss/1015346320 (cit. on p. 19).

[59] John Geweke. “Evaluating the Accuracy of Sampling-Based Approaches to the Calculation of Posterior Moments”. In: *IN BAYESIAN STATISTICS*. University Press, 1992, pp. 169–193 (cit. on p. 19).

[60] Philip Heidelberger and Peter D Welch. “Simulation run length control in the presence of an initial transient”. In: *Operations Research* 31.6 (1983), pp. 1109–1144 (cit. on p. 19).

[61] Philip Heidelberger and Peter D Welch. “A spectral method for confidence interval generation and run length control in simulations”. In: *Communications of the ACM* 24.4 (1981), pp. 233–245 (cit. on p. 19).

[62] Adrian E Raftery, Steven Lewis, et al. “How many iterations in the Gibbs sampler”. In: *Bayesian statistics* 4.2 (1992), pp. 763–773 (cit. on p. 19).

[63] A. B. Newman, T. Treu, R. S. Ellis, and D. J. Sand. “The Dark Matter Distribution in A383: Evidence for a Shallow Density Cusp from Improved Lensing, Stellar Kinematic, and X-ray Data”. In: ApJ 728, L39 (Feb. 2011), p. L39. DOI: 10.1088/2041-8205/728/2/L39. arXiv: 1101.3553 [astro-ph.CO] (cit. on pp. 25, 28).

[64] A. Morandi, M. Limousin, J. Sayers, S. R. Golwala, N. G. Czakon, E. Pierpaoli, E. Jullo, J. Richard, and S. Ameglio. “X-ray, lensing and Sunyaev-Zel’dovich triaxial analysis of Abell 1835 out to R_{200}”. In: MNRAS 425 (Sept. 2012), pp. 2069–2082. DOI: 10.1111/j.1365-2966.2012.21196.x. arXiv: 1111.6189 [astro-ph.CO] (cit. on pp. 25, 26, 28).

[65] J. Hlavacek-Larrondo, S. W. Allen, G. B. Taylor, A. C. Fabian, R. E. A. Canning, N. Werner, J. S. Sanders, C. K. Grimes, S. Ehlert, and A. von der Linden. "Probing the Extreme Realm of Active Galactic Nucleus Feedback in the Massive Galaxy Cluster, RX J1532.9+3021". In: ApJ 777, 163 (Nov. 2013), p. 163. DOI: 10.1088/0004-637X/777/2/163. arXiv: 1306.0907 (cit. on p. 27).

[66] D. Carter and N. Metcalfe. "The morphology of clusters of galaxies". In: MNRAS 191 (May 1980), pp. 325–337 (cit. on p. 28).

[67] B. Binggeli. "The shape and orientation of clusters of galaxies". In: A&A 107 (Mar. 1982), pp. 338–349 (cit. on p. 28).

[68] D. Fabricant, G. Rybicki, and P. Gorenstein. "X-ray measurements of the nonspherical mass distribution in the cluster of galaxies A2256". In: ApJ 286 (Nov. 1984), pp. 186–195. DOI: 10.1086/162586 (cit. on p. 28).

[69] D. A. Buote and C. R. Canizares. "X-ray constraints on the shape of the dark matter in five Abell clusters". In: ApJ 400 (Dec. 1992), pp. 385–397. DOI: 10.1086/172004 (cit. on p. 28).

[70] A. K. D. Evans and S. Bridle. "A Detection of Dark Matter Halo Ellipticity using Galaxy Cluster Lensing in the SDSS". In: ApJ 695 (Apr. 2009), pp. 1446–1456. DOI: 10.1088/0004-637X/695/2/1446. arXiv: 0806.2723 (cit. on p. 28).

[71] H. Kawahara. "The Axis Ratio Distribution of X-ray Clusters Observed by XMM-Newton". In: ApJ 719 (Aug. 2010), pp. 1926–1931. DOI: 10.1088/0004-637X/719/2/1926. arXiv: 0911.0390 (cit. on p. 28).

[72] M. Oguri, M. Takada, N. Okabe, and G. P. Smith. "Direct measurement of dark matter halo ellipticity from two-dimensional lensing shear maps of 25 massive clusters". In: MNRAS 405 (July 2010), pp. 2215–2230. DOI: 10.1111/j.1365-2966.2010.16622.x. arXiv: 1004.4214 (cit. on p. 28).

[73] M. Oguri, M. B. Bayliss, H. Dahle, K. Sharon, M. D. Gladders, P. Natarajan, J. F. Hennawi, and B. P. Koester. "Combined strong and weak lensing analysis of 28 clusters from the Sloan Giant Arcs Survey". In: MNRAS 420 (Mar. 2012), pp. 3213–3239. DOI: 10.1111/j.1365-2966.2011.20248.x. arXiv: 1109.2594 (cit. on p. 28).

[74] C. S. Frenk, S. D. M. White, M. Davis, and G. Efstathiou. "The formation of dark halos in a universe dominated by cold dark matter". In: ApJ 327 (Apr. 1988), pp. 507–525. DOI: 10.1086/166213 (cit. on p. 28).

[75] J. Dubinski and R. G. Carlberg. "The structure of cold dark matter halos". In: ApJ 378 (Sept. 1991), pp. 496–503. DOI: 10.1086/170451 (cit. on p. 28).

[76] M. S. Warren, W. H. Zurek, P. J. Quinn, and J. K. Salmon. “The shape of the invisible halo: N-body simulations on parallel supercomputers”. In: *After the first three minutes*. Ed. by S. S. Holt, C. L. Bennett, and V. Trimble. Vol. 222. American Institute of Physics Conference Series. Apr. 1991, pp. 216–223. DOI: 10.1063/1.40467 (cit. on p. 28).

[77] Y. P. Jing and Y. Suto. “High-Resolution Numerical Simulations for Galaxy Formation”. In: *New Trends in Theoretical and Observational Cosmology*. Ed. by K. Sato and T. Shiromizu. 2002, p. 167. eprint: astro-ph/0201147 (cit. on p. 28).

[78] P. F. Hopkins, N. A. Bahcall, and P. Bode. “Cluster Alignments and Ellipticities in ΛCDM Cosmology”. In: ApJ 618 (Jan. 2005), pp. 1–15. DOI: 10.1086/425993. eprint: astro-ph/0409652 (cit. on p. 28).

[79] J. C. Muñoz-Cuartas, A. V. Macciò, S. Gottlöber, and A. A. Dutton. “The redshift evolution of Λ cold dark matter halo parameters: concentration, spin and shape”. In: MNRAS 411 (Feb. 2011), pp. 584–594. DOI: 10.1111/j.1365-2966.2010.17704.x. arXiv: 1007.0438 (cit. on p. 28).

[80] D. Lemze, R. Wagner, Y. Rephaeli, S. Sadeh, M. L. Norman, R. Barkana, T. Broadhurst, H. Ford, and M. Postman. “Profiles of Dark Matter Velocity Anisotropy in Simulated Clusters”. In: ApJ 752, 141 (June 2012), p. 141. DOI: 10.1088/0004-637X/752/2/141. arXiv: 1106.6048 (cit. on p. 28).

[81] M. Limousin, A. Morandi, M. Sereno, M. Meneghetti, S. Ettori, M. Bartelmann, and T. Verdugo. “The Three-Dimensional Shapes of Galaxy Clusters”. In: Space Sci. Rev. 177 (Aug. 2013), pp. 155–194. DOI: 10.1007/s11214-013-9980-y. arXiv: 1210.3067 (cit. on p. 28).

[82] G. Despali, G. Tormen, and R. K. Sheth. “Ellipsoidal halo finders and implications for models of triaxial halo formation”. In: MNRAS 431 (May 2013), pp. 1143–1159. DOI: 10.1093/mnras/stt235. arXiv: 1212.4157 [astro-ph.CO] (cit. on p. 28).

[83] M. Meneghetti, E. Rasia, J. Vega, J. Merten, M. Postman, G. Yepes, F. Sembolini, M. Donahue, S. Ettori, K. Umetsu, I. Balestra, M. Bartelmann, N. Benítez, A. Biviano, R. Bouwens, L. Bradley, T. Broadhurst, D. Coe, N. Czakon, M. De Petris, H. Ford, C. Giocoli, S. Gottlöber, C. Grillo, L. Infante, S. Jouvel, D. Kelson, A. Koekemoer, O. Lahav, D. Lemze, E. Medezinski, P. Melchior, A. Mercurio, A. Molino, L. Moscardini, A. Monna, J. Moustakas, L. A. Moustakas, M. Nonino, J. Rhodes, P. Rosati, J. Sayers, S. Seitz, W. Zheng, and A. Zitrin. “The MUSIC of CLASH: Predictions on the Concentration-Mass Relation”. In: ApJ 797, 34 (Dec. 2014), p. 34. DOI: 10.1088/0004-637X/797/1/34. arXiv: 1404.1384 (cit. on p. 28).

[84] J. Bardeen, L. N. Cooper, and J. R. Schrieffer. “Theory of Superconductivity”. In: *Physical Review* 108 (Dec. 1957), pp. 1175–1204. DOI: 10.1103/PhysRev.108.1175 (cit. on pp. 38, 43).

[85] A. G. Kozorezov, A. F. Volkov, J. K. Wigmore, A. Peacock, A. Poelaert, and R. den Hartog. "Quasiparticle-phonon downconversion in nonequilibrium superconductors". In: Phys. Rev. B 61 (May 2000), p. 11807. DOI: 10.1103/PhysRevB.61.11807 (cit. on p. 40).

[86] A. Kozorezov. "Energy Down-Conversion and Thermalization in Metal Absorbers". In: *Journal of Low Temperature Physics* 167 (May 2012), pp. 473–484. DOI: 10.1007/s10909-011-0426-1 (cit. on p. 40).

[87] T. Guruswamy, D. J. Goldie, and S. Withington. "Quasiparticle generation efficiency in superconducting thin films". In: *Superconductor Science Technology* 27.5, 055012 (May 2014), p. 055012. DOI: 10.1088/0953-2048/27/5/055012. arXiv: 1401.1937 [cond-mat.supr-con] (cit. on pp. 40, 157).

[88] M. Kurakado. "Possibility of high resolution detectors using superconducting tunnel junctions". In: *Nuclear Instruments and Methods* 196 (May 1982), pp. 275–277. DOI: 10.1016/0029-554X(82)90654-1 (cit. on p. 40).

[89] R. Barends, J. J. A. Baselmans, S. J. C. Yates, J. R. Gao, J. N. Hovenier, and T. M. Klapwijk. "Quasiparticle Relaxation in Optically Excited High-Q Superconducting Resonators". In: *Physical Review Letters* 100.25, 257002 (June 2008), p. 257002. DOI: 10.1103/PhysRevLett.100.257002. arXiv: 0802.0640 [cond-mat.supr-con] (cit. on pp. 41, 112).

[90] R. Barends, S. van Vliet, J. J. A. Baselmans, S. J. C. Yates, J. R. Gao, and T. M. Klapwijk. "Enhancement of quasiparticle recombination in Ta and Al superconductors by implantation of magnetic and nonmagnetic atoms". In: Phys. Rev. B 79.2, 020509 (Jan. 2009), p. 020509. DOI: 10.1103/PhysRevB.79.020509. arXiv: 0811.1961 [cond-mat.supr-con] (cit. on pp. 41, 86).

[91] A. G. Kozorezov, A. A. Golubov, J. K. Wigmore, D. Martin, P. Verhoeve, R. A. Hijmering, and I. Jerjen. "Inelastic scattering of quasiparticles in a superconductor with magnetic impurities". In: Phys. Rev. B 78.17, 174501 (Nov. 2008), p. 174501. DOI: 10.1103/PhysRevB.78.174501 (cit. on pp. 41, 86).

[92] D. C. Mattis and J. Bardeen. "Theory of the Anomalous Skin Effect in Normal and Superconducting Metals". In: *Physical Review* 111 (July 1958), pp. 412–417. DOI: 10.1103/PhysRev.111.412 (cit. on p. 42).

[93] J. Gao. "The Physics of Superconducting Microwave Resonators". PhD thesis. California Institute of Technology, 2008 (cit. on pp. 42, 51, 62, 89, 105, 112, 134).

[94] R. E. Glover and M. Tinkham. "Conductivity of Superconducting Films for Photon Energies between 0.3 and $40kT_c$". In: *Physical Review* 108 (Oct. 1957), pp. 243–256. DOI: 10.1103/PhysRev.108.243 (cit. on p. 42).

[95] C. S. Owen and D. J. Scalapino. “Superconducting State under the Influence of External Dynamic Pair Breaking”. In: *Physical Review Letters* 28 (June 1972), pp. 1559–1561. DOI: 10.1103/PhysRevLett.28.1559 (cit. on p. 43).

[96] J. Gao, J. Zmuidzinas, A. Vayonakis, P. Day, B. Mazin, and H. Leduc. “Equivalence of the Effects on the Complex Conductivity of Superconductor due to Temperature Change and External Pair Breaking”. In: *Journal of Low Temperature Physics* 151 (Apr. 2008), pp. 557–563. DOI: 10.1007/s10909-007-9688-z (cit. on p. 46).

[97] R. M. J. Janssen, A. Endo, P. J. de Visser, T. M. Klapwijk, and J. J. A. Baselmans. “Equivalence of optical and electrical noise equivalent power of hybrid NbTiN-Al microwave kinetic inductance detectors”. In: *Applied Physics Letters* 105.19, 193504 (Nov. 2014), p. 193504. DOI: 10.1063/1.4901733. arXiv: 1408.3272 [physics.ins-det] (cit. on p. 46).

[98] S. R. Golwala. “MUSICentric Summary of MKID Response and Sensitivity”. Internal Report. 2011 (cit. on pp. 48, 68, 114).

[99] J. M. Martinis, M. Ansmann, and J. Aumentado. “Energy Decay in Superconducting Josephson-Junction Qubits from Nonequilibrium Quasiparticle Excitations”. In: *Physical Review Letters* 103.9, 097002 (Aug. 2009), p. 097002. DOI: 10.1103/PhysRevLett.103.097002 (cit. on p. 50).

[100] P. J. de Visser, S. Withington, and D. J. Goldie. “Readout-power heating and hysteretic switching between thermal quasiparticle states in kinetic inductance detectors”. In: *Journal of Applied Physics* 108.11 (Dec. 2010), p. 114504. DOI: 10.1063/1.3517152 (cit. on pp. 50, 60).

[101] H. McCarrick, D. Flanigan, G. Jones, B. R. Johnson, P. Ade, D. Araujo, K. Bradford, R. Cantor, G. Che, P. Day, S. Doyle, H. Leduc, M. Limon, V. Luu, P. Mauskopf, A. Miller, T. Mroczkowski, C. Tucker, and J. Zmuidzinas. “Horn-coupled, commercially-fabricated aluminum lumped-element kinetic inductance detectors for millimeter wavelengths”. In: *Review of Scientific Instruments* 85.12, 123117 (Dec. 2014), p. 123117. DOI: 10.1063/1.4903855. arXiv: 1407.7749 [astro-ph.IM] (cit. on p. 50).

[102] Ran Duan. “Instrumentation for Kinetic-Inductance-Detector-Based Submillimeter Radio Astronomy”. PhD thesis. California Institute of Technology, 2015 (cit. on pp. 51, 103, 140, 150, 204).

[103] B. A. Mazin. “Microwave kinetic inductance detectors”. PhD thesis. California Institute of Technology, California, USA, Nov. 2005 (cit. on pp. 51, 69, 112).

[104] O. Noroozian. “Superconducting Microwave Resonator Arrays for Submillimeter/Far-Infrared Imaging”. PhD thesis. California Institute of Technology, 2012 (cit. on pp. 51, 89).

[105] Jonas Zmuidzinas. “Superconducting microresonators: Physics and applications”. In: *Annu. Rev. Condens. Matter Phys.* 3.1 (2012), pp. 169–214 (cit. on p. 56).

[106] A. B. Pippard. “Field Variation of the Superconducting Penetration Depth”. In: *Royal Society of London Proceedings Series A* 203 (Sept. 1950), pp. 210–223. DOI: 10.1098/rspa.1950.0135 (cit. on p. 57).

[107] A. B. Pippard. “An Experimental and Theoretical Study of the Relation between Magnetic Field and Current in a Superconductor”. In: *Royal Society of London Proceedings Series A* 216 (Feb. 1953), pp. 547–568. DOI: 10.1098/rspa.1953.0040 (cit. on p. 57).

[108] L. J. Swenson, P. K. Day, B. H. Eom, H. G. Leduc, N. Llombart, C. M. McKenney, O. Noroozian, and J. Zmuidzinas. “Operation of a titanium nitride superconducting microresonator detector in the nonlinear regime”. In: *Journal of Applied Physics* 113.10 (Mar. 2013), p. 104501. DOI: 10.1063/1.4794808. arXiv: 1305.4281 [cond-mat.supr-con] (cit. on pp. 57, 100).

[109] D. J. Goldie and S. Withington. “Non-equilibrium superconductivity in quantum-sensing superconducting resonators”. In: *Superconductor Science Technology* 26.1, 015004 (Jan. 2013), p. 015004. DOI: 10.1088/0953-2048/26/1/015004. arXiv: 1208.0685 [cond-mat.supr-con] (cit. on pp. 60, 86).

[110] H. Paik and K. D. Osborn. “Reducing quantum-regime dielectric loss of silicon nitride for superconducting quantum circuits”. In: *Applied Physics Letters* 96.7, 072505 (Feb. 2010), p. 072505. DOI: 10.1063/1.3309703. arXiv: 0908.2948 [cond-mat.supr-con] (cit. on p. 62).

[111] D. S. Wisbey, J. Gao, M. R. Vissers, F. C. S. da Silva, J. S. Kline, L. Vale, and D. P. Pappas. “Effect of metal/substrate interfaces on radio-frequency loss in superconducting coplanar waveguides”. In: *Journal of Applied Physics* 108.9 (Nov. 2010), p. 093918. DOI: 10.1063/1.3499608 (cit. on p. 62).

[112] M. S. Khalil, F. C. Wellstood, and K. D. Osborn. “Loss Dependence on Geometry and Applied Power in Superconducting Coplanar Resonators”. In: *IEEE Transactions on Applied Superconductivity* 21 (June 2011), pp. 879–882. DOI: 10.1109/TASC.2010.2090330. arXiv: 1008.2929 [cond-mat.supr-con] (cit. on p. 62).

[113] MS Khalil, MJA Stoutimore, FC Wellstood, and KD Osborn. “An analysis method for asymmetric resonator transmission applied to superconducting devices”. In: *Journal of Applied Physics* 111.5 (2012), p. 054510 (cit. on p. 62).

[114] J. Zmuidzinas. “Nonuniform photon absorption in submm MKIDs”. Internal Report. 2008 (cit. on p. 68).

[115] Rodolphe Boudot and Enrico Rubiola. “Phase noise in RF and microwave amplifiers”. In: *Ultrasonics, Ferroelectrics, and Frequency Control, IEEE Transactions on* 59.12 (2012), pp. 2613–2624 (cit. on p. 80).

[116] J. Zmuidzinas. “Thermal noise and correlations in photon detection”. In: Appl. Opt. 42 (Sept. 2003), pp. 4989–5008. DOI: 10.1364/AO.42.004989 (cit. on p. 81).

[117] P. J. de Visser, J. J. A. Baselmans, P. Diener, S. J. C. Yates, A. Endo, and T. M. Klapwijk. "Number Fluctuations of Sparse Quasiparticles in a Superconductor". In: *Physical Review Letters* 106.16, 167004 (Apr. 2011), p. 167004. DOI: 10.1103/PhysRevLett.106.167004. arXiv: 1103.0758 [cond-mat.supr-con] (cit. on p. 86).

[118] P. J. de Visser, D. J. Goldie, P. Diener, S. Withington, J. J. A. Baselmans, and T. M. Klapwijk. "Evidence of a Nonequilibrium Distribution of Quasiparticles in the Microwave Response of a Superconducting Aluminum Resonator". In: *Physical Review Letters* 112.4, 047004 (Jan. 2014), p. 047004. DOI: 10.1103/PhysRevLett.112.047004. arXiv: 1306.4992 [cond-mat.supr-con] (cit. on p. 86).

[119] J. Gao, J. Zmuidzinas, B. A. Mazin, H. G. LeDuc, and P. K. Day. "Noise properties of superconducting coplanar waveguide microwave resonators". In: *Applied Physics Letters* 90.10, 102507 (Mar. 2007), p. 102507. DOI: 10.1063/1.2711770. eprint: cond-mat/0609614 (cit. on p. 87).

[120] J. Gao, M. Daal, A. Vayonakis, S. Kumar, J. Zmuidzinas, B. Sadoulet, B. A. Mazin, P. K. Day, and H. G. Leduc. "Experimental evidence for a surface distribution of two-level systems in superconducting lithographed microwave resonators". In: *Applied Physics Letters* 92.15, 152505 (Apr. 2008), p. 152505. DOI: 10.1063/1.2906373. arXiv: 0802.4457 [cond-mat.supr-con] (cit. on p. 87).

[121] P. W. Anderson, B. I. Halperin, and C. M. Varma. "Anomalous low-temperature thermal properties of glasses and spin glasses". In: *Philosophical Magazine* 25 (Jan. 1972), pp. 1–9. DOI: 10.1080/14786437208229210 (cit. on p. 87).

[122] W.A. Phillips. "Tunneling states and the low-temperature thermal expansion of glasses". English. In: *Journal of Low Temperature Physics* 11.5-6 (1973), pp. 757–763. DOI: 10.1007/BF00654457 (cit. on p. 87).

[123] W. A. Phillips. "REVIEW ARTICLE: Two-level states in glasses". In: *Reports on Progress in Physics* 50 (Dec. 1987), pp. 1657–1708. DOI: 10.1088/0034-4885/50/12/003 (cit. on p. 87).

[124] D. P. Pappas, M. R. Vissers, D. S. Wisbey, J. S. Kline, and J. Gao. "Two Level System Loss in Superconducting Microwave Resonators". In: *IEEE Transactions on Applied Superconductivity* 21 (June 2011), pp. 871–874. DOI: 10.1109/TASC.2010.2097578 (cit. on p. 88).

[125] J. Gao, M. Daal, J. M. Martinis, A. Vayonakis, J. Zmuidzinas, B. Sadoulet, B. A. Mazin, P. K. Day, and H. G. Leduc. "A semiempirical model for two-level system noise in superconducting microresonators". In: *Applied Physics Letters* 92.21, 212504 (May 2008), p. 212504. DOI: 10.1063/1.2937855. arXiv: 0804.0467 [cond-mat.supr-con] (cit. on p. 88).

[126] O. Noroozian, J. Gao, J. Zmuidzinas, H. G. LeDuc, and B. A. Mazin. "Two-level system noise reduction for Microwave Kinetic Inductance Detectors". In: *American Institute of Physics Conference Series*. Ed. by B. Young, B. Cabrera, and A. Miller. Vol. 1185. American Institute of Physics

Conference Series. Dec. 2009, pp. 148–151. DOI: 10.1063/1.3292302. arXiv: 0909.2060 [physics.ins-det] (cit. on pp. 89, 130, 131).

[127] S. Kumar, J. Gao, J. Zmuidzinas, B. A. Mazin, H. G. LeDuc, and P. K. Day. "Temperature dependence of the frequency and noise of superconducting coplanar waveguide resonators". In: *Applied Physics Letters* 92.12, 123503 (Mar. 2008), p. 123503. DOI: 10.1063/1.2894584. arXiv: 0802.4268 [cond-mat.supr-con] (cit. on p. 89).

[128] J. Burnett, L. Faoro, I. Wisby, V. L. Gurtovoi, A. V. Chernykh, G. M. Mikhailov, V. A. Tulin, R. Shaikhaidarov, V. Antonov, P. J. Meeson, A. Y. Tzalenchuk, and T. Lindström. "Evidence for interacting two-level systems from the 1/f noise of a superconducting resonator". In: *Nature Communications* 5, 4119 (June 2014), p. 4119. DOI: 10.1038/ncomms5119. arXiv: 1311.1655 [cond-mat.mes-hall] (cit. on pp. 89, 134).

[129] J. R. Pardo, J. Cernicharo, and E. Serabyn. "Atmospheric transmission at microwaves (ATM): an improved model for millimeter/submillimeter applications". In: *IEEE Transactions on Antennas and Propagation* 49 (Dec. 2001), pp. 1683–1694. DOI: 10.1109/8.982447 (cit. on pp. 90, 159).

[130] C. R. Masson. "Atmospheric Effects and Calibrations". In: *IAU Colloq. 140: Astronomy with Millimeter and Submillimeter Wave Interferometry*. Ed. by M. Ishiguro and J. Welch. Vol. 59. Astronomical Society of the Pacific Conference Series. 1994, pp. 87–95 (cit. on p. 89).

[131] O. P. Lay and N. W. Halverson. "The Impact of Atmospheric Fluctuations on Degree-Scale Imaging of the Cosmic Microwave Background". In: ApJ 543 (Nov. 2000), pp. 787–798. DOI: 10.1086/317115. eprint: astro-ph/9905369 (cit. on pp. 89, 90).

[132] A. Kolmogorov. "The Local Structure of Turbulence in Incompressible Viscous Fluid for Very Large Reynolds' Numbers". In: *Akademiia Nauk SSSR Doklady* 30 (1941), pp. 301–305 (cit. on p. 90).

[133] G. I. Taylor. "The Spectrum of Turbulence". In: *Royal Society of London Proceedings Series A* 164 (Feb. 1938), pp. 476–490. DOI: 10.1098/rspa.1938.0032 (cit. on p. 90).

[134] V. I. Tatarskii. *Wave Propagation in Turbulent Medium*. McGraw-Hill, 1961 (cit. on p. 90).

[135] O. P. Lay. "The temporal power spectrum of atmospheric fluctuations due to water vapor". In: A&AS 122 (May 1997), pp. 535–545. DOI: 10.1051/aas:1997154 (cit. on p. 90).

[136] R. S. Bussmann, W. L. Holzapfel, and C. L. Kuo. "Millimeter Wavelength Brightness Fluctuations of the Atmosphere above the South Pole". In: ApJ 622 (Apr. 2005), pp. 1343–1355. DOI: 10.1086/427935. eprint: astro-ph/0412031 (cit. on p. 90).

[137] J. R. Pardo, E. Serabyn, and J. Cernicharo. "Submillimeter atmospheric transmission measurements on Mauna Kea during extremely dry El Nino conditions: implications for broadband opacity contributions". In: J. Quant. Spec. Radiat. Transf. 68 (Feb. 2001), pp. 419–433. DOI: 10.1016/S0022-4073(00)00034-0 (cit. on p. 91).

[138] J. Sayers, N. G. Czakon, P. K. Day, T. P. Downes, R. P. Duan, J. Gao, J. Glenn, S. R. Golwala, M. I. Hollister, H. G. LeDuc, B. A. Mazin, P. R. Maloney, O. Noroozian, H. T. Nguyen, J. A. Schlaerth, S. Siegel, J. E. Vaillancourt, A. Vayonakis, P. R. Wilson, and J. Zmuidzinas. "Optics for MUSIC: a new (sub)millimeter camera for the Caltech Submillimeter Observatory". In: *Society of Photo-Optical Instrumentation Engineers (SPIE) Conference Series*. Vol. 7741. Society of Photo-Optical Instrumentation Engineers (SPIE) Conference Series. July 2010, p. 0. DOI: 10.1117/12.857324 (cit. on pp. 92, 158).

[139] Tim Jenness, John F. Lightfoot, and Wayne S. Holland. "Removing sky contributions from SCUBA data". In: vol. 3357. 1998, pp. 548–558. DOI: 10.1117/12.317389 (cit. on p. 93).

[140] C. Borys, S. C. Chapman, and D. Scott. "Using SCUBA to place upper limits on arcsecond-scale cosmic microwave background anisotropies at 850μm". In: MNRAS 308 (Sept. 1999), pp. 527–538. DOI: 10.1046/j.1365-8711.1999.02753.x. eprint: astro-ph/9808031 (cit. on p. 93).

[141] L. A. Reichertz, B. Weferling, W. Esch, and E. Kreysa. "The fastscanning observing technique for millimeter and submillimeter astronomy". In: A&A 379 (Nov. 2001), pp. 735–739. DOI: 10.1051/0004-6361:20011227 (cit. on p. 93).

[142] P. D. Mauskopf. "Measurements of Anisotropies in the Cosmic Microwave Background at Small and Intermediate Angular Scales with Bolometric Receivers at MM Wavelengths". PhD thesis. UNIVERSITY OF CALIFORNIA, BERKELEY, 1997 (cit. on p. 93).

[143] B. A. Benson. "Spectral measurements of the Sunyaev-Zel'dovich effect". PhD thesis. Stanford University, California, USA, Dec. 2004 (cit. on p. 93).

[144] R. Adam, B. Comis, J. F. Macías-Pérez, A. Adane, P. Ade, P. André, A. Beelen, B. Belier, A. Benoît, A. Bideaud, N. Billot, N. Boudou, O. Bourrion, M. Calvo, A. Catalano, G. Coiffard, A. D'Addabbo, F.-X. Désert, S. Doyle, J. Goupy, C. Kramer, S. Leclercq, J. Martino, P. Mauskopf, F. Mayet, A. Monfardini, F. Pajot, E. Pascale, L. Perotto, E. Pointecouteau, N. Ponthieu, V. Revéret, L. Rodriguez, G. Savini, K. Schuster, A. Sievers, C. Tucker, and R. Zylka. "First observation of the thermal Sunyaev-Zel'dovich effect with kinetic inductance detectors". In: A&A 569, A66 (Sept. 2014), A66. DOI: 10.1051/0004-6361/201322902. arXiv: 1310.6237 (cit. on pp. 93, 194).

[145] George Rieke. *Detection of Light: from the Ultraviolet to the Submillimeter*. Cambridge University Press, 2003 (cit. on p. 95).

[146] H. G. Leduc, B. Bumble, P. K. Day, B. H. Eom, J. Gao, S. Golwala, B. A. Mazin, S. McHugh, A. Merrill, D. C. Moore, O. Noroozian, A. D. Turner, and J. Zmuidzinas. "Titanium nitride films for ultrasensitive microresonator detectors". In: *Applied Physics Letters* 97.10, 102509 (Sept. 2010), p. 102509. DOI: 10.1063/1.3480420. arXiv: 1003.5584 [cond-mat.supr-con] (cit. on pp. 100, 204).

[147] C. M. McKenney, H. G. Leduc, L. J. Swenson, P. K. Day, B. H. Eom, and J. Zmuidzinas. "Design considerations for a background limited 350 micron pixel array using lumped element superconducting microresonators". In: *Society of Photo-Optical Instrumentation Engineers (SPIE) Conference Series*. Vol. 8452. Society of Photo-Optical Instrumentation Engineers (SPIE) Conference Series. Sept. 2012, p. 0. DOI: 10.1117/12.925759 (cit. on pp. 100, 204).

[148] J. Gao, M. R. Vissers, M. O. Sandberg, F. C. S. da Silva, S. W. Nam, D. P. Pappas, D. S. Wisbey, E. C. Langman, S. R. Meeker, B. A. Mazin, H. G. Leduc, J. Zmuidzinas, and K. D. Irwin. "A titanium-nitride near-infrared kinetic inductance photon-counting detector and its anomalous electrodynamics". In: *Applied Physics Letters* 101.14, 142602 (Oct. 2012), p. 142602. DOI: 10.1063/1.4756916. arXiv: 1208.0871 [cond-mat.supr-con] (cit. on pp. 100, 204).

[149] E. Shirokoff, P. S. Barry, C. M. Bradford, G. Chattopadhyay, P. Day, S. Doyle, S. Hailey-Dunsheath, M. I. Hollister, A. Kovács, H. G. Leduc, C. M. McKenney, P. Mauskopf, H. T. Nguyen, R. O'Brient, S. Padin, T. J. Reck, L. J. Swenson, C. E. Tucker, and J. Zmuidzinas. "Design and Performance of SuperSpec: An On-Chip, KID-Based, mm-Wavelength Spectrometer". In: *Journal of Low Temperature Physics* 176 (Sept. 2014), pp. 657–662. DOI: 10.1007/s10909-014-1122-8 (cit. on pp. 100, 204).

[150] J. Hubmayr, J. Beall, D. Becker, H.-M. Cho, M. Devlin, B. Dober, C. Groppi, G. C. Hilton, K. D. Irwin, D. Li, P. Mauskopf, D. P. Pappas, J. Van Lanen, M. R. Vissers, Y. Wang, L. F. Wei, and J. Gao. "Photon-noise limited sensitivity in titanium nitride kinetic inductance detectors". In: *Applied Physics Letters* 106.7, 073505 (Feb. 2015), p. 073505. DOI: 10.1063/1.4913418. arXiv: 1406.4010 [astro-ph.IM] (cit. on pp. 100, 204).

[151] L. J. Swenson, P. K. Day, C. D. Dowell, B. H. Eom, M. I. Hollister, R. Jarnot, A. Kovács, H. G. Leduc, C. M. McKenney, R. Monroe, T. Mroczkowski, H. T. Nguyen, and J. Zmuidzinas. "MAKO: a pathfinder instrument for on-sky demonstration of low-cost 350 micron imaging arrays". In: *Society of Photo-Optical Instrumentation Engineers (SPIE) Conference Series*. Vol. 8452. Society of Photo-Optical Instrumentation Engineers (SPIE) Conference Series. Sept. 2012, p. 0. DOI: 10.1117/12.926223. arXiv: 1211.0315 [astro-ph.IM] (cit. on pp. 100, 204).

[152] S. Hailey-Dunsheath, E. Shirokoff, P. S. Barry, C. M. Bradford, G. Chattopadhyay, P. Day, S. Doyle, M. Hollister, A. Kovacs, H. G. LeDuc, P. Mauskopf, C. M. McKenney, R. Monroe, R. O'Brient, S. Padin, T. Reck, L. Swenson, C. E. Tucker, and J. Zmuidzinas. "Status of SuperSpec: a broadband, on-chip millimeter-wave spectrometer". In: *Society of Photo-Optical Instrumentation Engineers (SPIE) Conference Series*. Vol. 9153. Society of Photo-Optical Instrumentation Engineers (SPIE) Conference Series. Aug. 2014, p. 0. DOI: 10.1117/12.2057229. arXiv: 1501.02295 [astro-ph.IM] (cit. on pp. 100, 204).

[153] C. Ji, A. Beyer, S. Golwala, and J. Sayers. “Design of antenna-coupled lumped-element titanium nitride KIDs for long-wavelength multi-band continuum imaging”. In: vol. 9153. Society of Photo-Optical Instrumentation Engineers (SPIE) Conference Series. 2014, p. 15. DOI: 10.1117/12.2056777 (cit. on pp. 100, 204).

[154] R. Duan, S. McHugh, B. Serfass, B. A. Mazin, A. Merrill, S. R. Golwala, T. P. Downes, N. G. Czakon, P. K. Day, J. Gao, J. Glenn, M. I. Hollister, H. G. Leduc, P. R. Maloney, O. Noroozian, H. T. Nguyen, J. Sayers, J. A. Schlaerth, S. Siegel, J. E. Vaillancourt, A. Vayonakis, P. R. Wilson, and J. Zmuidzinas. “An open-source readout for MKIDs”. In: *Society of Photo-Optical Instrumentation Engineers (SPIE) Conference Series*. Vol. 7741. Society of Photo-Optical Instrumentation Engineers (SPIE) Conference Series. July 2010, p. 1. DOI: 10.1117/12.856832 (cit. on p. 103).

[155] P. J. Petersan and S. M. Anlage. “Measurement of resonant frequency and quality factor of microwave resonators: Comparison of methods”. In: *Journal of Applied Physics* 84 (Sept. 1998), pp. 3392–3402. DOI: 10.1063/1.368498. eprint: cond-mat/9805365 (cit. on p. 103).

[156] J. B. Peterson and P. L. Richards. “A cryogenic blackbody for millimeter wavelengths”. In: *International Journal of Infrared and Millimeter Waves* 5 (Dec. 1984), pp. 1507–1515. DOI: 10.1007/BF01040502 (cit. on p. 107).

[157] H. Hemmati, J. C. Mather, and W. L. Eichhorn. “Submillimeter and millimeter wave characterization of absorbing materials”. In: Appl. Opt. 24 (Dec. 1985), pp. 4489–4492. DOI: 10.1364/AO.24.004489 (cit. on p. 107).

[158] M. C. Gaidis. “Superconducting Tunnel Junctions as Single Photon X-Ray Detectors.” PhD thesis. YALE UNIVERSITY., 1994 (cit. on p. 112).

[159] W. L. McMillan. “Transition Temperature of Strong-Coupled Superconductors”. In: *Physical Review* 167 (Mar. 1968), pp. 331–344. DOI: 10.1103/PhysRev.167.331 (cit. on p. 112).

[160] S. B. Kaplan, C. C. Chi, D. N. Langenberg, J. J. Chang, S. Jafarey, and D. J. Scalapino. “Quasiparticle and phonon lifetimes in superconductors”. In: Phys. Rev. B 14 (Dec. 1976), pp. 4854–4873. DOI: 10.1103/PhysRevB.14.4854 (cit. on p. 112).

[161] J. A. Schlaerth. “Microwave kinetic inductance detector camera development for millimeter-wave astrophysics”. PhD thesis. University of Colorado at Boulder, 2010 (cit. on pp. 112, 113, 157, 164).

[162] L. Li, L. Frunzio, C. M. Wilson, and D. E. Prober. “Quasiparticle nonequilibrium dynamics in a superconducting Ta film”. In: *Journal of Applied Physics* 93 (Jan. 2003), pp. 1137–1141. DOI: 10.1063/1.1533106 (cit. on p. 114).

[163] J. Gudmundsson. “FTS Manual - Rev A”. Internal Report. 2010 (cit. on p. 114).

[164] Clinton Bockstiegel. “Testing and Characterization of HEMT Amplifiers”. PhD thesis. University of Colorado, Boulder, 2011 (cit. on p. 117).

[165] Steven W Smith et al. “The scientist and engineer’s guide to digital signal processing”. In: (1997) (cit. on p. 127).

[166] J. Burnett, T. Lindström, M. Oxborrow, Y. Harada, Y. Sekine, P. Meeson, and A. Y. Tzalenchuk. “Slow noise processes in superconducting resonators”. In: Phys. Rev. B 87.14, 140501 (Apr. 2013), p. 140501. DOI: 10.1103/PhysRevB.87.140501. arXiv: 1210.2351 [cond-mat.supr-con] (cit. on p. 134).

[167] L. Faoro and L. B. Ioffe. “Internal Loss of Superconducting Resonators Induced by Interacting Two-Level Systems”. In: *Physical Review Letters* 109.15, 157005 (Oct. 2012), p. 157005. DOI: 10.1103/PhysRevLett.109.157005. arXiv: 1201.5299 [cond-mat.mes-hall] (cit. on p. 134).

[168] J. Sayers, C. Bockstiegel, S. Brugger, N. G. Czakon, P. K. Day, T. P. Downes, R. P. Duan, J. Gao, A. K. Gill, J. Glenn, S. R. Golwala, M. I. Hollister, A. Lam, H. G. LeDuc, P. R. Maloney, B. A. Mazin, S. G. McHugh, D. A. Miller, A. K. Mroczkowski, O. Noroozian, H. T. Nguyen, J. A. Schlaerth, S. R. Siegel, A. Vayonakis, P. R. Wilson, and J. Zmuidzinas. “The status of MUSIC: the multiwavelength sub-millimeter inductance camera”. In: *Society of Photo-Optical Instrumentation Engineers (SPIE) Conference Series*. Vol. 9153. Society of Photo-Optical Instrumentation Engineers (SPIE) Conference Series. Aug. 2014, p. 4. DOI: 10.1117/12.2055444 (cit. on pp. 152, 165, 204).

[169] A. D. Hincks, V. Acquaviva, P. A. R. Ade, P. Aguirre, M. Amiri, J. W. Appel, L. F. Barrientos, E. S. Battistelli, J. R. Bond, B. Brown, B. Burger, J. Chervenak, S. Das, M. J. Devlin, S. R. Dicker, W. B. Doriese, J. Dunkley, R. Dünner, T. Essinger-Hileman, R. P. Fisher, J. W. Fowler, A. Hajian, M. Halpern, M. Hasselfield, C. Hernández-Monteagudo, G. C. Hilton, M. Hilton, R. Hlozek, K. M. Huffenberger, D. H. Hughes, J. P. Hughes, L. Infante, K. D. Irwin, R. Jimenez, J. B. Juin, M. Kaul, J. Klein, A. Kosowsky, J. M. Lau, M. Limon, Y.-T. Lin, R. H. Lupton, T. A. Marriage, D. Marsden, K. Martocci, P. Mauskopf, F. Menanteau, K. Moodley, H. Moseley, C. B. Netterfield, M. D. Niemack, M. R. Nolta, L. A. Page, L. Parker, B. Partridge, H. Quintana, B. Reid, N. Sehgal, J. Sievers, D. N. Spergel, S. T. Staggs, O. Stryzak, D. S. Swetz, E. R. Switzer, R. Thornton, H. Trac, C. Tucker, L. Verde, R. Warne, G. Wilson, E. Wollack, and Y. Zhao. “The Atacama Cosmology Telescope (ACT): Beam Profiles and First SZ Cluster Maps”. In: ApJS 191 (Dec. 2010), pp. 423–438. DOI: 10.1088/0067-0049/191/2/423. arXiv: 0907.0461 [astro-ph.CO] (cit. on p. 184).

[170] D. Schwan, F. Bertoldi, S. Cho, M. Dobbs, R. Guesten, N. W. Halverson, W. L. Holzapfel, E. Kreysa, T. M. Lanting, A. T. Lee, M. Lueker, J. Mehl, K. Menten, D. Muders, M. Myers, T. Plagge, A. Raccanelli, P. Schilke, P. L. Richards, H. Spieler, and M. White. “APEX-SZ a Sunyaev-Zel’dovich galaxy cluster survey”. In: New A Rev. 47 (Dec. 2003), pp. 933–937. DOI: 10.1016/j.newar.2003.09.008 (cit. on p. 184).

[171] J. T. Dempsey, P. Friberg, T. Jenness, R. P. J. Tilanus, H. S. Thomas, W. S. Holland, D. Bintley, D. S. Berry, E. L. Chapin, A. Chrysostomou, G. R. Davis, A. G. Gibb, H. Parsons, and E. I. Robson.

"SCUBA-2: on-sky calibration using submillimetre standard sources". In: MNRAS 430 (Apr. 2013), pp. 2534–2544. DOI: 10.1093/mnras/stt090. arXiv: 1301.3773 [astro-ph.IM] (cit. on p. 184).

[172] M. Lueker, C. L. Reichardt, K. K. Schaffer, O. Zahn, P. A. R. Ade, K. A. Aird, B. A. Benson, L. E. Bleem, J. E. Carlstrom, C. L. Chang, H.-M. Cho, T. M. Crawford, A. T. Crites, T. de Haan, M. A. Dobbs, E. M. George, N. R. Hall, N. W. Halverson, G. P. Holder, W. L. Holzapfel, J. D. Hrubes, M. Joy, R. Keisler, L. Knox, A. T. Lee, E. M. Leitch, J. J. McMahon, J. Mehl, S. S. Meyer, J. J. Mohr, T. E. Montroy, S. Padin, T. Plagge, C. Pryke, J. E. Ruhl, L. Shaw, E. Shirokoff, H. G. Spieler, B. Stalder, Z. Staniszewski, A. A. Stark, K. Vanderlinde, J. D. Vieira, and R. Williamson. "Measurements of Secondary Cosmic Microwave Background Anisotropies with the South Pole Telescope". In: ApJ 719 (Aug. 2010), pp. 1045–1066. DOI: 10.1088/0004-637X/719/2/1045. arXiv: 0912.4317 (cit. on pp. 184, 202).

[173] NG Czakon, A Vayonakis, J Schlaerth, MI Hollister, S Golwala, PK Day, J-S Gao, J Glenn, H LeDuc, PR Maloney, et al. "Microwave kinetic inductance detector (MKID) camera testing for submillimeter astronomy". In: *AIP Conference Proceedings*. 1185. American Institute of Physics. 2009, pp. 172–175 (cit. on p. 195).

[174] J. Sayers, M. Zemcov, J. Glenn, S. R. Golwala, P. R. Maloney, S. R. Siegel, J. Wheeler, C. Bockstiegel, S. Brugger, N. G. Czakon, P. K. Day, T. P. Downes, R. P. Duan, J. Gao, M. I. Hollister, A. Lam, H. G. LeDuc, B. A. Mazin, S. G. McHugh, D. A. Miller, T. K. Mroczkowski, O. Noroozian, H. T. Nguyen, S. J. Radford, J. A. Schlaerth, A. Vayonakis, P. R. Wilson, and J. Zmuidzinas. "Peculiar Velocity Constraints from Five-Band SZ Effect Measurements Towards RX J1347.5-1145 with MUSIC and Bolocam from the CSO". In: *ArXiv e-prints* (Sept. 2015). arXiv: 1509.02950 (cit. on pp. 195, 205).

[175] S. R. Golwala, C. Bockstiegel, S. Brugger, N. G. Czakon, P. K. Day, T. P. Downes, R. Duan, J. Gao, A. K. Gill, J. Glenn, M. I. Hollister, H. G. LeDuc, P. R. Maloney, B. A. Mazin, S. G. McHugh, D. Miller, O. Noroozian, H. T. Nguyen, J. Sayers, J. A. Schlaerth, S. Siegel, A. K. Vayonakis, P. R. Wilson, and J. Zmuidzinas. "Status of MUSIC, the MUltiwavelength Sub/millimeter Inductance Camera". In: *Society of Photo-Optical Instrumentation Engineers (SPIE) Conference Series*. Vol. 8452. Society of Photo-Optical Instrumentation Engineers (SPIE) Conference Series. Sept. 2012, p. 5. DOI: 10.1117/12.926055. arXiv: 1211.0595 [astro-ph.IM] (cit. on p. 197).

[176] Andrew Gelman and Donald B Rubin. "Inference from iterative simulation using multiple sequences". In: *Statistical science* (1992), pp. 457–472 (cit. on p. 209).